New Materials for Controlled Singlet Oxygen Generation

Susan Callaghan

B. A. (Mod.) in Chemistry

Under the supervision of Prof. Dr. M. O. Senge

Submitted in fulfilment of the requirements for the degree of Doctor of Philosophy in Chemistry

School of Chemistry,

Trinity College Dublin,

The University of Dublin

February 2021

Statement of Authentication

I declare that this thesis has not been submitted as an exercise for a degree at this or any other university and it is entirely my own work.

I agree to deposit this thesis in the University's open access institutional repository or allow the Library to do so on my behalf, subject to Irish Copyright Legislation and Trinity College Library conditions of use and acknowledgement.

I consent to the examiner retaining a copy of the thesis beyond the examining period, should they so wish (EU GDPR May 2018).

Signature: _____

Susan Callaghan

Date: _____

Signature: _____

Prof. Dr. Mathias O. Senge

Date: _____

Summary

Singlet oxygen is notoriously uncontrollable, suffers from poor selectivity, and has fast decomposition rates in biological media. Across the scientific community, there is an enduring effort to refine singlet oxygen interactions to control its chemistry and enhance applications including photodynamic therapy. This body of work outlines the design of photosensitisers that employ interactions between singlet oxygen and aromatic units for therapeutic and oxygen storage applications. We also detail delivery systems that are capable of controlling the site of singlet oxygen generation. These systems were produced across four projects:

- In the first project, pyridone-substituted porphyrins were synthesised as photosensitisers for photodynamic therapy. We used Lindsey condensation and nucleophilic substitution reactions to synthesise tetrasubstituted porphyrins fashioned with pyridone or methylpyridone units. We showed that these compounds could generate singlet oxygen, storage it as an endoperoxide of the pyridone unit, and then slowly thermally release it. For the methylpyridon-substituted porphyrin thermal release occurred at 40 °C over 7 h. The initial design was optimised for biocompatibility using two synthetic strategies: (i) carboxylic acid groups were introduced and (ii) the porphyrin was octasubstituted with polar pyridone units. The optimised systems were capable of singlet oxygen generation, storage, and thermal release *in vitro*. The substitution pattern on the pyridone unit also attributed to the therapeutic effect and we found that the methylpyridone-substituted porphyrins gave a stronger therapeutic effect *in vitro* when compared to the pyridone-substituted porphyrins.
- We also describe a library of heavy-atom free BODIPY-based dyads with anthracene, pyrene, and perylene moieties that can produce singlet oxygen *via* a photoinduced electron transfer mechanism. We studied their absorption and emission properties and related their chemical structure to their singlet oxygen-generating ability. After identifying our most promising candidates, we synthesised a library of water-soluble derivates and tested their efficiency against breast cancer (MDA-MB-468) cells. We then identified our lead

compound, a BODIPY-phenylanthracene dyad, which has an IC_{50} value of 2.8×10^{-7} M. We further characterised its structure using X-ray crystallography and made progress towards an *in vivo* study by studying its phototoxicity against both the F98 and AY27 cell lines.

- We then designed short-chained anthracene strapped porphyrins for oxygen storage applications. The key synthetic step was a [2+2] condensation reaction between a bisaldehyde and a dipyrromethane. The strapped porphyrins also underwent [4+2] cycloaddition reactions across the anthracene strap to produce anthracene endoperoxides. X-ray crystallography showed that macrocyclic distortion was induced upon the introduction of the strap. Additionally, endoperoxide formation occurred on one face of the anthracene moiety. Bathochromic shifts in the absorption profiles of the endoperoxides and strapped porphyrins also indicated macrocyclic distortion. Moreover, we demonstrated, using ^{1}H NMR, the thermal decay of the endoperoxide to the parent porphyrin at 85 °C in DMSO-d_6. The thermal stability of the anthracene endoperoxides suggests that these compounds are promising candidates for molecular singlet oxygen storage devices.
- The laboratory work described in the final project was executed at the lab of Prof. T. Hasan at the Wellman Center for Photomedicine. We constructed a receptor-targeted (Cetuximab) liposome-based nanoconstruct that was capable of delivering a photosensitiser drug (benzoporphyrin derivative, BPD) and Irinotecan specifically to the tumour site. We investigated, using whole animal imaging techniques, the efficiency of the construct against an orthotopic pancreatic cancer model and compared it to commercially available Visudyne and Onivyde regimes. Overall, our construct provided a stronger therapeutic response and, at a low-dose, induced 80 days of tumour growth suppression. We also investigated the targeting specificity of the construct using *ex vivo* histology experiments and found that photodamage caused by our construct was localised to the tumour environment. Finally, we used the same targeting strategy to construct targeted BPD-containing constructs and attempted to excite them with X-ray radiation; however, this was unsuccessful.

Publications

- S. Callaghan, B. E. Vindstad, K. J. Flanagan, T. B. Melø, M. Lindgren, O. A. Gederaas, M. O. Senge, Structural, Photophysical and Photobiological Studies on a Lead BODIPY-anthracene Dyad, submitted article.

- G. Obaid, K. Samkoe, K. Tichauer, S. Bano, Y. Park, Z. Silber, S. Hodge, S. Callaghan, S. Mallidi, B. Pogue, T. Hasan, Establishing the Value of Targeted Nanomedicines as Platforms for Precision Medicine: Enlightening an Enigma with Quantitative Optical Molecular Imaging, submitted article.

- S. Callaghan, K. J. Flanagan, J. E. O' Brien, M. O. Senge, Short-chained Anthracene Strapped Porphyrins and their Endoperoxides, *Eur. J. Org. Chem*. **2020**, 2735–2744.

- S. Callaghan, M. A. Filatov, H. Savoie, R. W. Boyle, M. O. Senge, A lead BODIPY-phenylanthracene dyad for application in photodynamic therapy, Proc. SPIE 11070, 17th International Photodynamic Association World Congress, 110709I (7 August 2019); DOI: 10.1117/12.2525246.

- O. A. Gederaas, H. Husebye, A. Johnsson, S. Callaghan, A. Brunsvik, *In vitro* and *in vivo* effects of HAL on porphyrin production in rat bladder cancer cells AY27, *J. Porphyrins Phthalocyanines* **2019**, *23*, 813–820.

- S. Callaghan, M. A. Filatov, H. Savoie, R. W. Boyle, M. O. Senge, *In vitro* Cytotoxicity of BODIPY-anthracene and -pyrene Dyads for Application in Photodynamic Therapy, *Photochem. Photobiol. Sci.* **2019**, *18*, 495–504.

- S. Callaghan, M. O. Senge, The Good, the Bad, and the Ugly – Controlling Singlet Oxygen through Design of Photosensitizers and Delivery Systems for Photodynamic Therapy, *Photochem. Photobiol. Sci*. **2018**, *17*, 1490–1514.

- M. A. Filatov, S. Karuthedath, P. M. Polestshuk, S. Callaghan, K. J. Flanagan, M. Telitchko, T. Wiesner, F. Laquai, M. O. Senge, BODIPY-pyrene and perylene Dyads as Heavy Atom-free Singlet Oxygen Sensitizers, *ChemPhotoChem* **2018**, *2*, 1–11.

- M. A. Filatov, S. Karuthedath, P. M. Polestshuk, S. Callaghan, K. J. Flanagan, M. Telitchko, T. Wiesner, F. Laquai, M. O. Senge, Control of Triplet State Generation in Heavy Atom-free BODIPY-anthracene Dyads by Media Polarity and Structural Factors, *Phys. Chem. Chem. Phys.* **2018**, *20*, 8016–803.

- S. Callaghan, M. A. Filatov, E. Sitte, H. Savoie, R. W. Boyle, K. J. Flanagan, M. O. Senge, Delayed Release Singlet Oxygen Sensitizers based on Pyridone-appended Porphyrins, *Photochem. Photobiol. Sci.* **2017**, *16*, 1371–1374.

- **Cover Picture** “Delayed Release Singlet Oxygen Sensitizers based on Pyridone-appended Porphyrins” *Photochem. Photobiol. Sci*. **2017**, *16*, 1371–1374.

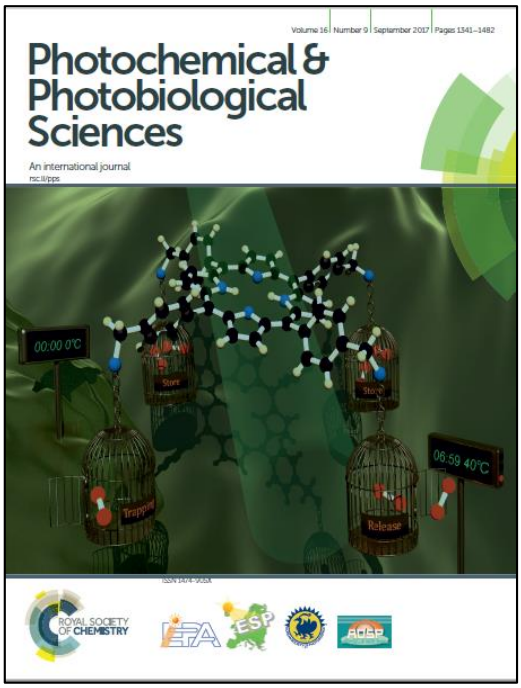

- **Inside Cover Picture** “The Good, the Bad, and the Ugly – Controlling Singlet Oxygen through Design of Photosensitizers and Delivery Systems for Photodynamic Therapy” *Photochem. Photobiol. Sci*. **2018**, *17*, 1490–1514.

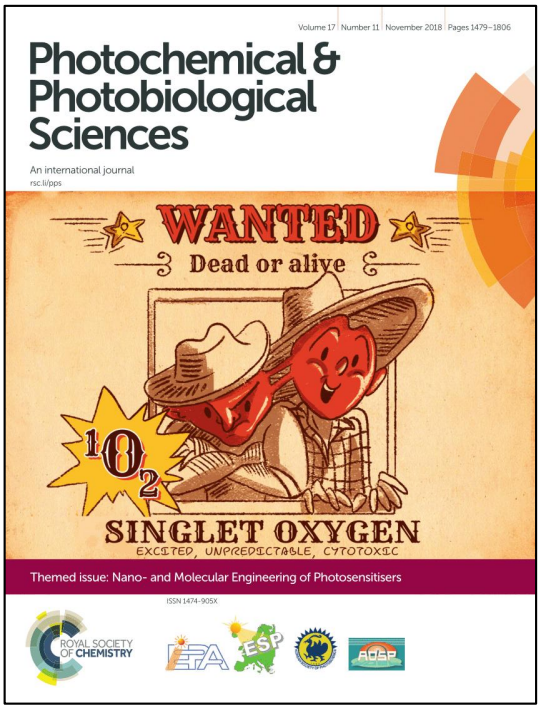

Conference Abstracts

Poster Presentations:

- S. Callaghan, M. A. Filatov, H. Savoie, R. W. Boyle, and M. O. Senge, "*In vitro* cytotoxicity and design of heavy-atom free BODIPY dyads for application in photodynamic therapy", in 17th International Photodynamic Association World Congress (28.06.19–04.07.19) Boston, USA, Abstract number: 11070–11321.

- S. Callaghan, M. A. Filatov, H. Savoie, R. W. Boyle, and M. O. Senge, "Heavy-atom Free BODIPY Based Photosensitizers for Application in Photomedicine", 27th PhotoIUPAC, Dublin (08.07.18–13.07.18), University College Dublin, Dublin, Ireland, Abstract P20.

- S. Callaghan, M. A. Filatov, and M. O. Senge "Turning on the Light: *In Vitro* Fluorescent Visualization of Oxidative Stress using Novel BODIPY Dyad Systems" in 16th Annual Symposium of the Centre for Synthesis and Chemical Biology (08.12.17), University College Dublin, Dublin, Ireland, Abstract P62.

- S. Callaghan, M. A. Filatov, H. Savoie, R. W. Boyle, and M. O. Senge "Turning on the Light: *In Vitro* Fluorescent Visualization of Oxidative Stress using Novel BODIPY Dyad Systems" in TetraPyrrole Discussion Group Meeting (11.09.17–13.09.17), The University of Sheffield, UK, P28.

- S. Callaghan, M. A. Filatov, H. Savoie, R. W. Boyle, and M. O. Senge "Turning on the Light: *In Vitro* Fluorescent Visualization of Oxidative Stress using Novel BODIPY Dyad Systems" in the 17th Congress of the European Society for Photobiology (4.09.17–8.09.17), Pisa Conference Center, Italy, P35.

- S. Callaghan, M. A. Filatov, H. Savoie, R. W. Boyle, and M. O. Senge “Novel Dyad Systems for Application in Photodynamic Therapy (PDT)” in the 16th International Photodynamic Association World Congress (08.06.17–13.06.17), University of Coimbra, Portugal, P19.

- S. Callaghan, M. A. Filatov, and M. O. Senge, “New Molecular Devices for the Control of Singlet Oxygen Generation in Photonic and Biomedical Applications” in Centre for Synthesis and Chemical Biology (09.12.16), Dublin, Ireland, P14.

- S. Callaghan, M. A. Filatov, and M. O. Senge, “New Molecular Devices for the Control of Singlet Oxygen Generation in Photonic and Biomedical Applications” in European Society for Photobiology Summer School (20.06.16–25.06.16), Brixen/Bressanone, Italy, P5.

Oral Presentations:

- S. Callaghan “Singlet Oxygen Traps: From Synthesis to Phototherapy” oral presentation at BOC Gases Award Presentation at Trinity College Dublin, (16.01.2020), Dublin, Ireland.

- S. Callaghan and M. O. Senge, “Trapping Singlet Oxygen: from Synthesis to Therapeutics” oral presentation at University College Dublin (28.05.2019), Dublin, Ireland.

- S. Callaghan, “Singlet oxygen traps: from synthesis to phototherapy” oral presentation at 17th International Photodynamic Association World Congress (28.06.2019-04.07.2019) Boston, USA. Talk in Session 6: Photosensitizing Systems, June 29th, Abstract number 11070–420.

- S. Callaghan “Beyond Photosensitization: The Chemical Binding of Singlet Oxygen for Application in Therapeutics and Diagnostics” in TetraPyrrole Discussion Group Meeting (11.09.17–13.09.17) at The University of Sheffield, UK, P26.7.

Acknowledgements

In the context of the enclosed work, I would like to take this opportunity to thank everyone who brought this thesis to *light*. Firstly, I would like to thank Prof. Dr. M. O. Senge for introducing me to the concept of photodynamic therapy and for kick-starting my scientific career. His continuous guidance, patience, and support from when I first joined his lab as an intern in 2015 has certainly led to the successful completion of this body of work. Working in his group has afforded me both professional and personal experiences that I would not have accumulated in any other research setting. I would also like to thank all the past and present members of the Senge research group, in particular, our lab managers Dr. S. Bernhard and Dr. N. Grover. Dr. M. Filatov deserves a special thank you for leading the photomedical project for the first year and a half of my PhD studies. His invaluable knowledge and intellectual input greatly contributed to both a steep initial learning curve and successful start to my PhD. The discussion of my work includes experiments carried out by our collaborators from the groups of Prof. R. W. Boyle in the University of Hull and Prof. F. Laquai in King Abdullah University of Science and Technology as well as work carried out by Dr. P. Polestshuk from Moscow State University. Additionally, I would like to thank Prof. M. Lindgren and Prof. O. A. Gederaas and Prof. T. Hasan for collaborations that lead to research trips and for facilitating the interdisciplinary nature of this thesis. These research trips and my training at the Senge group allowed me to develop a diverse skill set that I can bring forward to my future career. I would also like to thank Dr. J. O' Brien, Dr. M. Ruether, Dr. M. Feeney, and Dr. G. Hessman who helped with the characterisation of the compounds in this thesis. I would like to thank The Irish Research Council for supporting my PhD studies with a Postgraduate of Ireland Scholarship. Additional thanks to the Royal Society of Chemistry and Science Foundation Ireland for funding conference travel and research trip costs. Finally, I would like to thank my family, Mum, Dad, Ronan, and Shane, for making Mayo my oasis and supporting my studies in every way possible. I promise I'm finished with school now!

List of Abbreviations

AF488	Alexa fluor 488
ALA	Aminolevulinic acid
BAD	BODIPY anthracene dyad
BINAP	2,2′-Bis(diphenylphosphino)-1,1′-binaphthyl
BODIPY	Boron-dipyrromethene/4,4-difluoro-4-bora-3a,4a-diaza-s-indacene
BPD	Benzoporphyrin derivative monoacid ring A
BPD-PC	Benzoporphyrin derivative 20:0 lyso phosphocholine
[C2mim][OAc]	1-Ethyl-3-methylimidazolium acetate
calcd.	Calculated
Cet	Cetuximab
COX-2	Cyclooxygenase-2
CSS	Charge-separated state
3D	3-Dimensional
d	Doublet
DCM	Dichloromethane
dd	Doublet of doublets
DDQ	2,3-Dichloro-5,6-dicyano-1,4-benzoquinone
DIBAL	Diisobutylaluminium hydride
DIBO	Dibenzocyclooctyne
DIPEA	*N,N*-Diisopropylethylamine
DMF	Dimethylformamide

DMPC	1,2-Dimyristoyl-sn-glycero-3-phosphocholine
DMSO	Dimethyl sulfoxide
DMSO-*d*$_6$	Deuterated dimethyl sulfoxide
DNA	Deoxyribonucleic
DOPG	1,2-Dioleoylphosphatidylglycerol
DPBF	1,3-Diphenylisobenzofuran
DPBS	Dulbecco's phosphate
DPM	Dipyrromethane
DPPC	Dipalmitoylphosphatidylcholine
DSPC	1,2-Distearoyl-sn-glycero-3-phosphocholine
DSPE-mPEG2000	1,2-Distearoyl-sn-glycero-3-phosphoethanolamine-N-[carboxy (polyethylene glycol)-2000]
EC_{50}	Half maximal effective concentration
EDC	1-Ethyl-3-(3-dimethylaminopropyl)carbodiimide
EGFR	Epidermal growth factor receptor
EMA	European Medicines Agency
EPR	Enhanced permeability and retention
eq.	Equivalents
ESI	Electrospray ionisation
ET	Electron transfer
Et	Ethyl
et al.	et alia (and others)
EtOAc	Ethyl acetate
EtOH	Ethanol
Et_2O	Diethyl ether

Ex.	Excitation
FDA	Food and drug administration (U.S.A.)
HEPES	4-(2-hydroxyethyl)-1-piperazineethanesulfonic acid
HOMO	Highest occupied molecular orbital
H_2TPP	Free base tetraphenylporphyrin
Hp	Hematoporphyrin
HpD	Hematoporphyrin derivative
HPF	Hydroxyphenyl fluorescein
HRMS	High resolution mass spectrometry
IgG	Immunoglobulin G
IR	Infrared
ISC	Intersystem crossing
J	Coupling constant
LCMS	Liquid chromatography mass spectrometry
LD_{50}	Lethal dose where 50% of the cells are killed
LUMO	Lowest unoccupied molecular orbital
m	Multiplet
MALDI	Matrix assisted laser desorption ionization
MB	Methlyene blue
MeOH	Methanol
MMP	Matrix metallopeptidases
M.P.	Melting point
***m*THPC**	5,10,15,20-Tetrakis(hydroxymethyl)phosphonium chloride
MTS	3-(4,5-Dimethylthiazol-2-yl)-5-(3-carboxymethoxyphenyl)-2-(4-sulfophenyl)-2H-tetrazolium

MTT	3-(4,5-Dimethylthiazol-2-yl)-2,5-diphenyltetrazolium bromide
m/z	mass/charge
NBS	N-Bromosuccinimide
***n*-BuLi**	*n*-Butyllithium
NHS	N-Hydroxysuccinimide
NIR	Near infrared
NMR	Nuclear magnetic resonance
NSD	Normal-coordinate structural decomposition
Ox.	Oxidation
PBS	Phosphate-buffered saline
PDI	Polydispersion index
PDT	Photodynamic therapy
PEG	Polyethylene glycol
PeT	Photoinduced electron transfer
Ph	Phenyl
PhLi	Phenyllithium
ppm	Parts per million
PS	Photosensitiser
PUVA	Psoralen and ultraviolet A
Q-Tof	Quad-time of flight
RB	Rose Bengal
R_f	Retention factor
RPM	Revolutions per minute
rt	Room temperature
ROS	Reactive oxygen species

SCID	Severe combined immunodeficiency
SOSG	Singlet oxygen sensor green
t	Triplet
TEA	Triethylamine
TEG	Triethylene glycol
TFA	Trifluoroacetic acid
THF	Tetrahydrofuran
TPMIL	Targeted activatable multi inhibitory liposome
vs.	Versus
UV	Ultraviolet
UV-vis	Ultraviolet-visable spectroscopy
VEGF	Vascular endothelial growth factor

Explanatory note

The nomenclature used for the BODIPY and porphyrin cores through this work is as follows:

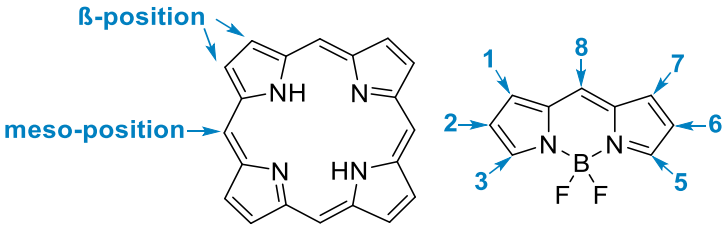

Table of Contents

Chapter 1: General Introduction

"universal cure"

Sidney Farber 1962

"The next step – the complete cure - is almost sure to follow"

Kenneth Endicott 1963

"We have a cure for breast cancer"

Emil Frei 1982

"It is now conceivable that our children's children will know the term cancer only as a constellation of stars"

Bill Clinton 2000

"Like many of you, I believe that the United States of America should be the country that ends cancer once and for all"

Barack Obama 2016

"Those who have not been trained in chemistry or medicine may not realise how difficult the problem of cancer treatment really is. It is almost-not quite, but almost-as hard as finding some agent that will dissolve away the left ear, say, and leave the right ear unharmed. So slight is the difference between the cancer cell and its normal ancestor."

William Woglom 1947

1.1 HISTORICAL CONTEXT

1.1.1 A brief history of cancer therapy

As we are aware, a cure for cancer remains elusive and as our collective understanding of the disease increases, it is becoming abundantly clear that the 'one shoe fits all' approach is not going to suffice. The word 'cancer', an umbrella term for diseases characterised by uncontrolled cell division, originates from the

Ancient Greek physician Hippocrates who referred to tumours as carcinos and carcinomas, deriving from the Greek word for crab. This was later translated to the Latin word cancer.[1] Even early Egyptians were aware of the disease; the Edwin Smith Papyrus provides a detailed description of breast tumours as 'like touching a ball of wrappings, or they may be compared to the unripe hemat fruit, which is hard and cool to the touch'. As for the authors comments regarding "therapy", "there is none".[2,3] Medical science has made steady advancements since these treatises but the turn of the 20th century marked an explosion of scientific knowledge and resultant modern treatment options. At the dawn of the 1900s, cancer therapy was dominated by surgery including William Halsted's radical mastectomy, in which the breast, muscles, and axillary lymph nodes were removed. Although success was noted for locally contained tumours, the mechanism of metastasis was not well understood, with many believing that if cancer occurred in a secondary location, it was not linked to the initial disease.[4]

Röntgen's discovery of X-rays in 1895 opened the door to new avenues of medical technologies. Among the first doctors to employ radiation therapy was Grubbe from Chicago who used X-rays to treat metastatic reoccurring breast cancer.[5] In 1898, the Curies discovered and later described the physiologic effects of radium, which could be inserted into tumours to give high radiation doses.[6] The obvious flaw in this approach, as with surgery, was that the cancers had to be detected early and display slow metastasis for effective treatment. The increased dose also highlighted another limitation of radiation therapy; namely, that it was itself cancer-causing. Both Marie Curie and Grubbe died riddled with cancer resulting from their career-long exposure to carcinogenic agents. In the decades that followed, radiation therapy evolved into a front line cancer therapy with breakthroughs including the discovery of high-energy γ-rays used in cobalt teletherapy,[7] electron linear accelerators,[8] and more recently, the development of stereotactic radiation therapy.[9]

In the mid-1900s, a new age of cancer therapy was ushered in with the first chemotherapeutic drug, Mustine (**1.1**), a member of the nitrogen mustard gas family. Nitrogen mustard gas had already proved itself as an agent of chemical warfare in World War I and its capacity to obliterate white blood cells, the Krumbhaar effect, was exploited by Goodman and Gilman to develop a new cancer therapy.[10] In 1942,

they tested their theory on a lymphoma patient but after an initial positive response, the patient relapsed. Their results were not published until after the war in 1946.[11] In the preceding years, it was found, with major contributions from chemist Haddow,[12] that the chlorine atoms were integral to the toxic chemical effects of these agents and later that the mechanism of action is related to the crosslinking of double-strand deoxyribonucleic acid (DNA) resulting in the cessation of cell division.[13] Bendamustine (**1.2**), Cyclophosphamide (**1.3**), and Chlorambucil (**1.4**), all mustard gas derivatives, are used today for the treatment of a range of cancers including chronic lymphocytic leukaemia and non-Hodgkin's lymphoma (**Fig. 1.1**).[14]

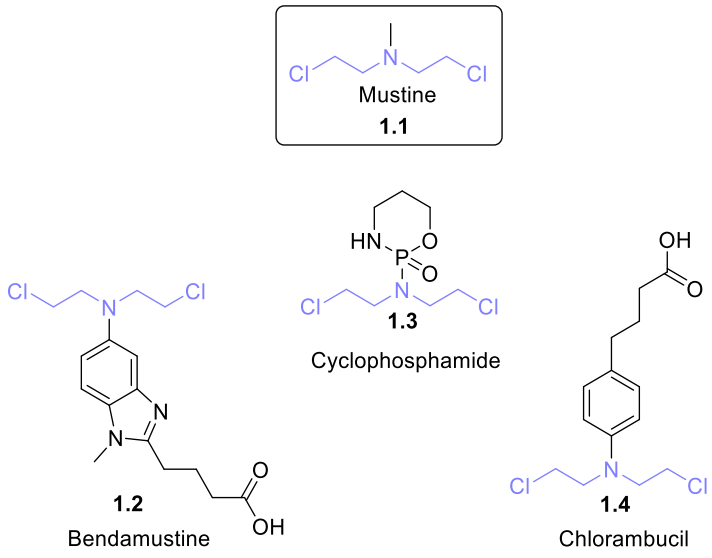

Figure 1.1: Structure of the first mustard gas, Mustine, and some of its contemporary derivatives.

Another notable early chemotherapeutic study was conducted by Farber. In 1946, he injected paediatric leukaemia patients with folic acid (**1.5**) based on a misguided interpretation of earlier work showing that the administration of folic acid to malnourished patients with blood disorders led to normal blood cell production. However, in the leukaemia patients, the administration of folic acid resulted in an acceleration of cancer growth due to the integral role of folic acid in DNA replication. Undeterred, in a reversal of logic, he reasoned that using folate antagonists to block the folate receptor could stagnate the growth of white blood cells. The folic acid antagonist, Aminopterin **1.6**, a competitive inhibitor of the enzyme dihydrofolate reductase (**Fig. 1.2**), was used to treat sixteen patients. Ten responded and for the first time a temporary remission was induced in childhood leukaemia patients but all

of the patients relapsed after a few months. His results were published in 1948 as the first reported treatment for cancer of bodily fluids as opposed to solid tumours.[15] In the mid-1950s, another anti-folate, Methotrexate (Amethopterin, **1.7**) was used to induce complete remission in a patient with choriocarcinoma and chorioadenoma.[16,17]

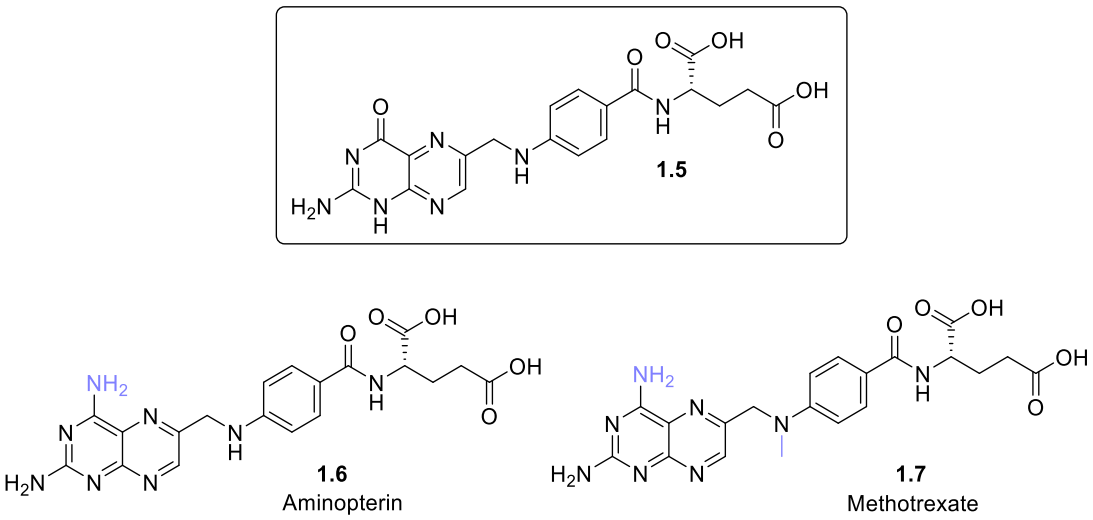

Figure 1.2: Structure of folic acid and its antagonists Aminopterin and Methotrexate.

There was great hope for a 'universal cure' in the years following Farber's work and an arsenal of chemotherapeutic drugs including natural product extracts Paclitaxel (Taxol)[18] and Vincristine,[19] metal-containing, Cisplatin,[20,21] Tamoxifen, an estrogen receptor modulator,[22] and antimetabolite, Fluorouracil,[23] were developed throughout the 1960s and 1970s; however, with many of the clinical trials only short remissions were induced. One explanation proposed for the relapses was acquired resistance to a single drug over time. From these observations, the scientific community reasoned that the administration of several drugs simultaneously would combat this. Thus, the age of combination chemotherapy and adjuvant therapies was born. This concept met opposition in the early days as higher drug doses also increased toxicity. On the other hand, others including Skipper were advocating for complete cell killing. Moreover, Skipper advised that the number of cancer cells present was linked to curability.[24,25]

Early regimes developed by DeVita had a high cost and patients on the MOMP regime (Methotrexate, Vincristine (Oncovin), Cyclophosphamide, and Prednisone) were hospitalised due to toxic drug effects.[26] Later Methotrexate was substituted with Procarbazine and the treatment duration was extended leading to the MOPP regime. It was first used to treat childhood acute lymphocytic leukaemia and later was found to cure patients with Hodgkin's lymphoma and non-Hodgkin's lymphoma.[27] In 1963, Carbone surgically removed breast tumours and then treated his patients with a round of chemotherapy to remove any remaining cancer cells. He noted that there was a marked decrease in the rate of relapse among his patients. This theory was later developed by Bonadonna[28] and although not a complete cure his clinical trial prevented relapse in one out of six patients.[29]

A final class of cancer therapies that brings us up to the 21st century are immunotherapeutics, which employ the immune system to elicit a therapeutic response. The most widely used class of immunotherapeutic agents are monoclonal antibodies, which are used to stimulate an immune response against cancer cells. In 1997, Rituximab, an IgG1 (immunoglobulin G) antibody, which targets cell surface receptor CD20, was approved by the Food and Drug Administration (FDA) for the treatment of non-Hodgkin's lymphoma.[30] In 1998, Trastuzumab (Herceptin), an antibody, which blocks the HER2-neu receptor, was approved by the FDA as the first antibody to be used to treat solid tumours and is widely used in the treatment of breast cancer.[31] These drugs are highly specific; however, high costs accompanied by their short shelf life has hindered universal application. For example, it costs approximately €42,000 to treat a leukaemia patient with the immunotherapeutic Alemtuzumab for one year. Another immunotherapy strategy is 'active cellular therapy' in which immune cells are removed from a patient and modified to attack tumour cells before being re-administered. One of these personalised therapies uses Sipuleucel-T (Provenge), an immunotherapy vaccine, which was approved in 2010 for the treatment of metastatic castration-resistant prostate cancer. It targets prostate acid phosphatase, an antigen expressed in prostate cancer (**Fig. 1.3**).[32]

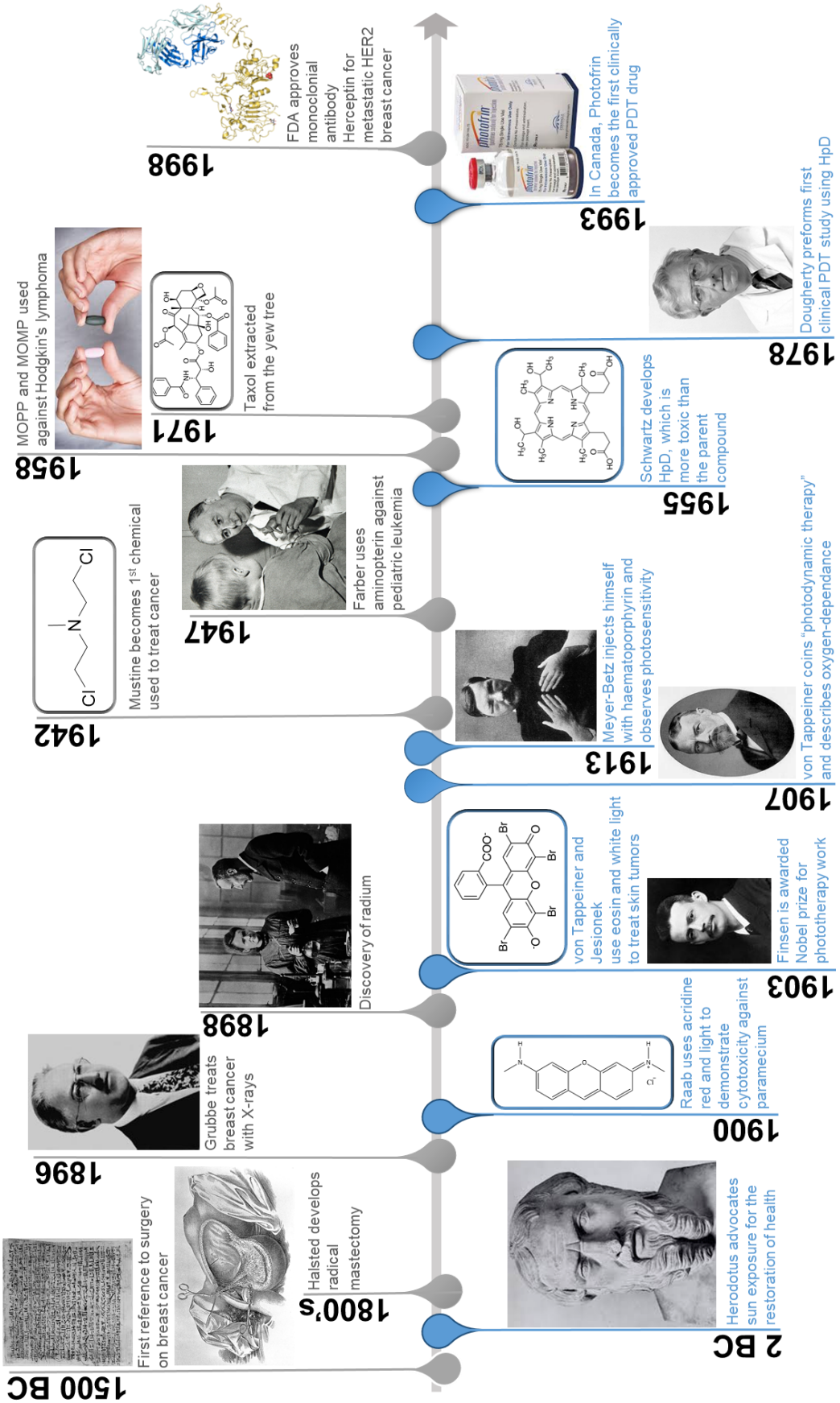

Figure 1.3: Timeline of historic milestones in cancer treatment (top) and photodynamic therapy (PDT, bottom).

1.1.2 The emergence of phototherapy

If the last century of oncology research has taught us anything it is that cancer is not one illness but a myriad of diseases all with distinct characteristics, prognoses, genetic markers, and mechanisms of action. So, instead of the 'universal cure', our canon will have to consist of a wide variety of treatment regimes and protocols. Alongside frontline therapies including surgery, radiation therapy, and chemotherapy, another treatment is attempting to find its feet in the realm of clinical oncology. Like the other treatments discussed, modern photomedicine has arisen from the dust of the 20th century. Phototherapy, using light to treat illness, has a long and rich history that can be traced to the beginning of medical practice.

Light's therapeutic capacity was realised by many ancient civilisations and can be linked to sun worship in many ancient religions. Ancient Egyptians used light and a plant, *Ammi majus* or bishop's weed, to treat vitiligo.[3] Another early advocate of light for health restoration was the Ancient Greek historian, Herodotus, who correlated bone strength with exposure to sunlight in a passage from "The Histories": "I noticed that the skulls of the Persians are so thin that the merest touch with a pebble will pierce them, but those of the Egyptians on the other hand [are] so tough that it is hardly possible to break them with a stone. I was told…that the reason was that the Egyptians shave their heads from childhood so that the bone of the skull is indurated by the sun".[33]

These sentiments continued throughout the centuries. In the 1800s it was known that sunlight had anti-bacterial properties[34] and in 1890, Palm treated rickets with phototherapy.[35] In the late 1800s, work by Finsen dubbed the 'grandfather of phototherapy', "opened a new avenue for medical science".[36] He is best known for employing the anti-bacterial properties of ultraviolet (UV) light to treat Lupus vulgaris, a disfiguring infection commonly found on the head and neck and for the development of the electric carbon arc lamp.[37] In 1899, he published a seminal book entitled 'Phototherapy'[38] and his career culminated in the 1903 Nobel prize one year before his death at the age of 43. UV light continued to be used in photomedicine throughout the 1900s; some examples include the treatment of arteriosclerosis, gout, diabetes, obesity, and respiratory tract infections.[39] The American Medical Association conducted a review of UV therapy in dermatology in 1932 and

documented 34 conditions that could benefit from phototherapy. Today, due to medical advancements including the development of antibiotics, UV treatment is not as prevalent as it once was; however, UV-B light is still employed in dermatology, most notably for the treatment of psoriasis.[40] Additionally, psoriasis can also be treated with UV-A and the drug 8-methoxypsoralen, in a treatment known as Psoralen and ultraviolet A (PUVA). This was first reported in 1974 by Parrish, Fitzpatrick, Tanenbaum, and Pathak who cleared psoriasis in all of their 21 patients.[41]

In addition to direct light treatment, another photomedical concept, the generation of toxic species by interactions between light and a chemical substance, gained traction in the early 1900s. The first report of what was later to be known as the photodynamic effect was serendipitously discovered by Raab, a student of von Tappeiner, who, while working with *Paramecium caudatum*, noticed that the cells died upon exposure to acridine orange and light but did not die if exposed to either alone.[42] von Tappeiner, together with dermatologist Jesionek, proceeded with this work and transitioned the photodynamic effect to a subclass of phototherapy by treating lupus and skin cancers with eosin.[43,44] In 1904, von Tappeiner demonstrated the phenomenon's oxygen-dependence and later coined the phrase "photodynamic therapy" (PDT), referring to oxygen dependant photosensitisation as opposed to the photosensitisation reactions used for developing photographic plates.[45,46]

In 1913, Meyer-Betz injected himself with 200 mg of hematoporphyrin, a compound derived from blood and first described by Scherer in 1841.[47] Although Scherer did not resolve the structure, the compound he prepared was a derivative of naturally occurring protoporphyrin IX. Upon exposure to light, Meyer-Betz experienced a severe photodynamic response involving blistering and swelling of the skin.[48] This was the first report of photosensitisation in humans, although earlier work by Hausmann and Pfeiffer described the effect in animals.[49–51] The development of the field was impeded by the First and Second World Wars but slowly the idea that this oxygen-dependent photosensitisation reaction could be used as a therapy emerged. In 1924, Policard observed that fluorescence in tumours was due to the selective accumulation of hematoporphyrin.[52] Auler and Banzer later confirmed these results

and then went on to show that the photodynamic effect could induce tumour necrosis in animals with Jensen's sarcoma and Flicks-Jobling carcinomas using a quartz lamp for the illumination step.[53] In 1948, the potential for hematoporphyrin in diagnostics was realised by Figge but the high phototoxicity of hematoporphyrin prevented diagnostics from becoming a mainstream application.[54]

Until this point, what was considered 'hematoporphyrin' was a mixture of porphyrins derived from blood. Schwartz and co-workers isolated hematoporphyrin but found it accumulated poorly in tumours. Another fraction that was treated with acid was identified to be more active and accumulated readily; however, Schwartz failed to identify the structure.[55] Lipson and Baldes used this hematoporphyrin derivative for the detection of a range of cancers including cancer of the cervix and the oesophagus[56,57] and later, in the first human patient, as a theragnostic agent for breast carcinoma (**Fig. 1.4**).[58]

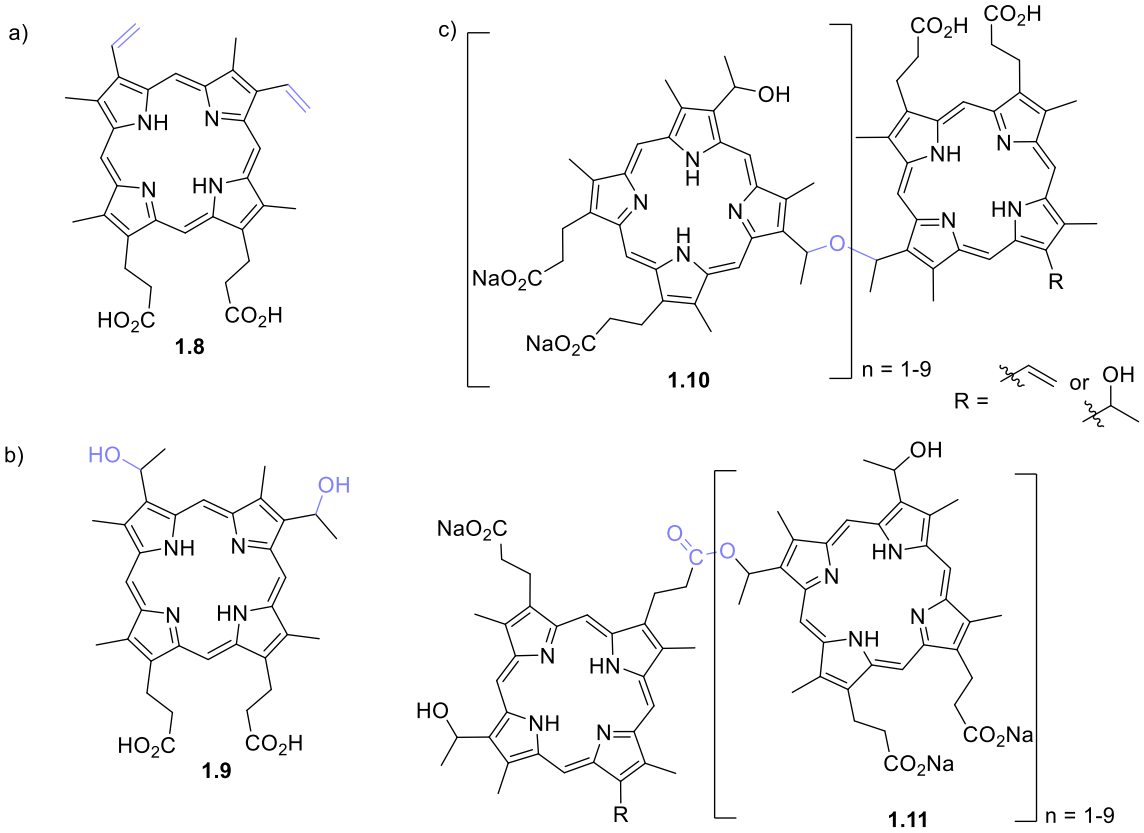

Figure 1.4: a) Protoporphyrin, b) hematoporphyrin, c) ester and/or ether linkage found in hematoporphyrin derivatives.

If Finsen is known as the 'grandfather of phototherapy', the title of 'father of phototherapy' goes to Dougherty. His early *in vivo* work produced reports of long term cures for tumours treated with hematoporphyrin derivative.[59] This work, along with others,[60,61] inspired the first human clinical trials involving PDT and an extensive study on a variety of cancers including carcinomas (breast, colon, prostate, squamous cell, basal cell, and endometrium), malignant melanoma, mycosis fungoides, chondrosarcoma, and angiosarcoma was published in 1978. They administered hematoporphyrin derivative and then exposed the malignant areas to red light. Results showed a response in 111 of the 113 malignant lesions.[62] This was followed with a litany of trials using hematoporphyrin derivative[63–65] and in 1993 Photofrin (commercial formulation of hematoporphyrin derivative) became the first PDT drug to be approved for clinical use against bladder cancer in Canada.[66] This was followed by the United States FDA approval in 1995 for the palliative treatment of oesophageal cancer.[67] Since then, many PDT drugs have been approved for clinical use including aminolevulinic acid (ALA)-based Levulan, which was shown by Kennedy, Pottier, and Pross[68] to metabolise to protoporphyrin IX. These compounds, along with other clinically relevant photosensitisers, will be discussed later in more detail.

A final aspect of phototherapy worth noting due to its continued clinical use is the treatment of neonatal jaundice with UV light. Like many origin stories, the story of phototherapy to treat hyperbilirubinemia (jaundice) began by chance. A nun at the premature unit at Rochford General Hospital in England, Sister Ward, was a firm believer in the benefits of sunshine and fresh air for new-born babies. She noticed that patches of skin not directly exposed to sunlight remained yellow while the rest of the body did not. These observations led researchers at Rochford Hospital to investigate further and they noted that bilirubin pigment levels in blood left in the sun dropped dramatically. This was followed by a controlled study and the results were published in 1958.[69] The therapy works by converting bilirubin into more soluble isomers that can be easily excreted. In 1968, Lucey published work that confirmed that phototherapy could be used as a safe and reliable treatment for neonatal jaundice and it became widely used by the 1980s (**Fig. 1.3**).[70]

1.2 PHOTODYNAMIC THERAPY

1.2.1 Overview of photodynamic therapy

Since its inception, PDT has established itself as a safe and reliable treatment for various cancers,[71,72] dermatological conditions,[73,74] age-related macular degeneration,[75] and has also gained traction in other areas including several infectious diseases.[76] Its underlying mechanism is well studied and understood and it is now accepted as a mainstream clinical therapy.[67]

PDT relies on the interaction between light, a photosensitiser, and ground-state triplet oxygen to produce singlet oxygen and/or other reactive oxygen species including hydroxyl radicals and superoxides. Firstly, a photosensitising drug is administered and 24-72 h are allowed to elapse to facilitate photosensitiser accumulation in the target tissue before the photosensitiser is selectively activated with light of an appropriate wavelength. Once triggered by light, the photosensitiser is promoted to an excited singlet state and then, *via* intersystem crossing, a longer-lived triplet state is occupied. From here reactive oxygen species, including singlet oxygen, are produced and depending on the cellular localisation of the photosensitiser and the degree of damage caused, cell death is induced (**Fig. 1.5**).[67] The extent of the photodynamic effect is reliant on photosensitiser distribution and localisation, both light and photosensitiser dose, photosensitiser clearance rates, and the degree of oxygenation in the target tissue.

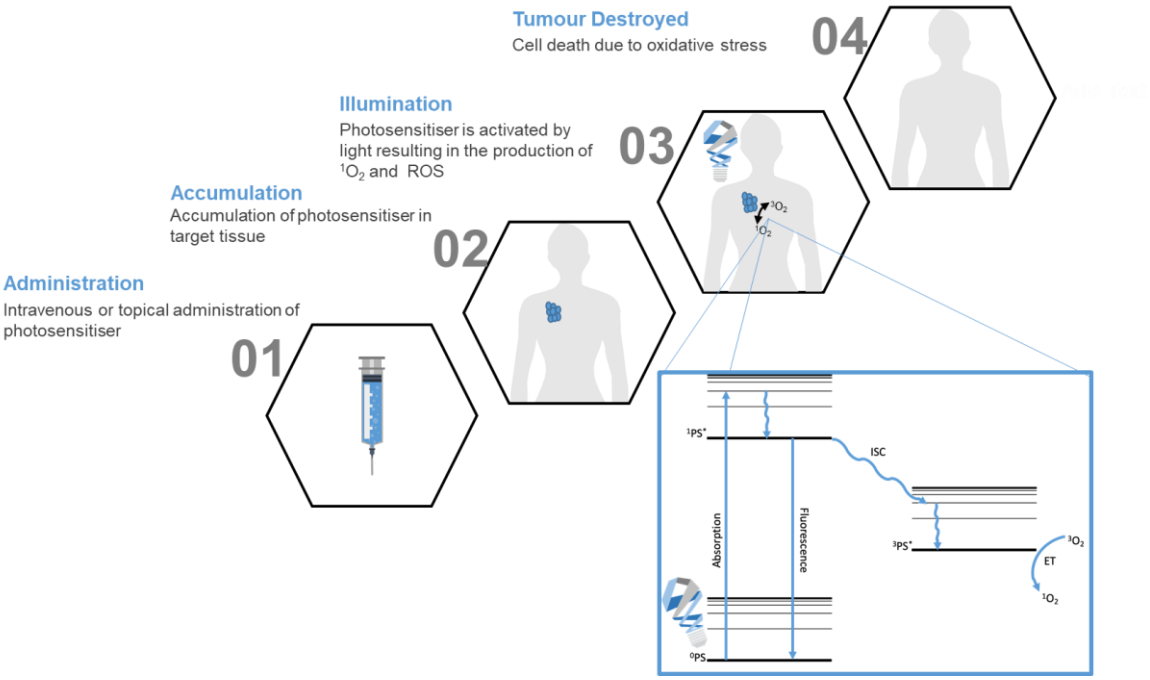

Figure 1.5: Schematic representation of PDT and Jablonski diagram representing the classic PDT mechanism (ROS = reactive oxygen species, ET = electron transfer, and ISC = intersystem crossing).

1.2.2 Singlet oxygen, reactive oxygen species, and photodynamic therapy

Singlet oxygen is integral to PDT as it is the principal cytotoxic agent that affords the therapeutic effect. Triplet oxygen is converted directly to singlet oxygen, *via* energy transfer, in Type II reactions.[77] The increased reactivity of singlet oxygen compared to triplet oxygen arises from the spin-paired electrons found in the π* orbital of singlet oxygen, as shown in **Fig. 1.6**. In contrast, in triplet oxygen, the two highest energy electrons are shared between two degenerate π* orbitals, resulting in a more stable configuration. Singlet oxygen can diffuse in cells (0.01–0.02 μm)[78] and has relatively fast decomposition (in the μs range) rates in cytoplasm, although newer studies suggest that at least the half-life may be longer than previously believed.[79] Singlet oxygen can be detected directly by its phosphorescence at 1275 nm or indirectly using fluorescent probes, some of which (including singlet oxygen sensor green (SOSG)), are suitable for biological systems.[80]

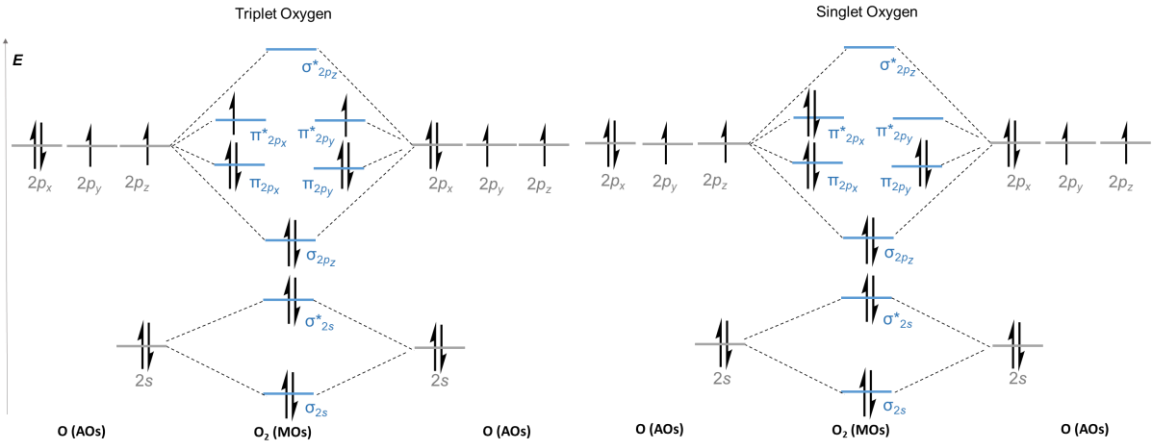

Figure 1.6: Electronic configuration of triplet and singlet oxygen.

In the Type 1 pathway, either a proton or an electron is transferred to an organic molecule in the cell to form radical anions and cations. Alternatively, electrons are transferred to molecular oxygen to form a superoxide anion, which is not particularly cytotoxic. This superoxide undergoes dismutation to form hydrogen peroxide, which plays a role in the function of many enzymes, and oxygen. Superoxides can also reduce metals that take part in the Fenton reaction,[81] in which hydroxide ions are converted to hydroxyl radicals and hydroxide ions, thus producing important reactive oxygen species. Superoxides can also produce peroxynitrite and singlet oxygen by reacting with nitric oxide and the hydroxyl radical, respectively.[77,82]

Reactive oxygen species and singlet oxygen induce direct photodamage in cells through oxidative stress. Hydroxyl radicals can either add to or oxidise carbon-containing biomacromolecules to form other highly reactive radicals that can then undergo chain reactions and cause extensive oxidative damage. Singlet oxygen induces oxidative stress by directly oxidising amino acids, including tryptophan, and unsaturated phospholipids to form hydroperoxides, resulting in loss of protein function or the initiation of chain reactions in the presence of transition metals, respectively.[83] The base pairs of DNA, especially guanine, can undergo cycloaddition reactions with singlet oxygen across the purine rings to form an unstable endoperoxides. Following subsequent rearrangement reactions and the formation of 8-oxo-G, G-C:T-A transversions can occur, which induce oxidative stress reponses including the expression of ICAM-1 and interleukins, genes involved with inflammation and cell damage.[84]

1.3.1 Synthesis and properties of porphyrins and BODIPYs

The structures of five leading PDT drugs currently in clinical use or of clinical interest are displayed in **Fig. 1.7**. There is a striking commonality in that they are all tetrapyrroles - this is not a coincidence. The chemical properties of this class of compounds, as well as their cousins the BODIPYs (boron dipyrromethenes), are particularly suited for application as photodynamic agents.

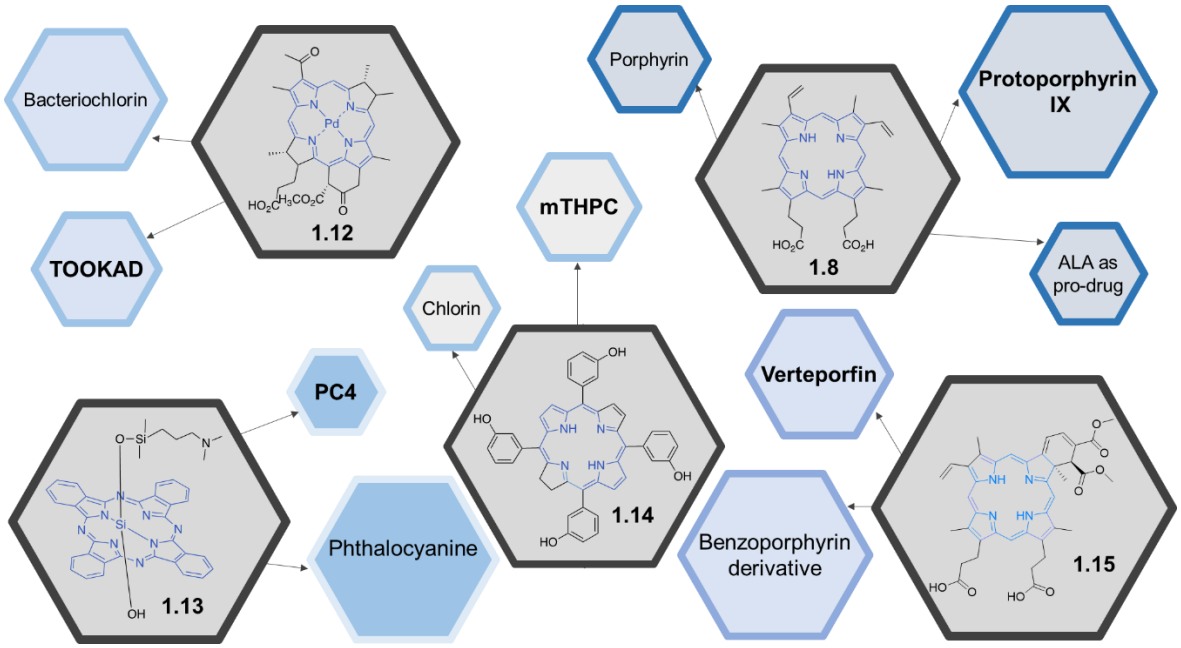

Figure 1.7: A selection of photosensitisers displaying the role of tetrapyrroles in the chemistry of photodynamic therapy.

The porphyrin core consists of four pyrrolic units connected *via* methine bridges to form a 22π-electron system, of which 18π-electrons are involved in aromaticity. Since Küster suggested the structure in 1912,[85] a range of derivatives have been discovered and applied to PDT. Members of the tetrapyrrole family differ by the modulation of their π-system, i.e. the degree of reduction (chlorin and bacteriochlorin) or the inclusion of heteroatoms (phthalocyanine). Additionally, in recent years, BODIPYs have established themselves as a promising class of compounds for PDT.[86] The first BODIPY was synthesised by Treibs and Kreuzer in

1968[87] and the structure consists of a dipyrromethene core with difluoroboron inserted at the nitrogen positions (**Fig. 1.8**).

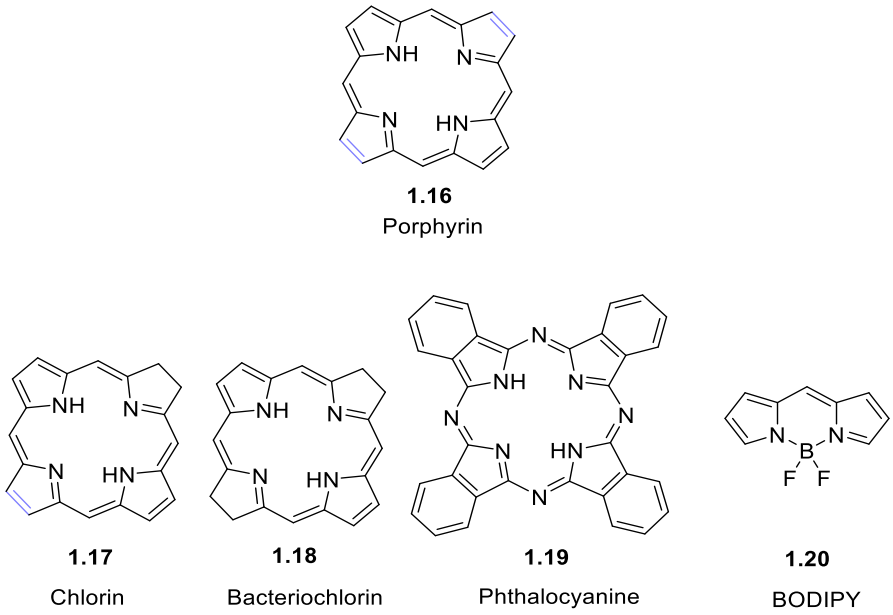

Figure 1.8: Examples of tetrapyrroles and the BODIPY core used in PDT drugs.

The aromatic system in tetrapyrroles and BODIPYs affords characteristic absorption properties that are advantageous for PDT. Firstly, in porphyrins, a strong Soret band is visible at approximately 400 nm and then four weaker Q bands are found between 450-700 nm. Chlorins, bacteriochlorins, and phthalocyanines have a stronger red-shifted absorption profile, making them optically more suited; however, they are less chemically stable and their chemistry is not as versatile. BODIPYs have strong absorption at approximately 500 nm, are chemically stable, and have a rapidly growing synthetic catalogue.

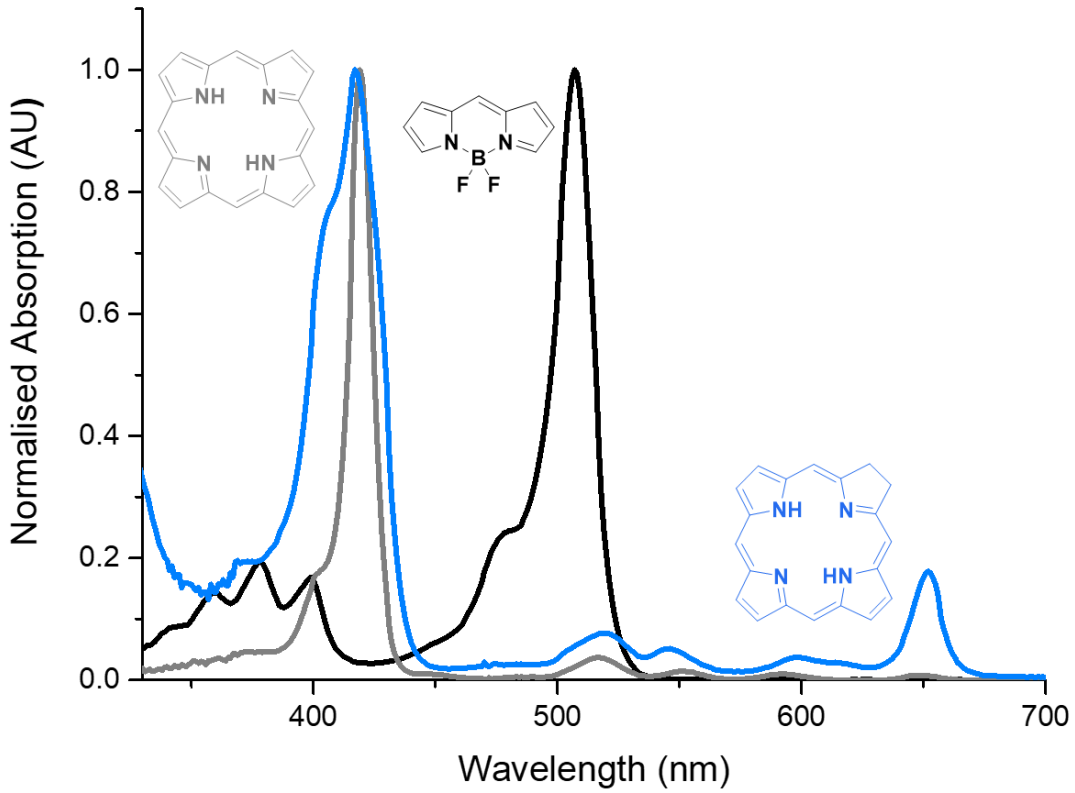

Figure 1.9: Normalised absorption spectra of 5,10,15,20-tetraphenylporphyrin (grey, H_2TPP), 5,10,15,20-tetrakis(3-hydroxyphenyl)chlorin (blue, *m*THPC), and 8-(10-bromoanthracen-9-yl)-4,4-difluoro-4-bora-3a,4a-diaza-s-indacene (black, substituted-BODIPY) in dichloromethane (DCM).

In the past, the limited synthetic control over the natural library of compounds has restricted the application of tetrapyrroles. Fortunately, over the last two decades' research has led to substantial advances in the area of synthetic tetrapyrrole and BODIPY chemistry and thus opened new doors for this class of compounds and their derivatives.[88] Particularly, the meso-and β-positions of tetrapyrroles and the 8-position of BODIPYs can be extensively modified (**Fig. 1.8**). BODIPYs are themselves chromophores and chemical modification is necessary to make them singlet oxygen generators (see Chapter 3).

The general condensation mechanism described in **Fig. 1.10** shows the steps to yield a porphyrin or BODIPY skeleton. The reactions differ by the reactant equivalence and reaction conditions. The mechanism is initiated by an acid catalyst and the activated carbonyl reacts with pyrrole, subsequently, water is eliminated.

The final steps for porphyrin synthesis are cyclisation followed by oxidation of the porphyrinogen to the porphyrin. For BODIPY synthesis, the dipyrromethane is oxidised to the dipyrromethene (DPM) and in the last step, boron is inserted using $BF_3 \cdot Et_2O$.

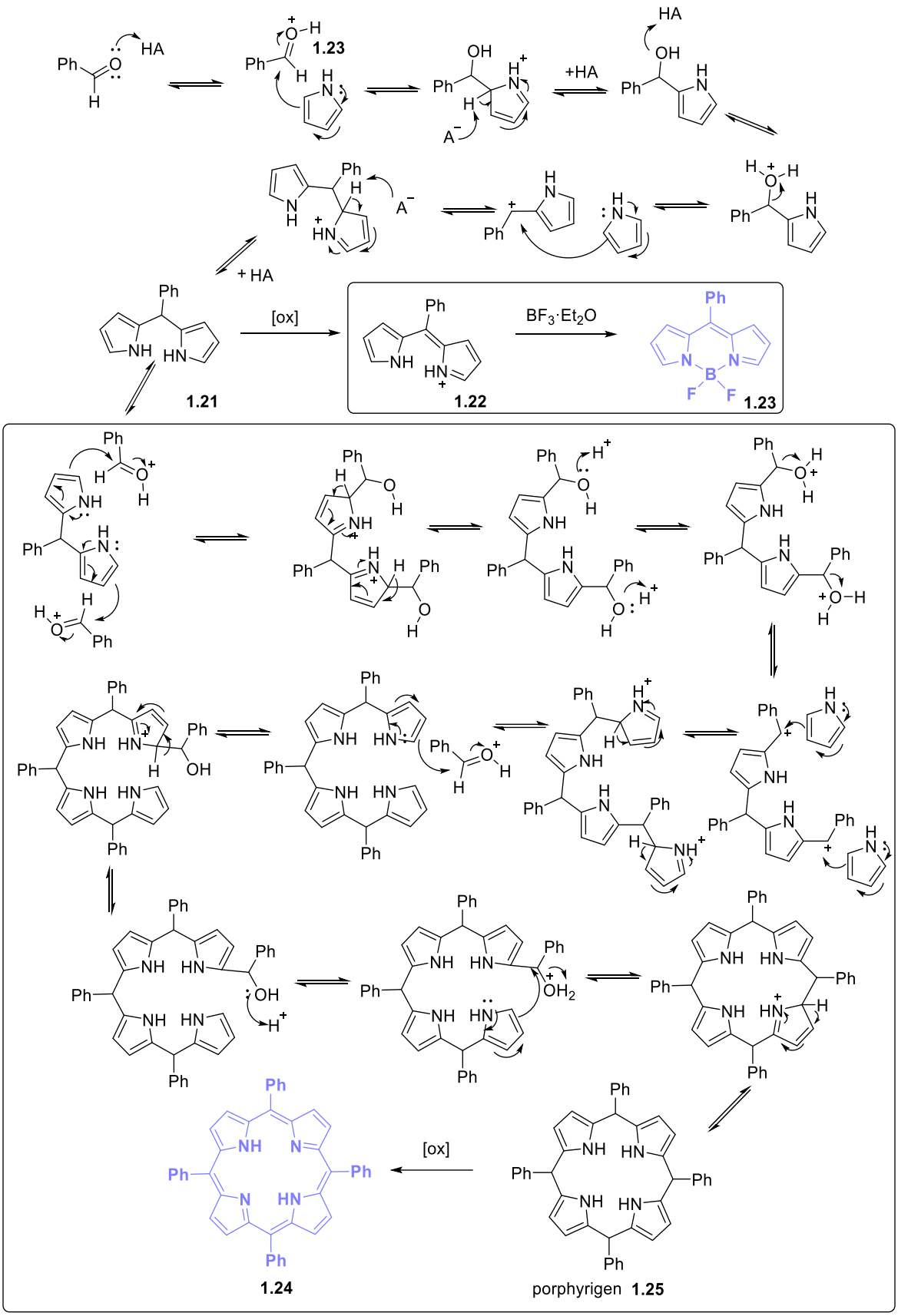

Figure 1.10: Condensation mechanism to yield a porphyrin or BODIPY illustrated using meso-phenyl derivatives.

Elementary symmetrical meso-substituted porphyrins can be synthesised by simple condensation reactions between pyrroles and aldehydes (**Fig. 1.11**). In 1935, Rothemund synthesised porphyrins by reacting pyrrole and aldehydes in methanol (MeOH) at rt for several weeks, heating to 85-90 °C, or heating to reflux in a sealed tube.[89,90] In the 1960s, the Adler-Longo method was developed. The major modification was heating the reactants to reflux in propionic acid. The reactions were performed at high concentrations and improved yields were reported (20 ± 3% for 5,10,15,20-tetraphenylporphyrin). They also noted dependence on oxygen availability for the formation of the porphyrin. The major limitation of this method is poor substrate tolerance as many aldehydes do not survive the harsh acidic conditions.[91] The most widely used method in contemporary porphyrin synthesis is the Lindsey method, due to its versatility and substrate scope. In this method, the reaction between pyrrole and aldehyde is catalysed by acid and performed in a chlorinated solvent at rt. In the second step, an external oxidant, for example, 2,3-dichloro-5,6-dicyano-1,4-benzoquinone (DDQ) or *p*-chloranil is used to oxidise the porphyrinogen to the porphyrin. As well as increased yields (approximately 40% for 5,10,15,20-tetraphenylporphyrin), the mild conditions allowed for a broader substrate scope. Today, the addition of an external oxidant is often used as an add-on to the Alder-Longo method.[92]

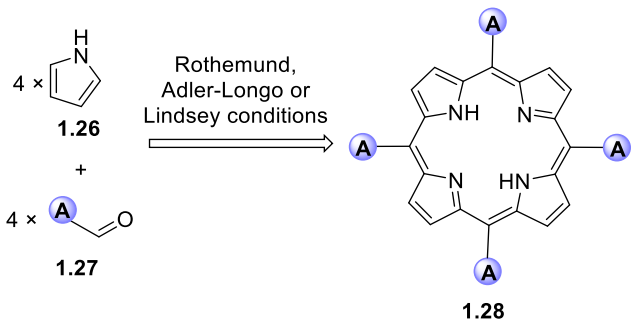

Figure 1.11: Simple condensation reactions to yield an A_4 porphyrin.

Hemaoglobin and cytochromes, prominent natural porphyrin-containing proteins, show synthetically onerous low symmetry. To achieve target porphyrins with various meso-substitution patterns more elaborate condensation reactions are employed. The first of which are mixed condensations. An inherent flaw of this methodology is the statistical mixture of products that require laborious work-up and result in the

target molecule being isolated in low yields. For a mixed condensation with four different aldehydes, there are six possible ABCD-meso-substituted (bearing four different meso-substituents) porphyrin products, with theoretical statistical yields between 6.25 and 25%.[93] To exact more control, [2+2] or [3+1] methodologies are employed to obtain ABCD-meso-substituted porphyrins. In the early development of these reactions, β-substituted porphyrins were the targets.[94] Usually, for [2+2] condensations, a reduction yields the dipyrromethanedicarbinol and this is followed by a Lewis base condensation with a DPM and finally an oxidation step. A common side reaction observed for these methodologies is scrambling of the pyrrole units but moderate to high yields have been reported (**Fig.1.12**).[95]

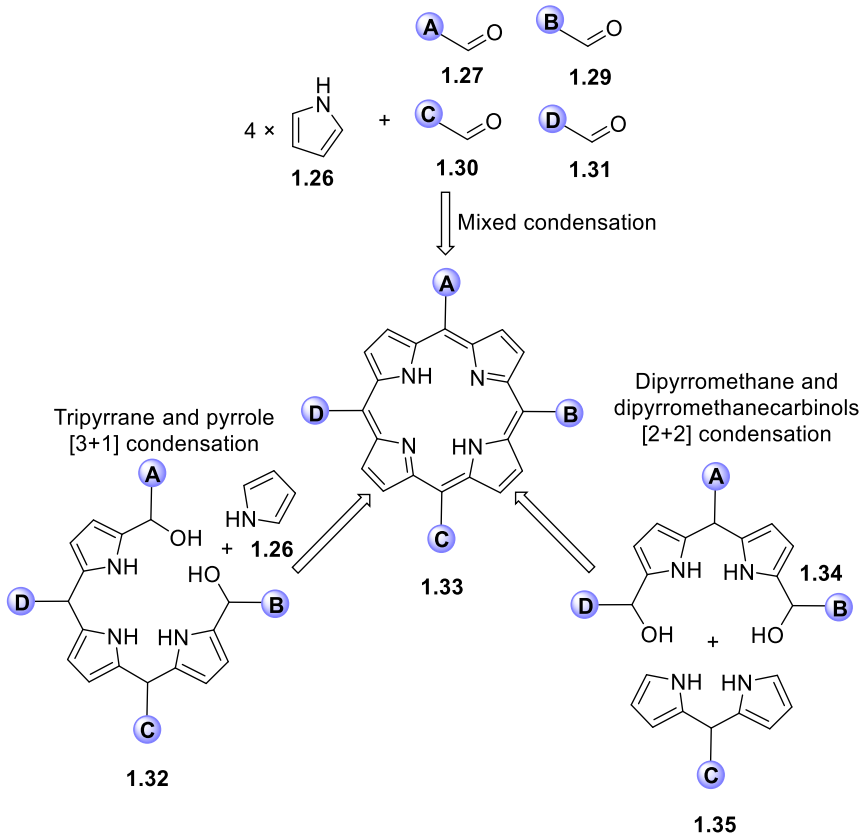

Figure 1.12: Possible methods to synthesise meso-substituted ABCD-porphyrins.

The final condensation strategy is a [2+2] condensation between a DPM and an aldehyde (**Fig. 1.13**). This reaction yields primarily A_2B_2-type porphyrins. Again, this reaction is acid-catalysed and when choosing this method, the possibility of scrambling must be considered.[96]

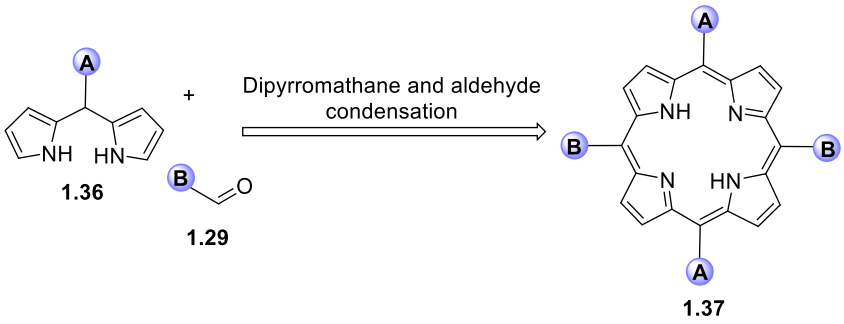

Figure 1.13: Possible ways to synthesise unsymmetric A_2B_2-porphyrins.

An alternative approach is the total synthesis of porphyrins. This methodology has produced highly complicated and unsymmetric porphyrins but it often involves long and cumbersome synthetic routes. The basic approach is the synthesis of a bilane precursor followed by metal-templated cyclisation and oxidation to the porphyrin.[97]

BODIPYs are also synthesised using condensation reactions. Functional groups can be introduced at the 8-position of the BODIPY through the aldehyde and at the 1, 2, 3, 5, 6, and 7 positions using functionalised pyrroles. The most common synthesis is between pyrrole and an aromatic aldehyde; however, the use of aliphatic aldehydes has not yet been reported. The mechanism is described in **Fig. 1.10** and this method is used for the generation of symmetric BODIPYs. The reaction is carried out using pyrrole as a solvent or pyrrole dissolved in dichloromethane (DCM) and is catalysed by an acid. This is followed by oxidation with an external oxidant and boron insertion. Often, halogenated aryl aldehydes are used to introduce a synthetic handle for further functionalisation.

Alternatively, 8-substituted BODIPYs can be generated from pyrroles and acid chlorides. This reaction proceeds through a DPM intermediate and is performed in DCM under moderate heating. In the second step, a base is used to mediate boron insertion using $BF_3{\cdot}Et_2O$. This method is used to introduce aliphatic groups at the 8-position and oxidation is not required. The final method for BODIPY synthesis employs ketopyrroles and is used to form unsymmetric BODIPYs. The ketopyrrole is first synthesised and then condensed with another pyrrole in DCM with a Lewis acid catalyst. Again, the final step is boron insertion (**Fig. 1.14**).[98]

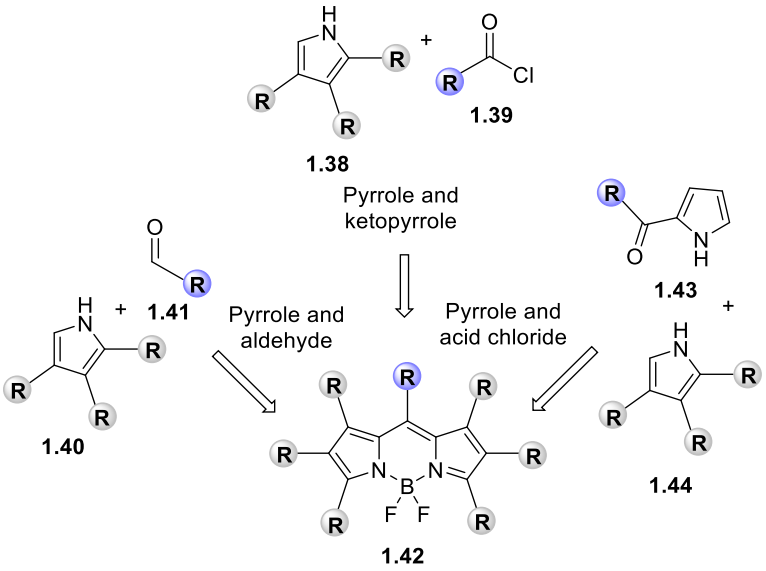

Figure 1.14: Methods to synthesise aryl-BODIPYs.

The development of functionalisation reactions is important for the application of both BODIPYs and porphyrins as they give access to a wide variety of symmetric and unsymmetric compounds through stepwise synthetic routes, which rely on the reactivity of the various positions. The most commonly used examples will be described below but this is not an exhaustive list. Extensive reviews and recent examples on the subject are referenced for further information.[88,98–100]

The simplest post-condensation porphyrin functionalisation is metallation and this can be achieved using metal salts of Zn^{2+}, Ni^{2+}, Mg^{2+}, and Cu^{2+}, to name a few. Metallated tetrapyrroles have an important role in biological systems; for example, iron in heme and magnesium in chlorophyll. The BODIPY's boron difluoride core can also be synthetically modified. For example, DPM can be reacted with 9-borabicyclo[3.3.1]nonane triflate or dibutylboron triflate to introduce bulky alkyl groups.[101] Alternatively, nucleophilic substitution can take place between an aryl Grignard or organolithium reagent and the fluorine atoms to yield boron aryl units.[102] Substituted acetylides may also be used to replace the fluorine atoms, under certain circumstances (for example terminal trimethylsilyl group), which allows for further reactions including Sonogashira couplings.[103] Reaction of the boron difluoride groups with sodium methoxide or alcohols and aluminium trichloride can introduce alkoxide groups at this position.[104,105] Alternatively, reaction with trimethylsilyl chloride and acetic acid can yield carboxylates.[106]

Due to the electrophilic nature of the meso- and β-porphyrin positions, direct substitution reactions are possible. Inhoffen applied Vilsmeier formylation chemistry to porphyrins by reacting metallated porphyrins, usually a Ni^{2+} or Cu^{2+} porphyrins, with a Lewis acid to generate Vilsmeier complexes. This was followed by hydrolysis to yield either the meso- or β-formylated porphyrin.[107] Nitration is another type of electrophilic substitution reaction that has been applied to porphyrin chemistry. The degree of nitration is dependent on reagent choice and can be mediated by nitric acid in acetic acid, nitric acid in sulfuric acid, copper nitrate in acetic acid, or zinc nitrate. Subsequently, the amino porphyrin can be accessed with tin chloride and hydrochloric acid or sodium borohydride, palladium, and carbon.[108–110]

Alternatively, the porphyrin can be activated with organolithium reagents to undergo direct nucleophilic reactions to introduce aryl and alkyl meso and β substituents. This chemistry was developed by the Senge group starting in the late 1990s. To perform this reaction, the lithium reagent is first generated *in situ* at low temperatures, leading to a Meisenheimer-type complex being formed on the porphyrin. This is followed by hydrolysis and then oxidation back to the porphyrin.[111,112] Another useful strategy is halogenation, as it allows for a range of subsequent functionalisation reactions. Smaller halogens, fluorine and chlorine, halogenate the meso-positions while bromination occurs more readily at the β-positions, as the β-positions are less sterically hindered. Regiochemistry is also controlled by temperature, reaction time, and position blocking strategies.

The 2- and 6-positions of the BODIPY core also undergo electrophilic attack. Sulfonation can be achieved using chlorosulfonic acid, followed by the addition of base[113] and nitration can occur in the presence of nitric acid at 0 ºC.[114] Halogenation has been shown to occur on all the positions of the BODIPY core. However, halogenation will only occur at the 1- and 7-positions if all others are blocked.[115] Palladium-mediated C–H functionalisation has been used to extend the conjugation of the BODIPY core at the 2- and 6-positions and employs an alkene with an electron-withdrawing group, a palladium catalyst, and an oxidant.[116]

Once halogenated (by reaction or introduction in the condensation), transition metal catalysed reactions are a natural progression to functionalise both the BODIPY and

porphyrin periphery. They generally proceed by oxidative addition of the halogenated starting material to the palladium-based catalyst, followed by transmetallation and then reductive elimination to yield the coupled product and the regenerated catalyst. The most common cross-coupling reaction is the Suzuki reaction in which a halogenated species is reacted with a boroylated aryl or alky reagent in the presence of a palladium catalyst.[117] This reaction has been performed on both halogenated BODIPYs and porphyrins.[118] Other organometallic couplings used on halogenated BODIPYs and porphyrins are Sonogashira reactions with terminal alkynes,[119] Heck reactions, which use activated alkenes to introduce alkenyl substituents[120] and Stille couplings, which use stannanes.[121,122] Halogenated porphyrins can also undergo Buchwald-Hartwig reactions to yield aminoporphyrins.[123] Alternatively, 3,5 chlorinated BODIPYs can undergo nucleophilic substitution reactions to introduce alkoxides, thioalkoxides, and amines (**Fig. 1.15** and **Fig. 1.16**).[124]

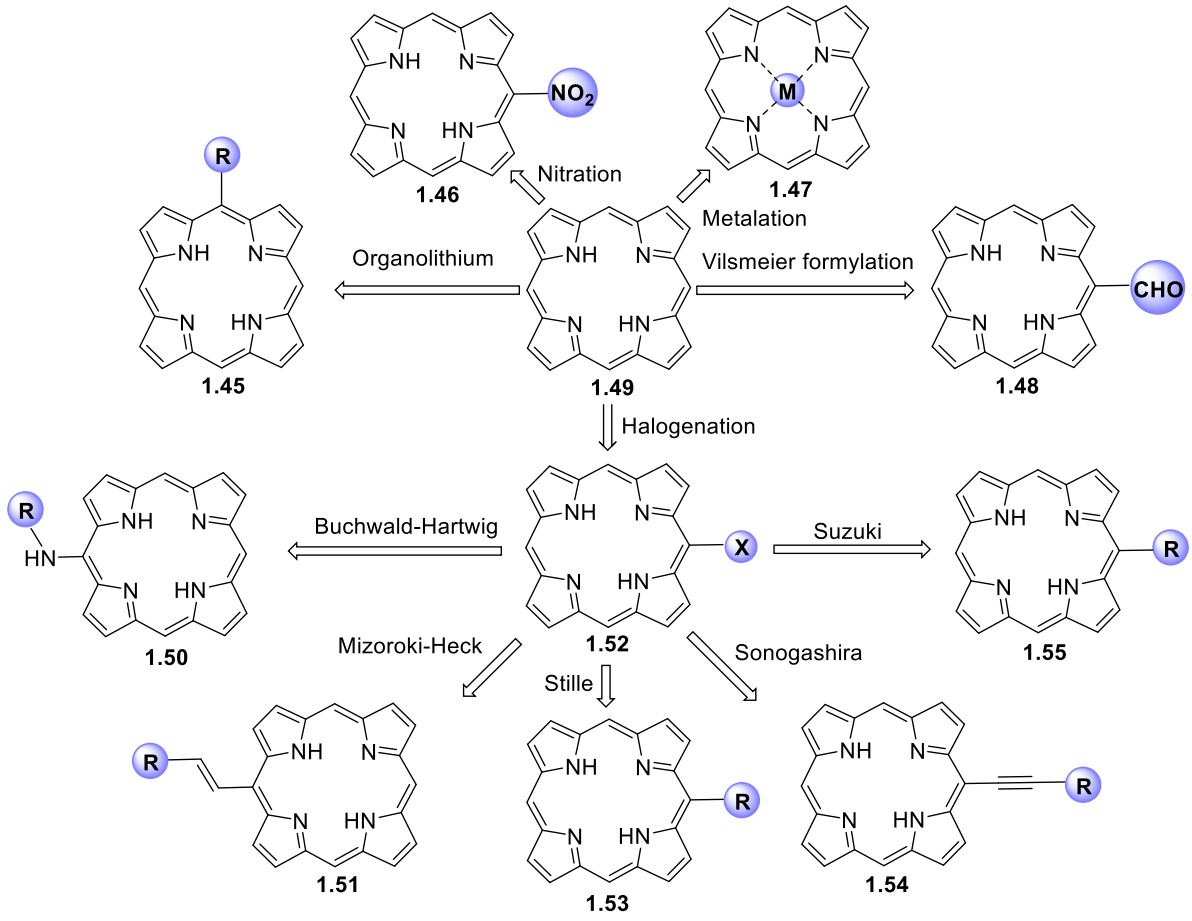

Figure 1.15: Schematic representation of exemplary porphyrin functionalisation methods.

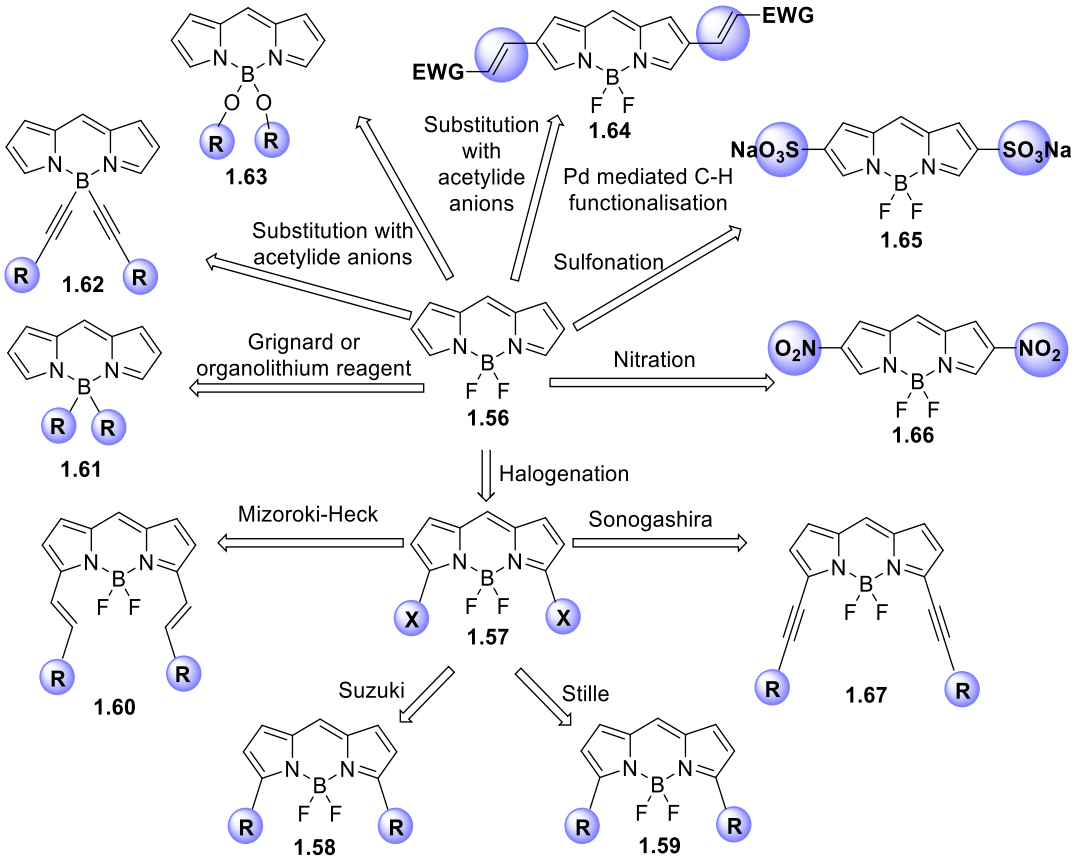

Figure 1.16: Schematic representation of exemplary BODIPY functionalisation methods.

1.4 PHOTOSENSITISERS AND PHOTODYNAMIC THERAPY EFFECTS

1.4.1 The ideal photosensitiser

As physicists primarily optimise light sources and pharmacists study pharmacokinetics, chemists occupy themselves with the challenges associated with the design and synthesis of photosensitising drugs. These compounds are designed to have high singlet oxygen quantum yields, as well as other ideal properties, that maximize functionality and provide an efficient and effective route from production to cell delivery. These properties include but are not limited to, solubility in the cellular environment, low dark toxicity, optimal photophysical properties that complement biological media, a facile and reproducible synthesis, chemical purity, minimal side effects, negligible aggregation in formulations, straightforward administration, swift excretion from the body but targeted distribution lasting long enough to provide the therapeutic effect, and resistance to photobleaching (**Fig. 1.17**).[67] To date, the identification of a molecule that has all of the aforementioned properties has eluded us and compounds with strong singlet oxygen-generating ability have been prioritised in the search. This has resulted in a trade-off, with many of the photosensitisers in clinical use having less than ideal side effects; however, over the past few decades' incremental optimisations have been made.

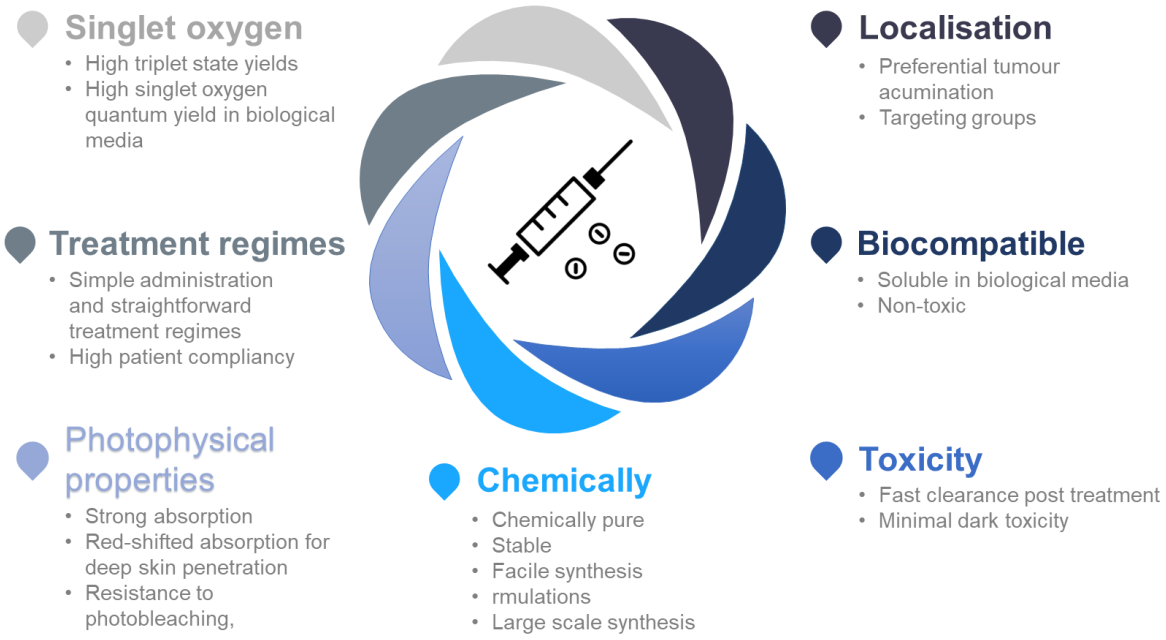

Figure 1.17: Properties of an ideal photosensitiser.

Photosensitisers can be classified into first, second, and third generations. Hematoporphyrin and its derivatives were the first photosensitisers used in a clinical setting and thus are the first generation of PDT agents. Although they are strong singlet oxygen generators and are still used in clinics as Photofrin (an oligomeric mixture of porphyrins), patients suffer from high photosensitivity. Additionally, Photofrin has weak absorption at its maximum (630 nm).[125]

Second generation photosensitisers are characterised by their chemically defined structures and possess properties of the ideal photosensitiser. One such compound, *m*THPC (**1.14**), marketed as Temoporfin, was approved for the treatment of head and neck cancer in 2001.[126] The chlorin structure gives rise to a maximum at 650 nm (**Fig. 1.9**) and it can be effective at very low-doses. Grosjean *et al.* treated early-stage oesophagus and bronchi cancers with a dose of 0.15 mg/kg (in most cases), using 652 nm or 514 nm light sources and they reported a 77% positive response, making *m*THPC much more potent than Photofrin; however, they also reported skin photosensitivity post-treatment.[127]

Benzoporphyrin derivative monoacid A (BPD, **1.15**), also known as Verteporfin, is a second-generation BPD with an optimised absorption profile (maximum at 690 nm), allowing for 50% greater tissue penetration when compared to Photofrin.[128] It also has fast tumour uptake of 30–150 min following intravenous administration of the liposomal formulation and rapid clearance rates of a couple of days.[129] Verteporfin is clinically available as Visudyne (a liposomal formulation of Verteporfin) and can be used for the treatment of age-related macular degeneration.[130] Another class of tetrapyrroles not yet clinically approved are phthalocyanines (**1.13**). They have a have strong absorption band at 680 nm with a molar absorption coefficient of 1×10^5 $M^{-1}\,cm^{-1}$. Additionally, the insertion of metals, such as zinc, increases the triplet state lifetime to >100 µs. Moreover, issues with excessive aggregation in aqueous solution and slow clearance are being overcome by peripheral functionalisation.[131]

The final example of a second-generation photosensitiser is different from the others. Specifically, the administered compound, ALA, is not an active photosensitiser but a metabolic precursor of protoporphyrin IX (**1.8**). Protoporphyrin IX, the active photosensitiser, is naturally generated in the mitochondria through the

heme biosynthetic pathway. Heme then acts as a trigger for the feedback regulatory system, following the insertion of iron into protoporphyrin IX using ferrochelatase. However, the addition of exogenous ALA causes a build-up of protoporphyrin IX and thus the therapeutic response. Esterified forms of ALA have been developed to increase bioavailability. The methylester derivative of ALA is marketed as Mervix, while ALA is marketed as Levulan. They are used to treat malignant and non-malignant skin conditions including actinic keratosis and basal cell carcinoma.[132]

The third generation of photosensitiser drugs are currently under development and are a major theme of this thesis. They are designed using rational principles aimed to bring us a step closer to the ideal photosensitiser. Some of these strategies include targeting groups for specificity (see 1.4.2), expanding conjugation to alter the absorption profile, inclusion in nanoconstructs to increase biocompatibility,[133] and/or controlling singlet oxygen generation and effects to enhance the therapeutic outcomes. The topic of singlet oxygen modulation for PDT applications has been reviewed in detail by Callaghan and Senge.[134]

1.4.2 Photosensitiser uptake and cellular localisation

Following photosensitiser administration, either systemically, locally, or topically, its biodistribution has a major impact on the efficiency of reactive oxygen generation and thus the photodynamic response. Across a wide variety of photosensitisers, preferential tumour accumulation has been observed. Figge noted this phenomenon as early as 1948 in an extensive *in vivo* study on hematoporphyrin across a selection of cancers.[54] However, it is important to note that there is also accumulation in other organs, which can make the term 'preferential tumour accumulation' misleading. An example of this is the biodistribution of 4,4',4'',4'''-(5,10,15,20-porphyrintetrayl)tetrabenzenesulfonic acid, which is known to accumulate in tumour tissue but also in other organs especially the liver and kidneys. Notably, both of these organs are involved in porphyrin metabolism.[135,136] Additionally, dose and time after administration should be considered when evaluating tumour uptake. The mechanism of selective accumulation is unclear but most likely is a culmination of many factors relating to the chemical properties of the photosensitiser molecule and the target tissue physiology.

When it comes to photosensitiser design, hydrophobicity has been shown to increase uptake. Moan and co-workers studied hematoporphyrin derivatives and reported a correlation between the degree of hydrophobicity and cellular uptake.[137] Later, Oenbrink *et al.* also documented increased uptake in V79 Chinese hamster cells for the more hydrophobic members of their synthetic porphyrin library.[138] However, there is a pay-off as excessive hydrophobicity renders the molecule incompatible with biological media. Hydrophobic compounds, especially those with π-stacking abilities tend to aggregate in polar solvents, of which hematoporphyrin derivative is a good example.[137] Hematoporphyrin was shown to accumulate and be retained in tumour tissue and could not be removed by diffusion into hematoporphyrin-free media.[139] Bellnier and Li suggested this could be due to porphyrin aggregation trapping the compound in the cell.[140] Another explanation is that it may bind to cellular components including albumin, a major porphyrin transporter,[141] low-density lipoproteins,[142] and collagen.[143] Another example of how chemical modification can modulate uptake is the development of ALA derivatives. Esterified ALA derivatives including methyl, pentyl, hexyl, and benzyl are more lipophilic and display increased cellular uptake.[144,145]

The differences in the microenvironment of tumour tissue compared to normal tissue is also thought to affect the uptake and retention of photosensitisers. Firstly, tumours express angiogenesis factors that lead to hypervasculation,[146] which is characterised by increased permeability due to elevated levels of vascular permeability factors.[147,148] This increased permeability may allow photosensitisers, especially when bound to large serum proteins, to enter the tumour tissue at increased rates. Another contributing factor to this phenomenon may be the poor lymphatic drainage found in tumour tissue. In normal tissue, the lymphatic system clears biomolecules found in the interstitial space but without a functional lymphatic system, biomolecules are retained to a greater extent.[149] Finally, Guinnilo showed that the cellular environment of tumour tissue is acidic,[150] likely due to increased CO_2 levels resulting from a high metabolic rate. Later, Thomas and Girotti provided evidence suggesting that this could affect photosensitiser retention. By administering glucose to reduce the cellular pH prior to PDT they found that there was a greater accumulation of hematoporphyrin derivative in tumour cells.[151] The combined effect of high permeability, low pH, and retention due to the lack of a

functional vascular system is suggested as a possible mechanism for the preferential accumulation of photosensitisers in tumour tissue; however, the details have yet to be definitively elucidated.

Preferential accumulation alone does not result in an optimal therapeutic response as photosensitivity post-treatment is still a major drawback of PDT. To combat this, another strategy to aid photosensitiser accumulation is the introduction of bioconjugates to specifically target cancer tissue. These targeting groups can be covalently bound to the photosensitiser or incorporated into the delivery system (see Chapter 5).

Firstly, glycoporphyrins offer increased solubility in addition to the ability to target specific lectin receptors. The high rate of glycosylation[152] in malignant tissue results in the upregulation of surface saccharides and transporters.[153] This is one of the earliest bioconjugate strategies and numerous tetrapyrrole-glycoconjugates have been applied to PDT.[154,155] As an example, pyropheophorbide, a 2-deoxyglucosamide, was shown to accumulate in a 9L glioma rat model by targeting a glucose transporter. Fluorescence imaging showed preferential accumulation and photoinduced mitochondrial damage was evident.[156] Similarly, bile acid-porphyrin conjugates were used by Králová *et al.* to target and image these surface saccharides and they showed selective phototoxicity against a variety of cells line as well as in a mouse model bearing a 4T1 mammary carcinoma.[157] Our group also developed *m*THPC bile acid conjugates that targeted a sodium-dependent bile acid transporter, a receptor which is upregulated in Barret's oesophageal cancer. Although uptake was demonstrated, phototoxicity was not shown to induce cell death.[158]

Vitamins, retinoic acid, and folates have been used for targeted PDT. Folate receptors are over-expressed in cancer tissue and taken up by endocytosis thus making them a delivery mechanism for conjugated photosensitisers. In 2012, Syu *et al.* developed folate-conjugated *m*THPC-loaded micelles that accumulated in folate receptor-overexpressing cancer cells both *in vitro* and *in vivo* and displayed positive solid tumour toxicity.[159] Porphyrin-retinamide conjugates were developed

by Sibrian-Vazquez *et al.* and were taken up by RAR-positive neuroblastoma SK-N-DZ cells 20-50% more than in HEp2 cells. Moreover, moderate toxicity was noted.[160]

The final biomolecule targeting groups to be discussed are proteins. Low-density lipoproteins are molecular targets because they are overexpressed in cancer tissue, which again, is linked to cancer's high metabolic rate. They function as carriers for hydrophobic molecules and thus can solubilise photosensitisers.[161] In one example, a chlorin-e_6-conjugate was developed by Schmidt-Erfurth *et al.* and enhanced cellular uptake and phototoxicity were noted in Y79 human retinoblastoma cells.[162] Protein-targeting using antibodies is pursued in PDT because of unique antigen specificity. In 2005, Savellano *et al.* conjugated a BPD to Cetuximab (Cet), an anti-epidermal growth factor receptor, often overexpressed in cancers. This construct was used to kill epidermal growth factor receptor-overexpressing epidermal carcinoma and ovarian cancer cells using the photodynamic effect. When compared with free Verteporfin, enhanced specificity was noted.[163] In a second example, Mitsunaga *et al.* also investigated phthalocyanine- conjugated antibodies that target epidermal growth factor receptors, Trastuzumab- (anti-HER1) and Panitumumab (anti-HER2). These compounds were not taken up by the cells and were instead bound to the membrane but both showed targeted photodynamic toxicity.[164] The Boyle Group also made considerable contributions to this field by developing conjugation methods using isothiocyanate moieties.[165,166,167] They conjugated a porphyrin-based photosensitiser to radiolabelled internalising and non-internalising antibodies with loading ratios between 1.4 and 2.5. Overall, they showed that the internalising conjugates displayed enhanced phototoxicity compared to the non-internalising conjugates[165] and this approach was also utilised in the development of anti-EpCAM, anti-CD104, and LAG3 scFv (targets antigens associated with colorectal malignancies) antibody conjugates and again selective phototoxicity was observed.[166,167]

Once in the tumour tissue, the subcellular localisation of the photosensitiser can modulate the cell death response. The short half-lives and diffusion constants of reactive oxygen species limit the photodynamic effect to the area of localisation. Cellular localisation can be identified using confocal laser scanning fluorescence

microscopy and the colocalisation of organelle-specific probes can increase the accuracy of identification.[168]

Some photosensitisers do not localise in a particular cellular location such as pyropheophorbide, a methyl ester, which has been shown to localise in the Golgi apparatus, endoplasmic reticulum, lysosomes, and mitochondria but for most photosensitisers, one main organelle is targeted.[169] Ideally, a photosensitiser should be hydrophilic with less than two negative charges to cross the plasma membrane. Strongly polar and hydrophobic molecules generally cannot diffuse across the plasma membrane and thus have to rely on endocytosis for uptake. Deuteroporphyrin IX and its halogenated derivatives were shown to localised in the plasma membrane of murine L1210 leukaemia cells.[170] Similarly, in human carcinoma cells, Photofrin mainly accumulated in the plasma membrane following a 3 h incubation period (and in the Golgi apparatus after longer incubation times). At a dose of 28 μg/mL, membrane disruption and cell swelling were observed after PDT.[171] *m*THPC (**1.14**) is a clinically relevant photosensitiser and it primarily accumulates in the Golgi apparatus and endoplasmic reticulum in MCF-7 cells. Following PDT, photodamage was primarily localised to these organelles.[172]

Mitochondria are the powerhouses of the cell and thus are an important localisation site for photosensitisers. As a generalisation, cationic, hydrophobic photosensitisers tend to localise in the mitochondria. These include the cyanide dye, *N,N′*-bis(2-ethyl-1,3-dioxolane)kryptocyanine, which was shown to induce phototoxicity in human bladder, squamous, and colon carcinoma cells.[173] Additionally, zinc(II) phthalocyanines with lipophilic side-chains have been shown to localise in mitochondria and kill HeLa cells.[174] Finally, another clinically relevant photosensitiser, Verteporfin, has been shown to localise in the mitochondria but this is dependent on both cell type and formulation method.[175]

Many photosensitisers localise in lysosomes, but studies have shown that photodamage is not as efficient in lysosomes compared to other organelles. MacDonald *et al*. showed that pyropheophorbide a-mediated photodamage was more effective in mitochondria than in lysosomes.[176] Woodburn *et al.* modified hematoporphyrin and protoporphyrin IX (**1.8**) to give derivatives with anionic,

cationic, or hydrophobic side chains and studied their uptake in V79 Chinese hamster lung fibroblasts and C6 glioma cells. They found that compounds with cationic charges localised in mitochondria, while those with anionic charges localised in lysosomes (**Fig. 1.18**).[177]

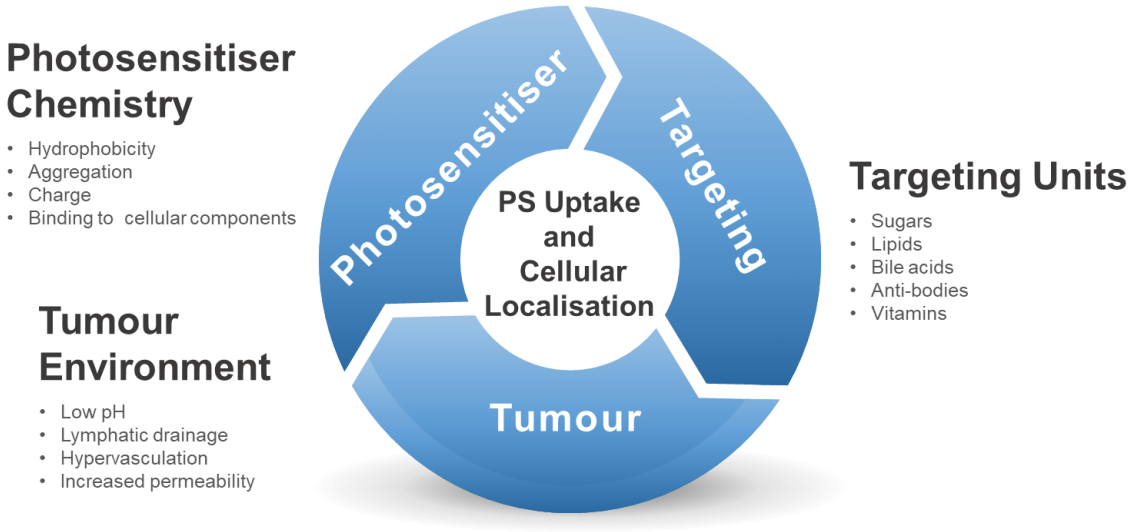

Figure 1.18: Factors, speculated or proven, effecting photosensitiser uptake and cellular localisation.

1.4.3 How photodynamic therapy affects the cellular and tumour environment

In addition to direct photodamage caused by singlet oxygen and other reactive oxygen species, PDT can induce cellular stress that leads to the initiation of cell death pathways. Apoptosis, the primary cell death pathway following PDT, is a controlled pathway characterised by morphological changes including blebbing and cell shrinkage. In the early 1990s, apoptosis was first identified as a PDT cell death pathway in mouse lymphoma L5178Y cells.[178] Release of cytochrome c and the destruction of anti-apoptotic proteins, Bcl-2 and Bcl-xL, initiates photodamage in the mitochondria and endoplasmic reticulum.[179,180] Additionally, lysosomal damage resulting in the release of lysosomal proteases can indirectly promote apoptosis in mitochondria, which is mediated by the protein tBid.[181] The apoptotic response following light treatment is swift and DNA damage is evident within minutes.

In PDT, cells that do not undergo apoptosis are likely to undergo autophagy. Xue and co-workers expressed cell lines without essential components to apoptosis including Bax and caspase-3 and they found that autophagy was the dominant cell death pathway.[182] Autophagy is used by cells to recycle components when under stress and may protect cells from mitochondrial damage.[183] This function is carried out in the lysosomes and thus lysosomes are a target for PDT.[184]

More recently, paraptosis has been identified as a PDT cell death pathway. Its exact mechanism of action is not well understood but is thought to involve the endoplasmic reticulum and mitochondria. The pathway is characterised by excessive vacuolisation of the cytosol without DNA damage. An example of paratosis after PDT was reported by the Kessel group.[185] The final cell death pathway is necrosis; however, it is not commonly the intentional outcome of PDT as it is non-specific and arises from high light doses or photodamage of the membrane, leading to cell lysis. Luo and Kessel demonstrated the dependence of dose on cell death pathways. At a low chloroaluminum phthalocyanine dose and 45 mJ cm^{-2} of light in murine leukemia P388 and L1210 cells, apoptosis was induced but at higher doses membrane damage was observed (**Fig. 1.19**).[186]

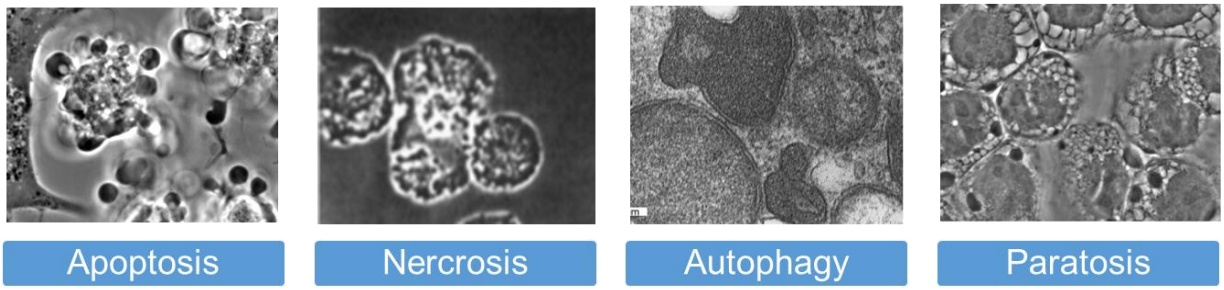

Figure 1.19: Microscopic image of cell death induced by PDT; reproduced from ref. 186 and 187.[186,187]

In addition to inducing cell death pathways, PDT can cause other effects on the tumour microenvironment. Once a tumour has reached a threshold volume it begins the process of angiogenesis to sustain growth by generating blood vessels to supply oxygen and nutrients.[188] PDT can cause vascular shutdown and thus starve the tumour of essential supplies. This was shown by Henderson *et al.* in 1989 using Photofrin and a fibrosarcoma tumour *in vivo* model.[189] However, vasculature damage can result in tumour hypoxia and make subsequent PDT less effective.

Additionally, this situation may also initiate vascular endothelial growth factor (VEGF), matrix metallopeptidases (MMPs), and cyclooxygenase-2 (COX-2) derived prostaglandins, which are pro-angiogenesis signalling proteins.[190] Cell vasoconstriction, shrinkage, and eventually collapse are morphological changes resulting from PDT. Khurana *et al.* studied the effect of Visudyne on single vessels using confocal microscopy and Doppler optical coherence tomography. They found that at a light dose of 451±43 J/cm^2 and 2.5 mg/kg of body weight of Visudyne complete vascular collapse was observed.[191] The time between photosensitiser administration and light dose can also modulate the effectiveness of vascular damage. For example, a study of hypericin-mediated PDT in a RIF-1 tumour model showed that at an interval of 30 min, the functional vasculature was reduced to 10.9% after treatment. In contrast, 15 h and 6 h intervals resulted in functional blood vessels remaining after treatment.[192]

Oxidative stress can activate the immune system leading to an anti-tumour response.[193] It begins with a dramatic increase in cytokine levels. One such cytokine is interleukin-1β, which when blocked results in a reduction in *in vivo* cure rates.[194] Additionally, when anti-inflammatory cytokines including interleukin-10 and TGF-β are blocked the photodynamic response is enhanced.[195] Then, infiltrating cells are activated including neutrophils, monocytes, and macrophages and again their absence has been shown to reduce the PDT response.[196,197]

An adaptive immune response is also observed after PDT, in which antigen-presenting cells including dendritic cells present antigen-derived peptides to T lymphocytes thus activating CD4+ T helper cells, CD8+ cytotoxic T cells, and B cells that can migrate and kill tumour cells. Damage-associated molecular patterns and tumour antigens activate both innate and adaptive immune responses.[198] This was shown in an *in vivo* model by Korbelik *et al.* who reported that a EMT6 mammary carcinoma could be cured in immunonormal BALB/c mice. In contrast, severe combined immunodeficiency (SCID) mice were not cured, thus indicating the role of the immune response in eradicating cancerous cells.[199] A similar effect was reported in a human case study of a patient with angiosarcoma. Following PDT on one limb, lesions on an untreated limb went into remission two months later. Four months post-treatment, remission was induced in lesions on another limb. Following

a biopsy, CD4+T lymphocytes and CD8+T lymphocytes were shown to be present.[200] Immune suppression normally follows a large immune response to prevent over activation and this is also true following PDT. Elmets and Bowen showed that mice treated with hematoporphyrin derivative displayed a 50% suppression of contact hypersensitivity to 2,4-dinitro-fluorobenzene.[201]

1.5 EVALUATION AND LIMITATIONS OF PHOTODYNAMIC THERAPY

PDT has many advantages over conventional treatments. It is more selective and thus less toxic to healthy tissue than chemotherapeutic drugs, has better cosmetic results and a lower risk of infection compared to surgery, and unlike radiotherapy, it does not cause side effects such as infertility. Moreover, PDT does not cause organ damage due to toxic drug accumulation and has dual functionality as it targets both the tumour vasculature and cancerous cells. Finally, due to its unique mode of action, PDT is immune to many conventional chemotherapeutic resistance mechanisms, a property that shows potential for combinational therapies.[202,203] Despite this, PDT is not yet a widespread treatment due to its many limitations and the reluctance of clinical practice to incorporate new strategies.

As mentioned, singlet oxygen has a short lifetime and diffusion rate[79] in biological media and thus photodamage is contained to the site of generation. This can be directly influenced by photosensitiser distribution and the specific tumour vasculature. Many tumours generate their own vascular supply but often the inner tumour is hypoxic. This limits the generation of singlet oxygen, which is reliant on the tissue oxygen concentration. Treatment regimens often repeat cycles of light treatment to allow time for tissue oxygen levels to replenish. This is known as fractionated PDT.[204]

As well as singlet oxygen generation, the optical properties of photosensitisers are also a limitation of PDT. The optical window for biological media is between 650-1200 nm, where electromagnetic radiation has its maximum depth of penetration. This region avoids the absorption profiles of important biomolecules including water, melanin, and hemoglobin. Many photosensitisers on the market are activated by light between 400-600 nm and thus the light treatment is most effective on exposed areas including the skin and less effective on embedded cancers.[205]

Furthermore, higher energy light can lead to burning and poor patient compliance. Many porphyrin-based photosensitisers suffer from photobleaching, in which the photosensitiser is degraded upon prolonged exposure to light. For example, hematoporphyrin undergoes photooxidation, leading to its degradation.[206] BODIPYs may be an alternative to porphyrins as they are relatively photostable.[207] PDT it is

not as effective for the treatment of metastatic disease when compared to chemotherapy or immunotherapy. In many cases, clearance rates are not optimal and photosensitisers including protoporphyrin IX continue to circulate post-treatment, leading to sensitivity up to weeks post-treatment.[208]

In any case, PDT is a clinically relevant therapy that requires novel approaches to optimise current treatments and advance the development of third or fourth generation photosensitisers.

1.6 SINGLET OXYGEN AND AROMATIC UNITS

1.6.1 [4+2] Cycloaddition reactions

A large proportion of the work detailed in this thesis is underpinned by interactions between singlet oxygen and aromatic units, a phenomenon which has been known since the work of Dufraisse, Moureu, and Dean in 1926.[209] In this historic research, the authors synthesised rubene (naphthacene, **1.68**) and noticed a colour change in an aerated solution following irradiation with light. They isolated a compound containing a peroxide that decomposed upon heating to between 110 °C and 150 °C. This decomposition yielded the parent hydrocarbon and an oxygen species. In fact, what occurred was a reversible [4+2] cycloaddition involving oxygen and the aromatic system, compound **1.68**, to form an endoperoxide, compound **1.69** (**Scheme 1.1**).[210,211]

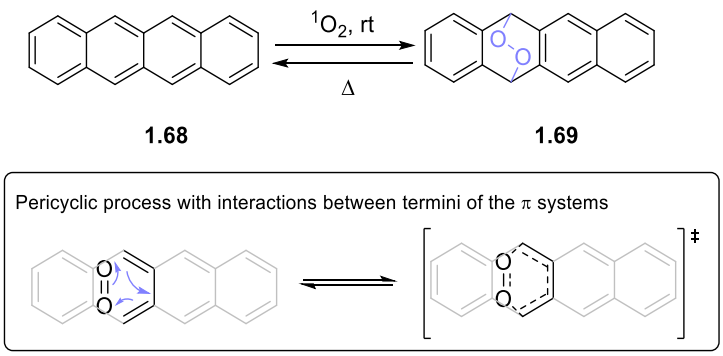

Scheme 1.1: The reversible [4+2] cycloaddition reaction between rubene and oxygen, first demonstrated by Dufraisse, Moureu, and Dean.[209]

In 1964 Foote identified singlet oxygen as the driving force behind these reactions[212] and then in 1967 Wasserman and Scheffer[213] proved that the released oxygen species is in the singlet state. They achieved this by studying the thermal decomposition (heating reactants in benzene or chloroform for 2-4 days) of 9,10-diphenylanthracene endoperoxides in the presence of starting materials for singlet oxygen mediated oxidations. In one example, 2,5-diphenyl-4-methyloxazole, **1.70** was converted to *N*-acetyldibenzamide **1.72** in an 82% yield (**Scheme 1.2**), thus confirming that singlet oxygen was generated from the endoperoxide.[213]

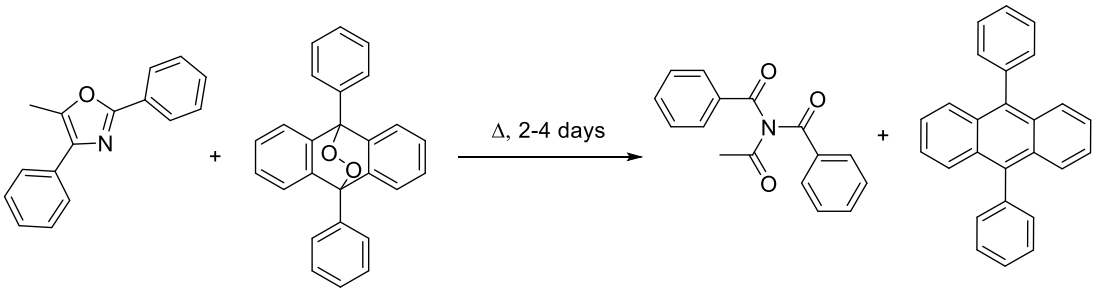

1.70 **1.71** **1.72** **1.73**

Scheme 1.2: One of the reactions Wasserman and Scheffer used to prove that the thermal decomposition of endoperoxides yield singlet oxygen.

Other polyaromatic molecules capable of this transformation were identified[214] and [4+2] cycloadditions remain the most popular method of endoperoxide synthesis; however, some polyaromatics including unsubstituted benzene and naphthalene do not undergo these reactions, hence their endoperoxides were synthesised using other methods.[215,216] On the other end of the scale, as well as reacting readily with singlet oxygen, compound **1.74** also reacts with molecular oxygen *via* a polar transition state to form the endoperoxide, **1.75**.[217] Factors to consider when synthesising endoperoxides include the size of the aromatic system, steric effects, and substitution patterns. For example, pentacene is more reactive towards electrophilic singlet oxygen than anthracene due to its increased electron density.[218] Moreover, the introduction of electron-donating groups near the site of singlet oxygen addition increases the rate of endoperoxide formation.[219] The influence of steric effects on endoperoxide formation can be observed in compounds **1.74** and **1.76**. Endoperoxide formation is possible in both systems because the aromatic rings are under steric stress. Compound **1.74** is non-planar despite all carbons being sp^2 hybridised but this strain is released upon endoperoxide formation.[217] Similarly, in compound **1.76** the aromatic rings are deformed to allow for interaction with singlet oxygen.[220]

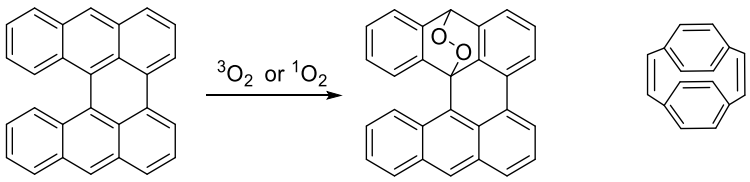

Scheme 1.3: Structure of hydrocarbon **1.74** that can react with both singlet and triplet oxygen. Structure of endoperoxide forming hydrocarbons that are influenced by steric effects, both **1.74** and **1.76**.

The decay properties of endoperoxides are highly dependent on each system but decay is mediated by photolysis and/or thermolysis. Endoperoxide decay proceeds by either cycloreversion reactions, to yield the parent hydrocarbon and an oxygen species, or by homolytic cleavage of the oxygen-oxygen bond, leading to decomposition products (quinones and hydro-ketones) and/or rearrangement products. The homolysis mechanism becomes prominent in higher arenes, while cycloreversion is more commonly observed for naphthalenes. This idea, represented in **Fig. 1.20**, was suggested by Turro *et al.* and evidenced with thermodynamic studies.[221]

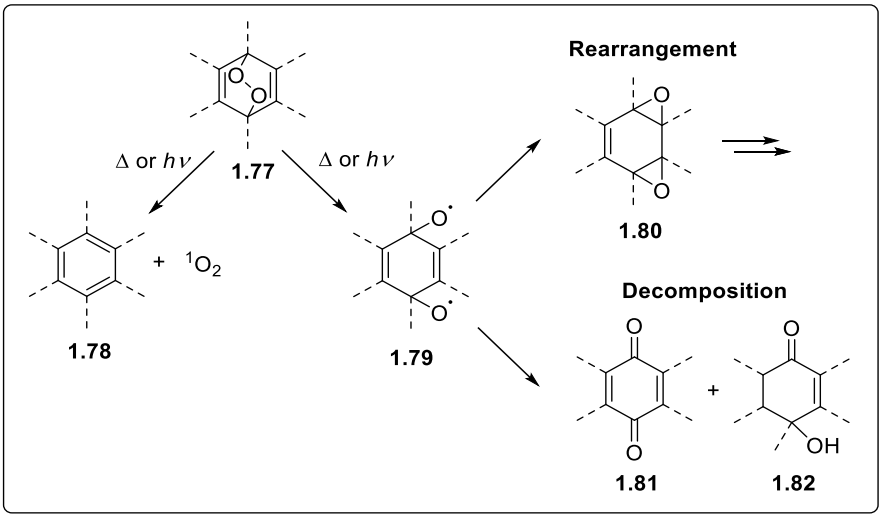

Figure 1.20: Possible thermolysis and photolysis pathways of endoperoxide decomposition.

The aromatic substitution patterns can also affect the decay properties. To exemplify this **Table 1.1** displays the half-lives of a variety of substituted naphthalene endoperoxides. With increasing substitution, cycloreversion occurs over longer

timescales due to the electron-donating group stabalisation of the endoperoxide. Additionally, steric effects can modulate endoperoxide stability. The 1,8-dimethyl naphthalene isomer, **1.85** is more stable than the 1,4-isomer (**1.84**) due to repulsion between adjacent methyl groups in **1.85**, resulting in a shorter half-life. It is also interesting to note that the authors did not observe the endoperoxide of 1-methylnaphthalene.[222] In 2015, Klaper and Linker extended the naphthalene derived endoperoxide library and studied their stability.[223]

Table 1.1: Thermal cycloreversion half-lives at 25 ºC of methyl naphthalene endoperoxides.[222]

Endoperoxide	$t_{1/2}$ (h)	Endoperoxide	$t_{1/2}$ (h)
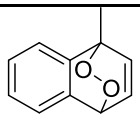 **1.83**	Not observed	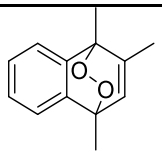 **1.86**	70
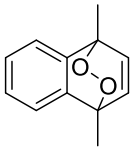 **1.84**	5	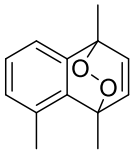 **1.87**	290
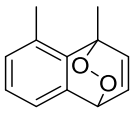 **1.85**	30	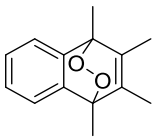 **1.88**	stable*

*During the timescale of the experiments

Bearing in mind that in the aforementioned studies the endoperoxides were synthesised from a parent hydrocarbon and singlet oxygen generated from an external source, Rihter *et al.* incorporated an endoperoxide forming unit onto a photosensitiser scaffold to allow for the generation and trapping of singlet oxygen in the same molecule. This report helped endoperoxide forming reactions transition into practical applications. His self-sensitising molecule was 1,6,10,15,19,24,28,33-octabutoxynaphthalocyanine (**Scheme 1.4**, compound **1.89**). Irradiation of **1.89** in benzene generated singlet oxygen from the triplet excited state of the phthalocyanine core, which was subsequently added to the aromatic periphery, resulting in the formation of the endoperoxide bearing compound **1.90**.

Decomposition of compound **1.90** to the parent phthalocyanine, **1.89**, occurred thermally or photochemically under visible light.[224]

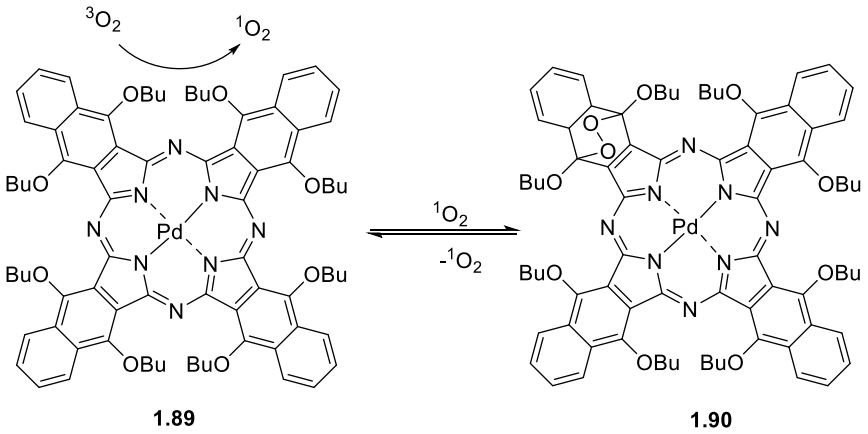

Scheme 1.4: Structure of naphthalocyanine system capable of singlet oxygen generation, trapping and thermal release.

1.6.2 Application of [4+2] cycloaddition reactions

A major application of this reaction, which will be discussed in more detail in Chapter 2, is slow-release or fractional PDT but this transformation is also employed for oxygen storage systems, bioimaging, and even photolithography. In the following paragraphs, some examples will be highlighted.

Firstly, the endoperoxide of 1,4-dimethylnaphtlene, **1.84** is used as a singlet oxygen generator under both mild and dark conditions where thermal release occurs at 25 °C. The endoperoxide is formed at 0 °C and can be stored at -80 °C for several months.[222] In 1985, this concept was applied to polymeric systems. Methyl-substituted poly(vinylnaphtha-1-enes) were prepared by Saito *et al.* and their endoperoxides, which were generated using methylene blue (MB), were shown to release singlet oxygen between 0-35 ºC.[225] Similar to the monomers, they can generate singlet oxygen under mild conditions but can also be used under solvent-free conditions and the residue can be easily removed after thermal decomposition.[225]

[4+2] Cycloaddition reactions play a role in biological probes and imaging agents. The activity of SOSG is based on endoperoxide formation and this probe is widely used to detect singlet oxygen and for bioimaging. It has a very low fluorescent

quantum yield of approximately 1.9%, as a result of photoinduced electron transfer (PeT). However, following interaction with singlet oxygen, the orbital energies are perturbed and photo-induced electron transfer is unable to occur. The fluorescence quantum yield of the resultant endoperoxide is 37% with a maximum emission at 525 nm. It is used both *in vitro* and *in vivo* and in bench assays but quantitative measurements are limited by its inherent singlet oxygen-generating ability (**Scheme 1.5**).[80,226]

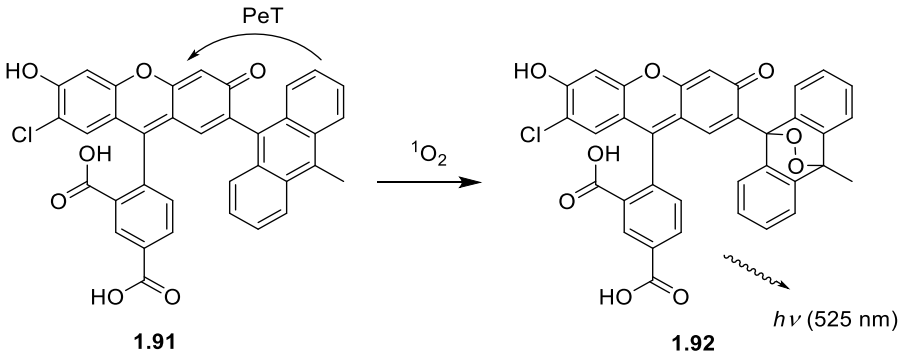

Scheme 1.5: Structure of singlet oxygen sensor green (SOSG) showing that its function is reliant on a [4+2] cycloaddition reaction.

Perhaps, a more synthetically eloquent example was provided by Mokhir and co-workers who detailed a library of phosphoramidites, which contained an anthracene-based linker and other molecular fragments including nucleosides, fluorogenic agents, and a cholesteryl derivative. In the presence of singlet oxygen, the linker was cleaved by endoperoxide formation *via* a cycloaddition, which was followed by decomposition to release of the attached units. They applied this concept to the design of a singlet oxygen probe for live mammalian cells. The attached fluorophores were quenched when the linker was intact and activated upon cleavage. They reported that the fluorescence intensity of the probe is related to the concentration of singlet oxygen within the cells and responsive to both photogenerated singlet oxygen and singlet oxygen resulting from the decomposition of the endoperoxide, compound **1.94**, **Scheme 1.6**.[227]

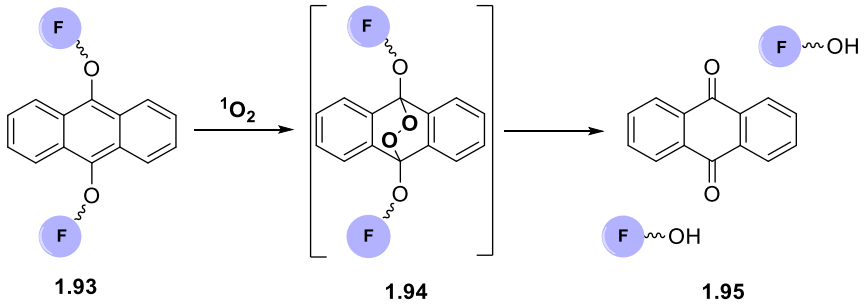

1.93 1.94 1.95

Scheme 1.6: Singlet oxygen responsive linker with intermediate endoperoxide formation.

In a final example, a 9,10-diphenylanthracene-based monolayer or thin film was used to write on a micrometre surface using [4+2] cycloaddition reactions. The anthracene unit was anchored to a silicon surface using amide bonds. The system was sensitised using MB and visible light. The generation of endoperoxides led to quenched fluorescence that could be restored (up to 90%) upon heating and this cycle could be repeated (**Fig. 1.21**).[228]

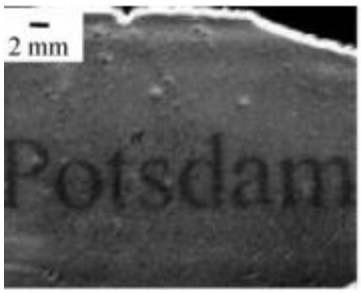

Figure 1.21: Fluorescence image of a pattern generated on 9,10-diphenylanthracene monolayer; reproduced from ref. 228.[228]

Chapter 2: Pyridone-substituted Porphyrins for Slow Singlet Oxygen Release

"That her dark hair would weave a snare that I might one day rue;
I saw the danger, yet I passed along the enchanted way,
And I said, let grief be a fallen leaf at the dawning of the day"

Patrick Kavanagh, 1946

2.1 INTRODUCTION

2.1.1 Singlet oxygen slow-release systems

A major roadblock to the widespread clinical application of PDT is a lack of patient compliance with treatment regimens due to the pain associated with intense and prolonged light exposure. In addition to this, blistering and itching caused by photosensitivity continues post-treatment.[229] On the other hand, long treatment times and intense light are required to give an effectual therapeutic response as singlet oxygen has a limited half-life in biological media.[79] A practical solution to these issues is rest periods between successive light exposures, with the added advantage of allowing tissue oxygen levels to recover. However, as singlet oxygen generation only occurs in the presence of light, the therapeutic effect is fragmented. Thus, designing systems that can generate, store, and slowly release singlet oxygen in cells after irradiation has been terminated could facilitate an enhanced PDT effect for clinical application. The aforementioned [2+4] cycloaddition reactions between singlet oxygen and aromatic units have found application in PDT as these reactions can mediate slow singlet oxygen release.

Thermolysis of endoperoxide gold nanoparticles is an option for delayed singlet oxygen release. Gold nanoparticles functionalised with anthracene endoperoxide derivatives were shown to release singlet oxygen for up to several weeks upon photothermal or magnetic activation.[230,231] In 2016, Kolemen *et al*. demonstrated

that singlet oxygen release could be mediated by near-infrared (NIR) light *in vitro*.[232] In their work, they described an anthracene-based endoperoxide linked to a gold nanorod (**2.1**, **Fig. 2.1**), with each nanorod carrying 6.5×10^9 anthracene derivatives. They showed that when a dimethyl sulfoxide (DMSO) solution of the nanoconstruct and a singlet oxygen scavenger, in this case, 1,3-diphenylisobenzofuran (DPBF), was either irradiated with a laser at 830 nm or gradually heated from 25 °C to 100 °C, there was a decrease in DPBF absorption due to singlet oxygen release from the endoperoxide. In contrast, a control of only the gold nanorods gave no response. To demonstrate this *in vitro*, HeLa cells were treated with the functionalised nanorods and incubated for 24 h. The cells were then exposed to Cyto-ID, to detect oxidative stress, and 808 nm near-IR light (2.0 W/cm^2) for 10 min. After 24 h, a reduction in cell viability was confirmed by an 3-(4,5-dimethylthiazol-2-yl)-2,5-diphenyltetrazolium bromide (MTT) assay. Although it was demonstrated that the chemical generation of singlet oxygen can cause apoptosis *in vitro* using light-induced thermolysis, optimisations of the light dose are required to transition this concept to a clinical setting.[232]

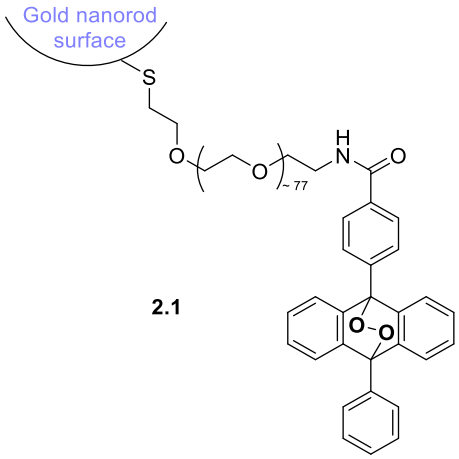

Figure 2.1: Structure of photothermally activated anthracene-based slow-release PDT photosensitiser.

Naphthalene is another option for singlet oxygen slow-release PDT systems. Lv *et al.* designed a system with naphthalene endoperoxides and an iridium(III) complex conjugated to a polymeric carrier. Gold nanorods were also included to trigger photothermal singlet oxygen release upon irradiation at 808 nm. Phototoxicity was

demonstrated in HeLa cells and attributed to both photothermal and oxidative cellular damage.[233]

Recently, 1,4-dimethylnaphthalene derivatives were applied to PDT by the Akkaya group. They synthesised a trimethylsilyl 1,4-dimethylnaphtalene endoperoxide, compound **2.2**, that was stable at rt for up to 800 h. Upon the addition of fluoride ions from tetrabutylammonium fluoride (20 mM), the trimethylsilyl group underwent cleavage and the resulting 1,4-dimethylnaphthalene endoperoxide, compound **2.3**, decayed with a half-life of 5 h to release singlet oxygen. This fluoride-mediated controlled singlet oxygen release was demonstrated *in vitro*. MCF-7 cells were incubated with varying concentrations of the endoperoxide and sodium fluoride, as the fluoride ion source. Toxicity attributed to released singlet oxygen was observed; however, it was also noted that sodium fluoride is not ideal for *in vivo* models due to its inherent toxicity (**Scheme 2.1**).[234]

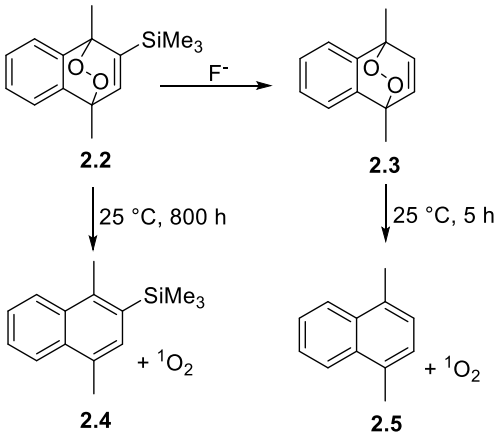

Scheme 2.1: Fluoride ion controlled slow-release singlet oxygen system.

2.1.2 The pyridone moiety in photodynamic therapy

Pyridone moieties are important 'trapping units' for slow-release singlet oxygen systems for biomedical applications because their water-solubility facilitates *in vitro* studies and endoperoxide formation and decay occurs at biologically relevant temperatures. Firstly, they have been used in photomedicine for the regeneration of anoxic tissue, a major contributor to necrosis during grafting.[235] Benz *et al.* studied a library of substituted pyridone-based endoperoxides and found that at 37 °C in water they had varying half-lives and cycloreversion yields. Compound **2.6** was determined to have a half-life of 8.5 h and a cycloreverson yield of 78% in water at

37 °C (**Scheme 2.2**), which are important properties for biological applications. This compound was incubated with fibroblasts and smooth muscle cells, which were grown under anoxic (0% oxygen) conditions. Vitamin C was added to quench singlet oxygen and avoid oxidative damage. Cell survival was increased due to the photochemically generated oxygen thus demonstrating the potential of these systems in aiding the treatment of necrotic wounds.[236]

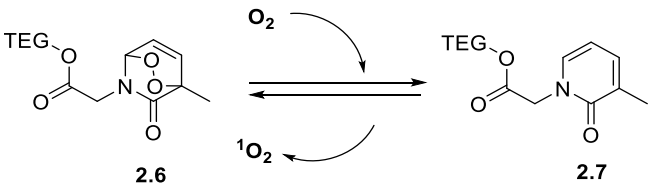

Scheme 2.2: Pyridone-based singlet oxygen controlled slow-release systems (TEG = triethylene glycol).

In the same year, Changtong *et al.* reported 2-pyridone moieties that were conjugated to a porphyrin. This single construct was capable of singlet oxygen generation by the porphyrin photosensitiser, storage on the pyridone units, and subsequent thermal release. They showed that endoperoxide decay between 25 °C and 50 °C was reversible and followed first-order kinetics. Interestingly, the endoperoxide could be generated at rt and singlet oxygen release continued for several h post-irradiation.[237]

Although the aforementioned work highlighted these pyridone-based compounds as potential PDT agents, they were limited by poor water-solubility. In 2016, Akkaya and co-workers validated the concept *in vitro* using halogenated distryl BODIPYs fashioned with 2-pyridone moieties. These systems were delivered to cells using micelles. BODIPY **2.8** (**Fig. 2.2**) was transformed into the endoperoxide using light irradiation in the presence of MB. The efficiencies of the native BODIPY and its endoperoxide bearing analogue were compared in cytotoxicity studies. HeLa cells were treated with varying (9 nM – 2.5 µM) concentrations of each compound and irradiated with red light for 10 min every hour for 24 h. These light-dark cycles were followed by 24 h of incubation in the dark. Increased cytotoxicity was observed for the endoperoxide bearing BODIPY as opposed to the parent functionalised BODIPY. They also studied the release of singlet oxygen from the endoperoxide

using DPBF as a singlet oxygen trap. Irradiation of the parent halogenated BODIPY in a DMSO solution resulted in singlet oxygen generation and a decrease in DPBF absorbance. This was followed by a dark stage in which DPBF absorbance continued to decrease. The pattern continued over several light-dark cycles, in essence, showing that singlet oxygen is produced from the photosensitiser but also released from the endoperoxides under dark conditions making these compounds applicable to fractional PDT.[238]

Since the first publication of the results disclosed in this chapter,[239] the pyridone unit has established itself as a useful moiety for PDT photosensitisers. Some examples will be highlighted in the following paragraphs. In 2018, Xiao *et al.* demonstrated the pyridone trapping principle with an aza-BODIPY core. They synthesised an aza-BODIPY photosensitiser with 2-pyridone units, compound **2.9**. This was reacted with 1,2-distearoyl-sn-glycero-3-phosphoethanolamine-N-[methoxy(polyethylene glycol)-2000] (DSPE-mPEG2000), to generate biocompatible nanoparticles through self-assembly. These constructs generate singlet oxygen, which is trapped and slowly released *via* the pyridone units. They demonstrated cellular uptake and phototoxicity in HeLa cells and preferential tumour accumulation *in vivo*. HeLa tumours implanted in nude mice displayed 93% inhibition (**Fig. 2.2**).[240]

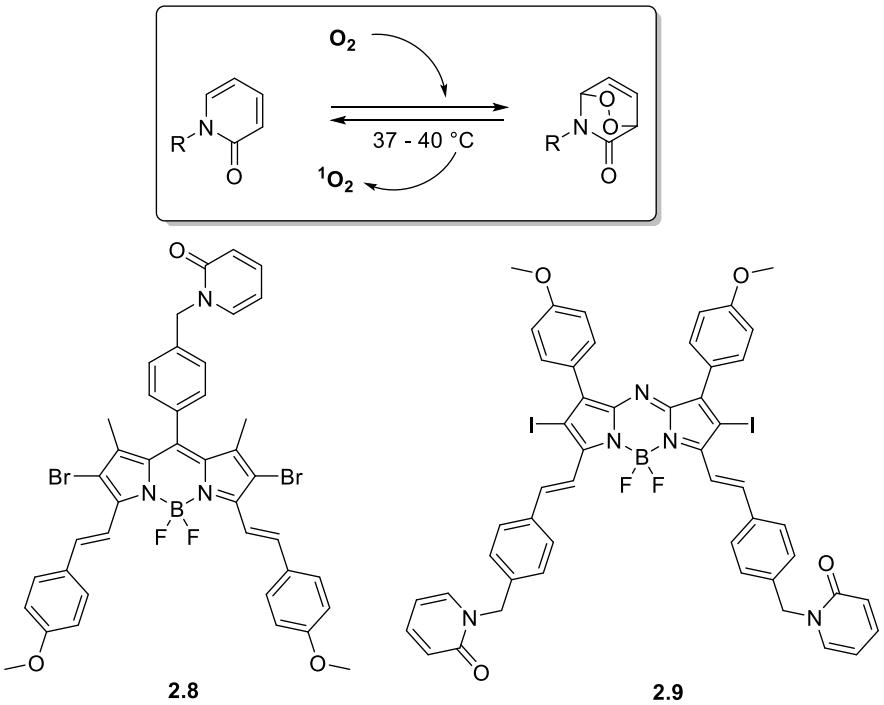

Figure 2.2: Structure of pyridone-based slow-release photosensitisers with BODIPY and aza-BODIPY cores.

Another nanoconstruct with pyridone units for application in PDT was published in 2019 by Jiao *et al*.[241] They constructed a silica nanocarrier with a protoporphyrin IX derivative to generate single oxygen, a pyridone storing unit, and a cyanine derivative to monitor singlet oxygen production. The cellular uptake of the system in HeLa cells was sufficient and upon light irradiation, fractional PDT was demonstrated. They noted higher phototoxicity resulting from their system compared to a traditional protoporphyrin IX photosensitiser in HeLa cells and were able to monitor singlet oxygen production under dark conditions in living cells using fluorescent bleaching.[241]

A pyridone-containing phenalenone has also been designed, compound **2.11**. The phenalenone unit generates singlet oxygen, which is trapped by the pyridone units and then thermally released. This was demonstrated in HeLa cells and apoptosis was initiated during both light and dark cycles.[242]

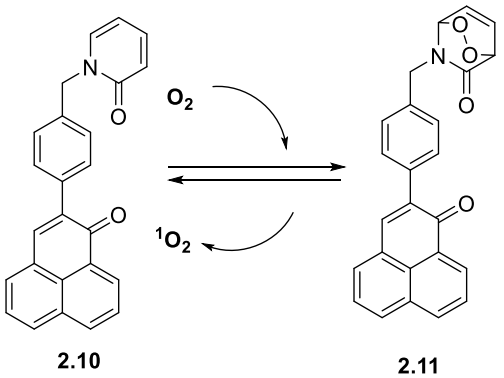

Scheme 2.3: Structure of pyridine-functionalised phenalenone.

In a final recent example of a pyridone modified system. Chen *et al.* functionalised Erlotinib, an epidermal growth factor receptor (EGFR) targeting chemotherapeutic drug, with a pyridone unit using 'click' chemistry.[243] They showed that uptake was greater in Hcc827 cells, an Erlotinib-sensitive human lung cancer cell line with high EGFR expression, when compared to HepG2 cells, with high differentiation and proliferation, or H1975 cells, an Erlotinib-resistant human lung cancer cell line. Endoperoxide bearing Erlotinib showed a two-fold increase in anticancer activity in the cell models when compared to Erlotinib and the pyridone-substituted Erlotinib. This principle was also demonstrated in tumour bearing Kunming mice with the endoperoxide functionalised Erlotinib showing a better antitumor response than unsubstituted Erlotinib. This approach is particularly interesting because it does not require light or tissue oxygen.[244]

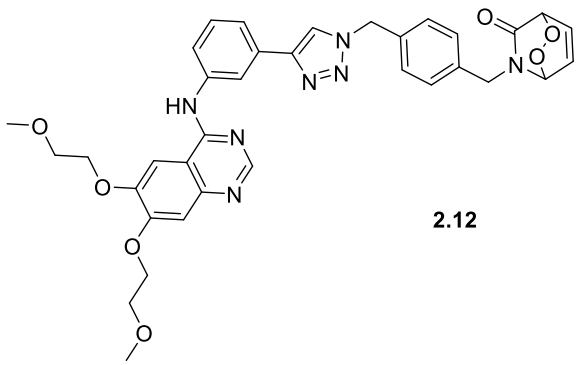

Figure 2.3: Structure of pyridone endoperoxide functionalised Erlotinib.

2.2 OBJECTIVES

Practical limitations of PDT are patient discomfort and compliance issues associated with irradiation protocols that cause skin burning and inflammation. To address this, we aimed to synthesise compounds that can produce singlet oxygen under dark conditions and thus allow for either a reduction in irradiation time or fractional irradiation protocols. We also aimed to design a system that could increase the therapeutic response by continuing to generate singlet oxygen under dark conditions. The approach aimed to design compounds capable of singlet oxygen generation, storage, and thermal release.

Pyridone was chosen as the trapping unit because it has inherent water-solubility and endoperoxide thermal decay properties that can be chemically tuned for biological conditions and thus medical applications. It was envisioned that pyridine-octa- and -tetra substituted porphyrins would show increased water-solubility and singlet oxygen trapping ability, correlating to an enhanced therapeutic effect. The porphyrin core was chosen as it is a versatile synthetic scaffold and an efficient singlet oxygen generator. The target compounds were tetrapyridone-substituted porphyrins with carboxylic acid units, compounds **2.13** and **2.14**, and octapyridone-substituted porphyrins, compounds **2.15** and **2.16** (**Fig. 2.4**). We aimed to produce these compounds using Lindsey condensation and nucleophilic substitution reactions as key synthetic steps. Target compounds, **2.13**–**2.16**, differed by their substitution pattern and we aimed to study the effect of this variation on thermal decay and the resulting permutations in the therapeutic response. We also aimed to investigate the *in vitro* cytotoxicity of the target compounds to evaluate their biocompatibility and applicability to PDT.

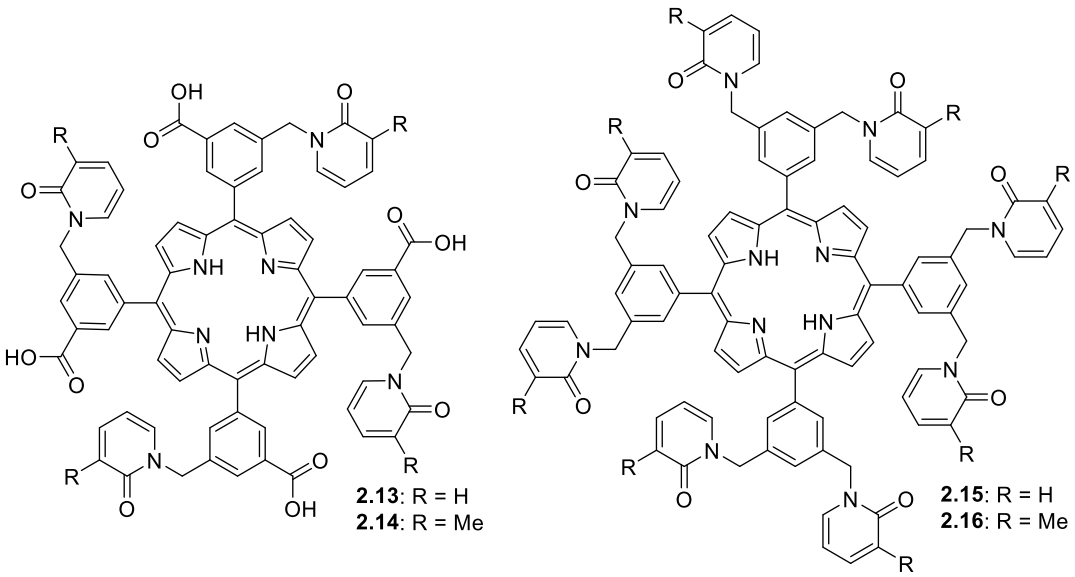

Figure 2.4: Structures of target pyridone-appended photosensitisers.

2.3 RESULTS AND DISCUSSION*

2.3.1 Pyridone-substituted A_4-porphyrins

Pyridone-substituted porphyrins were investigated as potential PDT photosensitisers. Initially, symmetric porphyrins bearing four pyridone units were synthesised. Porphyrin **2.17** was synthesised under Lindsey conditions[92] and characterised in accordance with a previously published procedure.[237] Porphyrins **2.18** and **2.19** were prepared by a nucleophilic substitution reaction between porphyrin **2.17** and either 2-hydroxypyridine or 3-methyl-2-hydroxypyridine, with the pyridone in a 15-fold excess and in the presence of NaH (**Scheme 2.4**). Yields of 52% and 63% were obtained for **2.18** and **2.19**, respectively.

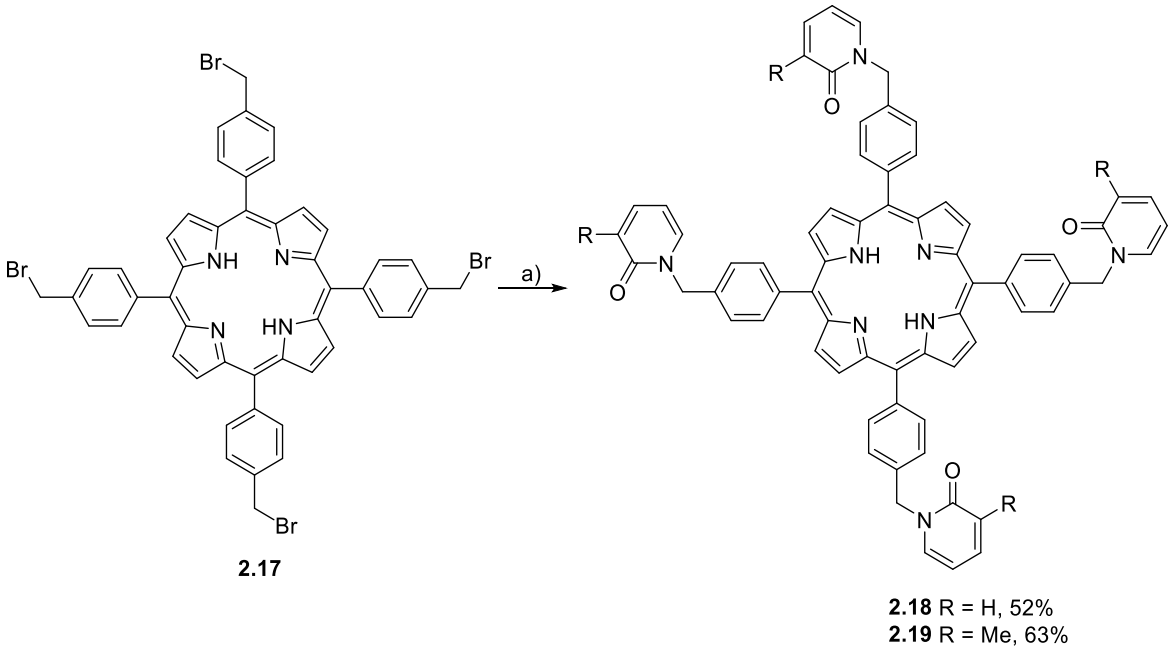

Scheme 2.4: Synthesis of pyridone-substituted A_4-porphyrins. a) 2-Hydroxypyridine or 3-methyl-2-hydroxypyridine (15 eq.), NaH (15 eq.), THF, rt, 5-6 h.

The introduction of four pyridone units did not show the expected water-solubility and thus *in vitro* studies failed. SOSG assays were performed on porphyrins **2.18** and **2.19.** As described in **Scheme 1.5**, SOSG consists of an anthracene unit that

*Contributions to the results in this chapter were made by Dr. M. A. Filatov and the Boyle Group.

quenches a fluorophore. Upon cycloaddition between singlet oxygen and the anthracene unit, quenching is disrupted and fluorescence is enhanced.[226] Porphyrins **2.18** and **2.19** were irradiated with broadband light (400–700 nm) in tetrahydrofuran (THF) at 0 °C for 1 h to ensure complete conversion of the pyridone moieties to endoperoxides. After irradiation, SOSG (0.1 eq.) was added and fluorescence was monitored with time while heating to 20 °C or 40 °C. The results indicate that the release of singlet oxygen from the endoperoxide of compound **2.18** took place at 20 °C over 5 h. In contrast, the endoperoxide of compound **2.19** did not release singlet oxygen under the same conditions but when heated to 40 °C the release took place over 7 h (**Fig. 2.5**). This is explained by the electron-donating effect of the methyl group, which increases the stability of the endoperoxide and thus decomposition occurs at higher temperatures.[239] This observation is in agreement with a previous publication on simple 2-pyridone derivatives, which reported that the endoperoxide of 2-pyridone has a half-life of 30 min at 37 °C, while 3-methyl-2-pyridone-endoperoxide is considerably more stable with a half-life of 8 h.[236]

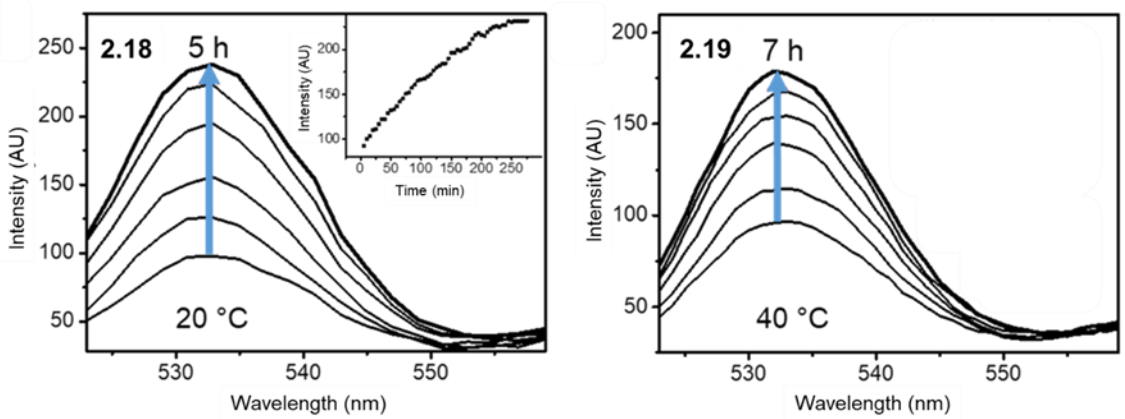

Figure 2.5: Singlet oxygen sensor green (SOSG) assay to detect singlet oxygen release from endoperoxides of compounds **2.18** (left) and **2.19** (right). Rise of SOSG fluorescence was monitored in THF with the excitation/emission pair 490/525 nm. Inset: 535 nm emission changes with time.

2.3.2 Synthesis of water-soluble pyridone-substituted A_4-porphyrins

To improve the water-solubility of the initial systems, optimisations were undertaken: i) the introduction of more pyridone moieties (compounds **2.15** and **2.16**) and ii) the introduction of carboxylic acid groups on the meso-aryl substituents (compounds

2.13 and **2.14**). Firstly, the synthesis of the octapyridone-porphyrins involved bromination of 3,5-dimethylbenzoate **2.20** to yield compound **2.21** (**Scheme 2.5**). This was followed by reduction of the ester to alcohol **2.22** with diisobutylaluminium hydride (DIBAL) and subsequent oxidation to aldehyde **2.23** with MnO_2. A two-step approach was taken for the synthesis of **2.23** from **2.21** to achieve better control as partial reduction to the aldehyde was expected to be problematic. Compounds **2.20**–**2.23** were synthesised and characterised in accordance with literature procedures.[245–247]

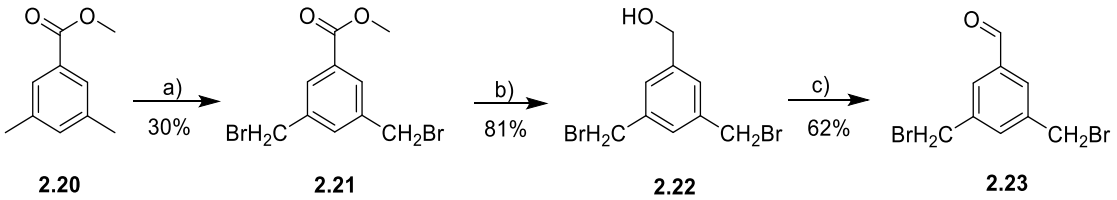

Scheme 2.5: Synthetic route to aldehyde **2.23**. a) NBS (2 eq.), benzoyl peroxide (cat.), CCl_4, reflux; 3.5 h; b) 1. DIBAL (2 eq.), toluene, 0 °C, 2. 70 °C, 3 h, 3. HCl (aq.); c) MnO_2 (10 eq.), DCM, rt, 24 h.

Then, aldehyde **2.23** was used in a pyrrole condensation under Lindsey conditions to yield octabromoporphyrin **2.25** in 39% yield (**Scheme 2.6**). This synthetic procedure was adapted from literature.[248]

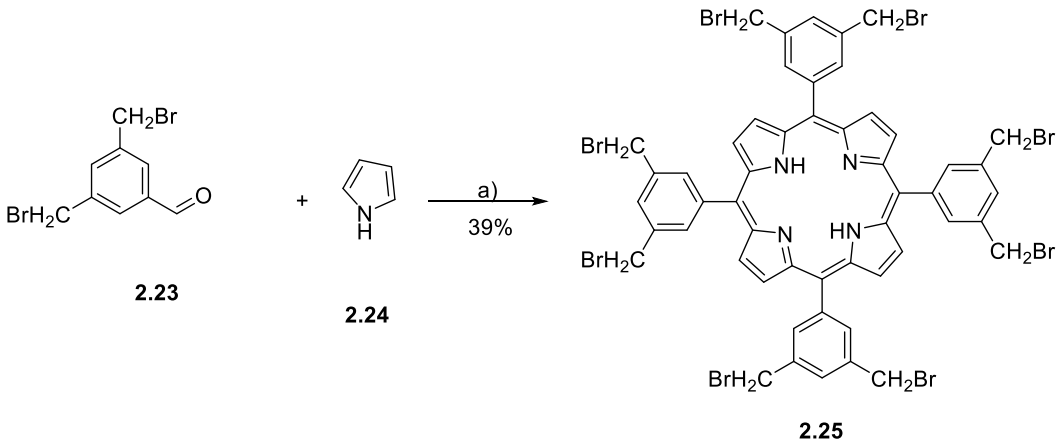

Scheme 2.6: Lindsey condensation reaction to yield porphyrin **2.25**. a) 1. $BF_3 \cdot Et_2O$ (cat.), DCM, rt, 3 h, 2. DDQ (0.75 eq.), rt, 1 h, 3. TEA (cat.).

Treatment of **2.25** with excess 2-hydroxypyridine or 3-methyl-2-hydroxypyridine in the presence of NaH yielded the target octapyridone-substituted systems **2.15** and **2.16** in 58% and 65% yields, respectively (**Scheme 2.7**).

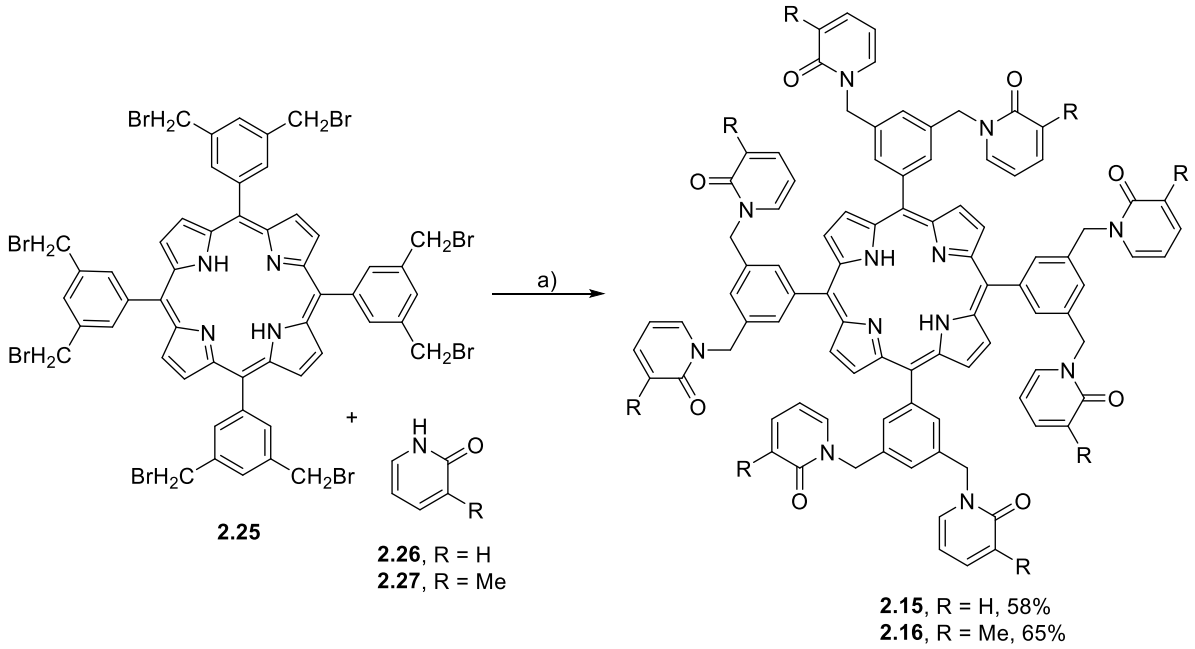

Scheme 2.7: Nucleophilic substitution reaction to yield target octa-substituted pyridone porphyrins. a) NaH (30 eq.), THF, 66 °C, 5 h.

The second approach required selective monooxidation of dibromide **2.23** (**Scheme 2.8**). We attempted the optimisation of this step, which is described in **Table 2.1**, with the best result affording an 11% yield using bis(tetrabutylammonium)dichromate. The initial approach using Na_2CO_3 and NaOH resulted in over-oxidation (**Table 2.1**, Entries 1 and 2),[249] therefore, a weaker oxidising agent MnO_2 was chosen.[250] Insufficient oxidation occurred with the resulting low yields unsuitable for continuing the synthetic route (Entries 3–6). Finally, by adapting a literature procedure using bis(tetrabutylammonium)dichromate the target compound **2.28** was obtained in a yield of 11%; moderate, considering the synthetic challenge.[251]

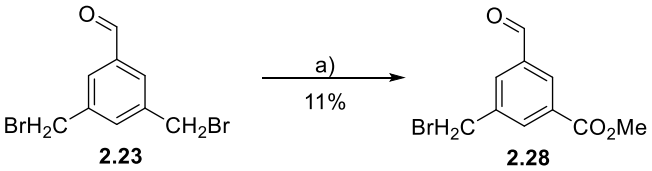

2.23 **2.28**

Scheme 2.8: Monooxidation of **2.23**. a) $(Bu_4N)_2Cr_2O_7$ (0.66 eq.), $CHCl_3$, 70 °C, 1 h.

Table 2.1: Attempted optimisation to yield compound **2.28**.[249–251]

Entry	Reagent	Solvent	Eq.	Temp. (°C), Cond.	Time (h)	Result
1	Na_2CO_3 and NaOH	H_2O	1.1	120, bench	5.5	Not isolated
2	Na_2CO_3 and NaOH	H_2O	1.1	140, bench	24	Over Ox. of **2.23**
3	MnO_2	$CHCl_3$	4.6	70, bench	96	5%
4	MnO_2	THF	4.6	65, bench	48	1%
5	MnO_2	$CHCl_3$	9.2	70, microwave	2.8	Not isolated
6	MnO_2	DCM	9.2	70, pressure tube	19	6%
7	$(Bu_4N)_2Cr_2O_7$	$CHCl_3$	0.66	70, bench	1	Not isolated (impure)
8	$(Bu_4N)_2Cr_2O_7$	$CHCl_3$	0.66	70, bench	1	9%
9	$(Bu_4N)_2Cr_2O_7$	$CHCl_3$	0.66	70, bench	1	11%

Aldehyde **2.28** and pyrrole were then used to access the tetra brominated porphyrin fashioned with esters, compound **2.29**; a 42% yield was obtained (**Scheme 2.9**).

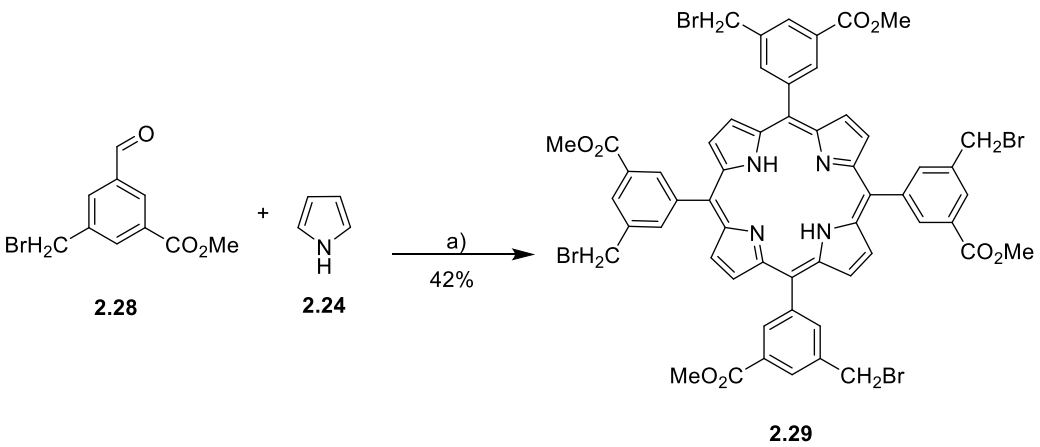

Scheme 2.9: Synthesis of tetrabrominated porphyrin with ester functionalities. a) 1. $BF_3 \cdot Et_2O$ (cat.), DCM, rt, 2 h. 2. DDQ (0.75 eq.), rt, 30 min. 3.TEA (cat.).

Following a nucleophilic substitution reaction with the corresponding pyridones (15-fold excess), compounds **2.30** and **2.31** were obtained, in 77% and 57% yields, respectively. Finally, conversion to the carboxylic acid was achieved using excess KOH to yield target compounds **2.13** and **2.14**. All of the pyridone-substituted porphyrins were purified by recrystallisation as degradation during silica column chromatography was observed (**Scheme 2.10**).[239]

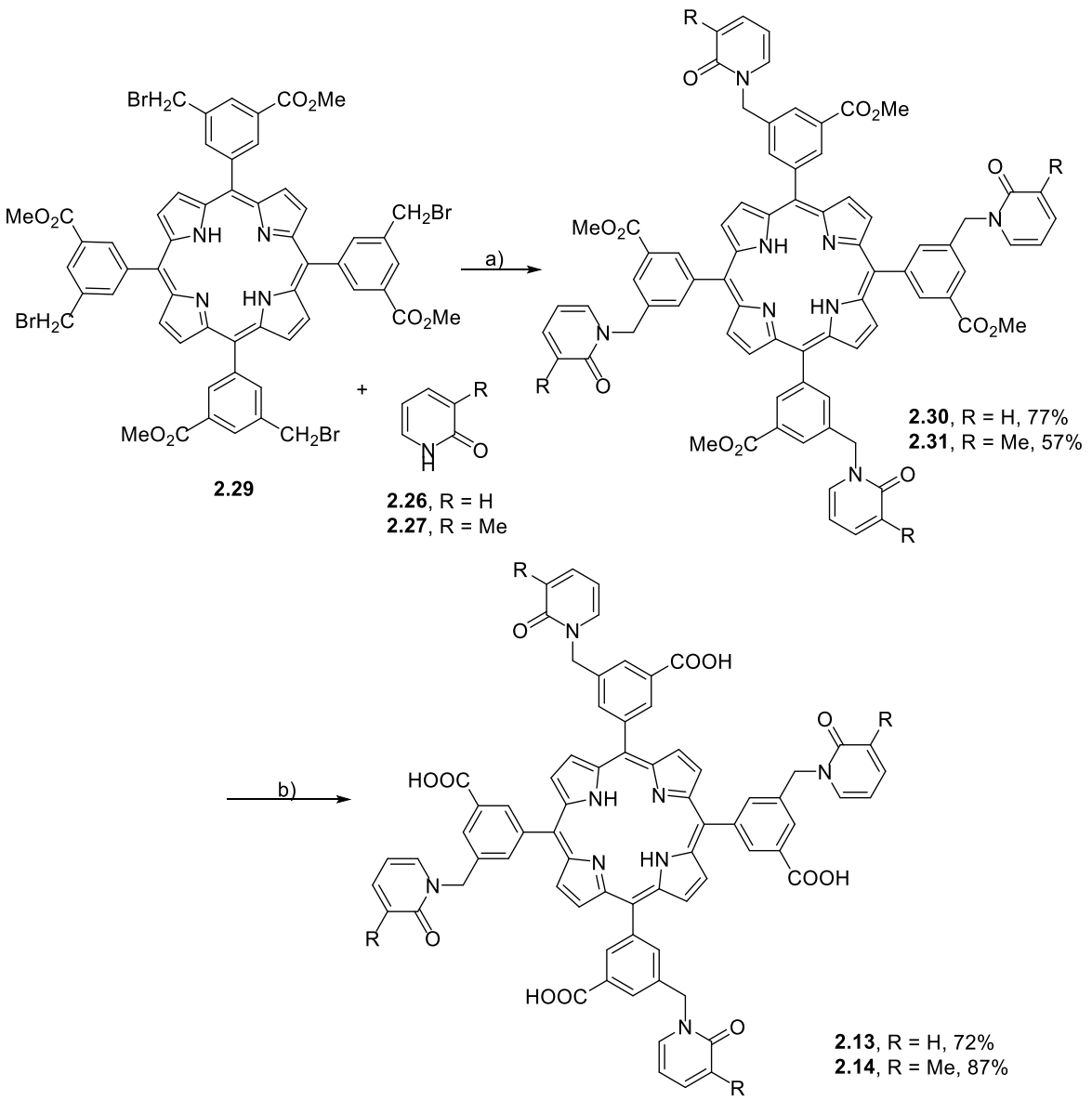

Scheme 2.10: Synthesis of tetrasubstituted pyridone porphyrins with carboxylic acid functionalities. a) NaH (15 eq.), THF, 70 °C, 5 h; b) KOH (30 eq.), THF, 66 °C, 24 h.

2.3.3 *In vitro* studies on pyridone-substituted A_4-porphyrins

Compounds **2.13**–**2.16** displayed increased water-solubility and, in collaboration with the group of Prof. Ross Boyle at the University of Hull, were tested for *in vitro* cytotoxicity. Human adenocarcinoma cells (HT-29) were treated with various concentrations of compounds **2.13**–**2.16** (in duplicate) and incubated in the dark for 1 h at 37 °C in an atmosphere of 5% CO_2. For each experimental point, one plate was irradiated with 20 J/cm^2 of broadband visible light (400–700 nm), while the second plate served as a "dark toxicity" control. Following 24 h of incubation, cell

viability was determined using MTT assays. Upon the reduction of MTT by NAD(P)H-dependent oxidoreductase enzymes to formazan, a colour change from yellow to purple is observed and this can be used to monitor metabolic activity and thus cell viability. The formazan is dissolved in solution and absorption spectroscopy is then used to quantify cell viability.[252]

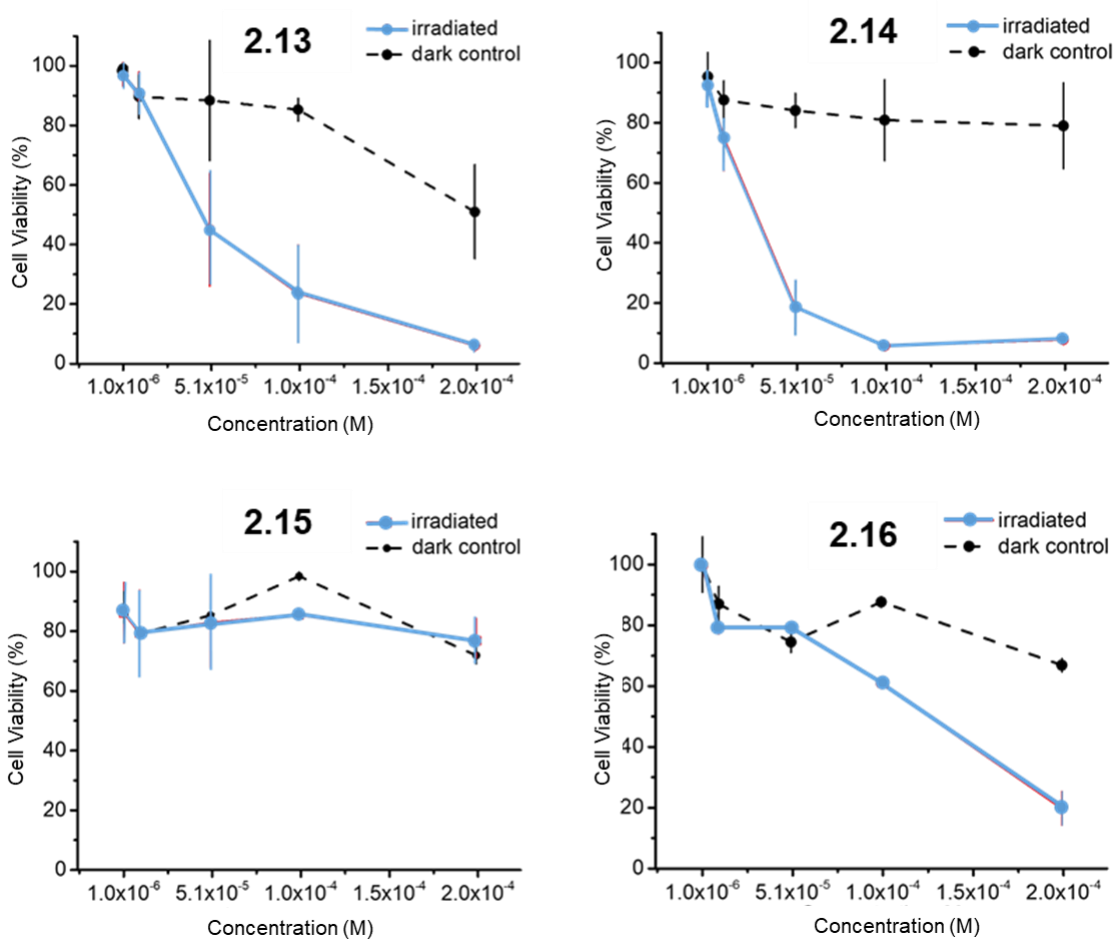

Figure 2.6: HT-29 cell viabilities after 1 h of incubation with porphyrins **2.13**–**2.16** with (blue) and without (black) light irradiation (400–700 nm, 20 J/cm^2).

From the data presented in **Fig. 2.6** it can be seen that compounds **2.13** and **2.14**, bearing carboxylic acid moieties, showed significant toxicity under light conditions and minimal toxicity in the dark. Most promisingly, compound **2.14** displayed efficient cytotoxicity (less than 20% viability) at a concentration of 51 μM. For these compounds, the presence of the methyl group had little effect on endoperoxide stability *in vitro*. In contrast, compound **2.16** bearing eight methylated pyridone units gave a better response than the non-methylated **2.15**. At the highest concentration

of 200 µM, 80% cell inactivation was observed for compound **2.16** in comparison to 23% for compound **2.15** (**Fig. 2.6**). It can be concluded that the methyl group stabilises the endoperoxide and thus the slow-release effect is more pronounced, resulting in a stronger therapeutic response.[239]

2.3.4 Synthesis of pyridone-substituted A_3B-porphyrins

In an extension of this project, unsymmetric analogues were synthesised with the aim of incorporating an anchor group for conjugation to nanoplatforms such as hydrogels. To achieve this synthetically, mixed condensations were employed.

First, a synthetic route towards pyridone hexasubstituted porphyrins was investigated. Compound **2.23** was synthesised as previously described (**Scheme 2.5**) and condensed with aldehyde **2.32** and pyrrole. The mixed condensation, which yielded compound **2.33**, was then optimised. It was found that the logical 3:1 ratio gave a lower yield (10%) compared to a 2:1 ratio (12%), possibly due to the relative reactivities of the aldehydes (**Scheme 2.11**). As expected, the A_4 porphyrin was the major product. A nucleophilic substitution reaction was attempted with 2-hydroxypyridine but the target compound was not isolated as recrystallisation proved difficult.

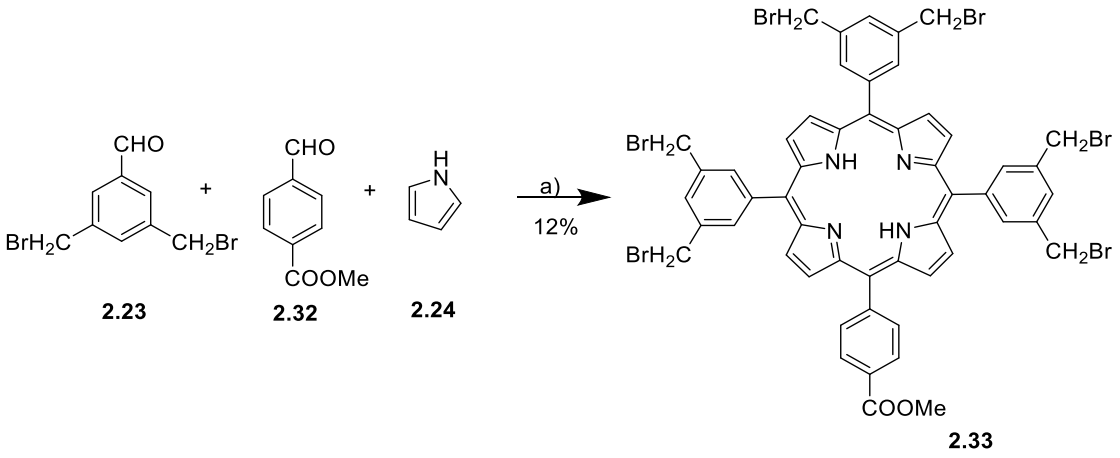

Scheme 2.11: Synthesis of hexabrominated A_3B-porphyrin. a) 1. $BF_3 \cdot Et_2O$ (0.1 eq.), DCM, rt, 2 h. 2. DDQ (0.75 eq.), rt, 24 h. 3. TEA (cat.).

In the first synthetic step on the route to the tri-substituted porphyrin, a cyanide reduction, adopted from literature,[253] yielded aldehyde **2.35** in a 90% yield (**Scheme 2.12**).

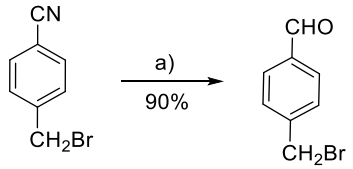

Scheme 2.12: Reduction to yield aldehyde **2.35**. a) 1. DIBAL (1.2 eq.), toluene, 0 °C. 1 h, 2. $CHCl_3$. 3. HCl (aq.).

Aldehyde **2.35** was then condensed in a ratio of 2:1 with aldehyde **2.32** and pyrrole. The condensation resulted in the target A_3B porphyrin, **2.36**, in a yield of 14% and a yield of 18% for the A_4 porphyrin as a second product.

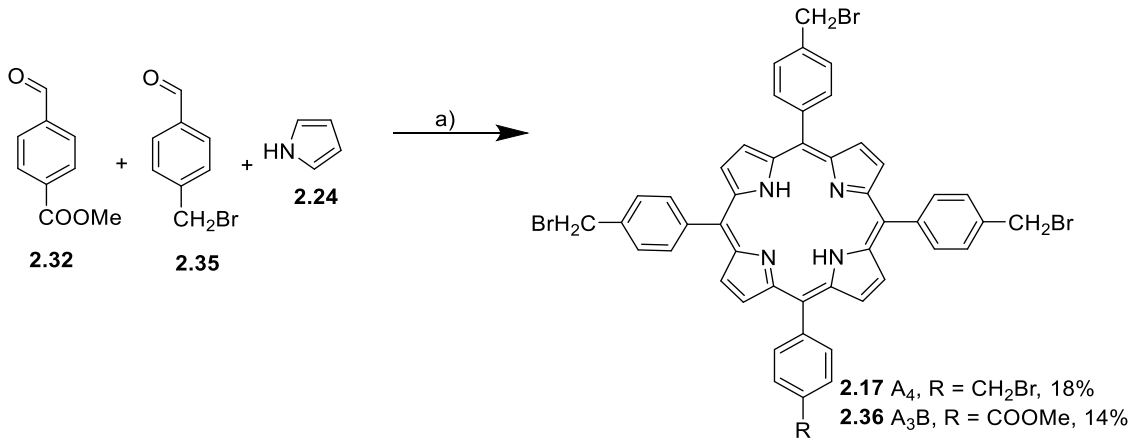

Scheme 2.13: Synthesis of pyridone-substituted AB_3-porphyrin a) 1. $BF_3 \cdot Et_2O$ (0.1 eq.), DCM, rt, 1.5 h. 2. DDQ (0.75 eq.), rt, 2 h. 3. TEA (cat.).

The A_3B porphyrin, **2.36** was substituted with 2-hydroxypyridine or 3-methyl-2-hydroxypyridine to afford porphyrins **2.37** and **2.38** in yields of 23% and 19%, respectively (**Scheme 2.14**). Again, these compounds were purified using recrystallisation techniques.

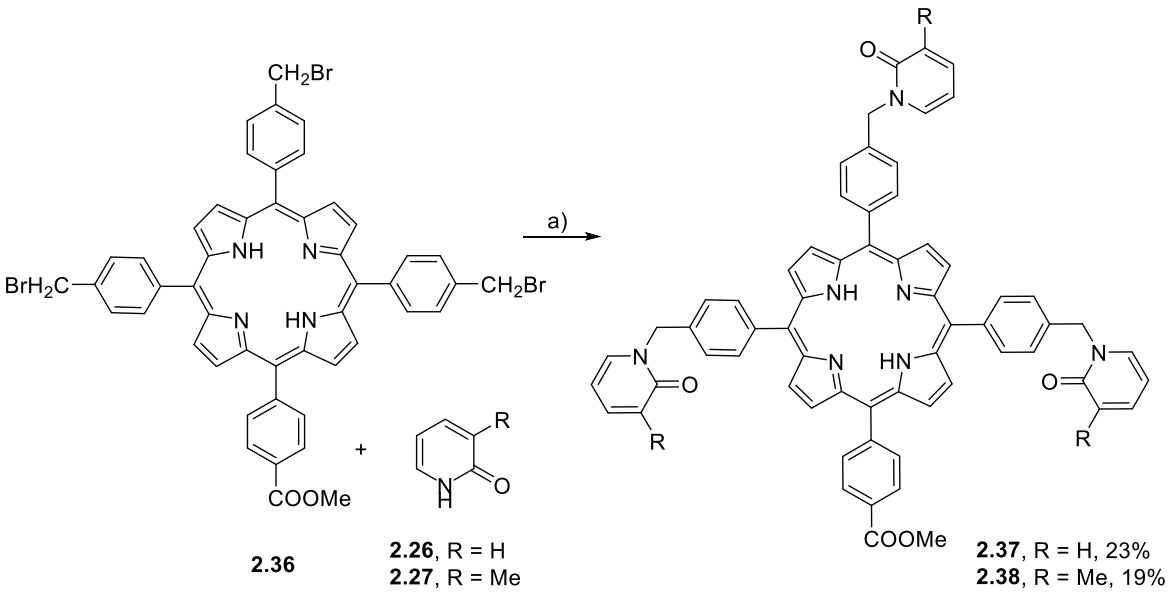

2.36 **2.26**, R = H **2.27**, R = Me **2.37**, R = H, 23% **2.38**, R = Me, 19%

Scheme 2.14: Synthesis of pyridone-substituted AB_3-porphyrin. a) NaH (15 eq.), THF, 66 °C, 5 h.

2.4 CONCLUSION AND FUTURE WORK

In summary, we have successfully synthesised water-soluble pyridone-substituted porphyrins and evaluated their applicability to PDT. Upon interaction with light, the porphyrin core generates singlet oxygen, a fraction of which undergoes [4+2] cycloaddition reactions across the pyridone subunits, leading to singlet oxygen storage. We were able to show that singlet oxygen was released from the endoperoxide of compound **2.18** at 20 °C over 5 h. In contrast, the endoperoxide of compound **2.19** released singlet oxygen at 40 °C over 7 h, indicating that the endoperoxide substitution pattern affects the endoperoxide stability and thus its thermal decay. Of note for biological applications, a methyl substitution pattern (compounds **2.13** and **2.16**) results in endoperoxide decay at clinically relevant temperatures. *In vitro* studies show that the water-soluble compounds were uptaken into cells. Additionally, photodynamic action and singlet oxygen slow-release effects resulted in cytotoxicity. Compound **2.14**, with methyl-substituted endoperoxides, displayed the strongest response with less than 20% cell viability at a concentration of 51 µM under light irradiation. This work is among the first examples of endoperpeoxides being applied to PDT.

This was a proof-of-concept study but looking forward, these systems can be optimised further to provide an alternative to conventional PDT regimes, especially *via* improvements of the irradiation protocols. Additionally, PDT in the dark can be envisioned. One possibility is to incorporate these trapping units as part of larger multifunctional constructs or further increase the number of traps using carrier systems, for example a hydrogel system. It is expected that a hydrogel framework would increase the water-solubility of the porphyrin and allow for increased payloads. We have made steps towards the synthesis of compounds for incorporation in carrier systems. For example, the methyl ester anchoring group can easily be converted to a carboxylic acid moiety for conjugation to the amino groups of chitosan hydrogels (**Scheme 2.15**).

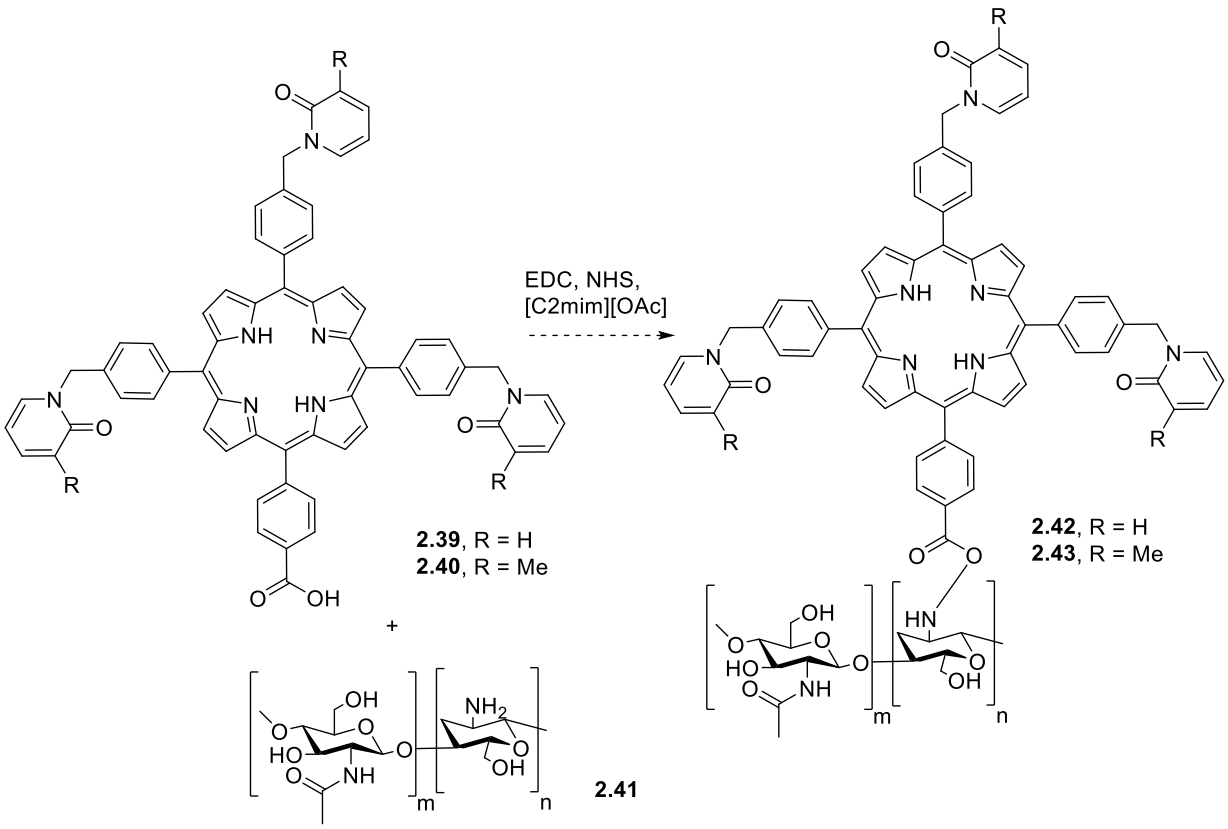

Scheme 2.15: Schematic illustration of possible pyridone-substituted porphyrin hydrogels. 1-Ethyl-3-methylimidazolium acetate ([C2mim][OAc]), 1-ethyl-3-(3-dimethylaminopropyl)carbodiimide (EDC), N-hydroxysuccinimide (NHS).

Chapter 3: Heavy-atom Free Singlet Oxygen Generating BODIPY Dyads

"Life … is a relationship among molecules and not a property of any molecule"

Linus Carl Pauling

quoted in Force of Nature: The Life of Linus Pauling, 1997

3.1 INTRODUCTION

As mentioned in Chapter 1 porphyrins and their derivatives are the cornerstone of PDT photosensitisers. However, in recent decades BODIPY-based systems have established themselves as feasible agents for both phototherapy and diagnostics because of their tuneable photophysical properties.[86] Inherently, BODIPYs are chromophores and therefore populate excited singlet states upon the absorption of light;[98] however, by exploiting photophysical phenomena such as the heavy atom effect and PeT, triplet state population can be increased. In many cases, this results in the generation of singlet oxygen and thus facilitates the possibility of PDT applications. By employing rational design principles and chemical modification to tune the photophysical properties, we can modulate the properties of BODIPYs to make them efficient photosensitisers.

3.1.1 Examples of singlet oxygen-generating BODIPYs

In the section, we aim to highlight strategies used to generate singlet oxygen and examples will be given, although many more may be found in the literature.[86,254] Some examples were also reviewed by us in the context of this thesis.[134] The first strategy to be discussed, and arguably the most widely used, is halogenation. This is a synthetically accessible method to initiate the heavy atom effect. The heavy atom effect was first described by McClure in 1949.[255] He studied a library of substituted aromatic compounds and noticed a reduction in phosphorescence with increasing atomic number of the substituents.[255] The heavy atom effect results in an increased rate of spin-forbidden process, in this case, singlet to triplet transitions.

Singlet to triplet transitions are forbidden by selection rules because the singlet and triplet states have different multiplicity. The transition is mediated by spin-orbit coupling or the quantum mixing of states. Spin-orbit coupling is the interaction between the spin magnetic moment of an electron and the magnetic field resulting from the apparent nuclear motion. The magnitude of the nuclear magnetic field is directly proportional to nuclear charge and thus is dependent on the atomic number of the substituent. Therefore, compounds substituted with atoms of large atomic numbers can often result in spin-orbit mixing. Subequently, intersystem crossing (ISC) from the singlet excited state to the triplet is observed. This results in an increased excited triplet state population from which singlet oxygen is generated (**Fig 3.1**).[256]

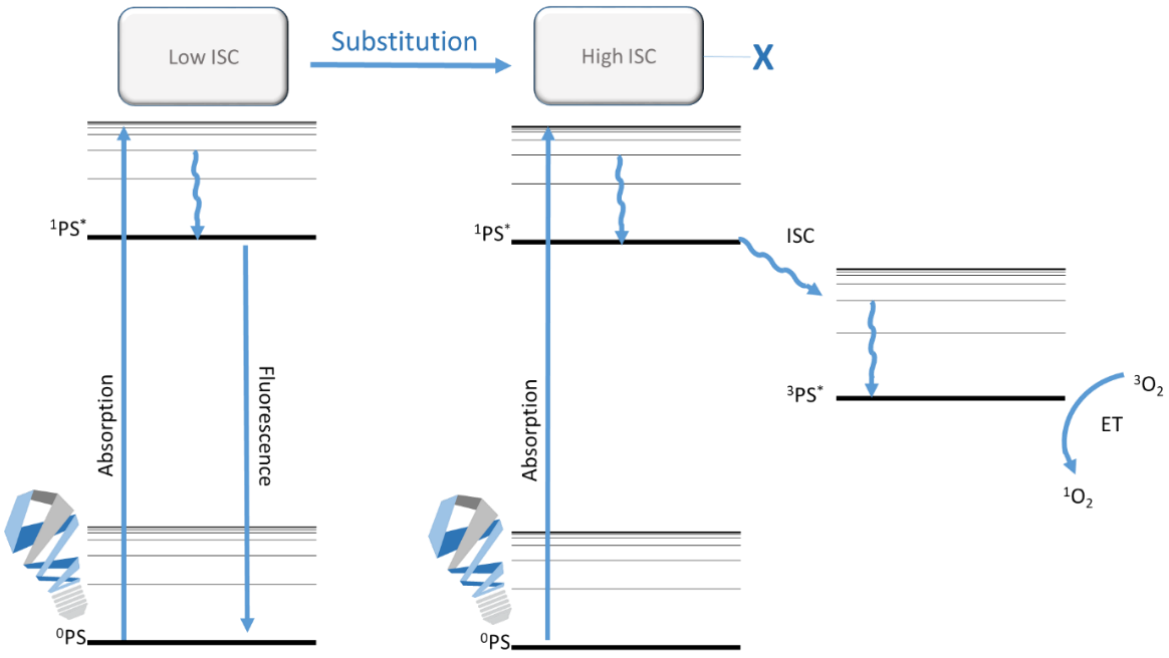

Figure 3.1: Jablonski diagrams describing the heavy atom effect. Intersystem crossing (ISC), electron transfer (ET), halogen (X).

Yogo *et al.* investigated the singlet oxygen-generating abilities of **3.1** using the singlet oxygen trap, DPBF. Compound **3.1** displayed singlet oxygen-generating abilities in a range of solvents and a low fluorescent quantum yield (Φ_f = 0.02 in MeOH) as the two processes compete. They also showed that **3.1** was more resistant to photobleaching compared to Rose Bengal (RB) by measuring the

absorption spectra after repeated laser illumination. They used **3.1** to demonstrate the photodynamic effect in HeLa cells and observed cytotoxicity (**Fig. 3.2**).[207]

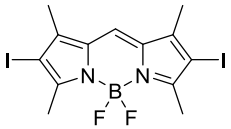

3.1

Figure 3.2: Structure of an iodinated BODIPY photosensitiser capable of singlet oxygen generation.

In another interesting example of how halogenation can modulate photophysical properties, compounds **3.2**–**3.4**, with increasing number of iodine atoms, were shown to generate singlet oxygen to a similar degree ($^1O_2\ \Phi$ = 0.83±0.07–0.87±0.06) using RB as a reference. Notably, the introduction of iodine at the 3- and 5-positions resulted in an increase in fluorescence (**Fig. 3.3**).

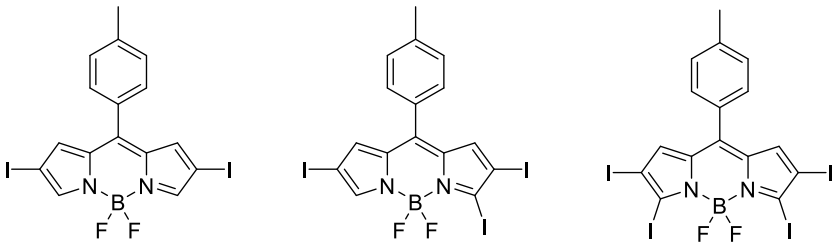

3.2

$^1O_2\ \Phi$ relative to RB:
0.83±0.07
Φ_f in hexane:
0.012

3.3

$^1O_2\ \Phi$ relative to RB:
0.86±0.09
Φ_f in hexane:
0.060

3.4

$^1O_2\ \Phi$ relative to RB:
0.87±0.06
Φ_f in hexane:
0.099

Figure 3.3: Structure of iodinated BODIPY photosensitisers with increasing fluorescence quantum yields. Rose Bengal (RB).

Halogenated aza-BODIPYs have also been studied for application in PDT due to their red-shifted absorption spectra. Using direct methods, compound **3.5** was shown to have a singlet oxygen quantum yield of 0.74 and a maximum absorption at 680 nm.[257] The photodynamic effect was shown using compound **3.5** both *in vitro* and *in vivo*, with a reported 71% ablation of mammary tumours in a mouse model (**Fig. 3.4**).[258]

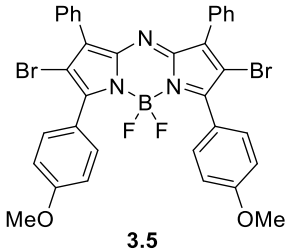

3.5

$^1O_2$ Φ : 0.74

Figure 3.4: Structure of singlet oxygen-generating aza-BODIPY.

In 2005, O'Shea and co-workers incorporated a singlet oxygen-generating halogenated BODIPY into a pH-responsive PDT system. In this proof-of-concept study, pH-dependence was exploited to selectively activate singlet oxygen generation by modulating a PeT process. They designed aza-BODIPY (compounds **3.6**) with pH-responsive amine units covalently attached at the 2- and 6-positions (**Fig. 3.5**). Their compounds displayed increased singlet oxygen production under acidic conditions (compounds **3.7**) due to the deactivation of the PeT mechanism and subsequent singlet oxygen generation from the aza-BODIPY unit. This was shown to be reversible upon the introduction of neutralising equivalents of base. *In vitro* studies in a transformed fibroblast cell line demonstrated cytoplasmic localisation and cytotoxicity; however, a clear correlation between cellular pH and cytotoxicity was not shown.[259]

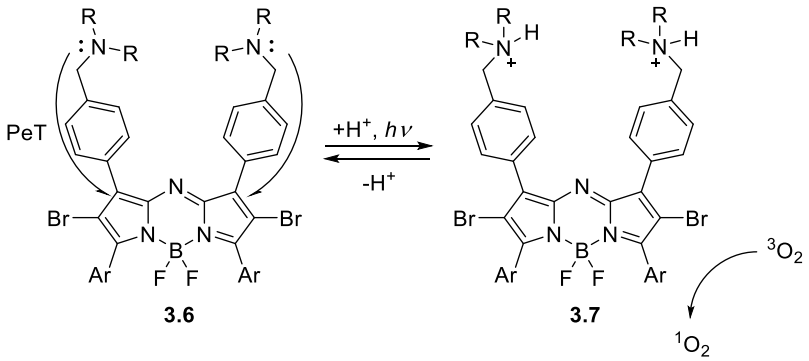

Figure 3.5: Structure of pH-responsive aza-BODIPY.

Another strategy to promote ISC is dimerisation as exemplified by compounds **3.8** and **3.9**, which give high singlet oxygen yields and low fluorescence compared to their monomers. Using DPBF as a singlet oxygen trap and MB as a reference, the

singlet oxygen quantum yields of **3.8** and **3.9** were determined to be 0.51 and 0.46, respectively. The singlet oxygen-generating ability is thought to arise from two excited singlet states when the chromophore units are connected orthogonally as they are isolated, computation studies have provided evidence for this. Compound **3.8** was shown to induce cytotoxicity against human erythroleukemia cells with an EC_{50} value of 50 nM.[260]

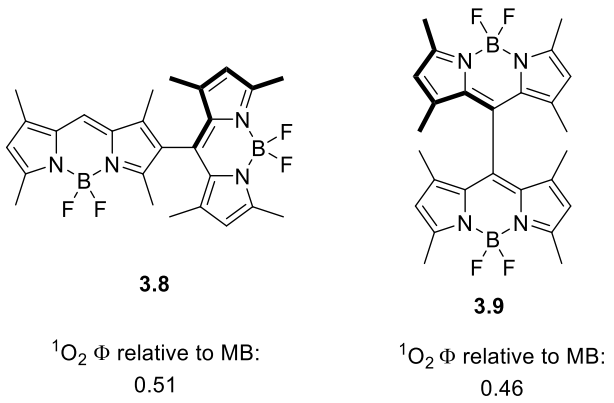

Figure 3.6: Structure of singlet oxygen-generating orthogonal dimers. Methylene Blue (MB).

Conjugation to a spin converter such as C_{60} can also give access to the triplet state, such as in the case of **3.10** and **3.11**. Fluorescence is quenched *via* intermolecular transfer to the C_{60} unit. Compound **3.10** was used for triplet-triplet annihilation applications and, using transient absorption spectroscopy, was shown to have a triplet state lifetime of 33.3 μs. Compound **3.11** has a triplet state lifetime of 123.2 μs and a singlet oxygen quantum yield of 0.009 in toluene using a BODIPY as the standard. Additionally, the extended conjugation resulting from the styryl groups results in a red-shifted absorption spectrum (absorption maximum of **3.11** at 657 nm in toluene). Although interesting organic photosensitisers, the application of these compounds in PDT is limited by solubility and biocompatibility issues (**Fig. 3.7**).[261,262]

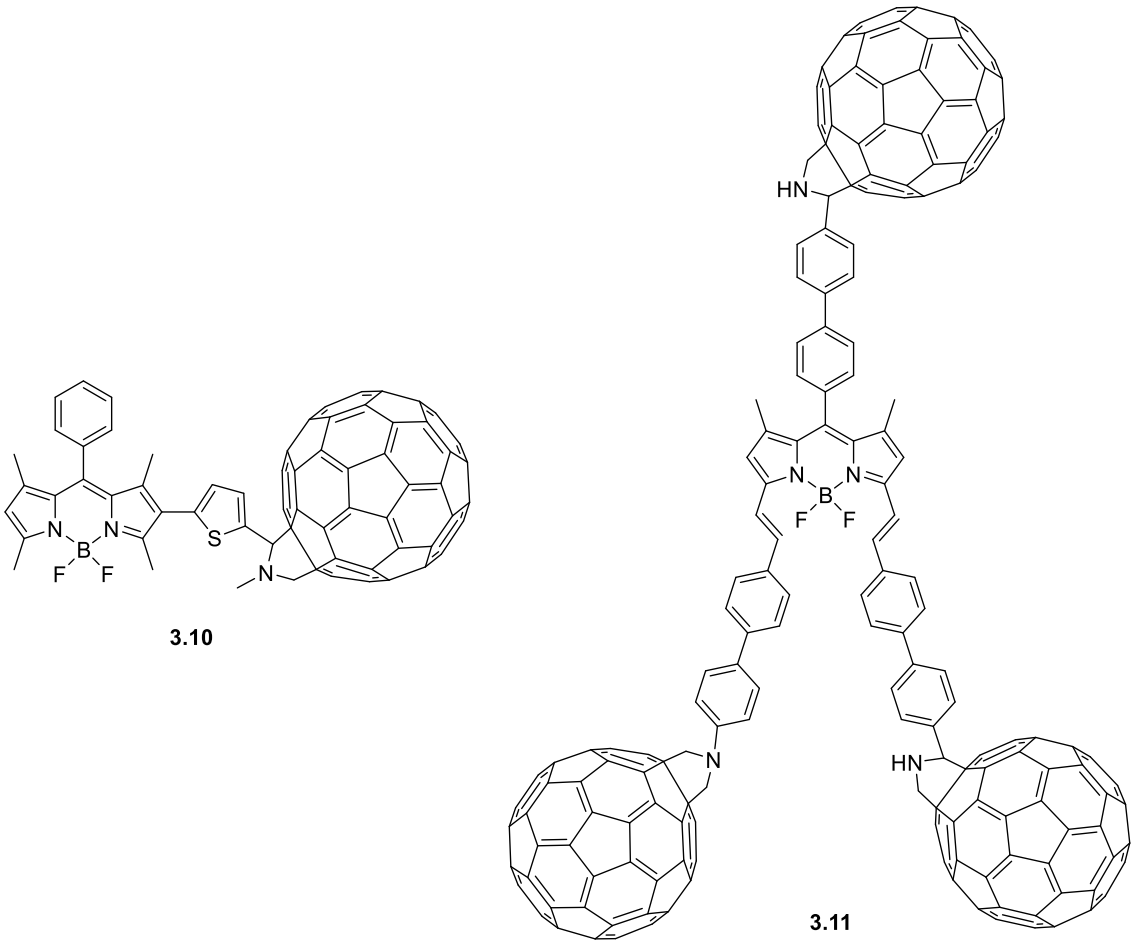

Figure 3.7: Structure of C_{60}-conjugated triplet state generators.

The final strategy to be discussed to access the triplet state involves reducing the energy gap between the singlet and triplet excited states. Nguyen *et al.* achieved this by making dyads with strongly donating groups at the 8-position of the BODIPY. In one recent example, compound **3.12**, a BODIPY core was fashioned with a phenoxazine group. BODIPY **3.12** had a reported 68% singlet oxygen quantum yield in toluene with respect to an iodinated BODIPY. The energy gap between the singlet and triplet states was reduced by 0.44 eV compared to a BODIPY without a donating group. The BODIPY was then incorporated into a micellar system for *in vitro* and *in vivo* studies. Dose-dependent phototoxicity was shown in HeLa cells and 70% tumour inhibition after three weeks, as well as imaging properties, were demonstrated *in vivo*.[263] The same group also reported a MeOPh-substituted thiophene-fused BODIPY, compound **3.13**, which has a singlet oxygen quantum

yield of 85% in acetonitrile and a fluorescence quantum yield of 17.11% in acetonitrile. It was concluded from an *in vitro* study that the IC_{50} value was 95 nM.[264]

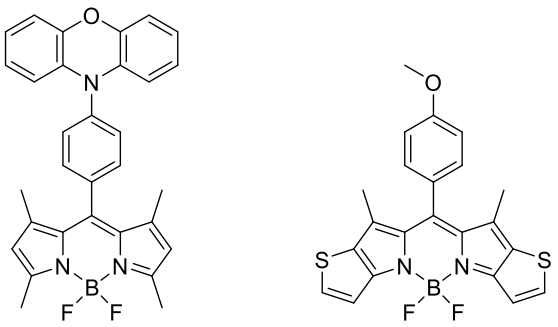

3.12 3.13

Figure 3.8: Structure of singlet oxygen-generating BODIPYs with electron-donating groups.

3.1.2 BODIPY-anthracene dyads and photoinduced electron transfer

In 2017, our group published another class of heavy atom free singlet oxygen-generating BODIPYs. BODIPY-anthracene dyads (BADs), e.g., compounds **3.15** and **3.14** were shown to have singlet oxygen quantum yields of 0.67 and 0.38, respectively. Upon light absorption, the singlet excited state is accessed.[265] As opposed to ISC being promoted by the heavy atom effect, in these compounds the triplet state is populated *via* a PeT process. Systems containing donor and acceptor units can undergo this process, in which an electron is transferred from the excited state of the donor (anthracene) to an acceptor (BODIPY), resulting in a highly dipolar excited state known as a charge-separated or charge transfer state. These charge-separated states can undergo radical-pair ISC or recombine to form local triplet excited states by spin-orbit charge-transfer ISC. The triplet and charge-separated states were identified by transient absorption spectroscopy (**Fig. 3.9**). Recently, Wang *et.al*. studied the electron spin dynamics of these compounds with time-resolved electron paramagnetic resonance spectroscopy and concluded that, in these systems, the triplet state is accessed by spin-orbit charge-transfer ISC.[266]

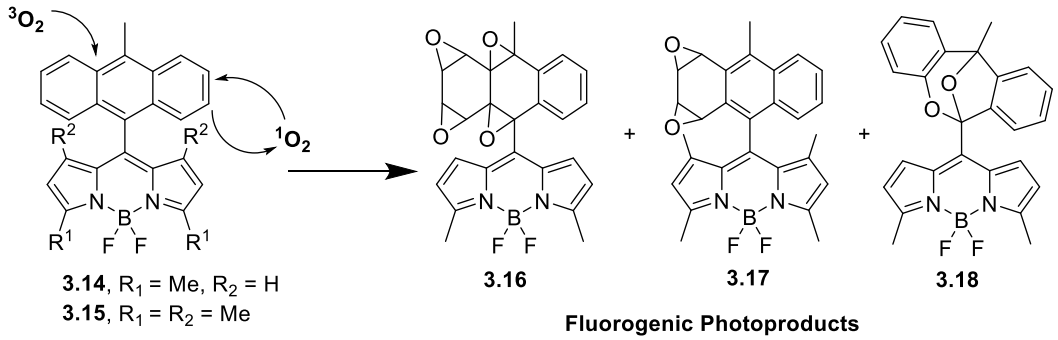

Scheme 3.1: BADs (**3.14 and 3.15**) and their photoproducts.

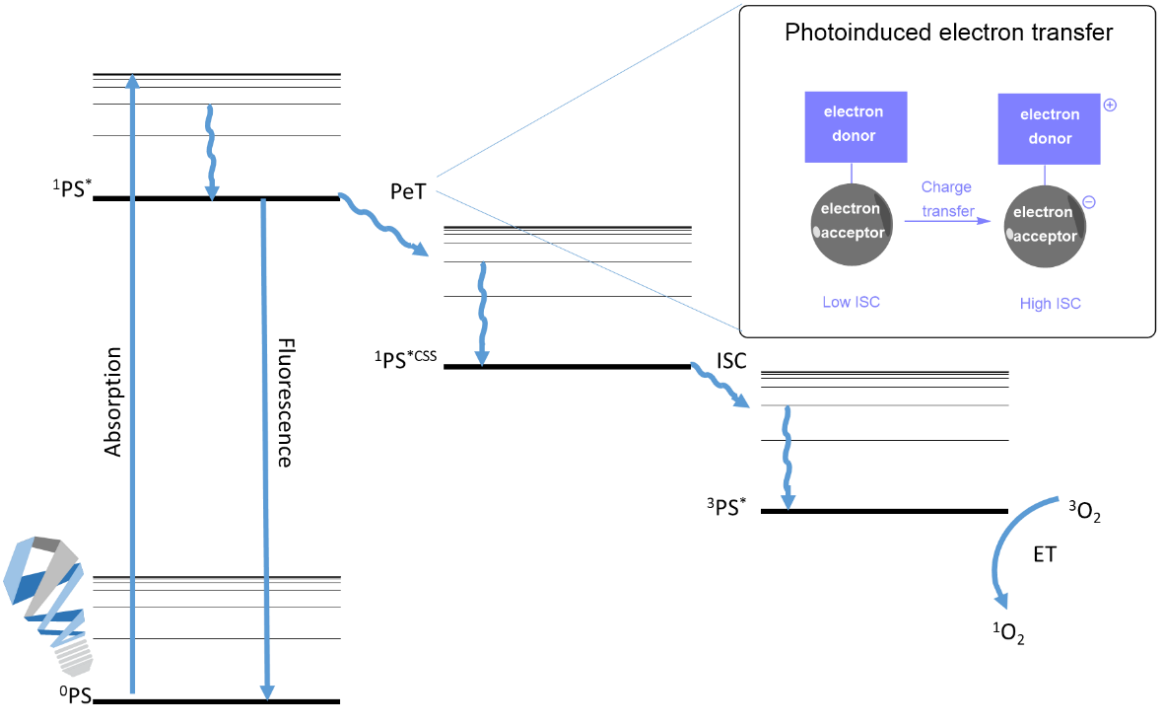

Figure 3.9: Jablonski diagram representing singlet oxygen generation in BADs. Inset: Schematic representation of photoinduced electron transfer. Charge-separated state (CSS), photosensitiser (PS), photoinduced electron transfer (PeT), electron transfer (ET), intersystem crossing (ISC).

In addition to photosensitisation, the aromatic unit in these systems is capable of endoperoxide formation *via* a [4+2] cycloaddition reaction between singlet oxygen and the anthracene unit. Homolysis of the oxygen-oxygen endoperoxide bond then occurs, which leads to rearrangement reactions, generating fluorogenic photoproducts (compounds **3.16**–**3.18**). These photoproducts complement the photodynamic effect by introducing the ability to visualise oxidative stress. The

photodynamic effect and fluorescence properties were demonstrated using human breast cancer cells (MDA-MB-468) following the synthesis of water-soluble BAD derivatives. Blebbing, characteristic of cell death, was observed and toxicity studies indicated LD_{50} values of 4 mM (**Fig. 3.10**).[265]

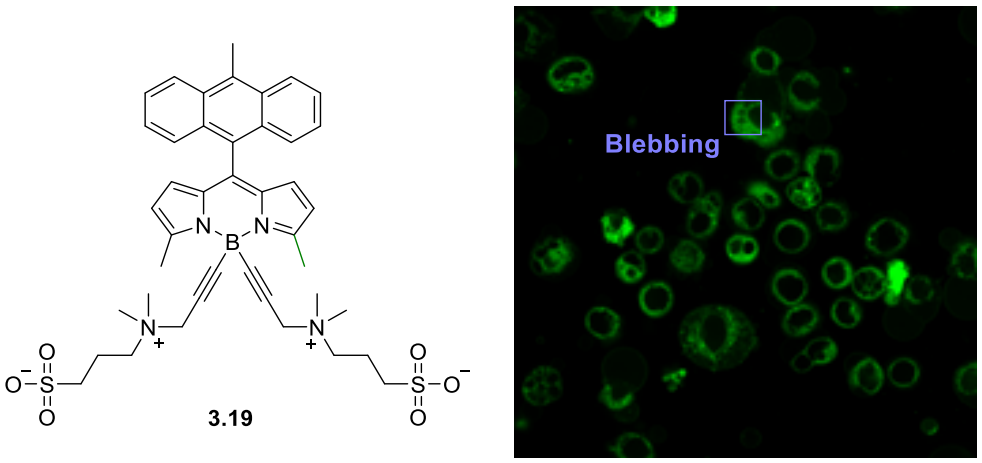

Figure 3.10: Example of water-soluble BAD and confocal microscopy image of MDA-MB-468 cells incubated with BODIPY-anthracene dyad, **3.19**, after 5 min; reproduced from ref. 265.[265]

3.1.3 Other photoinduced electron transfer-reliant photosensitisers

In 2007, Harriman *et al.* designed a photosensitiser with a BODIPY core and an *N*-methylpyridinium unit at the 8-position (**3.20**). Prior to methylation, the BODIPY is highly fluorescent but the methylation product (**3.20**) is a singlet oxygen generator *via* the formation of charge-separated states. This was facilitated by PeT from the BODIPY to the *N*-methylpyridinium unit, which was thermodynamically favourable because of the positive charge. Ultimately, a triplet state yield of 75% was obtained in acetonitrile.[267]

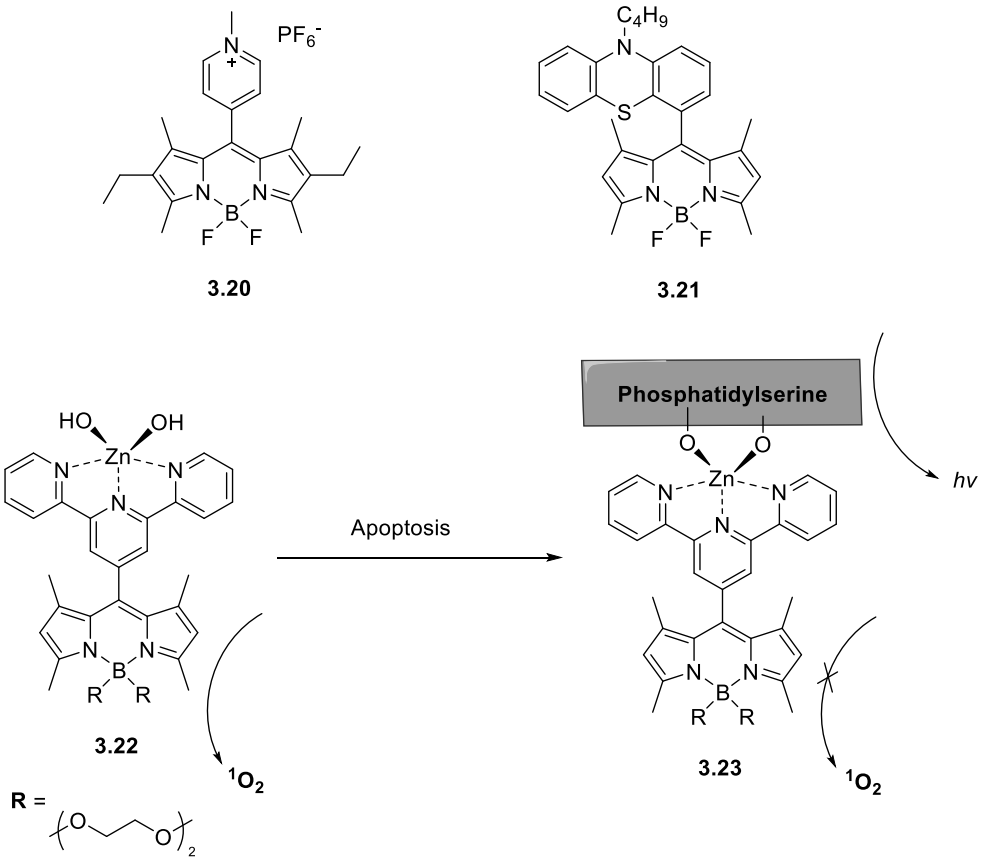

Figure 3.11: Examples of photosensitisers that generate triplet states *via* photoinduced electron transfer.

In recent years, there have been many other examples of photosensitisers that rely on PeT and charge-recombination. Firstly, Chen *et al.* described a BODIPY-phenothiazine dyad, **3.21**. The dyad has an orthogonal geometry with respect to the core in addition to a low fluorescence yield. A triplet state quantum yield of 97.5% was observed.[268] In 2019, Dong *et al.* reported BOPIPY-phenoxazine photosensitisers with similar properties.[269] In 2018, the Akkaya group reported a switchable system that was specifically applied to PDT. The system comprised of a BODIPY core fashioned with a Zn(II)-terpyridyl fragment (**3.22**), which acts as the electron acceptor, allowing PeT to occur. The subsequent generation of singlet oxygen was shown to induce apoptosis in K562 cells when exposed to light. Then, the Zn(II) ion interacted with phosphatidylserine, a lipid, which became exposed during apoptosis. In the resulting system, **3.23**, fluorescence is dominant to allow for imaging and the singlet oxygen-generating mechanism is quenched.[270]

3.2 OBJECTIVES

The development of effective strategies for modulating the photophysical properties of BODIPYs *via* chemical modification is key to their application as photosensitisers for PDT. BADs, first described by the Senge group, are a new class of photosensitisers, in which fluorescence is switched on by interaction with singlet oxygen.[265] Although interesting for applications in PDT, these novel photosensitisers are in their infancy with only two examples. We aimed to expand and optimise the library of BODIPY dyads capable of PeT mediated singlet oxygen generation and design compounds capable of both singlet oxygen and fluorescence generation for imaging purposes and to extensively investigate their applicability to PDT. We also aimed to gain an understanding of the compounds fundamental photophysical properties through the study of their absorption, fluorescence, and singlet oxygen-generating properties.

BODIPYs have been chosen as the central scaffold because of their chemically tuneable photophysical properties. 8-Substitutions with similar highest occupied molecular orbital (HOMO) energies to the previously reported anthracene systems, namely other anthracene derivatives, trimethoxyphenyl, perylene, and pyrene units (**Fig. 3.12**), are expected to generate singlet oxygen effectively. They were synthesised using two-step one-pot condensation and boron insertion reactions. We aimed to assess their applicability to PDT by synthesising water-soluble derivatives for *in vitro* studies. From our library, we hoped to identify and develop a lead compound that is suited to application in PDT.

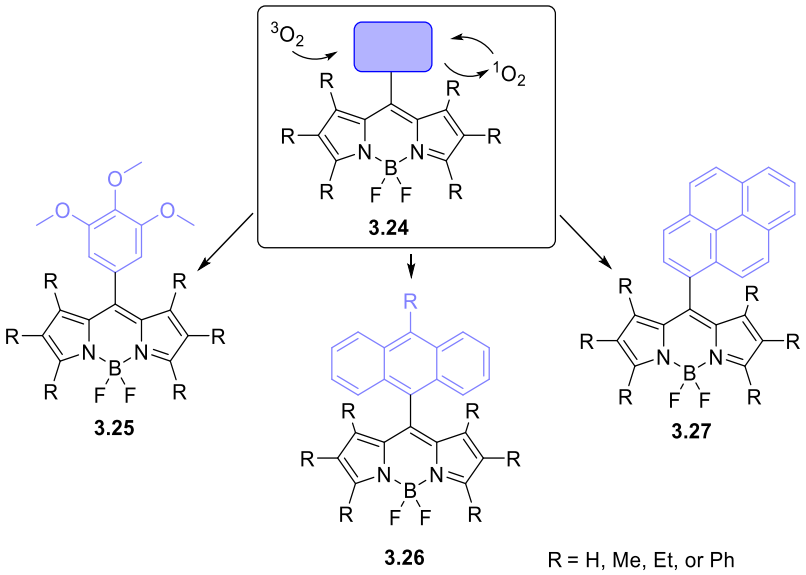

Figure 3.12: Schematic representation of target BODIPY dyads under investigation.

3.3 RESULTS AND DISSCUSSION[†]

3.3.1 Expanding the BODIPY dyad library

Following the initial success of the first two BADs, it was pertinent these photosensitisers were further investigated to assess their applicability to PDT. To realise this, the synthesis of an expanded library of dyads was performed. The library was designed to investigate the effect of varying the HOMO energies, by substituent variation, on PeT efficiency. In the PeT process, an electron is transferred from the HOMO of the anthracene unit to the BODIPY unit forming a charge-separated state (**Fig 3.13a**). Thus, 8-substituted BODIPYs with similar HOMO energies are expected to demonstrate effective PeT. It has been reported that pyrrole alkyl substitution can have a significant effect on the HOMO and lowest unoccupied molecular orbital (LUMO) energies.[271] The molecular energy of alkylated BODIPY cores, anthracene derivatives, pyrene, and perylene were calculated using density functional theory and they were shown to have comparable HOMO and LUMO energies (**Figure 3.13b**) and it can be seen that alkyl substituents reduce the electron-accepting ability of the BODIPY subunit. A series with a phenylene unit between the BODIPY core and aromatic unit was also included in the compound library to assess the effect of a spacer on the PeT process (**Figure 3.13**).[272,273]

[†] Contributions to the results presented in this chapter were made by Dr. M. A. Filatov, T. Wiesner, P. Gierlich, and Dr. K. J. Flanagan as well as our collaborators in the Boyle Group, University of Hull, the Arnaut Group, University of Coimbra, and Dr. P. Polestshuk, Moscow State University. Data for this chapter was collected during a research trip to NTNU in the group of Prof. O. A. Gederaas.

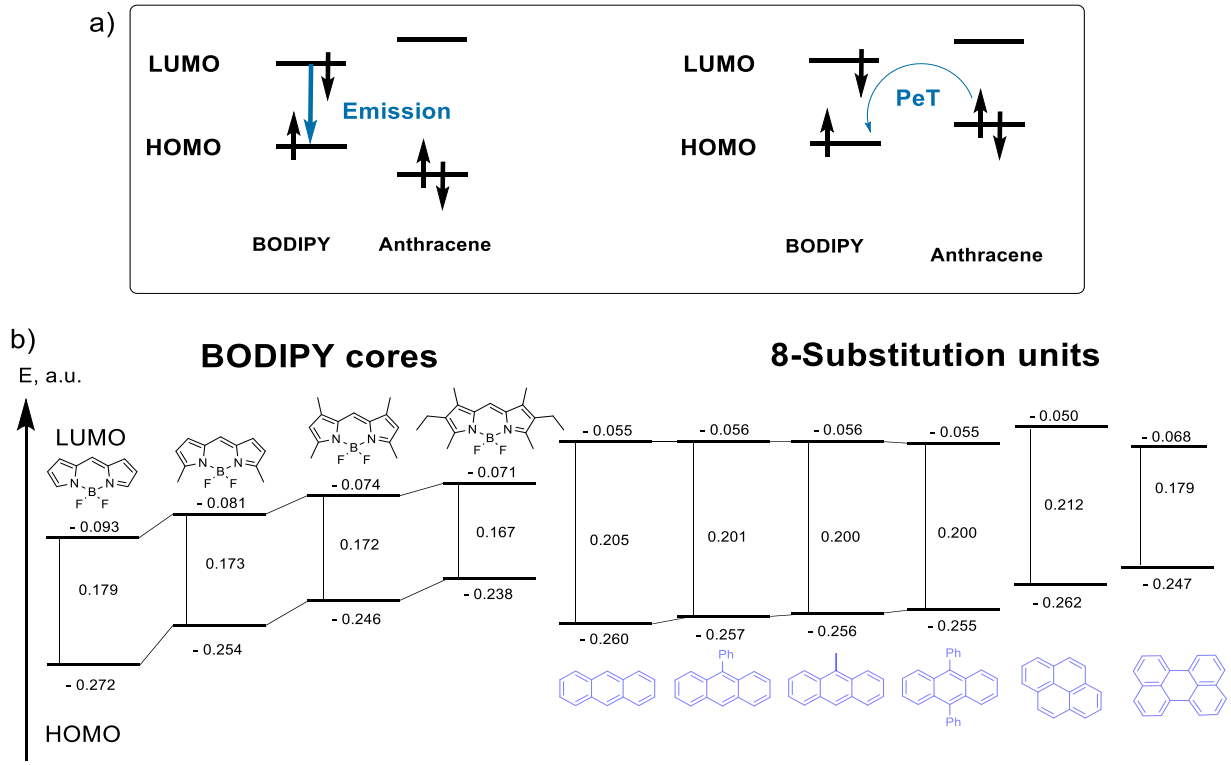

Figure 3.13: a) Diagram of emission *vs.* photoinduced electron transfer (PeT) mechanisms. b) Molecular orbital energies of the BODIPY cores and 8-substitution units of the dyads.

To that end, aldehydes of anthracene and pyrene derivatives were synthesised (compounds **3.30**, **3.31**, and **3.33**). Compound **3.28** was brominated to yield **3.29** in an 80% yield and then converted to aldehyde **3.30** using PhLi in a 50% yield, in accordance with literature procedures (**Scheme 3.2**).[274,275] A Suzuki coupling between compound **3.29** and formylphenylboronic acid afforded compound **3.31** in a 23% yield (**Scheme 3.2**). The procedure was adapted from literature.[274]

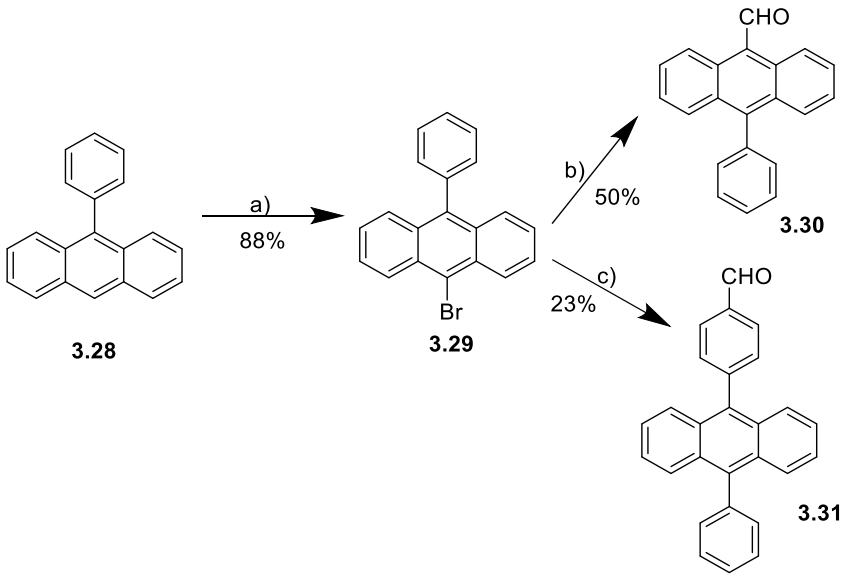

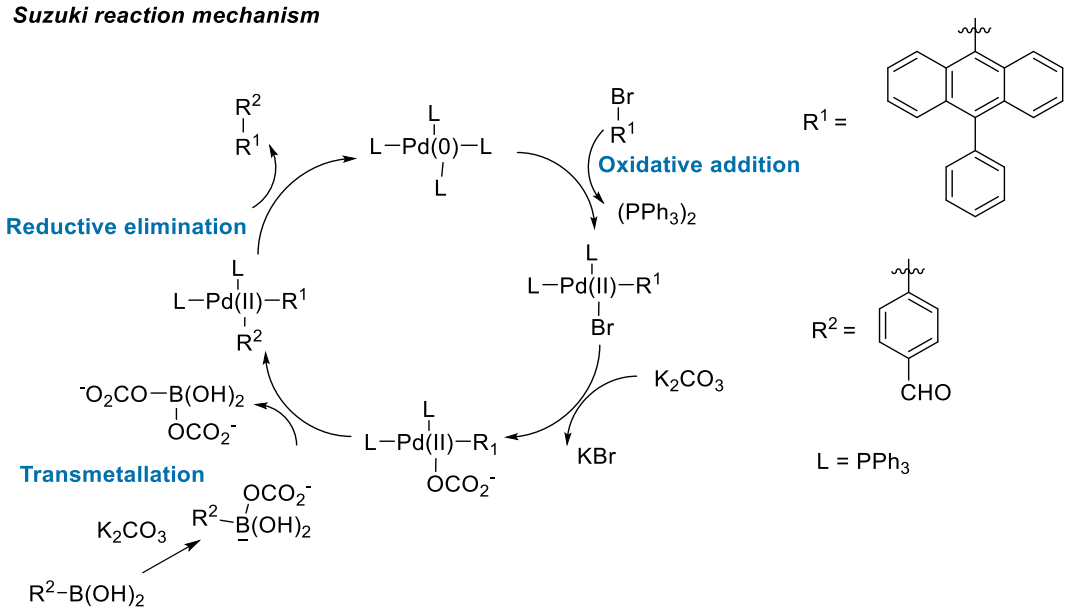

Scheme 3.2: Synthesis of anthracene aldehydes and Suzuki reaction mechanism. a) Br_2 (1 eq.), CH_3COOH, 80 °C, 20 min; b) 1. PhLi (1 eq.), THF, -78 °C, 1.5 h. 2. DMF, rt, 1 h; c) $Pd(PPh_3)_4$, (0.05 eq.), formylphenylboronic acid (1.2 eq.), K_2CO_3 (3 eq.), 100 °C, 48 h.

Similarly, a Suzuki reaction between compound **3.32** and formylphenylboronic acid afforded compound **3.33** in an 80% yield (**Scheme 3.3**).

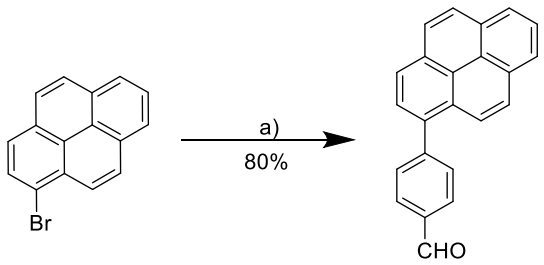

3.32 **3.33**

Scheme 3.3: Synthesis of pyrene aldehyde. a) $Pd(PPh_3)_4$ (0.05 eq.), formylphenylboronic acid (1.2 eq.), K_2CO_3 (3 eq.), benzene, H_2O, EtOH, 100 °C, 48 h.

Pyrroles, 2,4-dimethylpyrrole, and 3-ethyl-2,4-dimethylpyrrole were commercially sourced but 2-methyl-1H-pyrrole, compound **3.35** was synthesised by following an adapted literature reduction of compound **3.34**, yielding 51% (**Scheme 3.4**).[276]

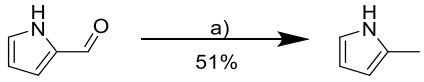

3.34 **3.35**

Scheme 3.4: Synthesis of 2-methyl-1H-pyrrole, compound **3.25**. a) 1. $LiAlH_4$ (3 eq.), THF, 0 °C, 30 min. 2. 66 °C, 36 h.

Compounds **3.30**, **3.31**, and **3.33** and commercial aldehydes 10-methylanthracene-9-carboxaldehyde, 9-carboxaldehyde, and 1-pyrenecarboxaldehyde, together with the corresponding pyrroles, were used in the general synthesis described in (**Scheme 3.5**).

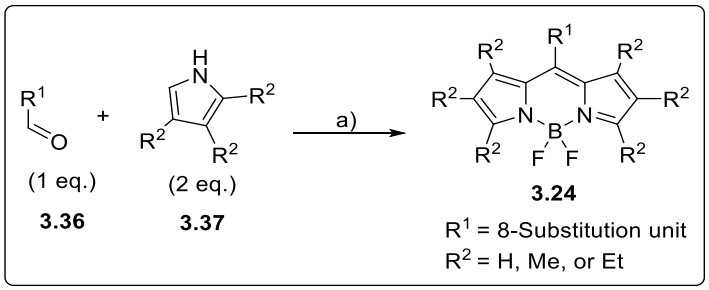

Scheme 3.5: General condensation reaction between an aromatic aldehyde and pyrrole/pyrrole derivative to yield BADs/BAD derivatives. a) 1. TFA (cat.), DCM (for substituted pyrroles), rt, 16 h. 2. DDQ (1 eq.), rt, 20 min. 3. DIPEA (10 eq.), $BF_3 \cdot Et_2O$ (10 eq.), rt, 1.5 h.

The BODIPY synthesis consisted of two steps in a one-pot reaction. Specifically, an acid-catalysed condensation between the aldehyde and pyrrole or a pyrrole derivative was followed by oxidation using DDQ to yield the dipyrromethene. Then, a boron insertion using $BF_3 \cdot Et_2O$ and base afforded the 8-substituted BODIPY. In the condensations between unsubstituted pyrrole and an aldehyde, pyrrole was used as the solvent as acid-catalysed polymerisation was a major side reaction. For condensations with substituted pyrroles, the pyrrole (2 eq.) was dissolved in DCM. The library of anthracene, pyrene, and perylene 8-substituted BODIPYs, compounds **3.14**, **3.15,** and **3.38**–**3.57** (**Fig. 3.14 and Fig 3.15**), was successfully synthesised using this method. The yields obtained (12–76%) were within expected ranges;[98] however, purification of the compounds was tedious, especially for compounds using unsubstituted pyrrole, a considerable degree of pyrrolic polymerisation was observed, which may have contributed to the lower yields. Column chromatography and recrystallisation techniques were used to purify the BODIPYs. To combat this, the pyrrole was freshly filtered through a silica plug before each condensation.

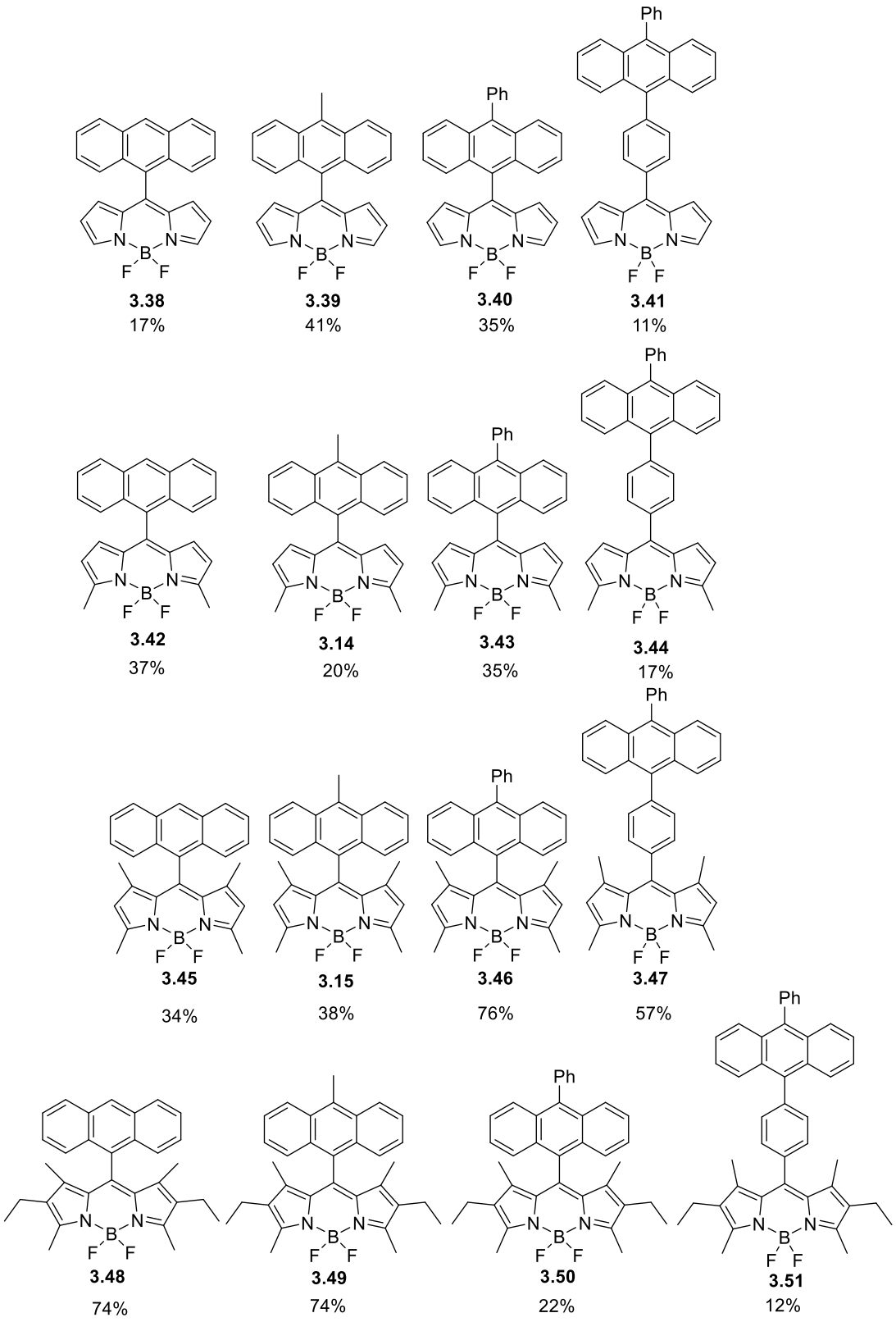

Figure 3.14: Expanded library of BODIPY-anthracene dyads with corresponding yields.

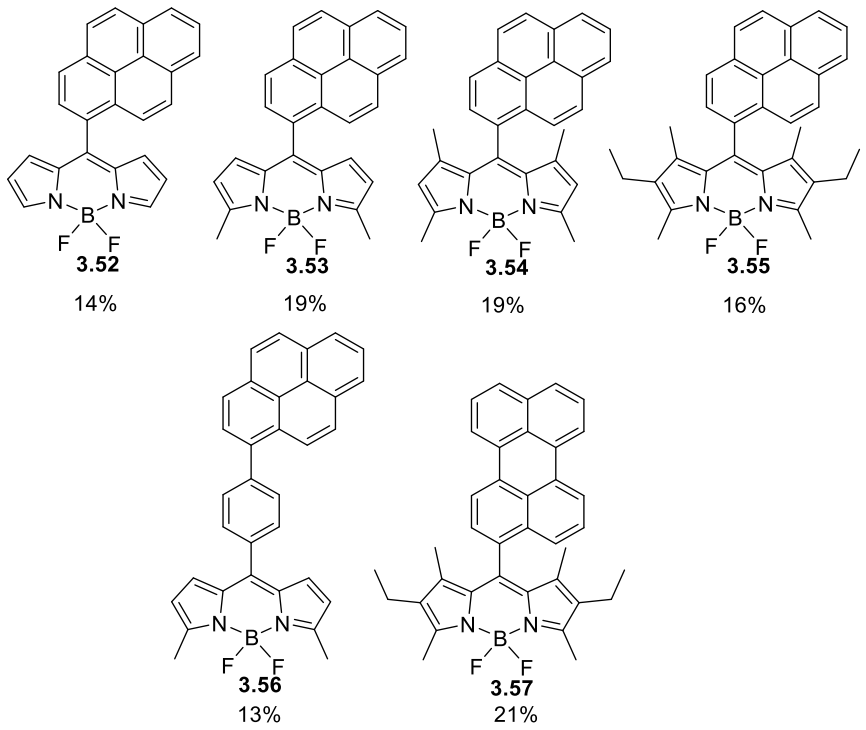

Figure 3.15: Expanded library of BODIPY-pyrene or -perylene dyads with corresponding yields.

Singlet oxygen and fluorescence quantum yield studies were carried out on the synthesised dyad series. As discussed, the decay of the BODIPY excited state can proceed by either fluorescence or a PeT mechanism via charge-separated states and these two pathways are in competition. If PeT is effective and yields the charge-separated state, ISC to the triplet state can occur (**Fig. 3.9**).

The next step was to investigate the photophysical properties of the dyad library. DPBF was used to trap singlet oxygen and the decrease in absorption with respect to time in hexane and EtOH was used to ascertain the singlet oxygen quantum yields.[265] Hexane and EtOH were chosen to compare the yields under different polarities. We found that in polar solvents the energy of the charge-separated state is stabilised, allowing for efficient PeT, whereas in non-polar solvents the charge transfer energy level is usually higher than the dyads first excited state, thus allowing control over ISC and triplet state formation. It must be noted that this indirect method of quantifying singlet oxygen quantum yields has limitations and it is reported that yields can be overestimated, especially in chlorinated solvents. Therefore, such solvents, including DCM, were not used in these experiments to minimise this

effect.[277] Fluorescence quantum yields were also obtained in both EtOH and hexane using fluorescein disodium salt as a standard. It is clear from the results in **Table 3.1** that both solvent polarity and subunit structure have an effect on the singlet oxygen and fluorescence quantum yields of the compounds, indicating that it is possible to modulate the photophysical properties of the photosensitiser using chemical modification and environmental polarity.

Table 3.1. Quantum yields of singlet oxygen photosensitisation and fluorescence by dyads in EtOH and hexane.

Compound	Φ_Δ EtOH	Φ_Δ Hexane	Φ_{em} EtOH	Φ_{em} Hexane
3.38	0.11	0.39	<0.001	0.135
3.39	0.05	0.38	0.002	0.041
3.40	0.12	0.43	0.002	<0.001
3.41	0.01	0.01	0.003	0.014
3.42	0.47	0.07	0.005	0.95
3.14	0.38	0.17	0.001	0.37
3.43	0.46	0.18	0.006	0.773
3.44	0.01	0.01	0.037	0.204
3.45	0.53	0.01	0.038	0.99
3.15	0.67	0.04	0.005	0.91
3.46	0.59	0.04	0.02	0.90
3.47	0.01	0.01	0.37	0.70
3.48	0.11	0.02	0.778	0.871
3.49	0.32	0.03	0.314	0.883
3.50	0.15	0.03	0.804	0.903
3.51	0.01	0.01	0.841	0.756
3.52	0.75	0.02	0.003	0.161
3.53	0.25	0.01	0.063	0.747
3.54	0.34	0.01	0.651	0.967
3.55	0.04	0.01	0.695	0.755
3.56	0.01	0.01	0.136	0.226
3.57	0.13	0.01	0.073	0.924

Singlet oxygen quantum yields were measured using DPBF as a singlet oxygen trap and RB as a reference photosensitiser. Fluorescein in 0.1 M NaOH (Φ_f = 0.95) was used as a reference for the fluorescent quantum yield measurements.[278]

Compound **3.15** displayed the second-highest singlet oxygen quantum yield of 0.67 in EtOH. In fact, the series of BODIPY dyads with tetramethyl-BODIPY substitution patterns, compounds **3.15**, **3.45**, **3.46**, and **3.54**, displayed efficient singlet oxygen generation in EtOH ($^1O_2\Phi$ = 0.34–0.67) when compared to the other pyrrole grouped

sub-series. This is in agreement with the low fluorescence quantum yields observed in the polar solvent (Φ_f >0.04). Corollary, in non-polar hexane, compounds **3.15**, **3.45**, **3.46**, and **3.54**, have low singlet oxygen quantum yields ($^1O_2\Phi$ = 0.01–0.04) and high fluorescence quantum yields (Φ_f >0.9), indicating that ISC is inefficient. This pattern of higher singlet oxygen quantum yield was also evident for dyads with a 3,5-dimethyl-BODIPY substitution pattern, compounds **3.14**, **3.42**, **3.43**, and **3.53**, and highly substituted BODIPY cores, compounds **3.48**–**3.50**, **3.55**, and **3.57**.

Overall compounds **3.14**, **3.42**, **3.43**, and **3.53** based on 1,7-dimethyl-substituted BODIPY scaffolds, showed lower singlet oxygen values in EtOH ($^1O_2\Phi$ = 0.25–0.47) when compared with the tetramethyl-BODIPY series but increased singlet oxygen production in hexane ($^1O_2\Phi$ = 0.01–0.18). The results show that increasing alkyl substituents reduce singlet oxygen quantum yields in polar solvent and this can be attributed to a reduction in the electron-accepting ability of the BODIPY subunit and thus the resultant PeT charge-separated state is of higher energy, which results in decreased triplet state population. In non-polar solvents the charge-separated state is less efficiently stabilised by dipole-dipole effects when compared to polar solvents and thus, overall, lower singlet oxygen quantum yields are obtained in non-polar solvents.

The exception to this is observed in the series of BODIPYs synthesised using unsubstituted pyrrole and anthracene aldehydes, compounds **3.38**–**3.40**. In EtOH, their singlet oxygen quantum yields are between 0.05–0.12 and in hexane between 0.38–0.43. This is a surprising result and, as of yet, not fully understood. However, it is thought to be a result of the stabilisation of the charge-separated state, possibly due to viscosity effects.[273] Compound **3.52**, the pyrene-substituted BODIPY, did not show this pattern and in fact, has the greatest singlet oxygen quantum yield of 0.75 in EtOH and again had a low fluorescence quantum yield. This is rationalised by the stronger dipole moment in the charge-separated state of this pyrene dyad (~23 D) in comparison to the anthracene derivative **3.38** (~18 D), resulting in increased stabilisation in polar solvents. The dipole moments were obtained using computational studies.[272]

In another noteworthy observation, compounds **3.41**, **3.44**, **3.47**, **3.51**, and **3.56** with phenyl spacers between the two dyad components, displayed negligible singlet oxygen quantum yields in both polar and non-polar solvents, which can be attributed to free rotation about the bond between the BODIPY and 8-substitution unit, resulting in the interruption of ISC. An orthogonal orientation has been shown to promote efficient ISC and thus the generation of charge-separated states.[279,280] According to computational studies, it is thought to be driven by a reduced singlet to triplet energy gap and may take place *via* hyperfine coupling. M06-2X functional studies completed on our compounds showed that, in fact, they were in an orthogonal conformation. This is in agreement with the higher singlet oxygen quantum yields observed for BODIPY cores with 1,7-dimethyl substitution patterns, compounds **3.14**, **3.42**, **3.43**, and **3.53**, which have relatively high singlet oxygen quantum yields as steric effects result in the orthogonal conformation. Moreover, the low rate of PeT is known to depend on the separation between the donor and acceptor units (**Table 3.1**).[281]

3.3.2 Water-soluble BODIPY dyad derivatives

To assess the applicability of these systems to PDT a library of water-soluble derivatives of the BODIPY dyads were synthesised for further *in vitro* studies. Firstly, we selected the parent BODIPYs (compounds **3.14**, **3.15**, **3.42**, **3.45**, **3.43**, **3.46**, and **3.53**) with promising singlet oxygen quantum yields in polar solvents ($^1O_2\Phi$ = 0.25–0.67 in EtOH). We also synthesised compound **3.58** using the general procedure described in **Scheme 3.5**, bearing a phenyl group that cannot undergo the PeT process to produce singlet oxygen. The singlet oxygen quantum yield was found to be <0.1 in both hexane and EtOH using DPBF as a singlet oxygen trap.

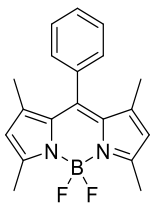

3.58

Figure 3.16: Structure of control BODIPY compound that does not generate singlet oxygen.

We then introduced water-solubility using a two-step approach. Fluorine substitution with *N,N*-dimethylaminopropyne-1 units was followed by quaternization of the dimethylamino group with 1,3-propanesultone. The products precipitated from the non-polar solvent to afford compounds **3.19** and **3.61**–**3.66** and control **3.67**, containing zwitterionic fragments that introduced water-solubility (**Scheme 3.6** and **Fig. 3.17**).[282] The series of water-soluble dyads were synthesised with substitution yields between 50–77% and quaternisation yields between 45–94% (**Fig. 3.17**).

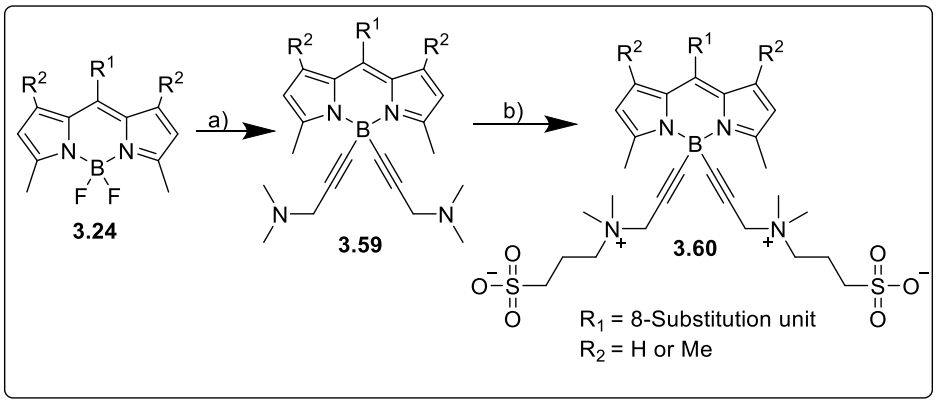

Scheme 3.6: General synthesis of water-soluble dyads. a) 1. 3-Dimethylamino-1-propyne (4.5 eq.), THF, rt, 30 min. 2. *n*-BuLi (4 eq.), THF, rt, 2 h; b) 1,3-propanesultone (6 eq.), EtOAc, 80 °C, 2 h.

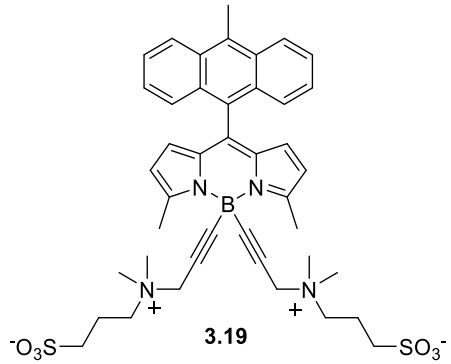

Step a): 70%
Step b): 86%

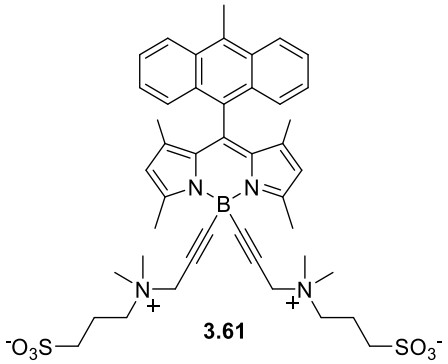

Step a): 77%
Step b): 78%

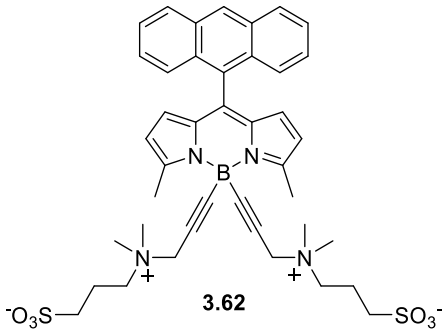

Step a): 74%
Step b): 71%

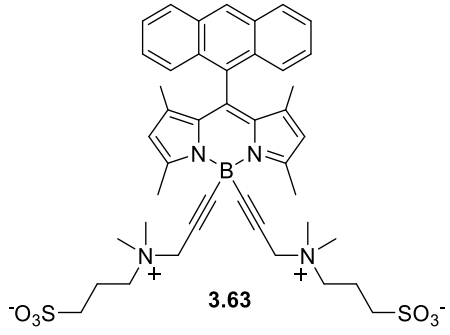

Step a): 59%
Step b): 95%

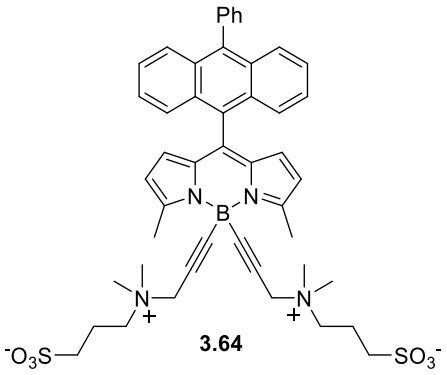

Step a): 61%
Step b): 55%

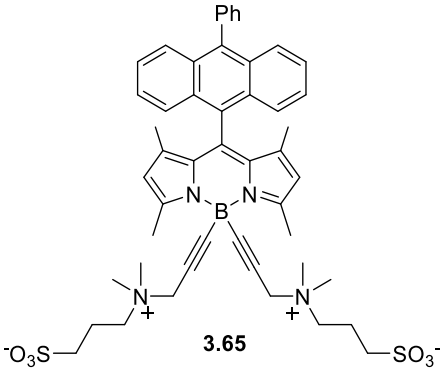

Step a): 50%
Step b): 54%

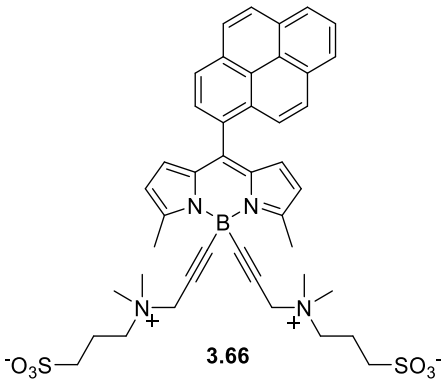

Step a): 60%
Step b): 89%

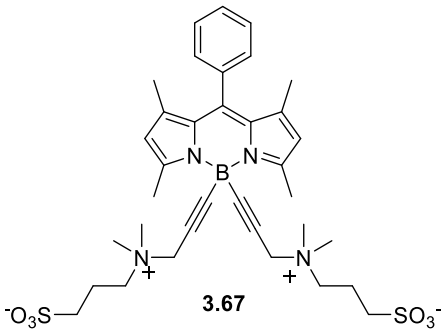

Step a): 69%
Step b): 45%

Figure 3.17: Library of synthesised water-soluble dyads, **3.19** and **3.61**–**3.67**.

The normalised absorption spectra of compounds **3.19** and **3.61**–**3.67** in water and EtOH are shown in **Fig. 3.18**. Two distinct units are evident with the anthracene or pyrene absorption maxima between 326 and 400 nm and the BODIPY unit absorbing between 501 and 527 nm (**Table 3.2**). The absorbance of anthracene is red-shifted compared to that of pyrene due to it having a smaller HOMO-LUMO gap (**Fig. 3.18**). The compounds do not display significant changes in the absorption maxima between the solvents; however, larger full width at half maxima are seen in water compared to EtOH due to the relative solvent polarity (**Fig. 3.18**).

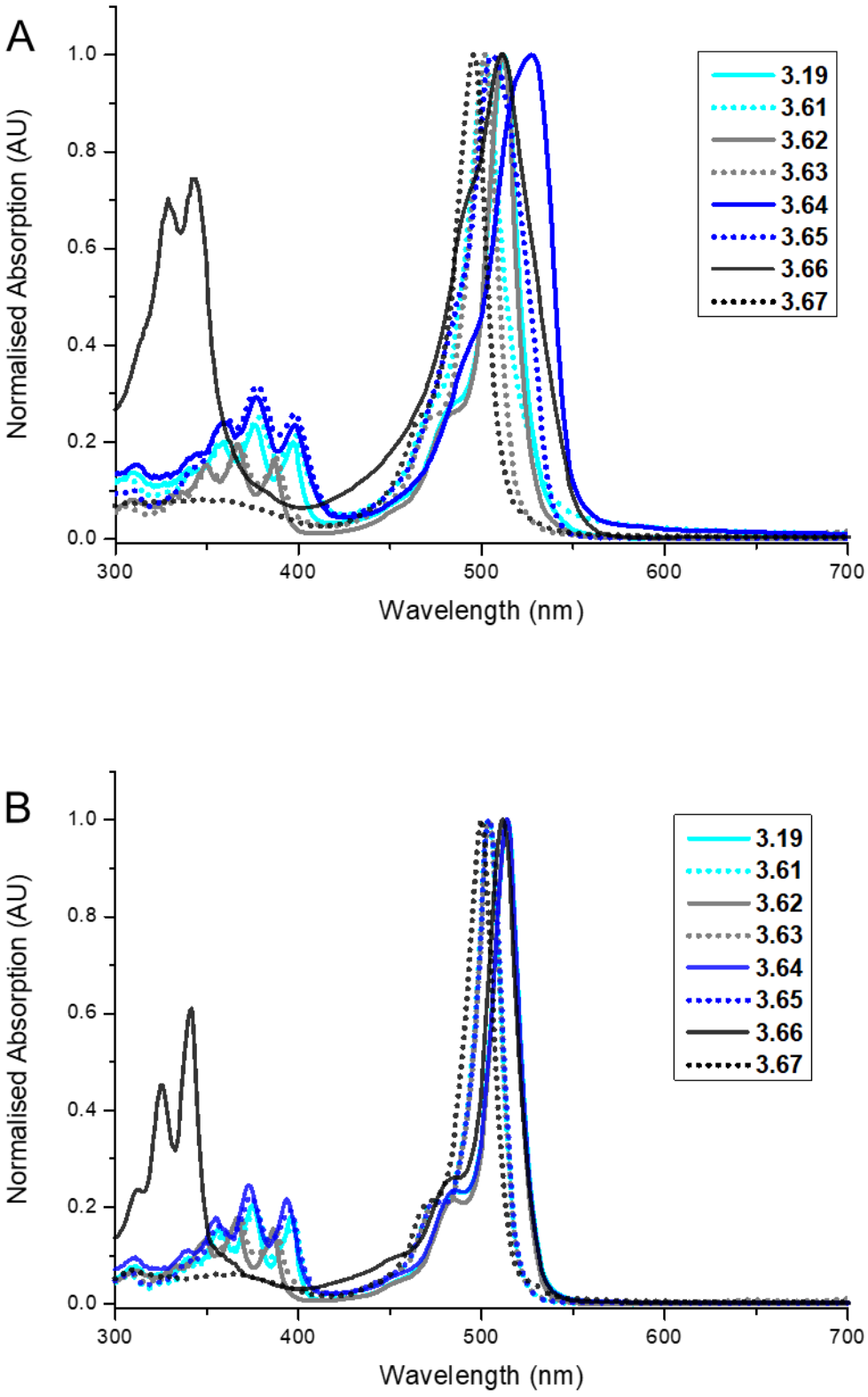

Figure 3.18: Normalised absorption spectra for compounds **3.19** and **3.61**–**3.67** in (a) water and (b) EtOH.

The fluorescence maximum and quantum yields are shown in **Table 3.2**. The quantum yields of the compounds were measured relative to the fluorescence of fluorescein in 0.1 M NaOH (Φ_f = 0.95) at a concentration of 1 × 10^{-5} M.[278] Compounds **3.19** and **3.61**–**3.66** display low fluorescence in both EtOH and water (Φ_f <5%). This is expected, as the PeT mechanism is in competition with fluorescence (**Fig. 3.9**). In contrast, compound **3.67** displays relatively high fluorescence in both water and EtOH, 20% and 22%, respectively, indicating that the triplet state is not readily populated. We also observed lower fluorescence quantum yields in water compared to EtOH due to the greater stabalisation of the charge-separated states in polar solvent. The same trend is not observed in **3.67**, which does not generate a charge-separated state (**Table 3.2**).

Table 3.2: Absorbance maxima, emission maxima, and fluorescence quantum yields of **3.19** and **3.61**–**3.67** in water and EtOH*

	Absorption λ_{max} (H_2O)	Absorption λ_{max} (EtOH)	Emission λ_{max} (H_2O)	Emission λ_{max} (EtOH)	Φ_f (H_2O)	Φ_f (EtOH)
3.19	359, 376, 397, 512 nm	356, 375, 396, 514 nm	532 nm	530 nm	0.001	0.001
3.61	360, 378, 399, 502 nm	362, 379, 400, 505 nm	512 nm	514 nm	>0.001	0.002
3.62	350, 367, 386, 511 nm	349, 366, 386, 514 nm	525 nm	523 nm	>0.001	0.008
3.63	351, 368, 388, 501 nm	350, 368, 387, 504 nm	505 nm	510 nm	0.022	0.030
3.64	360, 377, 398, 527 nm	355, 373, 394, 514 nm	522 nm	525 nm	0.002	0.002
3.65	360, 378, 398, 506 nm	357, 374, 395, 504 nm	505 nm	511 nm	0.004	0.011
3.66	329, 342, 511 nm	326, 342, 512 nm	511 nm	524 nm	>0.001	0.042
3.67	496 nm	500 nm	505 nm	508 nm	0.219	0.196

*Fluorescein in 0.1 M NaOH (Φ_f = 0.95) was used as a reference for the fluorescent quantum yield measurements.[278]

Singlet oxygen quantum yield studies were undertaken on the water-soluble derivatives, **3.19** and **3.61**–**3.66** and control (**3.67**) in EtOH (**Table 3.3**). Overall, they show comparable singlet oxygen quantum yields to that of the parent BODIPYs (**3.14**, **3.15**, **3.42**, **3.45**, **3.43**, **3.46**, **3.53**, and **3.58**). Notably, control **3.67** displays negligible singlet oxygen-generating abilities, as expected.

Table 3.3: Singlet oxygen quantum yields of the water-soluble dyads in EtOH and, for comparison, the singlet oxygen quantum yields of the parent dyads.*

Compound	Φ_Δ EtOH	Compound	Φ_Δ EtOH
3.14	0.38	**3.19**	0.38
3.15	0.67	**3.61**	0.52
3.42	0.47	**3.62**	0.64
3.45	0.53	**3.63**	0.39
3.43	0.46	**3.64**	0.48
3.46	0.59	**3.65**	0.66
3.53	0.25	**3.66**	0.03
3.58	<0.1	**3.67**	0.02

*Singlet oxygen quantum yields were measured using DPBF as a singlet oxygen trap and RB as a reference photosensitiser.

In collaboration with the Boyle Group, University of Hull, cytotoxicity studies were carried out on the water-soluble derivatives to determine if they had the potential to be used as PDT agents (**Fig. 3.19**). Human breast cancer (MDA-MB-468) cells were incubated with compounds **3.19** and **3.61**–**3.67** at various concentrations (8×10^{-4} – 5×10^{-8} M) for 1 h. Following this, they were irradiated with broad-band visible light (400−700 nm, 23.8 mW/cm^2). The cells were then returned to the incubator for 24 h and an MTT assay was performed to determine cell viability (**Fig. 3.19**).[252] LC_{50} values were then calculated (**Table 3.4**).

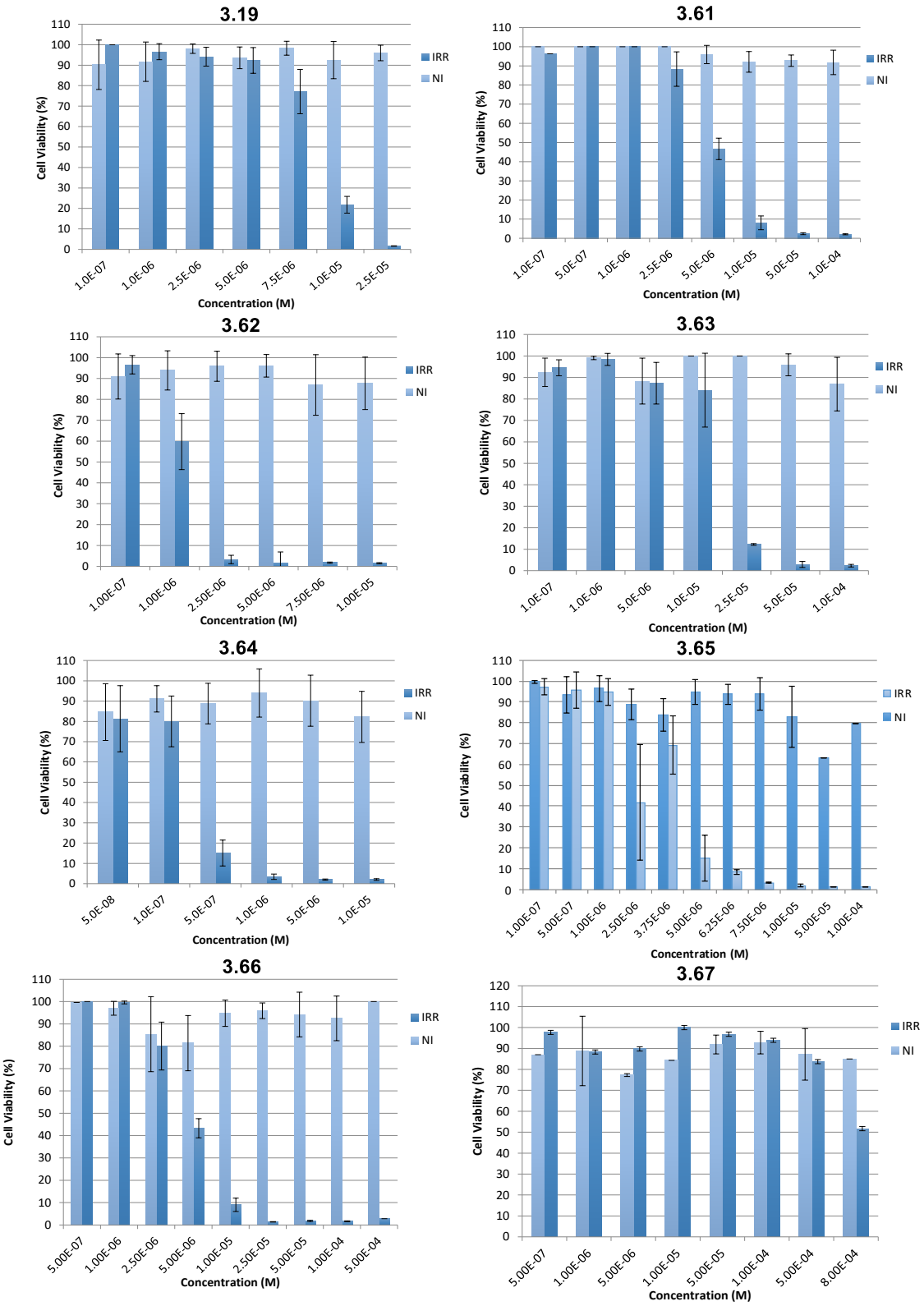

Figure 3.19: MDA-MB-468 cell viabilities after 1 h of incubation with **3.19** and **3.61**–**3.67** with and without light irradiation (400–700 nm, 20 J/cm^2) at various concentrations (8×10^{-4} –5×10^{-8} M). Standard deviations are indicated by the black bars (n=3).

Table 3.4: LD_{50} values of **3.19** and **3.61**–**3.67**.

Compound	LD_{50} Values (M)	Compound	LD_{50} Values (M)
3.19	8.7×10^{-6}	**3.64**	2.8×10^{-7}
3.61	6.1×10^{-6}	**3.65**	4.2×10^{-6}
3.62	1.3×10^{-6}	**3.66**	5.3×10^{-6}
3.63	1.7×10^{-5}	**3.67**	8.2×10^{-4}

Compounds **3.19** and **3.61** have previously been investigated[265] and are included as standards in this study. Compound **3.15** has a higher singlet oxygen quantum yield in EtOH (67%) when compared with **3.14** (38%). Similarly, compound **3.61** has a higher singlet oxygen quantum yield in EtOH (52%) when compared to compound **3.19** (38%) and this pattern is reflected in the *in vitro* studies. Although both compounds **3.19** and **3.61** induced some degree of photocytotoxicity at micromolar concentrations, at the same concentration of 5×10^{-6} M cell viability was reduced from 96% under dark conditions to 47% following illumination for compound **3.61** but there was a negligible reduction for compound **3.19** (**Fig. 3.19**). The LD_{50} values for compounds **3.19** and **3.61** are 8.7×10^{-6} M and 6.1×10^{-6} M, respectively (**Table 3.4**).

Compounds **3.62** and **3.63** contain anthracene at the 8-position of the BODIPY, which results in a decrease in the HOMO energy of the donor unit and thus a slower rate of PeT was observed, compared to compounds **3.19** and **3.61**. The parent BODIPYs (**3.42** and **3.45**) are reported to have similar singlet oxygen quantum yields in EtOH, 47% and 53%, respectively.[272,273] Compound **3.62** and compound **3.63** displayed singlet oxygen quantum yields in EtOH of 64% and 39%, respectively (**Table 3.3**). Compound **3.62** performed best and showed a marked reduction in cell viability to 3% at a concentration of 2.5×10^{-6} M after light treatment (**Fig. 3.19**). When this is directly compared to compound **3.19** at a concentration of 1×10^{-6} M, we observe improved photocytotoxicity (60% viability *vs.* no reduction in cell viability). Additionally, compound **3.62** demonstrated a lower LD_{50} value (1.3×10^{-6} M) than both compounds **3.19** and **3.61** (**Table 3.4**).

As we previously showed, **3.19** is able to undergo a cycloaddition reaction with self-sensitised singlet oxygen on the 9-methylanthracene subunit,[265] which, may in part, account for the reduced singlet oxygen quantum yield and lower cytotoxicity observed for this dyad. On the other hand, compounds **3.62** and **3.63** are based on unsubstituted anthracene, which is known to possess a relatively lower reactivity towards singlet oxygen, providing higher photostability and sensitisation efficiency for these dyads.[283]

The phenylanthracene-based BODIPYs, compounds **3.64** and **3.65**, again show micromolar and submicromolar activities under biological conditions and the parent BODIPYs (**3.43** and **3.46**) have similar singlet oxygen quantum yields of 46% and 59% in EtOH. Compounds **3.64** and **3.65** have singlet oxygen quantum yields in EtOH of 48% and 66%, respectively (**Table 3.3**). Dyad **3.64** has been identified as the highest-performing dyad of the study (LD_{50} value of 2.8×10^{-7} M, **Table 3.4**) with phototoxicity (89% cell viability under dark conditions *vs.* 15% cell viability following irradiation) at 5×10^{-7} M (**Fig. 3.19**). In contrast, **Fig. 3.19** shows that compound **3.65** does not display any photocytotoxicity at this concentration. Moreover, at a concentration of 5×10^{-6} M, dyad **3.64** effects a more profound reduction in cell viability after light treatment (15%) when compared to the standard **3.61** (47% viability).

In addition to the anthracene derivatives, we also tested a pyrene-BODIPY dyad, compound **3.66**, which showed cell phototoxicity and a singlet oxygen quantum yield in EtOH of only 3%. The parent BODIPY was previously shown to have a singlet oxygen quantum yield of 25% in EtOH. At a concentration of 1×10^{-5} M, there was a reduction in cell viability from 95% to 9% post illumination. At a lower concentration of 5×10^{-6} M, significant photocytotoxicity (43% viability) was also observed (**Fig. 3.19**). The efficiency of this photosensitiser is similar to that of compound **3.61**, which at a dyad concentration of 5×10^{-6} M showed a reduction in cell viability to 46% following light activation (**Fig. 3.19**).

The final compound tested was the control, **3.67**, which did not display significant sensitisation in EtOH. As seen in **Fig. 3.19**, there is nominal photocytotoxicity at appreciable concentrations with an LD_{50} value of 8.2×10^{-4} M. However, there was

a moderate decrease in cell viability (85% *vs.* 52%) at the highest concentration of 8×10^{-4} M when light was introduced. This would indicate that photosensitisation does take place at high concentrations but overall, there is minimal phototoxicity and thus PDT is, in fact, the predominant mechanism for cell toxicity observed in the active compounds. Importantly, this experiment also shows that the water-soluble aryl-BODIPYs are not inherently toxic at the concentrations under investigation.

Although the singlet oxygen quantum yields of the water-soluble BODIPYs in EtOH cannot fully account for the *in vitro* activities as factors including cell uptake have not been considered, we see similar toxicity patterns that are consistent with the synthetic tunability of this family of compounds. The control experiment, as well as the light-to-dark ratios, have consolidated that the water-soluble aryl-BODIPYs do not have inherent toxicity and that singlet oxygen generation is the predominant mechanism of action.

3.3.3 Further characterisation of the lead BODIPY

Compound **3.64** has been identified as the lead photosensitiser for application in PDT in a MDA-MB-468 cell viability study. Further characterisation of this compound is underway to fully elucidate its properties.

With the aim of transitioning compound **3.64** to an *in vivo* study, we performed another *in vitro* study using rat bladder cancer cells. The rat bladder cancer cells (AY27) were incubated with compounds **3.64**, **3.63**, and **3.61** at a concentration of 10 µM. Following this, they were irradiated with monochromatic blue light (435 nm, 12.9 mW/cm^2) at various time intervals, before further incubation for 24 h at 37 °C. The control dishes were treated with the same light conditions but did not contain the photosensitiser. In section **3.3.2**, the *in vitro* experiments investigated the effect of concentration on cell viability. In this study, the concentration was kept constant and illumination periods were varied. Additionally, a monochromatic light source was used. An MTT assay was performed 24 h after PDT treatment, as previously described, to determine cell viability (**Fig. 3.20**).

Fig. 3.20 shows that **3.64** has, marginally, the strongest therapeutic response against AY27 cells with a reduction to <5% cell viability after 120 s of illumination,

which is consistent with the previous study on MDA-MB-468 cells. Compound **3.61** has a similar response with significant cell death after 120 s but **3.63** has only moderate cytotoxicity after 240 s (approximately 80% viability). Two controls were performed in this study. Firstly, the light only control demonstrated no toxicity over the period of the experiment, indicating that this cell line is not susceptible to light. Interestingly, at approximately 20 s the viability decreases but it quickly recovered, which may be due to the initiation of cell repair mechanisms. We also performed a dark toxicity experiment with the AY27 cells in the presence of **3.64** and the dark toxicity was measured to be 102±4.9% (n=3), indicating that BODIPY **3.64** is itself non-toxic at this concentration (10 μM). This study demonstrates that compound **3.64** is the best candidate for an *in vivo* study in a AY27 cancer model.

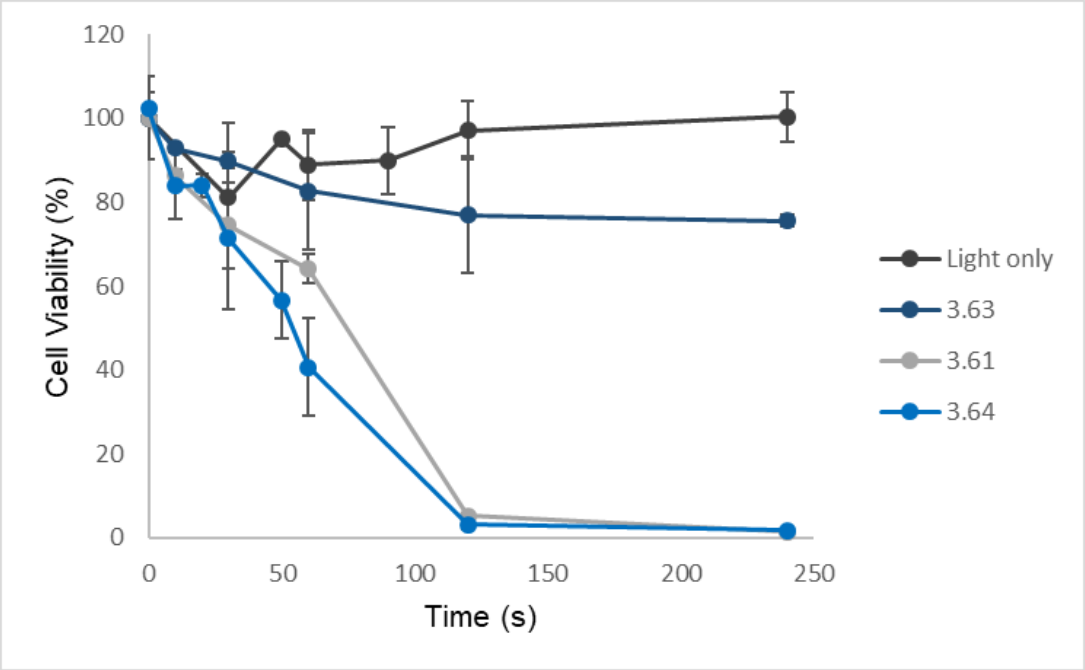

Figure 3.20: Cell survival curves of AY27 cells treated with 10 μM of **3.64**, **3.61**, and **3.61**. Viable cells were detected after varying exposure to light (0-240 s, 435 nm, 12.9 mW/cm^2). Control cells (light only) were exposed to light but not incubated with an active photosensitiser. Standard deviations are indicated by the black bars (n=4).

We then investigated a second cell line, the F98 cell line, with **3.64**. The F98 cell line originated from a rat brain tumour. Again, significant cytotoxicity (<5% cell viability) occurred following illumination for 120 s, indicating that the F98 cell line

could also be considered for *in vivo* studies. However, it is notable that the F98 cell line is more susceptible to light with the cell viability reducing to 60% after light treatment for 30 s; recovery does seem to be somewhat initiated with time (Fig. **3.21**). The dark toxicity of compound **3.64** in the F98 cell line was calculated to be 92.49±21.9% (n=3). Considering the sensitivity of this cell to both compound **3.64** and the light dose, the AY27 cell line is recommended for further studies.

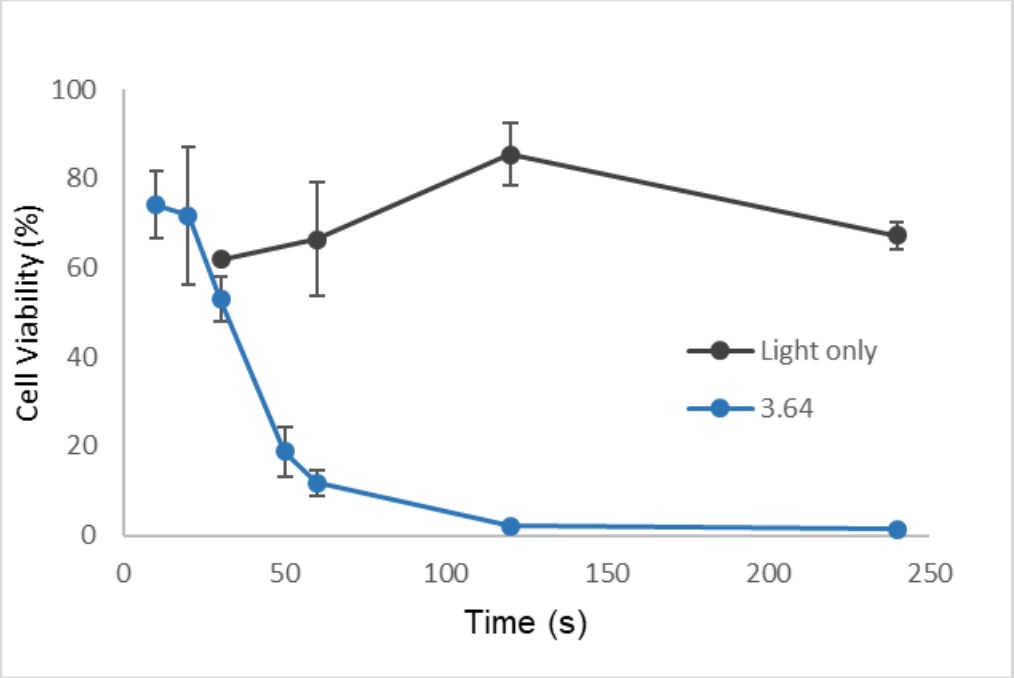

Figure 3.21: Cell survival curves of F98 cells treated with 10 μM of **3.34**. Viable cells were detected after varying exposure to light (0-240 s, 435 nm, 12.9 mW/cm^2). Control cells (light only) were exposed to light but not incubated with an active photosensitiser. Standard deviations are indicated by the black bars (n=4).

Next, a single-crystal X-ray structure was obtained showing a planar BODIPY core, the anthracene unit, and a zwitterionic fragment.‡ The normal plane angle between the anthracene unit and BODIPY core is 82.4(3)°, which is in agreement with previously reported BODIPY anthracene structures.[273] In this structure both nonpolar hexane and polar water molecules are incorporated into the unit cell, indicating a hydrophobic and hydrophilic end, which may have consequences for cellular localisation (**Fig. 3.22**). A general head-to-head crystal packing is observed

‡ The crystallographic data was collected by Dr. K. J. Flanagan.

with hydrogen bonding between the sulfonate moieties. Moreover, overlapping of the phenyl anthracene units is evident (**Fig. 3.23**).

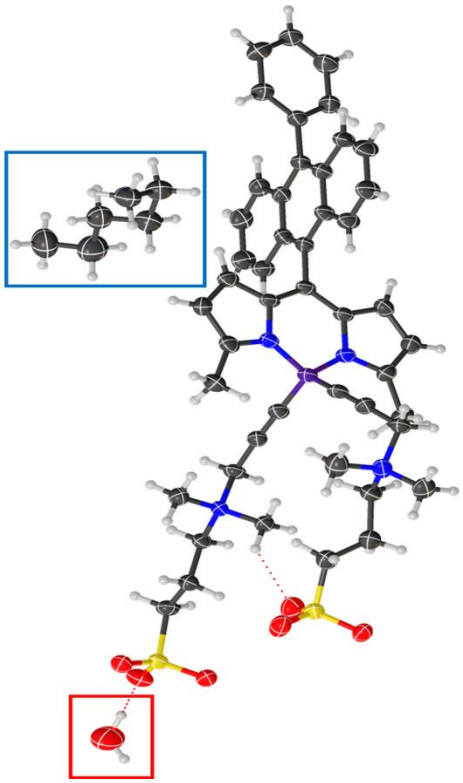

Figure 3.22: Molecular structure of **3.64** in the crystal showing water (red) and hexane (blue) solvents. Thermal ellipsoids give 50% probability.

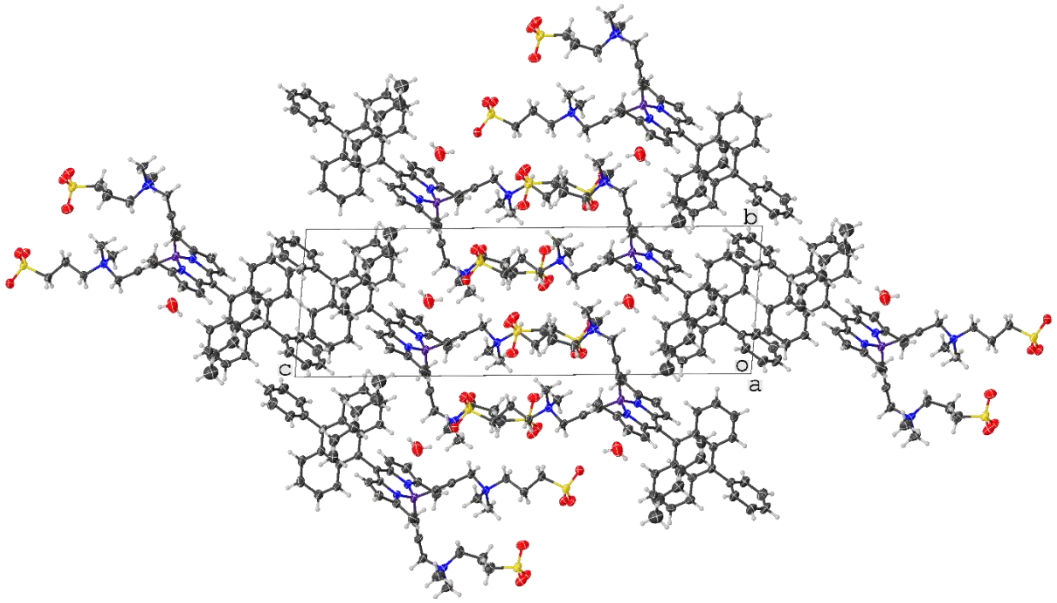

Figure 3.23: Moiety packing of **3.64**.

3.3.4 Methoxyphenyl-BODIPY dyads

In a publication by Nagano and co-workers, the HOMO energies of the trimethoxyphenyl/phenylanthracene units of a trimethoxyphenyl 8-substituted BODIPY and a phenylanthracene 8-substituted BODIPY were both reported as -0.1901 eV.[284] Thus, a trimethoxyphenyl-BODIPY series was synthesised, as they are also expected to display triplet state formation *via* the PeT process, compounds **3.70**–**3.77** (**Fig. 3.24**). The synthesis was performed using a condensation reaction between commercial aldehyde 3,4,5-trimethoxybenzaldehyde or 2,4,5-trimethoxybenzaldehyde and the corresponding pyrrole, followed by a boron insertion, in line with the other dyads (**Scheme 3.7**). 2,4,5-Trimethoxyphenyl bearing BODIPYs were chosen as it was envisioned that steric hindrance will induce orthogonality, which will result in higher singlet oxygen quantum yields in comparison to the 3,4,5-trimethoxyphenyl BODIPYs, as earlier discussed. The compounds were obtained in yields between 4–35%.

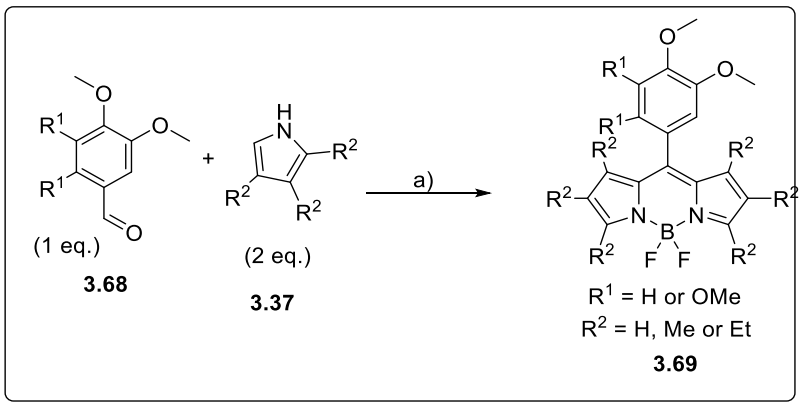

Scheme 3.7: Synthesis of trimethoxyphenyl-BODIPYs (a) 1. TFA (cat.), DCM (substituted pyrroles), rt, 16 h. 2. DDQ (1 eq.), rt, 20 min. 3. DIPEA (10 eq.), $BF_3 \cdot Et_2O$ (10 eq.), rt, 1.5 h.

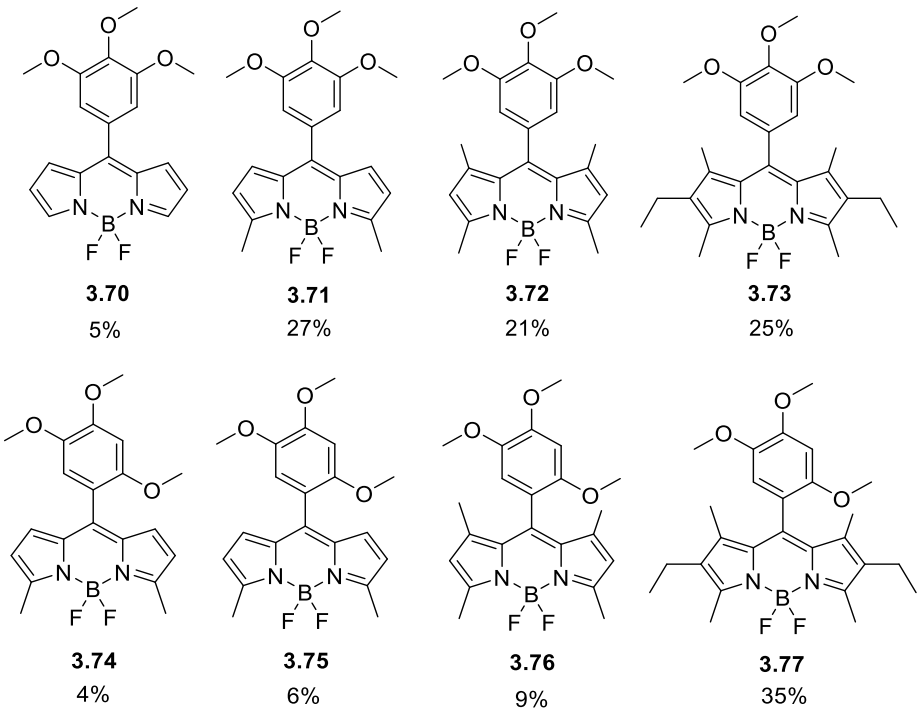

Figure 3.24: Structures of the synthesised methoxyphenyl-BODIPYs.

The trimethoxyphenyl 8-substitution induced approximately a 10 nm blue-shift in the absorption spectra when compared to the anthracene derivatives, rendering our current singlet oxygen yield measurement set-up, which employs a 532 nm laser, unusable. Instead, three of these compounds were converted to water-soluble derivatives (compound **3.80**–**3.82**, **Fig. 3.25**) and tested for application in PDT by our collaborators in the Arnaut group, University of Coimbra. The fluorescence quantum yields in EtOH were found to be 92%, 17%, and 4.5% for compounds **3.80**–**3.82**, respectively and cytotoxicity was not observed in any of the three compounds. For compounds **3.81** and **3.82** with low fluorescence quantum yields, a secondary process, probably quenching, may be at play. This warrants further study; however, at this time they are not being considered as suitable PDT agents.

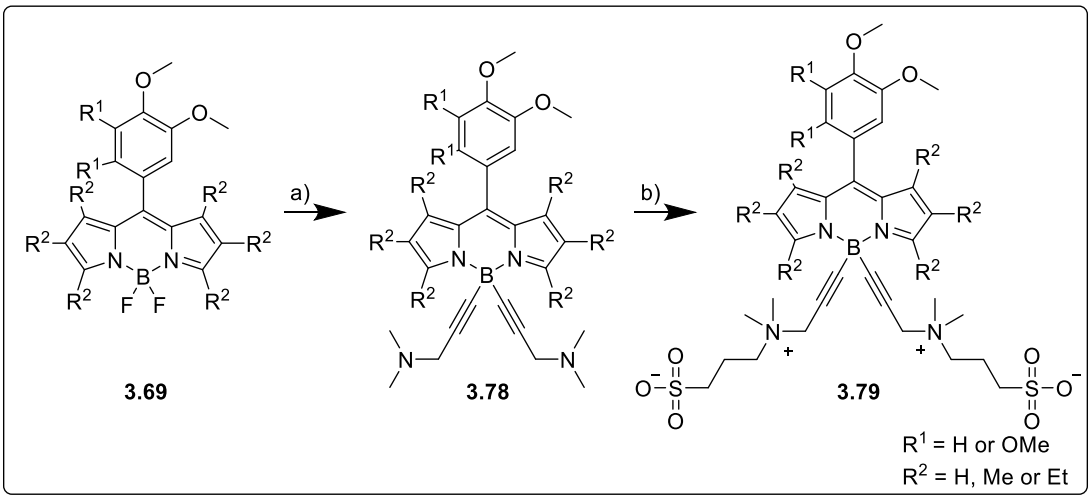

Scheme 3.8: General synthesis of water-soluble methoxyphenyl-BODIPY dyads. a) 1. 3-Dimethylamino-1-propyne (4.5 eq.), THF, rt, 30 min. 2. *n*-BuLi (4 eq.), THF, rt, 2 h; b) 1,3-propanesultone (6 eq.), EtOAc, 80 °C, 2 h.

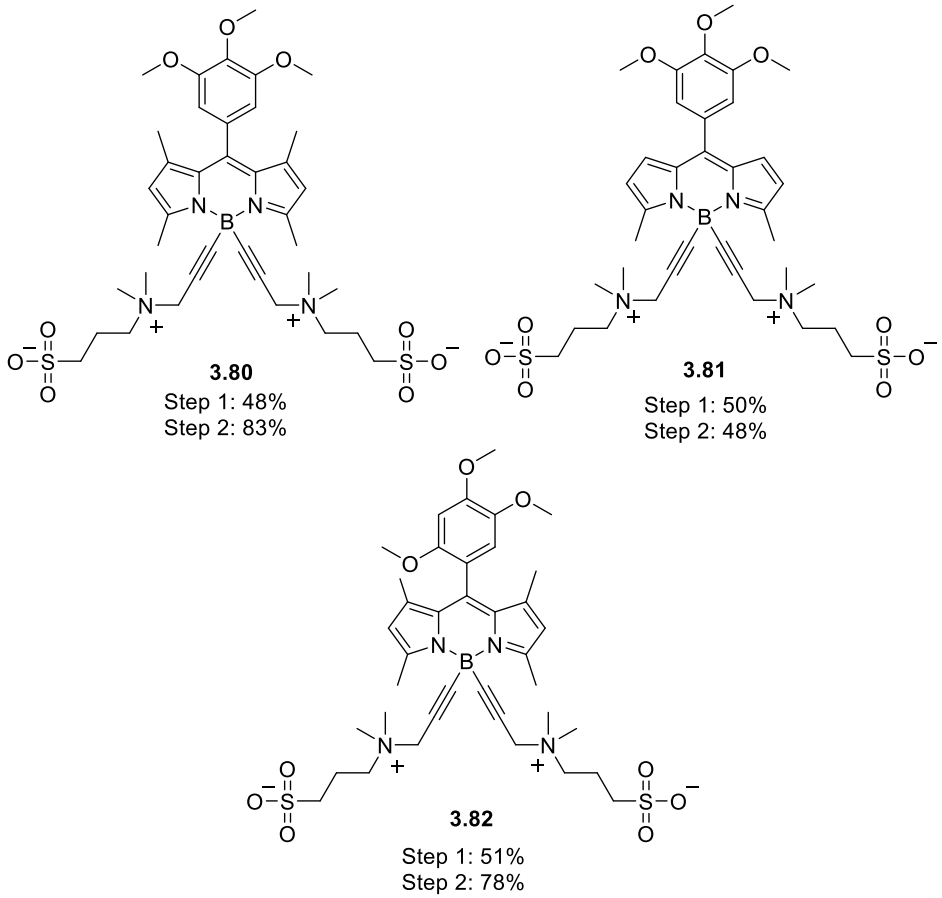

Figure 3.25: Structures of synthesised water-soluble methoxyphenyl-BODIPYs.

3.4 CONCLUSION AND FUTURE WORK

This chapter covered our work on singlet oxygen-generating heavy-atom free BODIPYs. A series of BODIPY dyads were synthesised using one-pot condensation reactions and their photophysical properties were determined. We demonstrated that singlet oxygen can be generated in these heavy-atom free dyads across a library of compounds including BODIPY-anthracene, pyrene, and perylene dyads. Therefore, it can be concluded that class of photosensitisers is chemically tuneable and diverse. We gained an understanding of the PeT mechanism that leads to the excited triplet state and its dependence on environmental polarity.

From here, we identified the BODIPYs with high singlet oxygen quantum yields and a library of eight water-soluble derivatives was synthesised to assess their applicability to PDT. Extensive *in vitro* analysis was performed and showed varying photocytotoxicity efficiencies. The cytotoxicity studies showed that all of the active compounds caused a reduction in cell viability after illumination in addition to minimal dark toxicity **Fig. 3.19**. These light-to-dark ratios are an important property for the development of successful photosensitisers as they contribute to tackling generalised photosensitivity, which plagues current PDT regimes.

We showed that three BADs (**3.62**, **3.64**, and **3.65**) were significantly more toxic than the standard, **3.61** (LD_{50} value = 6.1×10^{-6} M). In particular, the submicromolar activity of **3.64** (LD_{50} value = 2.8×10^{-7} M) is significantly more potent than that of **3.61**. This enhancement has considerable consequences for photosensitiser dosage. Coupled with the compounds low light-to-dark toxicity ratio and long-lived triplet state, the scope for the synthetic modification of **3.64** makes it suitable for future exploration. We obtained a single X-ray crystal structure of our lead BODIPY, which indicates hydrophobic and hydrophilic ends. We then demonstrated photocytotoxicity of the lead in both the AY27 and F98 cell lines and studied the effect of varying illumination duration parameters. We intend to continue the development of this class of photosensitisers with cell uptake and localisation studies to fully understand their mechanism of action and to investigate if the polarity of **3.64** plays a role in its mode of action and strong therapeutic effect. We intend to conduct *in*

vivo studies to further assess the feasibility of **3.64** for biomedical applications. Finally, we intend to explore options for optimising the absorption profile of **3.64** to aid tissue penetration. This is expected to involve the development of fluorine substitution chemistry.

Finally, we investigated another class of dyads, namely methoxyphenyl-BODIPYs. A library of eight compounds was synthesised and three were converted to water-soluble derivatives. Negligible cytotoxicity was observed but low fluorescence quantum yields open the door to a new field of study to understand the secondary processes taking place. In the future, an understanding of the underlying photophysical mechanisms is needed before potential applications can be considered. The first step will be transient absorption spectroscopy to provide an insight into the excited state properties of this compound and a study in a variety of solvents to confirm or rule out the existence of charge-separated states in these compounds.

Chapter 4: Short-chained Anthracene-strapped Porphyrins and their Endoperoxides

"Always the stairs, never the escalator."

Casey Neistat, 2016

4.1 INTRODUCTION

In previous chapters, we outlined systems that generate singlet oxygen and have aromatic trapping units for biomedical applications. With the same trapping mechanism, it is possible to conceive singlet oxygen storage devices. Here, we will revive strapped porphyrin synthetic chemistry, which had its hay day in the 1980s by designing and synthesising anthracene-containing strapped porphyrin systems to investigate [4+2] cycloaddition reactions as a possible mechanism for oxygen storage devices.

4.1.1 Capped and strapped porphyrin systems

There is a range of porphyrin structures containing straps and caps reported in the literature. Firstly, single-strapped systems are connected from meso- to meso-carbons, either in a '*cis*'[285] or '*trans*'[286] orientation (**4.2**), or from β- to β-carbons (**4.3**).[287] Doubly-strapped porphyrins are connected by two straps at the 5,15- and 10,20- positions. These can be further classified into '*cis*' α (**4.6**, where the straps are connected at the 5,10 and 15,20 meso positions and are across the same face of the porphyrin), '*cis*' β (**4.7**, where the straps are connected at the 5, 10 and 15,20 meso positions and are across the opposite faces of the porphyrin), and '*trans*' (**4.5**, where the straps are connected at the 5,15- and 10,20-meso-positions and are across the opposite faces of the porphyrin) atropisomers.[288] Straps, both double and single, that connect across the 10,20-positions or 5,15-positions (across the porphyrin core) are also known as 'basket handle' porphyrins. In capped systems, all four meso-carbons are connected to a central group or 'cap' above the porphyrin plane (**4.8**).[289] Finally, there are a few examples of other strapped systems including

gyroscope (**4.9**)[288,290] and cross-strapped (**4.10**)[291] porphyrins but these systems are not directly related to the current discussion (**Fig. 4.1**).

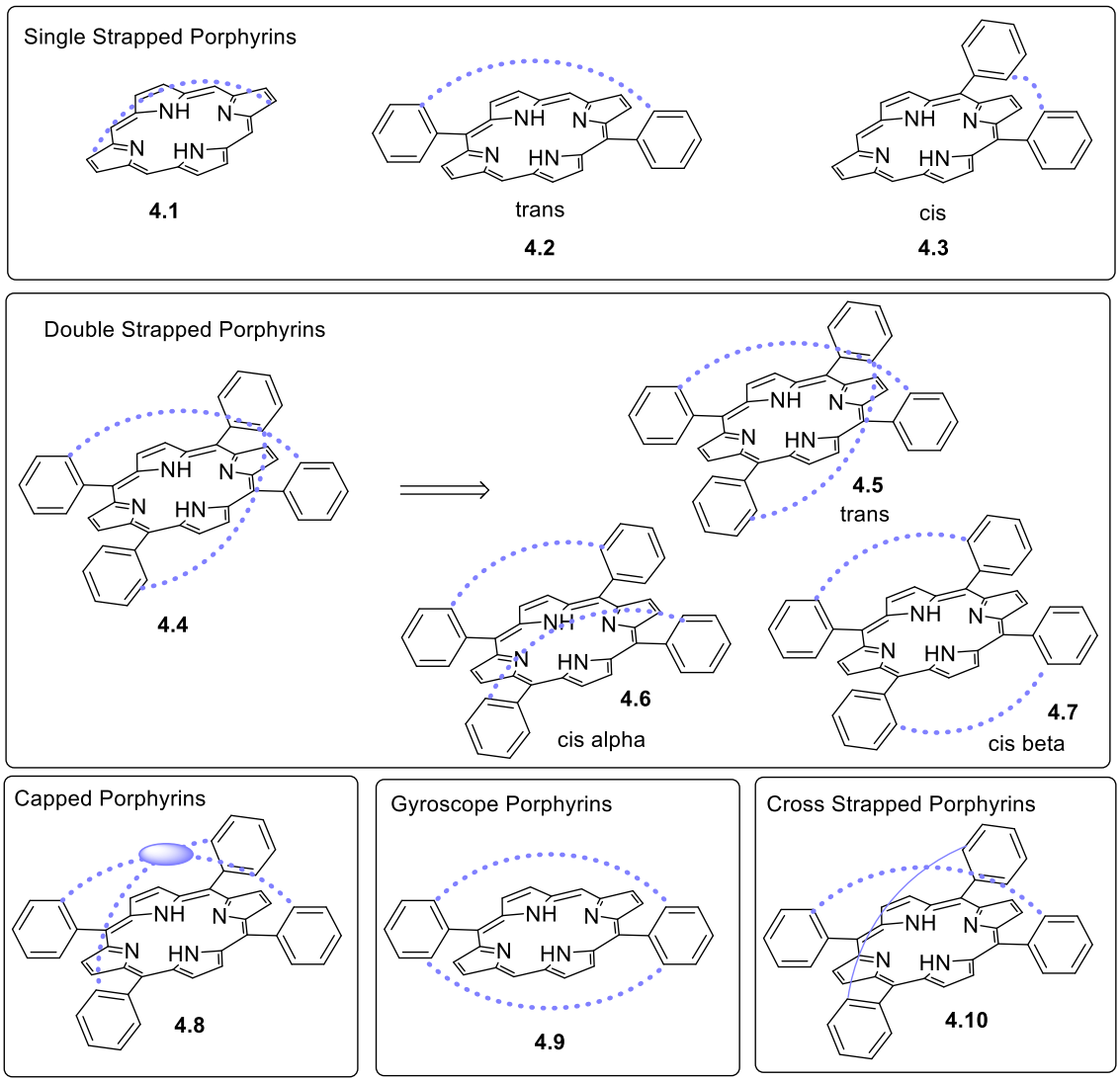

Figure 4.1: Schematic representation of strapped and capped porphyrin systems.

These compounds have been used in a variety of applications over the years. Capped, along with picket fence porphyrins, have helped us gain an understanding of the underlying structure and reactivity of biologically active sites such as hemoglobin and myoglobin[292] and strapped porphyrins have been used as chiral catalysts in synthetic chemistry.[293,294] Strapped systems are also capable of ion recognition, for fluoride, acetate, and dihydrogen phosphate.[295,296] The preparation and purification of strapped porphyrin systems in workable yields remain major roadblocks in the development of further applications. Thus, this discussion will centre around their synthesis and unique structural and chemical properties, many of which arise from their 3D structure.

4.1.2 Synthetic strategies towards capped and strapped porphyrin systems

The common synthetic strategies used to obtain strapped systems are variations on traditional condensation methods (see **1.3.1**). Arguably, the most widely used synthetic route to single-strapped basket handle porphyrins linked *via* two meso-positions (**4.2**) is a condensation reaction between a DPM and bisaldehyde, **Scheme 4.1** route **A**. This approach was used by Wytko *et at.* in 1992 to synthesise a phenanthroline-containing porphyrin. The condensation was performed under dilute conditions in DCM with DPM and a dialdehyde in a 2:1 ratio. Trifluoroacetic acid (TFA) was used as a catalyst and the porphyrin was isolated in a 42% yield, following oxidation with DDQ.[297] In a more recent study by Gehrold *et at.*, this approach was also used to synthesis a library of chiral and achiral single-strapped porphyrins on multigram scales, with the exception of using 2,3,5,6-tetrachloro-1,2-benzoquinone (*p*-chlorinal) as the oxidant.[286]

Alternatively, the bisaldehyde can be converted to the corresponding bis-DPM in a condensation reaction using excess pyrrole and then further condensed to yield the porphyrin, **Scheme 4.1** route **B**. The simplest method is to condense the bis-DPM with an aromatic aldehyde such as in the case of Lee and Galoppini in their synthesis of meso single-strapped systems. They performed a one-pot condensation and metallation in the presence of excess benzaldehyde and zinc acetate dehydrate, using propionic acid and DCM as the solvent. This was followed by oxidation with DDQ to yield the strapped Zn(II)porphyrin in a 27% yield and the free base porphyrin as a side product in >10% yield.[298] This approach not only provides access to meso-linked basket handle porphyrins but also β-linked systems (**4.1**). In 1983, the Dolphin group synthesised a β-strapped porphyrin. First, the bis-DPM of the strap was synthesised and then cyclised using toluenesulfonic acid. This was followed by oxidation and the porphyrin was obtained in a 40% yield.[299] In a second example of a β-strapped system, Traylor used the bis-DPM method but also took advantage of copper(II) ion chelation to orientate the DPMs into position for bond formation.[300]

Approach **C**, **Scheme 4.1**, is to introduce the strap after the condensation reaction. Battersby *et al.* provided an example of this during the synthesis of their strapped

Fe(II)porphyrin that contained a thiolate residue. The aim of the study was to synthesise a mimic of the carbon monoxide complex of cytochrome P450. The meso-substituted porphyrin was prepared and converted to its soluble acid chloride using oxalyl chloride. This porphyrin was then reacted with the diol containing strap at rt to yield the target porphyrin with ester linkages.[301]

Finally, the bisaldehyde can also be condensed directly with pyrrole, approach **D**, **Scheme 4.1**, as exemplified by Lee and Lee. The issue with this approach is poor control over product formation. A condensation between pyrrole, 2,4,6-trimethylbenzaldehyde, and the bisaldehyde strap gave the A_4 unstrapped porphyrin in a 0.4% yield, the '*trans*' isomer in a 0.2%, and the '*cis*' isomer in 1.5% yield.[285]

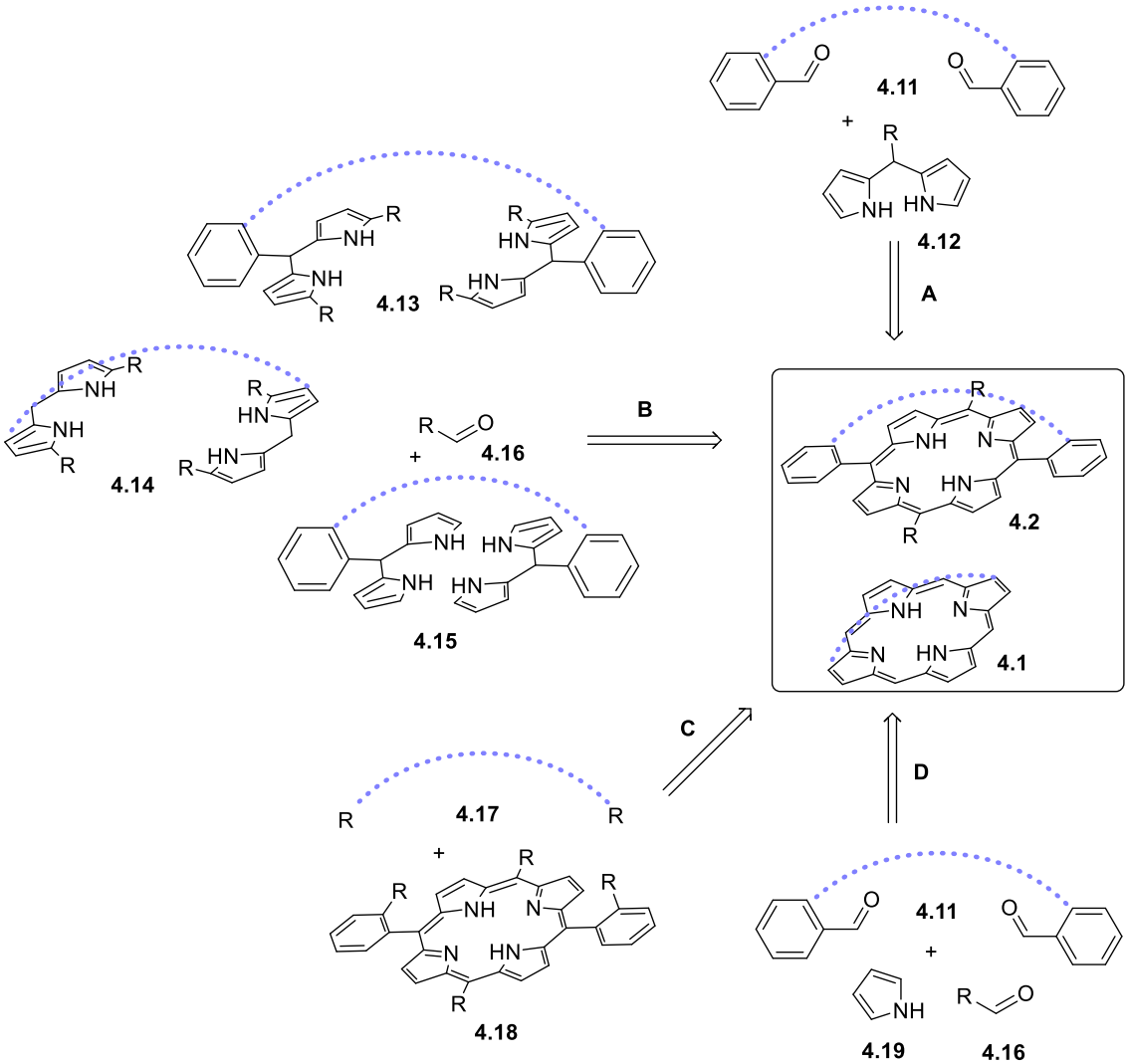

Scheme 4.1: Synthetic strategies towards single-strapped porphyrins.

There are two major strategies towards the synthesis of double-strapped systems (**4.4**), as exemplified by Momenteau and the chosen route can have a major effect

on the isomers obtained.[302] Firstly, they can be synthesised by direct condensation reactions between a bisaldehyde and pyrrole, approach **A**, **Scheme 4.2**. This approach was used by Reddy and Chandrashekar in 1992 to synthesise double-strapped porphyrins with an aromatic-containing strap and all three isomers were isolated with yields of less than 3%. In 1998, the Lindsey group investigated 18 dialdehydes by condensing them in equimolar concentrations with pyrrole using both $BF_3 \cdot OEt_2$ and TFA as the acid catalysts and DDQ or 3,4,5,6-tetrachloro-1,2-benzoquinone (*o*-chloranil), neutralised with triethylamine (TEA), for the oxidation step. Yields of up to 25% were reported.[303] More recently in 2014, Urbani and Torres used this approach in the synthesis of five porphyrins using an acid-catalysed condensation of a bisaldehyde and pyrrole in chloroform, followed by oxidation with DDQ. They studied the atropisomers and tautomers of these meso-strapped porphyrins.[288]

The second approach, **B**, **Scheme 4.2** involves the synthesis of a meso-substituted porphyrin and introduction of the strap at a later point. In 1983, Bisagni and coworkers contrasted methods A and B. They used the Adler-Longo method[91] for a direct condensation and obtained a mixture of all three isomers, although they required extensive purification. In the second approach, they condensed pyrrole with *o*-methoxybenzaldehyde in the presence of excess zinc acetate and isolated the porphyrin. Following purification with chromatography and demetallation, the free base porphyrin was obtained in a 10% yield. Demethylation in boiling pyridine hydrochloride (93% yield) was followed by the introduction of the strap. The brominated straps were reacted with the porphyrin in DMF at 100 ºC in the presence of excess anhydrous potassium carbonate. Although approach A required more synthetic steps, the '*trans*' isomer was the major product for all of the porphyrins in this library.[304] Approach B was also used in 1992 and 2004 as a method to introduce a 2,2′-bis(diphenylphosphino)-1,1′-binaphthyl (BINAP)-containing strap in the synthesis of a catalyst for enantioselective epoxidation of terminal olefins.[305,306] In the most recent publication, a reaction between the diacid chloride of a BINAP-based compound and ααββ-5,10,15,20-tetrakis(*o*-aminophenyl)porphyrin in the presence of *N,N*-diethylaniline afforded the BINAP-strapped porphyrin in a 31% yield. Metallation using $FeBr_2$ gave the target catalyst.

At least conceptually, there is a third option for the synthesis of double-strapped porphyrins, approach **C**, **Scheme 4.2**. This is a reaction between the DPM of the bisaldehyde and the bisaldehyde; however, to the best of our knowledge it has not been successfully reported.

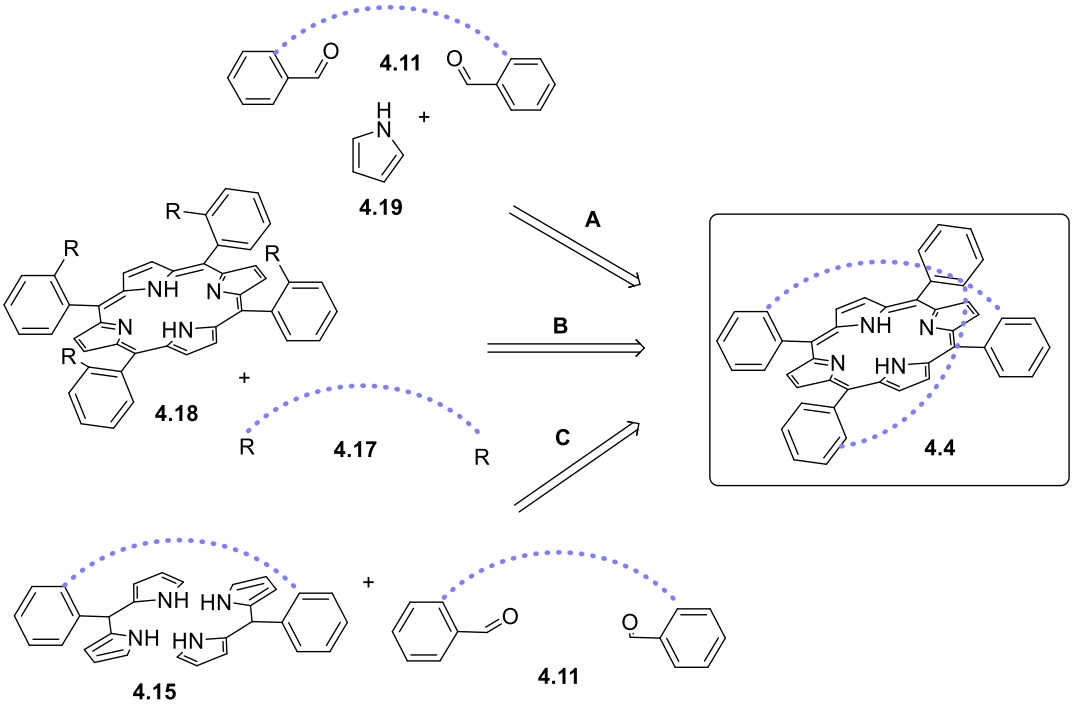

Scheme 4.2: Synthetic strategies towards double-strapped porphyrins.

The first approach (**Scheme 4.3**, **A**) for synthesising capped porphyrins (**4.8**) was exemplified by Peters and coworkers when they condensed pyrrole with the cap containing four aldehydes for 1.5 h in refluxing propionic acid and filtered the mixture through silica. Then, the product was oxidised with DDQ and the capped porphyrin was obtained in a 2% yield.[307] In 1996, Ibers and co-workers used this approach to make a capped porphyrin heme mimic[308] and more recently in 2010 capped porphyrins, for use in semiconductor systems, were prepared in this manner.[309]

In the second approach (**Scheme 4.3**, **B**), a porphyrin with appropriate functional groups is synthesised and then used to introduce the cap. This approach has the advantage of providing higher yields as the condensation step does not involve the strap; however, longer synthetic routes are necessary. Caps containing rigid 1,2,3-triazole groups have been introduced using click chemistry (yields 14% and 19%),[310] and Michael additions were employed to achieve aza-crown capped porphyrins (up to 91% yields).[311,312] The Peters group also used this approach to prepare a capped

porphyrin but found the direct method more useful. They reacted an atropisomer mixture of the starting meso-substituted porphyrin with the cap to obtain the desired porphyrin in a 15% yield; however, they noted that isolation involved extensive purification steps.[289]

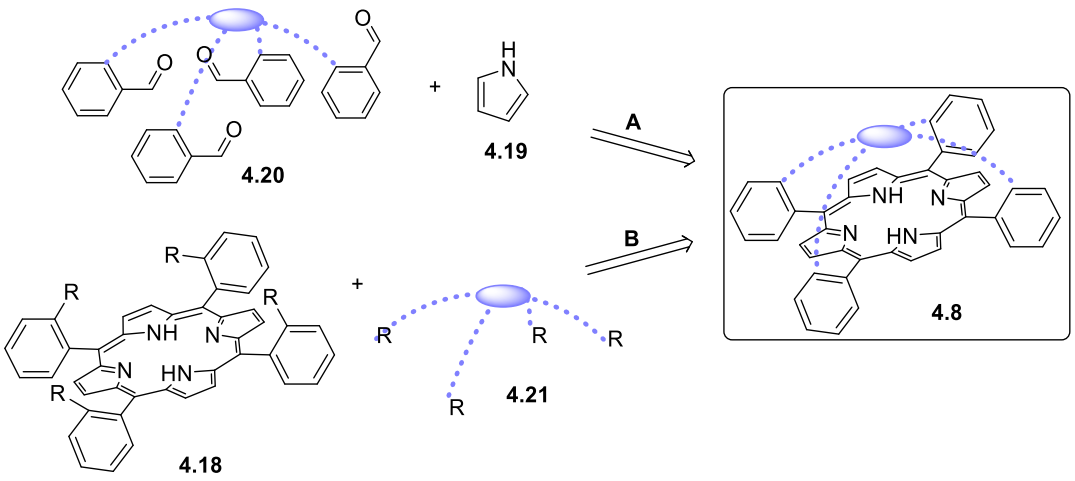

Scheme 4.3: Synthetic strategies towards capped porphyrins.

4.1.3 Short straps and macrocycle distortion

Porphyrin macrocycles can adopt non-planar confirmations given the correct conditions. A common method to introduce macrocyclic distortion is substitution of the periphery or core with bulky groups.[313] These distortion properties are also endowed by short strapped systems and the type of distortion induced can affect the nature of the cavity.[314] These systems have been extensively studied, especially as possible heme mimics, as the porphyrin cores in these active sites are distorted from planarity due to surrounding proteins.[315] In addition, macrocyclic distortion can lead to interesting chemical properties including catalytic activity.[316]

Early systems that achieved significant distortion using short alkyl chains were prepared in the 1980s. The Dolphin group synthesised a β-β-strapped system and reported the crystal structure of compound **4.22**, which displayed macrocyclic distortion. Using absorption spectroscopy, they showed that the degree of macrocyclic distortion is greater in **4.22** (n=9) when compared to systems with longer straps (n=10 or n=11) compounds **4.23** and **4.24**.[299] In 1986, Simons and co-workers synthesised double-strapped systems again with varying strap lengths of n=4, 5, and, 6 carbons (**Fig. 4.2**, compounds **4.25**–**4.27**). They were able to isolate

all the isomers of compounds **4.26** and **4.27** but for compound **4.25**, with the shortest strap, the '*trans*' isomer was not isolated. They also attempted zinc(II) insertions and found that the '*trans'* isomer could not be metallated. They showed, using absorption spectroscopy, that the '*trans*' isomer has a higher degree of distortion when compared with the '*cis*' isomers for each compound. However, for compound **4.25** distortion was also evident in the '*cis*' isomers (**Fig. 4.2**, compounds **4.25**–**4.27**).[287]

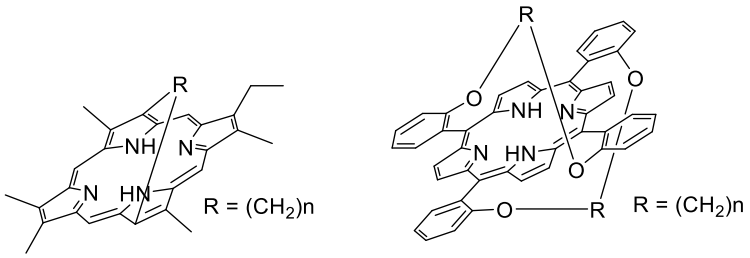

4.22 n= 9,
4.23, n=10,
4.24, n=11.

4.25 n= 4,
4.26, n=5,
4.27, n=6.

Figure 4.2: Early examples of short-chained strapped porphyrins displaying macrocycle distortion.

As previously mentioned, Reddy and Chandrashekar synthesised double-strapped phenylene-containing porphyrins (**Fig. 4.3**, compounds **4.28** and **4.29**) as well as their cobalt and zinc metal derivatives. The three isomers were identified and distortion was confirmed by NMR and absorption spectroscopy.[317] In follow up studies, they investigated their excited state properties and showed that distorted porphyrins have lower fluorescence intensities that their planar analogues and that small conformational changes can affect the energies of the HOMOs and LUMOs, thus affecting their light-absorbing properties and redox potentials in the singlet excited state.[318] Notably, triplet decay was not significantly affected.[319] They also synthesised basket handle porphyrins with pyrrole-brominated short-chains and their Cu(II) derivatives and showed that bromination enhanced distortion.[320]

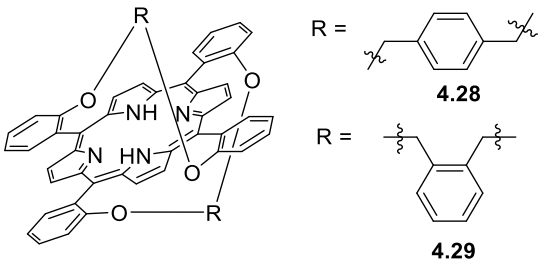

Figure 4.3: Distorted strapped porphyrins synthesised by Reddy and Chandrashekar.

Like many porphyrins, metallated distorted porphyrins are capable of coordinating ligands in the axial position and macrocyclic distortion is often evident in these systems. In the first of two recent examples, Zhou *et al.* reported three saddle-shaped nonplanar zinc porphyrins with two short alkyl straps of varying lengths and two X-ray crystal structures. The most deformed compound, **4.30**, was able to coordinate oxygen by activating free oxygen to form a superoxide ligand.[321]

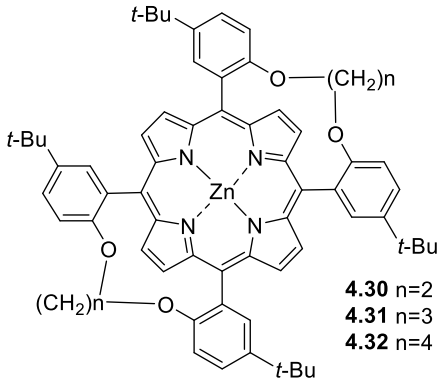

Figure 4.4: Distorted strapped Zn(II)porphyrins synthesised by Zhou *et al.*[321]

In 2017, an impressive synthetic effort by the Anderson group investigated the role of strap length on supramolecular assemblies. They synthesised thioester-linked alkyl strapped porphyrins metallated with zinc(II). These porphyrins were then used in a templated synthesis with pyridyl ligands to form conjugated cyclic porphyrin hexamers. The strap was expected to be located on the outside of the nano ring with the less hindered side of the porphyrin interacting with the ligand; however, it was found that interactions between the strap and the ligand directed axial coordination to the strapped face of the porphyrin, except when the strap was too short.[322]

4.1.4 Strapped anthracene-containing systems

Anthracene-containing strapped porphyrins are the foundation of this chapter and synthetically related compounds can be found in the literature (**Fig. 4.5**–**4.7**). In the late 1970s and 1980, Traylor and coworkers synthesised compounds **4.33** and **4.34** as part of a wider study related to ligand binding in natural hemeproteins.[323,324] It was previously established that the active sites of heme proteins are sterically hindered due to the presence of protein side chains, which block the path of incoming ligands.[325] Thus, they designed the strapped systems in **Fig. 4.5** to mimic this hindered active centre and studied oxygen and carbon dioxide binding with the iron centre. The anthracene unit was introduced in a double amide bond-forming reaction between an anthracene-containing acid chloride unit and amine-containing porphyrin. To further restrict the binding pocket, they performed a cycloaddition reaction with 1-phenyl-1H-pyrrole-2,5-dione in acetone to yield compound **4.35**. This is the only example, to the best of our knowledge, of a cycloaddition reaction being performed on such systems.[326]

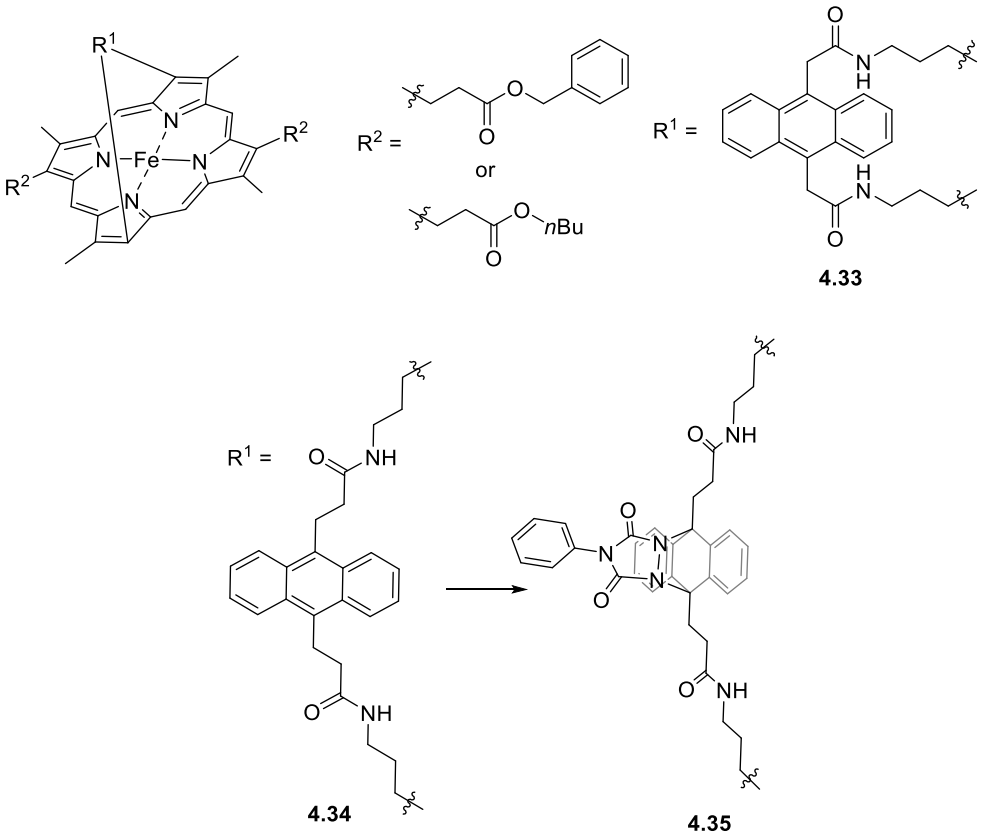

Figure 4.5: Early examples of anthracene-strapped porphyrin synthesised by Traylor and co-workers.

In 1980, the Battersby group synthesised and presented the X-ray crystal structure of an anthracene-containing porphyrin, **4.36**. The crystal structure showed that the anthracene unit was off-set to the mean plane of the porphyrin macrocycle and the macrocycle was not distorted.[327]

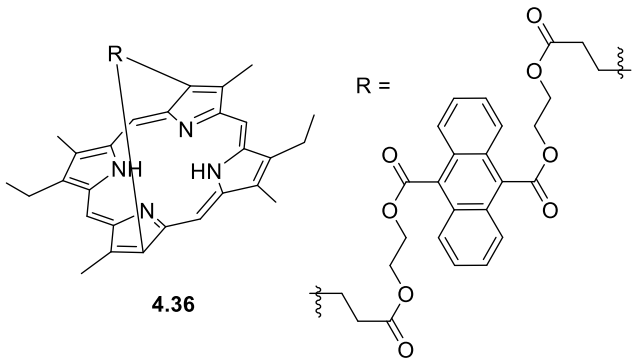

4.36

Figure 4.6: Anthracene-strapped porphyrin synthesised by the Battersby group.

In a final example, compound **4.37** was one of a series of strapped and dimeric porphyrins synthesised by Osuka *et al.* in 1990. In this synthetic study, the authors used direct condensation reactions and were able to confirm that strap length is inversely related to distortion using NMR and absorption spectroscopy.[328]

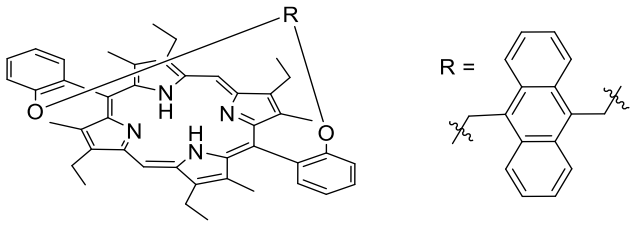

4.37

Figure 4.7: An anthracene-strapped porphyrin synthesised by Osuka *et al***.**

4.2 OBJECTIVES

In this study, we aimed to synthesise short-chained anthracene-strapped porphyrins to investigate [4+2] cycloaddition reactions between the anthracene strap and singlet oxygen generated from the excited state of the porphyrin (**Scheme 4.4**). We envisioned that the 3D structure of these systems and the close proximity of the anthracene trapping unit would have a significant effect on the resulting endoperoxide, possibly making steps towards a regioselective photochemical reaction by blocking one face of the anthracene. Alternatively, these systems were also expected to show potential as switchable oxygen storage devices, controlled by temperature. The key synthetic step in the preparation of the single-strapped system, **4.38**, was chosen to be a condensation reaction between DPM and an anthracene-containing bisaldehyde. For the double-strapped system, **4.39**, we aimed to use a direct condensation between the same anthracene-containing bisaldehyde and unsubstituted pyrrole; however, other methods were also considered. We then aimed to move on to the next stage of the study in which we focused on the preparation of the corresponding porphyrin endoperoxides (**4.40** and **4.41**) using broad-spectrum light.

We aimed to characterise these compounds using NMR spectroscopy, UV-vis spectroscopy, and most importantly, single-crystal X-ray crystallography to investigate if macrocycle distortion was induced by our short strap and/or more pronounced after the photochemical reaction between singlet oxygen and the aromatic unit. We also planed to investigate endoperoxide decay using NMR spectroscopy to assess if these compounds have switchable properties.

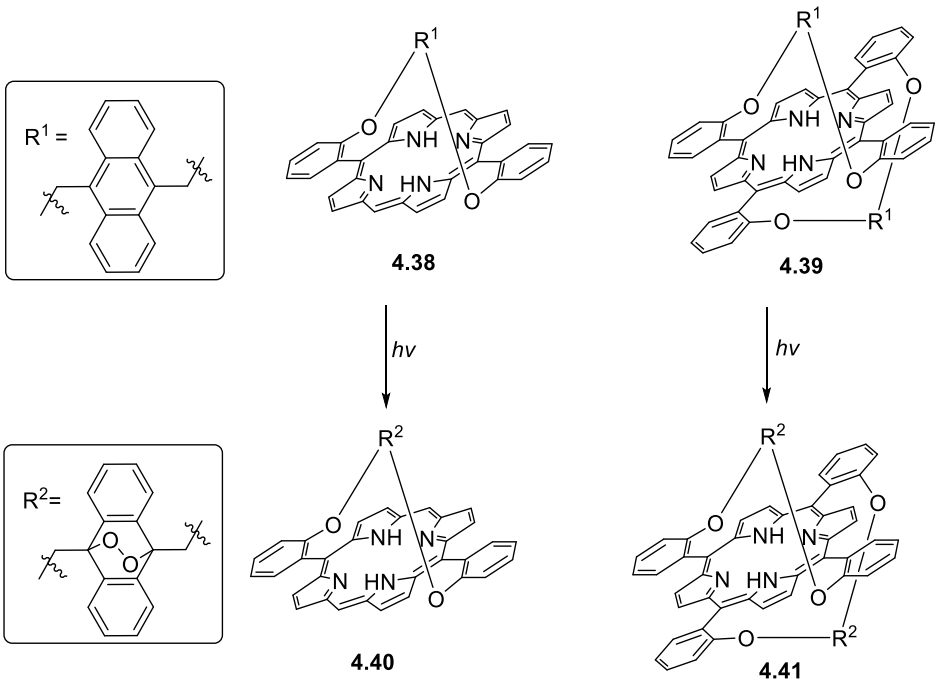

Scheme 4.4: Target short-chained anthracene-strapped porphyrins and their corresponding endoperoxides.

4.3 RESULTS DISSCUSSION§

4.3.1 Synthesis of anthracene-containing single-strapped porphyrins

As discussed, there are many synthetic approaches at hand to achieve strapped porphyrin systems. For our single-strapped system, we chose to condense an anthracene-containing bisaldehyde with DPM. This approach was chosen to ensure that the *trans* isomer would be the major product as we aimed to position the anthracene moiety on top of the porphyrin core.

Thus, we first introduced bromine to unsubstituted anthracene, **4.42** using paraformaldehyde, 33% HBr in acetic acid and $AlCl_3$. A substitution reaction with salicylaldehyde in the presence of base and KI in DMF yielded the bisaldehyde. This procedure was adapted from literature.[328] Both reactions produced high yields, up to 97% for a) and 60% for b), and were suitable for multigram scale syntheses (Tables **4.1** and **4.2**).

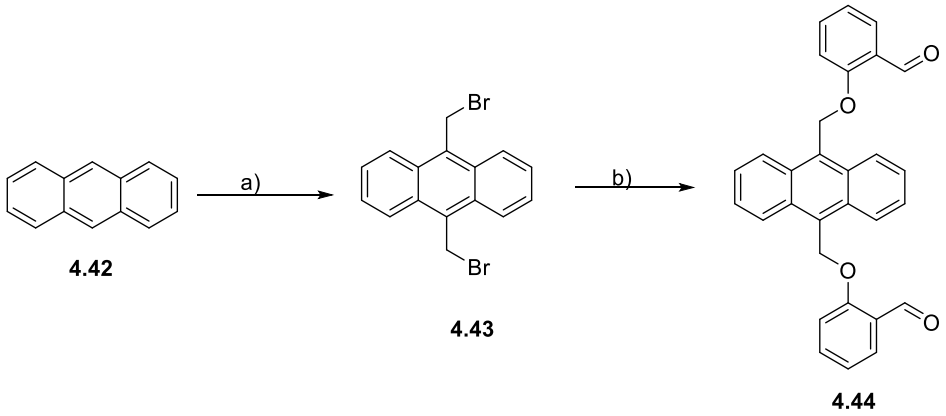

Scheme 4.5: Synthesis of bisaldehyde. a) Paraformaldehyde, 33% HBr in acetic acid, $AlCl_3$, 50 °C, 3 h; b) salicylaldehyde, K_2CO_3, DMF, KI, 60 °C, 24 h.

§ Contributions to the results presented in this chapter were made by Dr. K. J. Flanagan.

Table 4.1: Example scales and yields for step a) of the bisaldehyde (**4.44**) synthesis.

Entry	Scale	Yield
1	1.9 g	46%
2	12 g	97%
3	7.6 g	88%
4	7.6 g	76%

Table 4.2: Example scales and yields for step b) of the bisaldehyde (**4.44**) synthesis.

Entry	Scale	Yield
1	1 g	50%
2	25.6 g	60%
3	2.5 g	43%

We then synthesised DPM (**4.48**) using a literature adapted procedure and also prepared DPM derivatives (**4.49** and **4.50**) to expand the porphyrin library (**Scheme 4.6**).[329–331] Either paraformaldyehdye, benzaldehyde, or bromobenzaldehyde was condensed with excess pyrrole using TFA as the catalyst. The reactions were monitored using a bromine chamber. Yields between 28% and 79% were obtained and these condensation reactions were performed on gram scales.

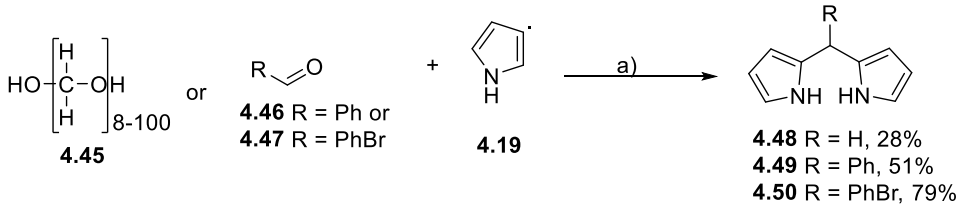

Scheme 4.6: Synthesis of DPMs. a) TFA (cat.), rt, 30 min.

Each DPM (**4.48**–**4.50**) was then condensed with the bisaldehye, **4.44** using DCM and TFA as an acid catalyst. After 3.5 h at rt, TEA was added to neutralise the TFA (**Scheme 4.7**). An oxidation step using *p*-chloranil followed. This step is key to inducing macrocyclic distortion, which will be discussed in detail. The porphyrinogen

is nonplanar and not rigid because of the lack of conjugation. Upon oxidation, the macrocycle is flattened and a 'bow string effect' induces distortion. The porphyrins were purified using column chromatography and recrystallisation and yields between 14% and 19% were obtained. The same synthetic strategy was employed by Osuka *et al.* for the synthesis of **4.37**, **Fig. 4.7** and they obtained a 25% yield, which is consistent with our moderate yields.

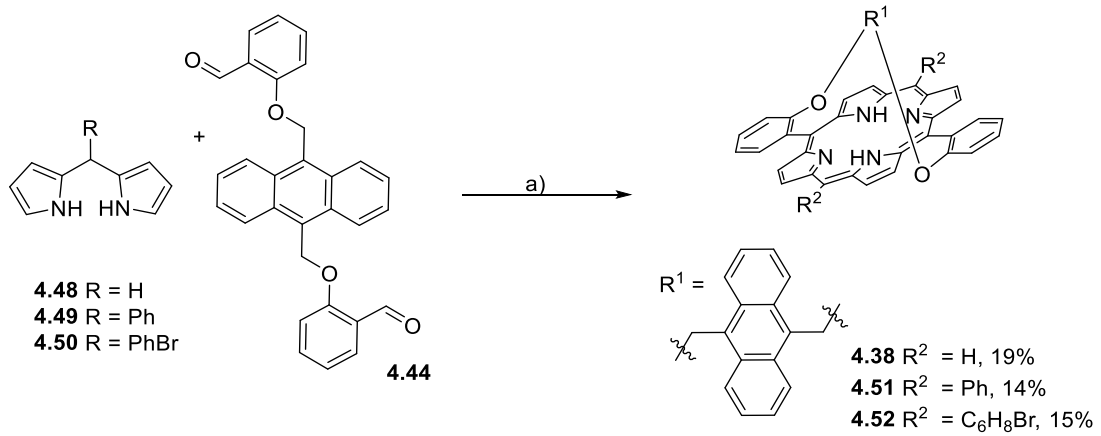

Scheme 4.7: Synthesis of single-strapped porphyrins. a) 1. DCM 2. TFA (cat.), 3.5 h, rt. 3. TEA, *p*-chloranil, 80 °C, 1 h.

We also synthesised the Zn(II) metallated derivatives of compounds **4.38**, **4.51**, and **4.52**. This was achieved using Zn(II)acetate, MeOH, and DCM and yields between 47% and 98% were obtained (**Scheme 4.8**). It was found that heating to 80 °C compared to initial attempts at rt, decreased the reaction time. The products were purified using silica chromatography and recrystallisation.

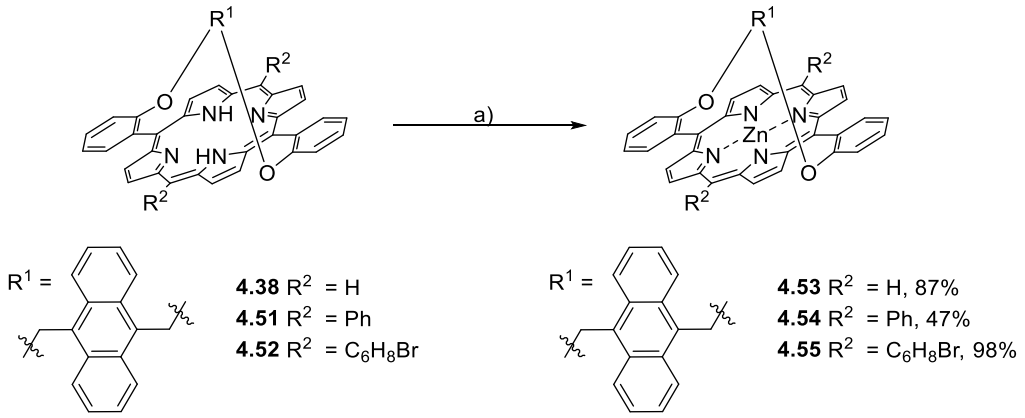

Scheme 4.8: Synthesis of Zn(II) single-strapped porphyrins. a) Zn(II)acetate, MeOH, DCM, 80 °C, 12 h.

4.3.2 Endoperoxide formation and macrocyclic distortion

The next stage of this project was the synthesis of endoperoxides from the parent strapped porphyrins (**4.38**, **4.51**, and **4.52**). The parent porphyrins were dissolved in chloroform-*d* and irradiated with a polychromatic light source in an NMR tube. The reactions were monitored by ^{1}H NMR and yields were quantitative in all cases.

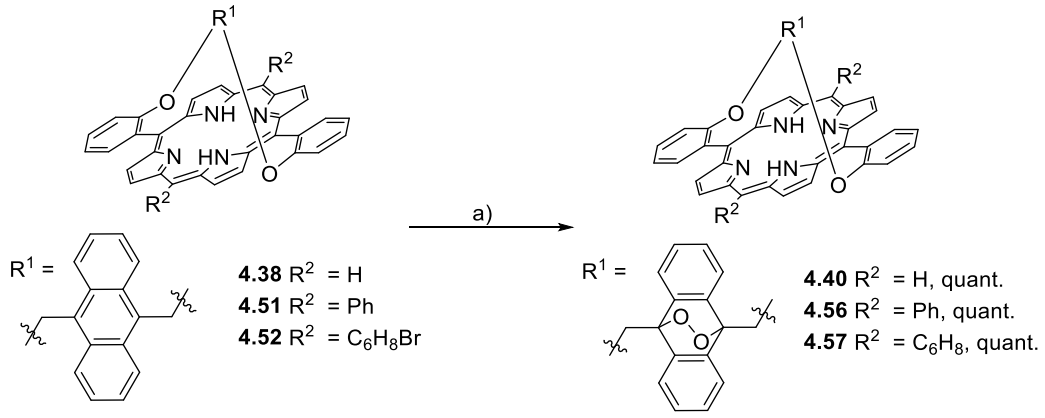

Scheme 4.9: Endoperoxide synthesis. a) Chloroform-*d*, *h*ν, 15 mins.

We then used endoperoxide **4.40** to study thermal decay. After endoperoxide formation, the chloroform-*d* was removed and replaced with DMSO-*d*$_6$. The sample was heated to 85 °C in accordance with other anthracene derivatives to the induce thermal decay of the endoperoxide.[283] At t = 0, the NH proton signal of endoperoxide **4.40** is observed at –3.34 ppm. In the aromatic region, we observed the CH protons of the anthracene endoperoxide as two multiplets at 5.91 and 4.81 ppm. It is

noteworthy that the CH protons of the anthracene endoperoxide have a lower chemical shift than unsubstituted anthracene, which is attributed to ring current effects. Following heating over 2 h, the signals of the CH protons of the anthracene endoperoxide at 5.91 and 4.81 ppm slowly decay with the appearance of aromatic signals at 5.74 and 4.97 ppm that correspond to the CH protons of anthracene. Only minor changes in the chemical shifts of the CH protons of the anthracene and endoperoxide units are noted as we expect they are under the influence of similar ring current effects. The NH protons also undergo changes. The endoperoxide signal at –3.34 ppm decays and the parent NH signal appears at –3.50 ppm. The endoperoxide NH signal is deshielded in comparison to the parent because of the electronegative oxygen atoms of the endoperoxide. Over the course of the 2 h, we also see an emergence of other signals, which are especially evident in the NH region. These signals may indicate the formation of rearranged endoperoxide porphyrin products; thus, it can be concluded that the thermal decay of **4.40** in DMSO-d_6 is not quantitative (**Fig. 4.8**).

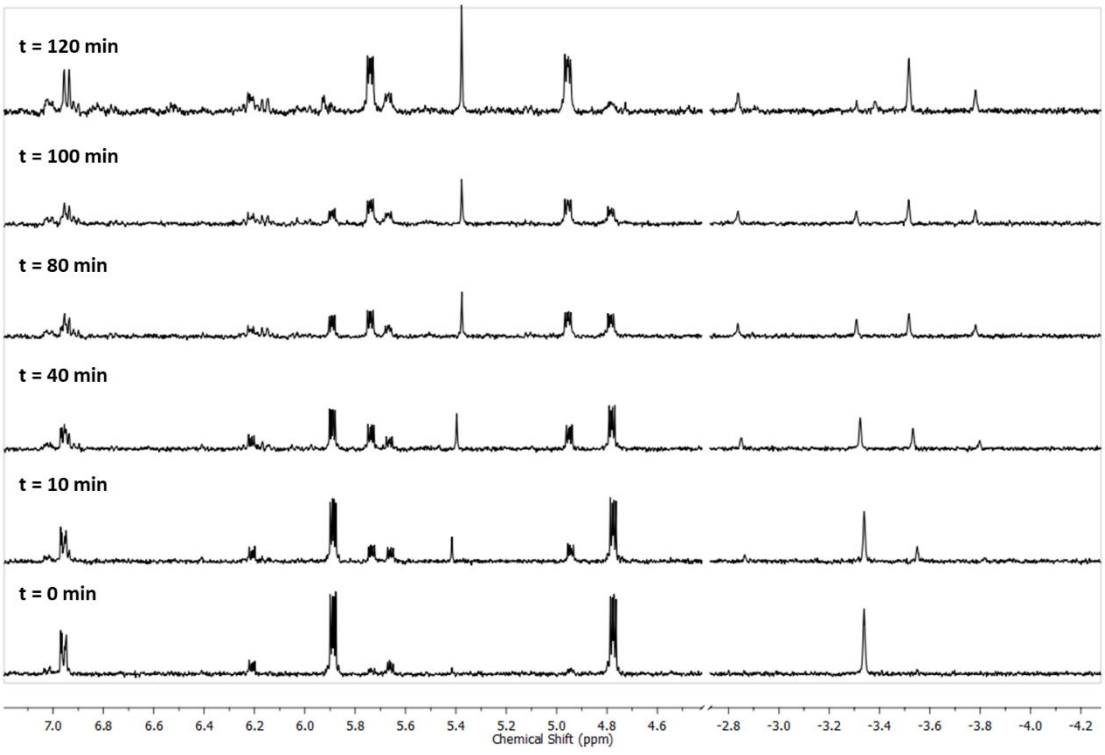

Figure 4.8: Formation of endoperoxide **4.40** and thermal decay to parent **4.38** in chloroform-*d*.

To further investigate changes in the macrocycle core upon endoperoxide formation and the introduction of a short strap we studied the absorption spectra of the strapped systems and compared them to 5,15-diphenylporphyrin, which acted as a non-strapped analogue. A marked red-shift in absorption is a hallmark of macrocyclic distortion due to the destabilisation of the porphyrin HOMO.[332,333] In **Fig. 4.9** the normalised absorption spectra of 5,15-diphenylporphyrin (blue), parent porphyrin, **4.38** (black) and endoperoxide, **4.40** (grey) recorded in DCM are presented to exemplify this phenomenon. We can see that 5,15-diphenylporphyrin has a maximum at 408 nm and upon the introduction of the strap, there is a red-shift of 10 nm to 418 nm in **4.38**. The formation of the endoperoxide induces a slight increase in macrocyclic distortion with a bathochromic shift of 2 nm from the parent porphyrin **4.40**. Also, of note are the signals between 330-400 nm in **4.38** that represent the anthracene moiety, which are not present in the endoperoxide absorption spectrum. The bathochromic shift is also repeated for compounds **4.51**, **4.56**, **4.52**, and **4.57**, which show a significant red-shift when compared to 5,15-diphenylporphyrin and a minor shift upon endoperoxide formation (**Table 4.3**).

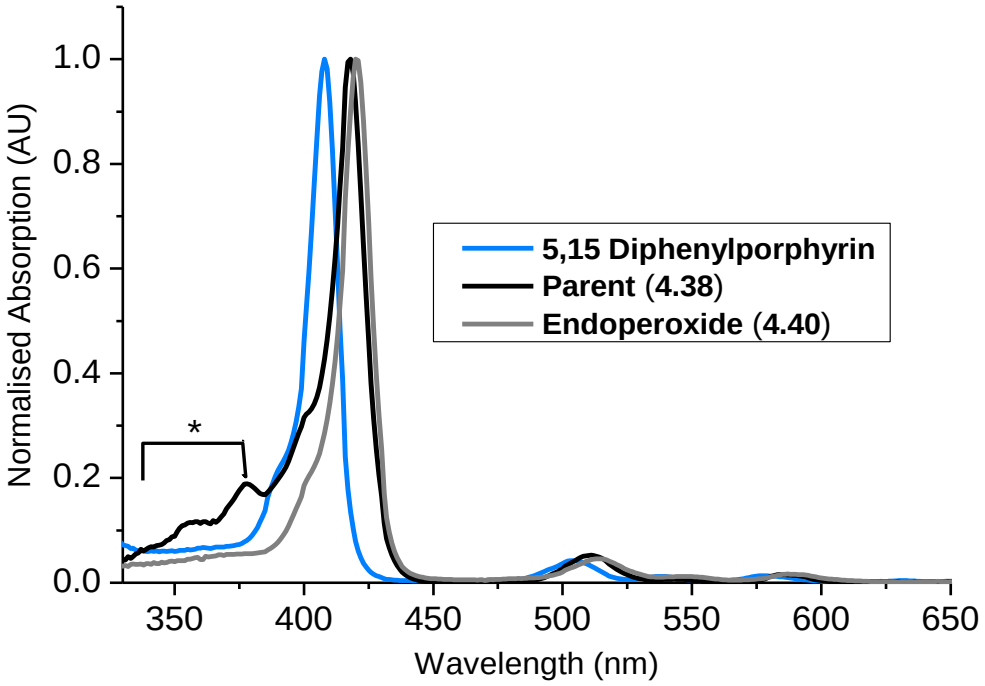

Figure 4.9: Normalised absorption spectra of porphyrins 5,15-diphenylporphyrin (blue), **4.80** (black), and endoperoxide, **4.40** (grey) recorded in DCM as an example to show how the strap induces distortion. *Absorption wavelength range for the anthracene moiety.

Table 4.3: Absorption maxima (λ_{max}) of the strapped porphyrins, endoperoxides, and 5,15-diphenylporphyrin recorded in DCM.

Porphyrin	λ_{max} (nm)
5,15-diphenylporphyrin	408, 504, 538, 577, 632
4.38	359, 378, 418, 511, 543, 584, 632
4.40	420, 515, 545, 587, 632
4.51	360, 384, 431, 526, 564, 600, 658
4.56	433, 528, 567, 601, 657
4.52	361, 382, 432, 527, 565, 601, 658
4.57	434, 529, 566, 604, 660

We obtained X-ray crystal structures of compounds **4.38** and **4.40**, which further confirm macrocyclic distortion (**Fig. 4.10**).** Again, we compared the structures to 5,15-diphenylporphyrin to study the effect of the strap and endoperoxide formation on macrocyclic distortion. There are two 5,15-diphenylporphyrin structures in the literature, one with DCM as a solvated counterpart and one without.[334]

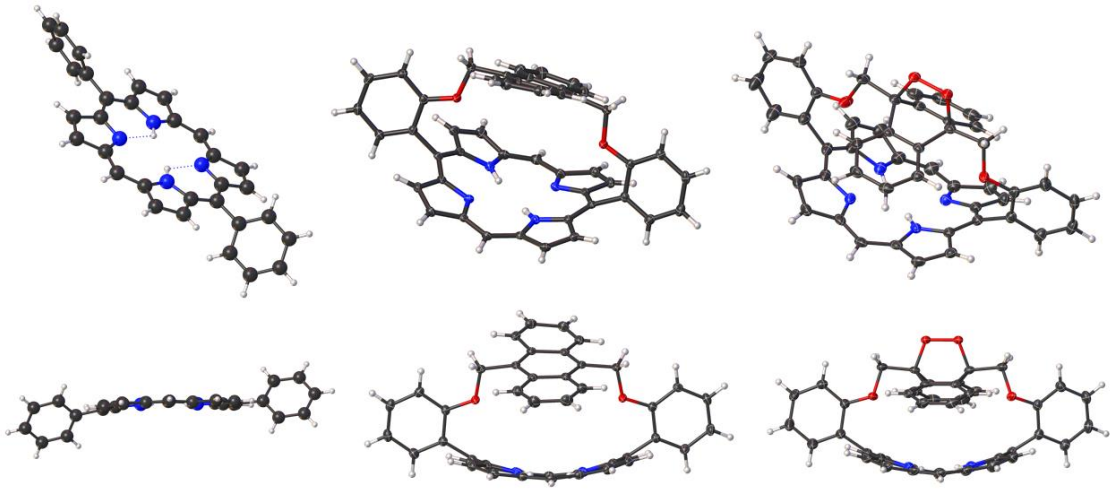

Figure 4.10: Molecular structure of 5,15-diphenylporphyrin, **4.38** and **4.40** (left to right) viewed at a tilted angle (top) and the side view (bottom). Thermal ellipsoids give 50% probability for **4.38** and **4.40**. The structure of 5,15-diphenylporphyrin is drawn isotropically.

** The crystallographic data was collected by Dr. K. J. Flanagan.

We represented this distortion in skeletal deviation plots, which show that the introduction of the strap (compounds **4.38** and **4.40**) drastically increases ring distortion, especially at the meso-carbons when compared to the two 5,15-diphenylporphyrin structures (**Fig. 4.11**).

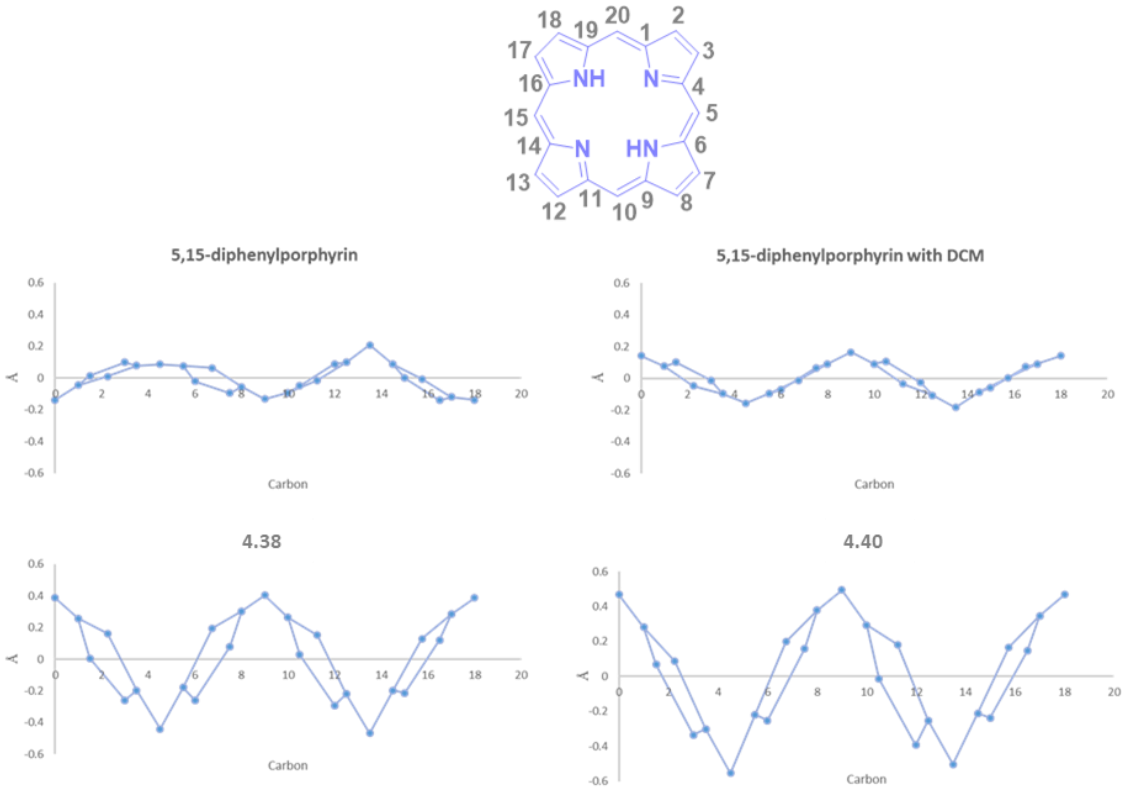

Figure 4.11: Top: Porphyrin core carbon numbering. Bottom: Skeletal deviation plots (C20 to C20) from the crystal structure of 5,15-diphenylporphyrin, 5,15-diphenylporphyrin with DCM, compound **4.38**, and compound **4.40** based on the atom displacement from the 24-atom mean plane.

We then used normal-coordinate structural decomposition (NSD) plots to identify the distortion modes present in the core of these structures.[335,336] Compounds **4.38** and **4.40** display contributions to the out of plane (*oop*) B_{1u} mode with a second smaller contribution to the domed (A_{2u}) mode, while both 5,15-diphenylporphyrin structures display a ruffled (B_{1u}) mode. The structure of compound **4.40** shows a slightly larger contribution to the B_{1u} mode than **4.38**, which is also reflected in the Δ_{oop}, indicating that the formation of the endoperoxide increases distortion compared to the parent. For the in plane (*ip*) distortion modes, both 5,15-

diphenylporphyrin structures have major contributions to the meso-stretching (B_{2g}) mode with a secondary contribution to the breathing (A_{1g}) mode. The structure of compound **4.38** has a contribution to the B_{2g} mode, which is lower than that of 5,15-diphenylporphyrin, and makes minor contributions to the other modes. The structure of compound **4.40** has roughly equal contributions to the *N*-stretching (B_{1g}) and the A_{1g} modes. Overall, we can see an inverse relationship between the *oop* and in-plane *ip* distortion modes in the strapped systems (compounds **4.38** and **4.40**) and out of plane distortions are more significant for the strapped systems (**Fig. 4.12**).

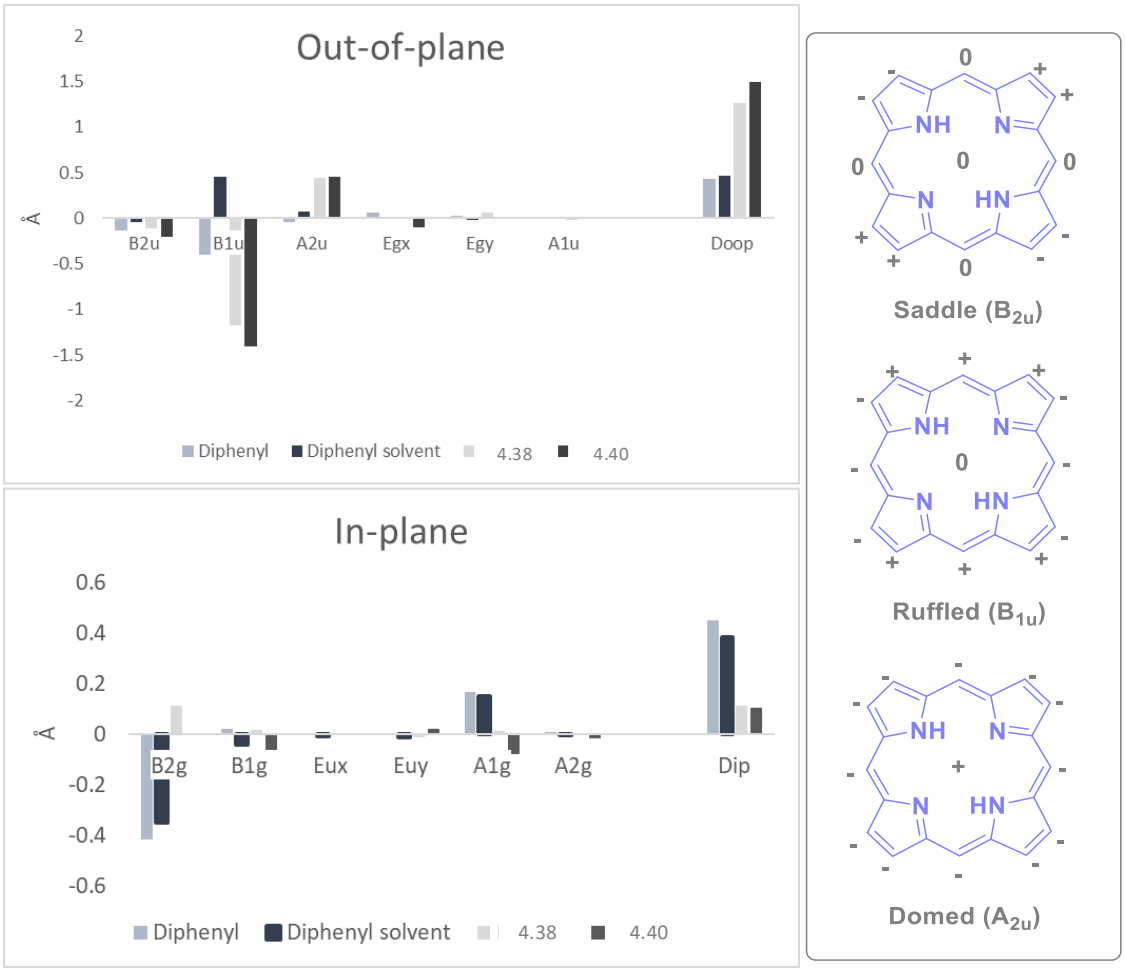

Figure 4.12: Left: Out-of-plane (top) and in-plane (bottom) distortion modes from the crystal structures of 5,15-diphenylporphyrin, 5,15-diphenylporphyrin with DCM, compound **4.38**, and compound **4.40** based on NSD. Right: Schematic illustration of relevant porphyrin *oop* distortion modes.

The bond lengths and angles of the porphyrin macrocycle are presented in **Table 4.4** and **Table 4.5**. Generally, there are no significant differences between the bond lengths of the 5,15-diphenylporphyrin structures and the structures of strapped systems, **4.38** and **4.40**.

In contrast, the bond angles do display notable changes. In anthracene strapped porphyrin **4.38**, the N–$C_{\alpha(1,9,11,19)}$–$C_{m(10,20)}$, $C_{\alpha(4,14)}$–$C_{m(5,15)}$–$C_{\alpha(6,16)}$, and $C_{m(10,20)}$–$C_{\alpha(1,9,11,19)}$–$C_{\beta(2,8,12,18)}$ angles are increased by 2°, 2.5°, and 1.8°, respectively, when compared to 5,15-diphenylporphyrin. Conversely, the $C_{\alpha(1,11)}$–$C_{m(10,20)}$–$C_{\alpha(9,19)}$ angle is reduced by 3°. A small change of 0.9° is observed in the $C_{m(5,15)}$–$C_{\alpha(4,6,14,16)}$–$C_{\beta(3,7,13,17)}$ and N–$C_{\alpha(4,6,14,16)}$–$C_{m(5,15)}$ angles. Similar changes are noted in the structure of **4.40**, and notably, the $C_{\alpha(4,14)}$–$C_{m(5,15)}$–$C_{\alpha(6,16)}$ angle shows a 1.3° reduction compared to **4.38**. The majority of the bond angles only deviate by less than 0.5° between **4.38** and **4.40**, suggesting that the cycloaddition to form the endoperoxide induced minor porphyrin core perturbation, which is in agreement with the absorption spectra, NSD plots, and skeletal deviation plots

Table 4.4: Averaged geometrical parameters for the bond lengths of 5,15-diphenylporphyrin, 5,15-diphenylporphyrin with DCM, compound **4.38**, and compound **4.40**.

Bond lengths (Å)	**5,15-diphenyl porphyrin[334]**	**5,15-diphenyl porphyrin -DCM[334]**	**4.38**	**4.40**
N–C_{α}	1.368(15)	1.367(16)	1.371(4)	1.368(11)
C_{α}–C_{β}	1.440(17)	1.442(16)	1.440(4)	1.438(11)
C_{α}–$C_{m(5,15)}$	1.408(17)	1.401(18)	1.401(4)	1.403(10)
C_{α}–$C_{m(10,20)}$	1.388(16)	1.389(14)	1.390(4)	1.390(12)
C_{β}–C_{β}	1.357(17)	1.355(14)	1.354(5)	1.353(11)

Table 4.5: Averaged geometrical parameters for the bond angles of 5,15-diphenylporphyrin, 5,15-diphenylporphyrin with DCM, compound **4.38**, and compound **4.40**.

Bond angles (°)	5,15-diphenyl porphyrin[334]	5,15-diphenyl porphyrin-DCM[334]	4.38	4.40
$N{-}C_{\alpha(4,6,14,16)}{-}C_{m(5,15)}$	124.5(11)	124.8(11)	125.4(13)	124.9(4)
$N{-}C_{\alpha(1,9,11,19)}{-}C_{m(10,20)}$	127.1(11)	126.9(12)	125.1(9)	125.4(4)
$N{-}C_{\alpha(4,6,14,16)}{-}C_{\beta(3,7,13,17)}$	108.7(10)	108.8(11)	108.8(8)	108.8(5)
$N{-}C_{\alpha(1,9,11,19)}{-}C_{\beta(2,8,12,18)}$	109.1(10)	108.9(11)	108.9(8)	108.7(7)
$C_{\alpha}{-}N{-}C_{a}$	107.7(10)	107.8(11)	107.6(3)	107.7(5)
$C_{\alpha(4,14)}{-}C_{m(5,15)}{-}C_{a(6,16)}$	122.7(10)	123.3(12)	125.2(12)	123.9(4)
$C_{\alpha(1,11)}{-}C_{m(10,20)}{-}C_{a(9,19)}$	129.1(12)	128.4(12)	126.1(11)	126.4(5)
$C_{\alpha(4,6,14,16)}{-}C_{\beta(3,7,13,17)}{-}C_{\beta(2,8,12,18)}$	107.3(10)	107.1(12)	107.4(13)	107.2(6)
$C_{\alpha(1,9,11,19)}{-}C_{\beta(2,8,12,18)}{-}C_{\beta(3,7,13,17)}$	107.2(11)	107.4(12)	107.3(13)	107.4(5)
$C_{m(5,15)}{-}C_{\alpha(4,6,14,16)}{-}C_{\beta(3,7,13,17)}$	126.7(10)	126.4(12)	125.8(11)	126.3(5)
$C_{m(10,20)}{-}C_{\alpha(1,9,11,19)}{-}C_{\beta(2,8,12,18)}$	123.8(12)	124.1(12)	125.6(11)	125.2(5)

The pyrrole tilt angles of the of N21, N22, and N23 pyrrole rings (**Table 4.6**) provide a clear trend with the 5,15-diphenylporphyrin structures displaying the smallest tilt followed by **4.38** and then **4.40**, with an average 9° increase from 5,15-diphenylporphyrin-DCM to **4.38**, and a 2.4–3.2° increase from **4.38** to **4.40**. The atom deviations paint a similar picture for the Δ24, ΔN, ΔC_m, ΔC_α, and ΔC_β deviations from the 24-atom least squares plane. Again, this is in agreement with the NSD results where there is a significant increase in the *oop* distortion modes following the introduction of the strap, as demonstrated by the increase in Δ_{oop}.

Table 4.6: Averaged geometrical parameters of the pyrrole tilt and atom deviations for 5,15-diphenylporphyrin, 5,15-diphenylporphyrin with DCM, compound **4.38**, and compound **4.40**.

Pyrrole tilt (°)	5,15-diphenyl porphyrin[334]	5,15-diphenyl porphyrin-DCM[334]	4.38	4.40
N21	3.6(4)	5.2(4)	14.5(5)	16.9(14)
N22	4.5(4)	5.1(4)	15.0(4)	17.3(2)
N23	5.3(4)	5.7(4)	14.8(7)	18.1(17)
N24	5.9(4)	4.8(4)	13.8(6)	16.0(17)
$\Delta 24^{e}$	0.091	0.095	0.258	0.306
ΔN^{f}	0.024	0.025	0.159	0.159
$\Delta C_{m(5,15)}{}^{g}$	0.142	0.162	0.425	0.505
$\Delta C_{m(10,20)}{}^{g}$	0.136	0.153	0.395	0.482
$\Delta C_{\alpha}{}^{h}$	0.082	0.092	0.238	0.286
$\Delta C_{\beta}{}^{i}$	0.064	0.065	0.157	0.201
$\Delta_{ip}{}^{b}$	0.450	0.383	0.114	0.105
$\Delta_{oop}{}^{c}$	0.429	0.462	1.261	1.496

Finally, we studied changes in the core size ($N_x \cdots N_x$) following the introduction of the strap and the length of the strap. We see that the 5,15-axis is longer than the 10,20-axis, giving a rectangular shape to the core of the 5,15-diphenylporphyrin structures but when the strap is introduced we get a 'square' shape resulting from the 5,15- and 10,20-axis being approximately the same length (structure of compounds **4.38** and **4.40**). We then quantified the strap length to be the distance between $C_{ortho} \cdots C_{ortho}$ of the 5,15-phenyl substituents. When no strap is included, the average distance between these two atoms is between 11.506–11.580 Å; however, upon the introduction of the strap, this distance is significantly shorted to 8.967(2) Å (**4.38**) and is 8.928(9) Å following endoperoxide formation (**4.40**).

Table 4.7: Core structural parameters of 5,15-diphenylporphyrin, 5,15-diphenylporphyrin with DCM, compound **4.38**, and compound **4.40**.

Structural parameters (Å)	5,15-diphenyl porphyrin[334]	5,15-diphenyl porphyrin-DCM[334]	4.38	4.40
$C_{ortho}\cdots C_{ortho}$ [a]	11.580(17)	11.506(2)	8.967(2)	8.928(9)
N21···N22[d]	2.757(15)	2.772(15)	2.882(2)	2.823(3)
N22···N23[d]	3.065(13)	3.238(15)	2.892(3)	2.912(3)
N23···N24[d]	2.750(15)	2.775(15)	2.886(2)	2.817(3)
N24···N21[d]	3.055(13)	3.031(15)	2.853(3)	2.893(3)

[a]Calculated distance between the C_{ortho} carbon atoms to simulate the length of the strap between the 5,15-substituted phenyl ring. [b]Simulated total in-plane distortion. [c]Simulated total out-of-plane distortion. [d]Calculated distance between the pyrrole nitrogen atoms. [e]Average deviation from the least-squares plane of the 24-macrocycle atoms. [f]Simulated displacement of the four internal nitrogen atoms from the 24-atom mean plane. [g]Average deviation of the meso-carbon atoms from the 24-atom mean plane. [h]Average deviation of the α-carbon atoms from the 24-atom mean plane. [i]Average deviation of the β-carbon atoms from the 24-atom mean plane.

4.3.3 Attempted synthesis of double-strapped porphyrins

We then turned our attention to the synthesis of the *trans* isomer of the double-strapped short-chained anthracene-containing porphyrin (compound **4.39**). We focused on the *trans* isomer because it is expected to induce the highest degree of macrocyclic distortion and the expected orientation of the anthracene unit across the porphyrin provides an analogous structure to that of our single-strapped system for investigating [4+2] cycloaddition reactions between the anthracene and singlet oxygen.

We adopted the direct synthesis approach by condensing pyrrole with the previously synthesised bisaldehyde (**4.44**) in a 2:1 ratio (**Scheme 4.2**, **Approach A**). This approach was used by Reddy and Chandrashekar in the synthesis of similar

compounds that had a phenyl moiety in the strap.[317] As the expected yields are lower than 1%, the condensations were performed on multigram scales. We first adapted their procedure and boiled the reactants in propionic acid for 1.5 h, followed by stirring at rt for 24 h to oxidise to porphyrinogen; however, this did not yield any compound. We then shortened the reaction time to 45 min to prevent decomposition under the harsh reaction conditions (**Table 4.8**, Entry 1–3). Mass spectrometry Q-TOF provided a signal at *m/z* = 1082.3865 but the product was not isolated. We then increased the scale to aid isolation and increased the reaction time to 1 h but the same result was obtained. In the next attempt, propanoic acid was replaced with acetic acid but this reaction did not yield porphyrin product (**Table 4.8**, Entry 4). In a final attempt, we used Lindsey conditions (**Table 4.8**, Entry 4–5) and reaction times of either 1 h or 2 h. We were able to detect porphyrin NH signals by ^{1}H NMR spectroscopy but purification and identification of the isomer were not achieved.

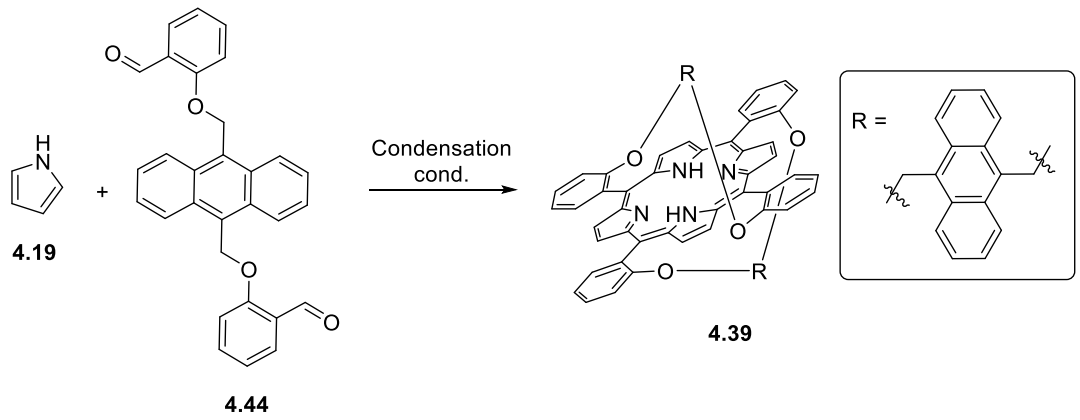

Scheme 4.10: Attempted synthesis of double-strapped porphyrin **4.39**.

Table 4.8: Condensation conditions and outcomes for the synthesis of compound **4.39** using the direct condensation approach.

Entry	Scale	Conditions	Outcome
1	10 g	1. Propionic acid (excess), 120 º C, 1.5 h 2. rt, 24 h	Failed
2	3 g	1. Propionic acid (excess), 120 º C, 45 min 2. rt, 24 h	MS found
3	15.2 g	1. Propionic acid (excess), 120 º C, 1 h 2. rt, 24 h	MS found
4	6.69 g	1. Acetic acid (excess), 100 º C, 1 h 2. rt, 24 h	Failed
2	2 g	1. DCM, $BF_3 \cdot Et_2O$ (cat.), rt, 1 h 2. DDQ (2 eq.)	Not isolated
3	3 g	1. DCM, $BF_3 \cdot Et_2O$ (cat.), rt, 2 h 2. DDQ (2 eq.)	Not isolated

In a second approach, we used bisaldehyde **4.44** to synthesise the bis-DPM (**4.58**) and then condensed this in a 1:1 ratio with the bisaldehyde. The bis-DPM was synthesised on a multigram scale using excess pyrrole. First, the reaction was initiated with TFA and stirred for 1 h at rt, resulting in a yield of 9% (**Table 4.9**, Entry 1). We then attempted to increase the yield by using 6 eq. of pyrrole in DCM to aid the dissolution of the bisaldehyde. Additionally, the reaction time was increased to 14 h and the temperature was maintained at rt. The reaction was monitored using a bromine chamber and a yield of 7% (**Table 4.9**, Entry 2) was obtained (**Scheme 4.11**).

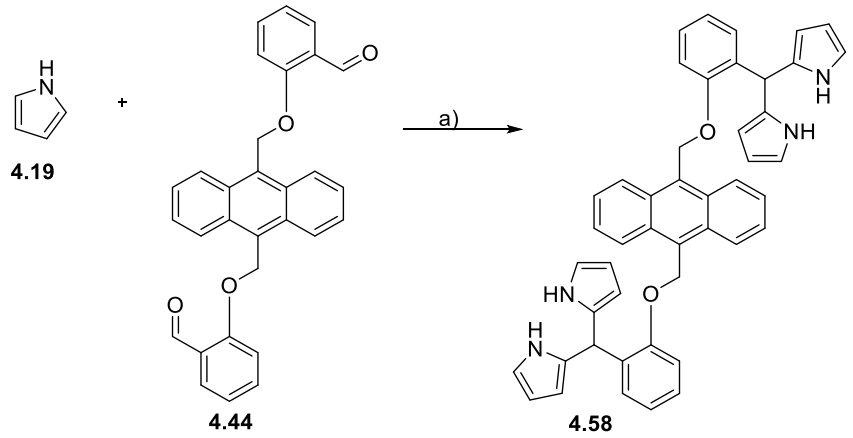

Scheme 4.11: Condensation to yield DPM **4.58**. a) TFA (cat.).

Table 4.9: Condensation to yield DPM **4.58**.

Entry	Scale	Cond.	Yield
1	1.5 g	Pyrrole (excess), 1 h, rt	9%
2	2 g	Pyrrole (6 eq.), DCM, 14 h, rt	7%

DPM **4.58** was found to degrade within one week. Therefore, it was condensed with the bisaldehyde directly after synthesis. The reaction was performed under Lindsey conditions using DCM. Following the addition of TFA, the reaction was stirred for 3 h at rt. *p*-Chloranil was used as an oxidant (**Scheme 4.12**). The product was identified by mass spectrometry (HRMS (MALDI-TOF) *m/z* calcd. for $C_{70}H_{51}N_4O_4$ $[M+H]^+$: 1083.3910, 1083.3909 found) but pure isolation was not achieved possibly due to π-stacking of the anthracene moieties.

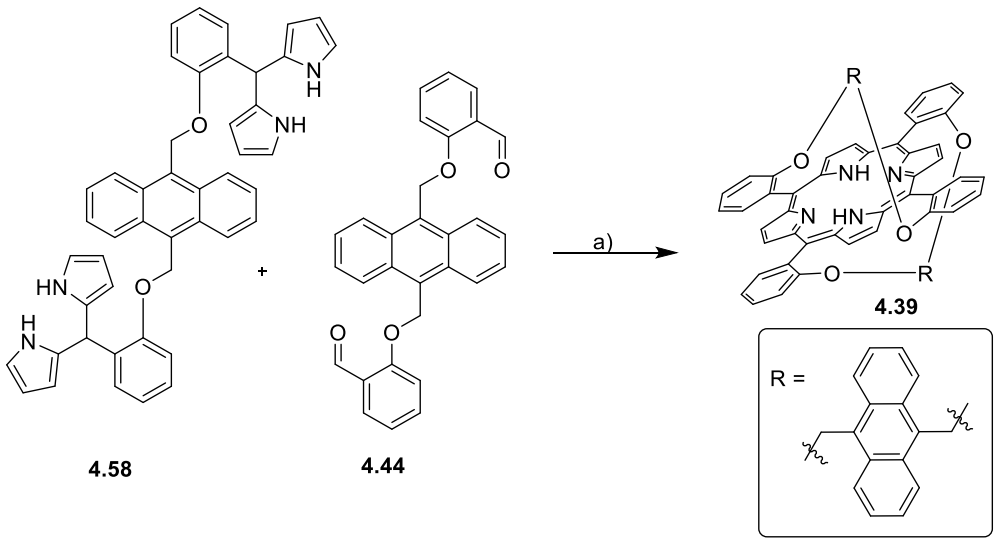

4.58 4.44 4.39

Scheme 4.12: Condensation to yield double-strapped system a) 1. DCM, TFA (cat.), rt, 3 h. 2. *p*-chloranil (6 eq.), 80 °C, 1 h.

A final attempt at this synthesis involved preparing DPM **4.60**. The procedure was adapted from literature[329–331]and the reaction was repeated several times with yields between 11-15%. (**Scheme 4.13**).

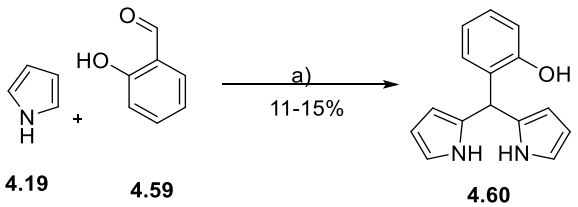

4.19 4.59 4.60

Scheme 4.13: Condensation to yield DPM **4.60** a) DCM, TFA (cat.), rt, 16 h.

Compound **4.60** was then used in the synthesis of porphyrin **4.40.** A crude yield of 11% was achieved on a 2 g scale. After several purification attempts using column chromatography (DCM and 0.5% MeOH) and recrystallisation. The crude product was used for the next step.

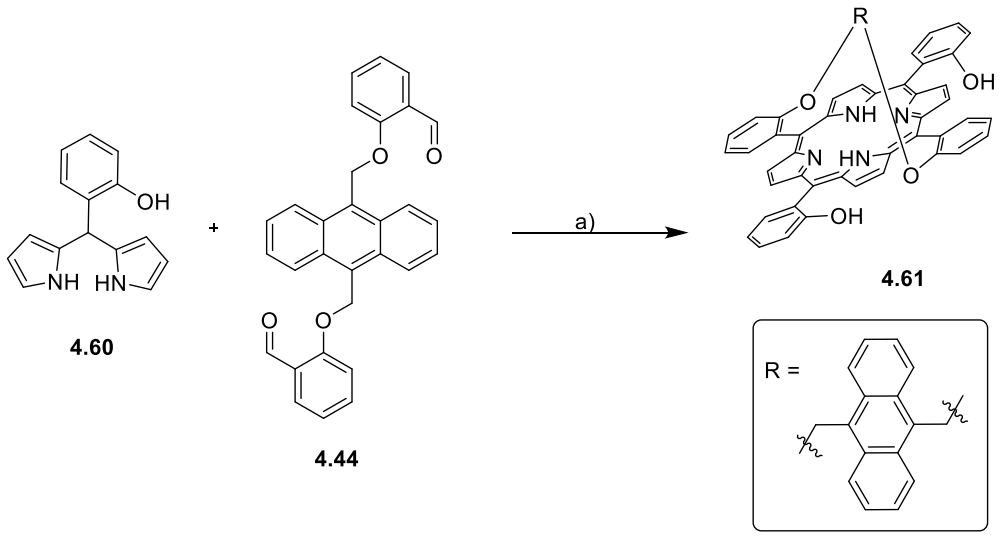

Scheme 4.14: [2+2] Condensation to yield porphyrin **4.61**. a) 1. DCM, TFA (cat.), rt, 3.5 h. 2. *p*-chlorinal (6 eq.), 60 °C, 1 h.

A nucleophilic substitution reaction between the alcohol moieties of porphyrin **4.61** and anthracene derivative **4.43** was performed. Like previous attempts, a positive mass spectrometry signal was obtained but the porphyrin was not isolated (**Scheme 4.15**).

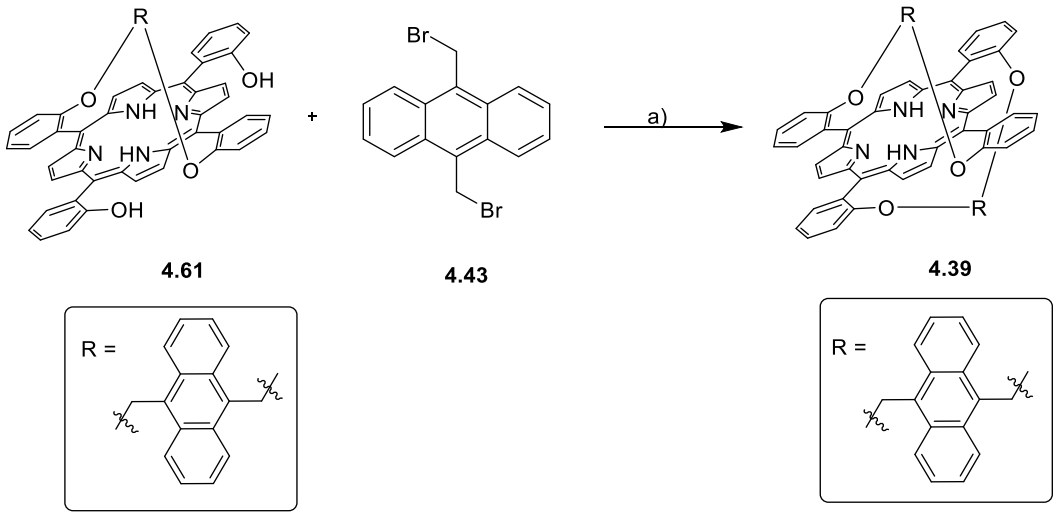

Scheme 4.15: Attempted substitution to yield porphyrin **4.39**. a) DMF, K_2CO_3 (6 eq.), 60 °C, 14 h.

4.4 CONCLUSION AND FUTURE WORK

In this chapter, short-chained anthracene strapped porphyrins were synthesised and studied for singlet oxygen storage applications. The synthetic approach taken was a [2+2] condensation reaction between the appropriate DPM and an anthracene-containing bisaldehyde, followed by oxidation with *p*-chlorinal. Moderate yields were achieved in line with previous reports. Upon exposure to light, the anthracene-strapped systems were converted to the corresponding endoperoxides *via* a [4+2] cycloaddition reaction. This was studied using ^{1}H NMR spectroscopy, absorption spectroscopy, and X-ray crystallography. We also used absorption spectroscopy and X-ray crystallography to confirm macrocyclic distortion due to the introduction of the strap. Additionally, a slight increase in distortion was evident upon endoperoxide formation and a minor bathochromic shift was observed in the absorption profiles. As seen in the X-ray structures, endoperoxide formation caused bending of the anthracene moiety to flank the core and formation of the endoperoxide occurred only on one face of the anthracene moiety. There was no evidence of the cycloaddition reaction occurring on the inside face of the anthracene strap in solution, as examined by NMR spectroscopy. Thus, it was concluded that, in these systems, this reaction is regioselective. This interesting structural effect has the potential for reversible on-off porphyrin core shielding and chemical modification of the strap may lead to a fully inaccessible core on one side. In the future, this approach may be utilised for selective oxygen sensing applications or switchable oxygen storage, controlled by temperature. ^{1}H NMR spectroscopy was also used to investigate the decay properties of these systems. The endoperoxides were formed in chloroform-*d* using broad-spectrum light and shown to thermally decay at 85 ºC in DMSO-d_6.

We also attempted the synthesis of the double-strapped short-chained anthracene containing porphyrin, compound **4.39**. We investigated direct synthesis, synthesis of the DPM followed by condensation with the bisaldehyde, and the synthesis of single-strapped porphyrin, **4.61** followed by a nucleophilic substitution reaction to introduce the second strap. Unfortunately, we were unable to isolate the target porphyrin. We did obtain positive mass spectrometry results, and this indicates that the compound was obtained but in extremely low yields, which hindered isolation. When we consider the macrocyclic distortion induced in the single-strapped system,

4.38 we would expect compound **4.39** to be highly distorted, which may contribute to the extremely low yields. Also, the notably low solubility of the bisaldehyde could prevent cyclisation and contribute to the low yield. When compared with other double-strapped systems such as those synthesised by Reddy and Chandrashekar,[317] we would expect the anthracene moiety to be much less soluble than the phenyl moiety found in their systems. Additionally, these solubility issues hindered the purification of the compound.

The future direction of this project will require restrategising and broadening the scope for the anthracene-strapped porphyrins to include capped porphyrin systems to completely block one face of the porphyrin macrocycle, in an attempt to develop regioselective light-induced cycloaddition reactions. To ease the synthesis of the double-strapped system we could extend the strap length by a few atoms, this however, would influence the expected distortion. In the future, these compounds could also be developed into switchable singlet oxygen storage devices, as demonstrated by this proof-of-concept study.

Chapter 5: Synthesis and Evaluation of Targeted Nanoconstructs for Medical Applications

"An té a bhíónn siúlach, bíonn scéalach"

Seanfhocal

"*I got one, Oops, it got away! I caught one, but it's trying to bite me!* It was a comedy of errors."

quoted in The Circuitous Route by a Group of Novices to a New FDA Approved Cancer Therapy: How Did We Do This?: Thomas J. Doughterty, 2015

5.1 INTRODUCTION

5.1.1 Liposomes and photodynamic therapy

Liposomes, which are widely used as drug delivery systems, are biodegradable nanostructures composed of a phospholipid bilayer. Liposomes form spontaneously when lipids are introduced to aqueous media, which is driven by hydrophilic repulsive interactions between the head groups of the lipids and water.[337] Commonly, cholesterol is incorporated into the bilayer to enhance stability under biological conditions and to reduce the permeability of encapsulated molecules. Polyethylene glycol (PEG) is also used in the design of biomedical liposomes to increase clearance rates and stability by preventing protein opsonisation.[338] Due to their ability to entrap small molecules, liposomes are primarily used to carry hydrophobic photosensitisers and can be chemically modified to target specific tissue and/or have increased biocompatibility and payloads.[339] As many photosensitisers, including porphyrins and their derivatives, are large conjugated systems that suffer from aggregation and quenching in polar solvents, formulation in liposomes provides a method to prevent photophysical deactivation by maintaining a distribution of the active photosensitiser monomers.

Liposomes have been applied to PDT for decades and there are many examples of liposomal photosensitiser formulations having enhanced therapeutic responses when compared directly to the corresponding free photosensitisers.[338] In one example, Molinari *et al.* showed that *m*THPC-loaded liposomes consisting of various amounts of dimyristoyl-sn-glycerophosphatidylcholine (DMPC) with a cationic surfactant were less toxic and gave a stronger therapeutic response in a human glioblastoma cell line when compared to the free chlorin. Additionally, they observed an increased encapsulation efficiency due to the incorporation of the surfactant.[340] In 1998, Jiang *et al.* formulated Photofrin in dipalmitoylphosphatidylcholine (DPPC) liposomes and treated U87 human glioma-bearing mice with PDT using the construct. When compared to PDT treatment with Photofrin in dextrose, a marked increase in therapeutic response was observed as well as increased tumour uptake of the liposomal formulation.[341] However, it should be noted that there is not always a direct correlation between liposome loading and therapeutic response. Venosa *et al.* reported that an undecanoyl ester of ALA had a higher loading efficiency into liposomes consisting of phosphatidylcholine and phosphatidylglycerol or phosphatidylcholine and phosphatidic acid when compared to free ALA. However, porphyrin production did not improve. This was attributed to poor cytoplasmic release and interaction between the derivatised ALA and the cell membrane. Thus, cellular mechanisms must also be considered when designing constructs.[342]

The first clinically approved liposomal photosensitiser formulation was Visudyne, which was developed by Novartis Ophthalmics (Switzerland) and QLT (Canada).[343] In 2000, it was approved by the FDA for the treatment of classic subfoveal choroidal neovascularisation due to age-related macular degeneration and this was soon followed by approval from the European Medicines Agency (EMA). The lipid bilayer consists of egg phosphatidylglycerol and dimyristoylphosphatidylcholine in the presence of antioxidants, butylated hydroxytoluene and ascorbyl palmitate. The active photosensitiser is BPD, which is also known commercially as Verteporfin. The lipid formulation increases cell specificity and tumour uptake by interacting with low-density lipoprotein receptors. The active photosensitiser, BPD, produces reactive oxygen species when exposed to 689 nm light and the resulting photodamage causes neovascular damage.[344]

5.1.2 Targeted liposomes for photodynamic therapy

Active targeting is a central theme in drug delivery research but certain common tumour characteristics make them more susceptible to the preferential accumulation of therapeutic agents when compared to normal tissue: These are (i) poor lymphatic drainage and (ii) vascular permeability in the nanometer range. These properties form the basis of the enhanced permeability and retention (EPR) effect. In the case of liposomes, where circulation times are increased by using dopants such as PEG or glycolipids, the EPR effect results in the passive preferential accumulation of drugs in tumours.[345]

In addition to this, active targeting can be achieved by including moieties that can specifically interact with cellular membrane components and this strategy becomes especially relevant when dealing with liposomes with long circulation times. Antibody targeting is widely used in clinical liposomal nanomedicine;[346,347] however, although specific they can be expensive to produce. A particularly important target for antibodies is EGFR, with EGFR expression found in up to 85% of patients with pancreatic ductal adenocarcinoma cancer.[348] An EGFR targeted liposomal doxorubicin formulation is currently in Phase II trials for EGFR-positive triple-negative breast cancer[349] and anti-EGFR antibodies are being used in the clinic for image-guided surgical resection of pancreatic ductal adenocarcinoma.[350]

There is much debate in the literature over the role of receptor-targeted delivery systems and the EPR effect in tumour targeting.[351] The EPR effect has been shown to play a crucial role in the accumulation of nanomedicines, as modelled by Schmidt and Wittrup.[352] They showed that as the nanoparticle size increases above 50 nm the effect of targeting becomes less important. However, a plethora of studies have concluded that the introduction of targeting ligands results in an increase in the therapeutic outcome, even without enhanced delivery or selectively, when compared with untargeted constructs. In one example, Han and Davis formulated a nanoconstruct containing a mucic acid polymer conjugate of Camptothecin-targeted with Herceptin. HER2 overexpressing BT-474 human breast cancer-bearing nude mice treated with the targeted construct showed complete tumour regression without increased selectivity compared to no tumour inhibition for the untargeted control.[353] HER2 was also conjugated to Doxorubicin-containing liposomes by

Kirpotin *et al.* and they showed that intracellular uptake increased by 6-fold in BT-474 breast tumours and improved treatment responses; however, the overall tumour accumulation did not differ greatly between the untargeted control and the targeted construct.[354] Similar results were obtained for other targeting antibodies. EGFR-targeted liposomes[355] and Transferrin-targeted polymeric nanoparticles[356] showed a greater therapeutic response against tumours compared to their untargeted counterparts but again without evidence of increased delivery or selectivity. Untangling the effects of the EPR effect and molecular targeting is the key challenge in the development of precision medicine and molecular targeted therapies and can only be achieved by defining the nuances between cellular uptake and tumour localisation.

5.1.3 Radiosensitisers

Radiation therapy is a conventional treatment for some cancers. The underlying principle is that ionising radiation interacts with water to induce radiolysis and the production of reactive oxygen species including hydroxyl radicals, hydrogen peroxide, and superoxide radicals. A major drawback of classic PDT is limited tissue penetration, as discussed in Chapter 1. One possible approach to overcoming this is the use of X-rays to activate the therapeutic response. Additionally, the combined effect of reactive oxygen species and radiation therapy, at least in theory, leads to lower required doses; thus, reducing damage to healthy tissue.

X-rays are capable of activating molecules known as radiosensitisers. Among other molecules,[357] some classic free base porphyrin photosensitisers are active radiosensitisers. In 1957, Mack *et al.* studied a group of 25 patients (twenty-four patients with squamous-cell carcinoma of the cervix and one patient with adenocarcinoma of the cervix) receiving radium or Röntgen-ray treatment with an additional injection of Hp prior to therapy. Overall, he noted increased tolerance and faster response time but not an extension of life.[358] In 1966, Cohen and Schwartz investigated HpD, copper HpD, and a copper HpD nitrate as potential radiosensitisers. They injected rhabdomyosarcoma-bearing mice with 0.01, 0.05, 0.25, or 1.25 mg/kg of the porphyrin before X-ray radiation (2.30×10^{-2} Gy/s, 24.12 Gy). At 0.05 mg, complete regression occurred for the period of the study (84–86 days) with HpD or copper HpD.[359] In a series of more recent publications, the Schaffer group showed that Photofrin is a promising radiosensitiser. In

2001, human bladder cancer cell line RT4-bearing mice were treated with 10 mg/kg of Photofrin and irradiated with X-rays (5 Gy). Photofrin treated mice responded following X-ray radiation with a tumour volume doubling time of 6.2 days compared to 10.9 days for the control group.[360] This was followed by a case study involving two patients. The first had unresectable bladder cancer and the second had recurrent inoperable bladder cancer. 24 h before radiation therapy (44.8 Gy + 14 Gy) they were administered 1 mg/kg of Photofrin. The results showed a 40% and 35% reduction in tumour volume for patients one and two, respectively.[361] In another example, Kulka *et al.* used colony-forming assays to test human bladder cancer (RT4), colon adenocarcinoma (HT-29), and glioblastoma (U-373 MG) cell lines for radiosensitivity. The cells were incubated with Photofrin prior to X-ray radiation (0.9 Gy/min, 0 to 8 Gy). The RT4 and U-373 MG cell lines under this treatment showed lower cell survival when compared to cells irradiated with X-ray alone. However, significant differences were not noted in the case of HT-29 cells under the same conditions.[362] Promising as this sounds, it should also be noted that radioprotective responses, under some conditions, are also reported in the literature. In one example, while investigating whether Hp could modify the sensitivity of NHIK 3025 cells to X-ray radiation under aerobic and hypoxic conditions, Moan *et al.* found that Hp (0.5 or 0.7 mM) had no effect on X-ray-irradiated (2.1 Gy/min, 0 to 50 Gy) aerobic cells and even had a radioprotective effect on X-ray irradiated hypoxic cells.[363]

Protoporphyrin IX has also proved itself capable of effecting the radiosensitivity of some cell lines and tissues. Takahashi and co-workers have worked extensively in this field.[364,365] In one study, they found that rat glioma cells (9L) incubated with 5-ALA (1 mM) and then treated with X-ray (0.8 Gy/min, 8 Gy) showed a reduced capacity for colony-forming when a single-dose was used. Both 9L and C6 rat glioma cells displayed radiosensitivity after multiple radiation doses. Confocal laser scanning microscopy was also used to confirm reactive oxygen specie production following X-ray treatment in the 9L cells.[366] In another study, they investigated clonogenic survival in HeLa cells incubated with 5-ALA and treated with X-ray irradiation (1 Gy/min, 3 Gy). They found that HeLa cells were sensitised to the treatment and, interestingly, that the expression of genes related to cell-cycle arrest and inhibition of DNA replication were altered. X-ray treatment alone and X-ray treatment with protoporphyrin IX displayed different gene expression profiles but the same overall qualitative gene expression. The increase in cellular reactive oxygen species was used to account for the difference in survival

outcomes. In a related study, they showed that 24 h later, HeLa cells treated with 1 μg/mL of protoporphyrin IX prior to radiation exposure (3 Gy) demonstrated a 70% loss of their clonogenic ability, with X-ray alone the number was only 50%.[364,365] A similar positive therapeutic response was reported for B16-BL6 melanoma cells and the study was then transitioned into an *in vivo* model. B16-BL6 tumour-bearing mice were found to be resistant to radiation and 5-ALA alone but when injected with 50 mg/kg of ALA 24 h prior to fractional irradiation (3 Gy × 10, 30 Gy), tumour suppression improved.[367,368]

The mechanism of action for radiosensitisers is not completely understood but does involve the generation of reactive oxygen species.[369] In 2000, Bistolfi proposed a dual mechanism for HpD radiosensitisation that involved the lipid peroxidation of biomembranes due to the formation of reactive oxygen species. He posed that the underlying mechanism relied on the emission of red light and water radiolysis.[370] For Photofrin, it was proposed that hydroxyl radicals were involved, resulting in the failure of repair mechanisms following ionising radiation damage that was insufficient to cause cell death.[371]

5.2 OBJECTIVES

Liposomes are biocompatible nanoconstructs capable of chemical modification to optimise the delivery of drugs. In this project, we aimed to synthesise multifunctional targeted liposomes for medical applications. We aimed to achieve this by lipid film synthesis, hydration, and extrusion techniques to formulate the liposomes and the incorporation of clinically approved Vertoporphyrin (BPD) and/or its lipidated derivative, benzoporphyrin derivative 20:0 lyso phosphocholine (BPD-PC), into the lipid bilayer. It was envisioned that the lipids would then be modified by employing click chemistry to introduce the EGFR inhibitor, Cet, to actively target overexpressing cells. In some cases, we aimed to also use active loading to incorporate the chemotherapeutic drug, Irinotecan (sold as Onivyde in a liposomal formulation).

We aimed to investigate our targeted systems for biomedical applications by evaluating the Irinotecan and BPD-PC-containing construct *in vivo* using an orthotopic pancreatic cancer model and ultrasound imaging to monitor tumour size and follow survival. We aimed to compare our constructs to the clinically relevant Visudyne and Onivyde regimes and to investigate the effect of multi-dose *vs.* single-dose treatments. Finally, we planned to employ histology to evaluate the potential therapeutic advantages of the targeted constructs over Visudyne.

In another subproject, we aimed to investigate the used of X-ray radiation to excite BPD and BPD-PC molecules in our targeted constructs and to investigate how this affects therapeutic efficiency, with the ultimate goal of designing a PDT-radiation therapy. We also aimed to image BPD-PC fluorescence using confocal microscopy to evaluate the targeting effect of our constructs. We aimed to use singlet oxygen, hydroxyl radicals, and pernitrate probes to identify the active species and then evaluate these systems *in vitro* using spheroids of head and neck cancer cell lines, Fadu, TR147, and SCC14.

5.3 RESULTS AND DISCUSSION††

5.3.1 Near-infrared light-active targeted liposomes

Near-infrared light-active targeted liposomes were synthesised as part of a wider study employing targeted nanoconstructs to distinguish between target-specific interactions and general uptake mechanisms, including the EPR effect, by quantifying specific interactions *in vivo*.[372]

To this end, we prepared liposomes consisting of DPPC (58.2 mol%), 1,2-dioleoyl-sn-glycero-3-phospho-rac-(1-glycerol) (DOPG, 7.9 mol%), cholesterol (28.9 mol%), DSPE-N-polyethyleneglycol-2000 (DSPE-mPEG2000, 4.3 mol%), DSPE-mPEG2000-DIBO (DIBO = dibenzocyclooctyne, 0.5 mol%), and DSPE-mPEG2000-NH_2 (0.2 mol%), which were extruded through a 100 nm polycarbonate membrane. This was followed by amide bond formation between IRdye-N-Hydroxysuccinimide (680 or 800 nm) and DSPE-mPEG2000-NH_2. The mol% of IRdye with respect to lipid content was found to be 0.013 ± 0.02% and 0.018 ± 0.003% for IRdye680 and IRdye800 nm, respectively. The final synthetic step employed copper-free azide chemistry between DSPE-mPEG2000-DIBO and an antibody conjugated to a fluorescent dye (IgG-AF488-PEG-N_3 or Cet-AF488-PEG-N_3, 50 eq., AF488= Alexafluor488), with efficiencies of 47.3% for Cet and 47.5% for IgG (constructs **5.1** and **5.2**). This was calculated by measuring the IR dye concentration using UV-vis, antibody concentration using Alexafluor488 fluorescence emission, and the mean liposome hydromantic size (**Fig. 5.1**–**5.3**). As a result, 23.8 Cet molecules per liposome and 23.6 IgG molecules per liposome were obtained. This degree of antibody conjugation has previously been reported as optimal for physiological conditions.[373,374] The Cet-functionalised liposomes were used as the active construct with targeting mediated by specific EGRF interactions.[375] In contrast, the IgG-containing liposomes were used as a comparison for non-specific interactions.

†† Contributions to the results in this chapter were made by Prof. G. Obaid, Dr. Ding, Dr. S. Bano, and J. Swain. The research was undertaken in the laboratory of Prof. Tayyaba Hasan.

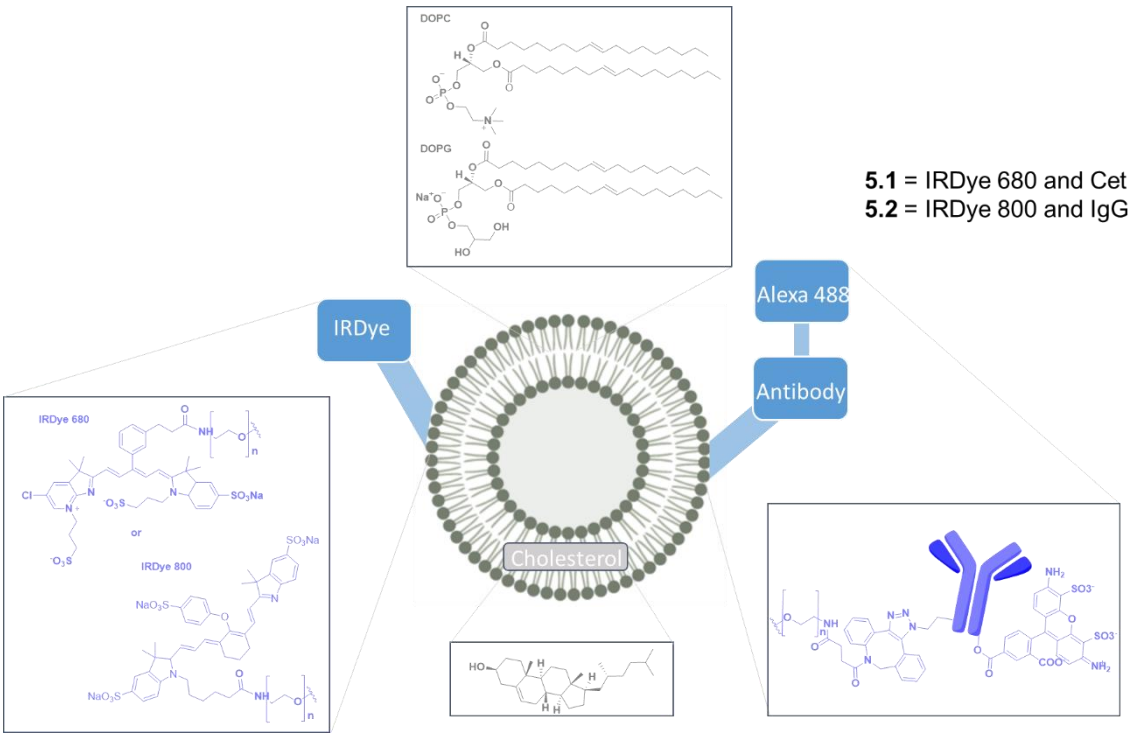

Figure 5.1: Schematic illustration of near-infrared light-active targeted liposomes, **5.1** (IRDye 680 and Cet), **5.2** (IRDye 800 and IgG), (IR = Irinotecan, Cet = Cetuximab, IgG = immunoglobulin G).

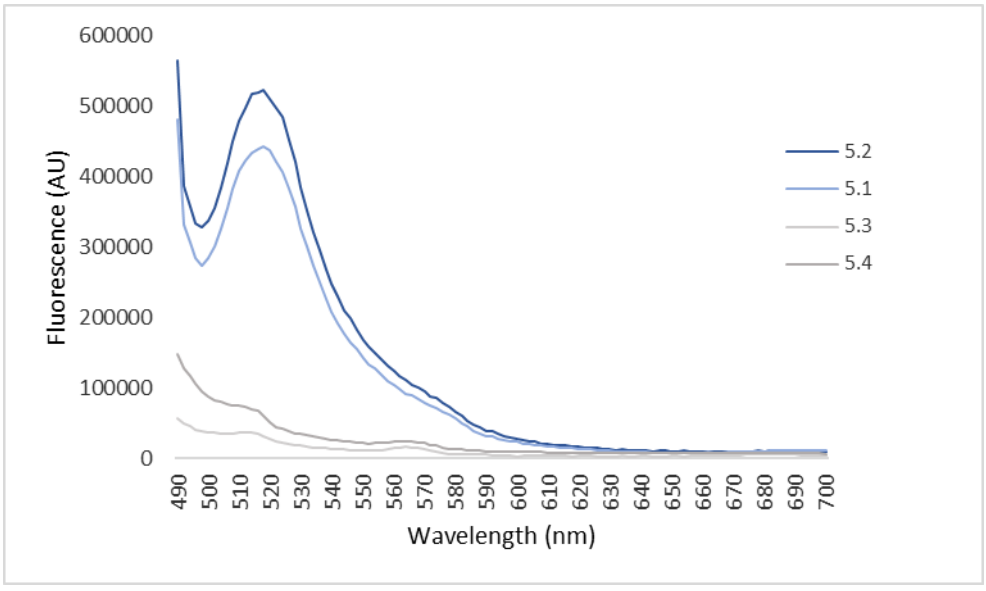

Figure 5.2: Fluorescence emission spectra (ex. 480 nm) of **5.1**– **5.4** at IR dye concentration of 10 nM in phosphate-buffered saline (PBS).

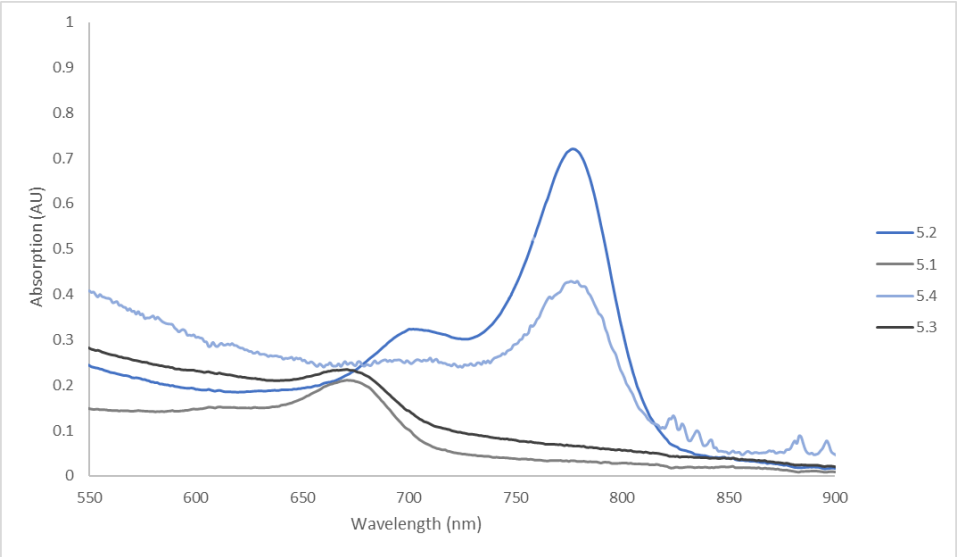

Figure 5.3: Absorption spectra of **5.1**–**5.4** at IR dye concentration of 10 µM in PBS.

For the current work, two parameters were studied. Firstly, the stability of the constructs post-synthesis was followed for a period of 40 d using dynamic light scattering. We monitored the mean polydispersion index to record changes in liposome size or aggregation and to assess the stability of the constructs. As presented in **Fig. 5.4**, the constructs remained stable for this duration. Additionally, the intensity weighted mean hydrodynamic size remained constant over the same period (**Fig. 5.4**), further indicating the stability of the constructs.

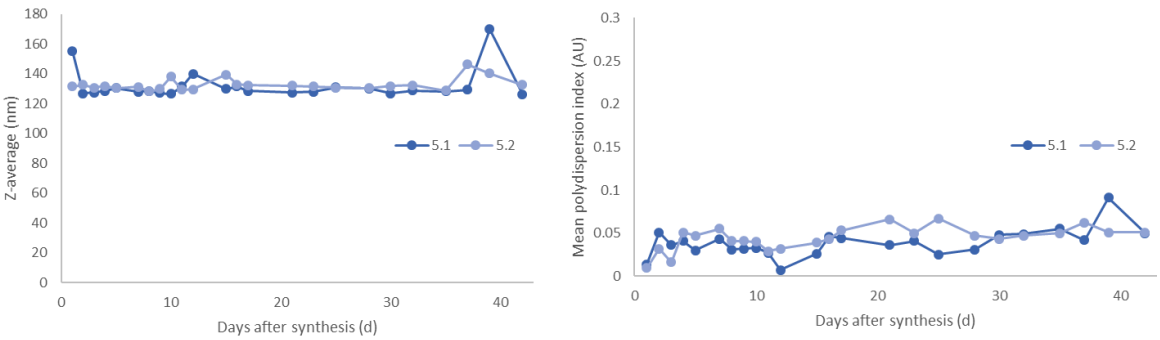

Figure 5.4: Near-infrared light-active targeted liposome stability. Changes in mean polydispersion index (PDI, right) and intensity weighted mean hydrodynamic size/Z-average (left) up to 40 d after synthesis.

The second parameter, the degree of opsonisation, was investigated because this property has potential implications on the biological activity of the constructs. Opsonisation can lead to a protein corona forming around the constructs, which may inhibit their activity. Particularly relevant to this study is that IgG is a reported dysopison[376] while Cet is not, which may affect the interactions of our specific and non-specific constructs.

Thus, to investigate whether opsonisation occurs with our constructs *in vivo*, we mixed untargeted constructs, **5.3** and **5.4**, **Fig. 5.5**, with IgG-AlexaFlour488-PEG-N_3 or Cet-AlexaFlour488-PEG-N_3 for 24 h at the same concentration (1 mg/mL)[377] as is found for IgG in *in vivo* serum. Following purification (sepharose CL-4B column using phosphate-buffered saline (PBS) as eluent), the fluorescence intensity of Alexafluor488 and absorbance of the IRDyes were used to determine the amount of antibody per liposome (**Fig. 2** and **Fig. 3**). It was concluded that negligible opsonisation occurred in our system with 0.14% protein-to-lipid content or 1.19 IgG molecules per construct. For comparison, a value of 0.41 Cet molecules per nanoconstruct was also calculated.

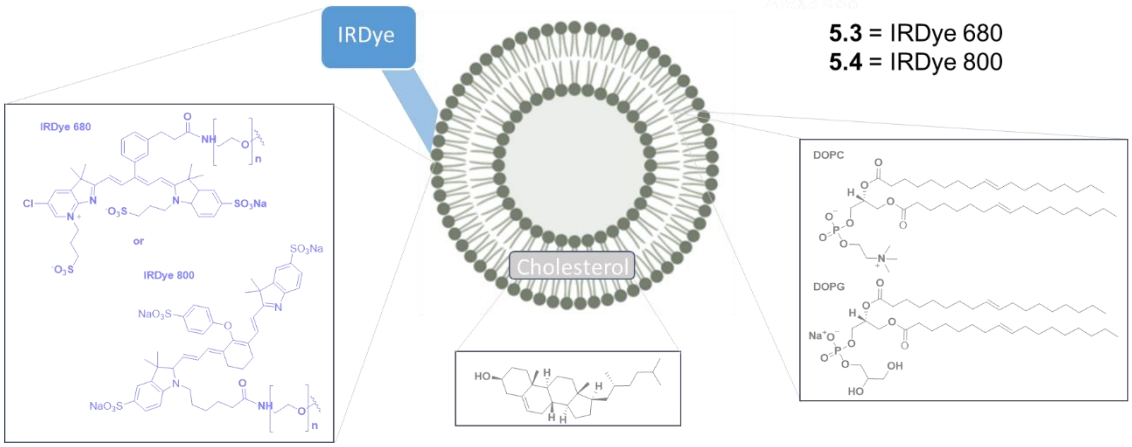

Figure 5.5: Schematic illustration of near-infrared light-active untargeted liposomes, **5.3** (IRDye 680) and **5.4** (IRDye 800).

5.3.2 Targeted photoactivatable multi inhibitory liposomes

We designed targeted photoactivatable multi-inhibitory liposomes (TPMIL, Fig. **5.6**, construct **5.5**) that can facilitate the delivery of both PDT and chemotherapeutic drugs (approximately 600 BPD-PC molecules per liposome and 16,000 Irinotecan molecules per liposome). BPD-PC is a lipidated derivative of BPD and was chosen to maximise inclusion in the liposome bilayer. The increased inclusion efficiency is mediated by Van der Walls interactions between the lipid chain of BPD-PC and the hydrophobic tail of the bilayer phospholipids. The construct is anchored with Cet to target EGFR over-expressing[378] pancreatic tumour cells and contains negatively charged DOPG molecules to maintain consistent uptake across varying EGFR-expressing cells.[379] We designed this construct to undergo photodynamic priming to increase drug delivery by changing the tumour microenviroment.[380]

TPMIL were prepared over a multi-step formulation. First, 1,2-distearoyl-sn-glycero-3-phosphocholine (DSPC, 53.2 mol%) doped with DSPE-mPEG (0.3 mol%), cholesterol (45.9 mol%), and BPD-PC (0.6 mol%) were used to prepare a lipid film, which was hydrated using EtOH and ammonium sulfate solution, followed by 5 freeze-thaw cycles. Then, the solution was extruded through two 100 nm polycarbonate membranes to obtain a standard liposome size. The liposomes were purified to remove free BPD-PC using size exclusion chromatography. Irinotecan in chloroform (20 mg/mL) was actively loaded into the core of the liposomes using heating at 65 ˚C for 30 min. In parallel, liposomes with 4.2% PEG surface coverage were prepared from DSPE-mPEG and DOPG and post inserted into the Irinotecan-containing liposomes at 65 ˚C for 60 min, followed by dialysis against HEPES saline for 24 h. In the final step of the formulation, Cet was introduced for targeting. DSPC-PEG2000-DIBO micelles were formulated in HEPES-saline and AF488-Cet-PEG-N_3 was conjugated using click chemistry. These micelles were post-inserted into the Irinotecan-containing liposomes at 37 ˚C for 12 h. The final Irinotecan percentage encapsulation was calculated to be 70% (using Irinotecan absorbance at 384 nm) and a value of 30 Cet per liposome was calculated using the fluorescence signal of Alexaflour488 (**Fig. 5.7**) and the polydispersion index. The nanoparticle size varied between 120-130 nm and was measured using dynamic light scattering.

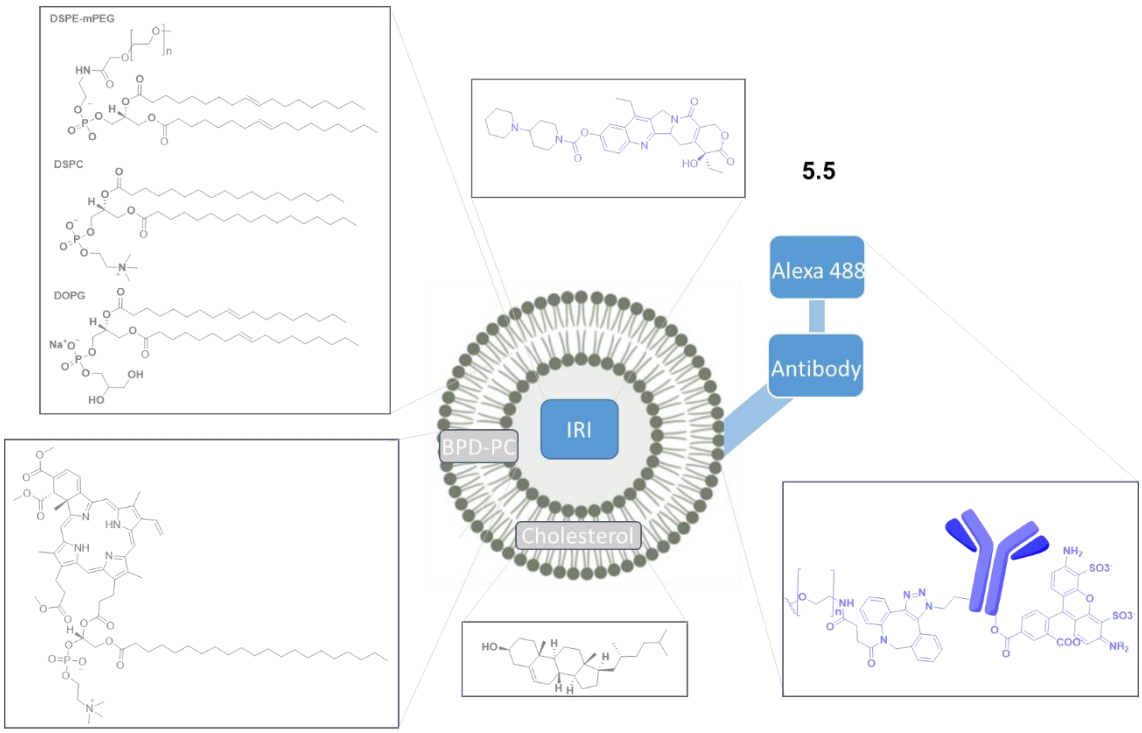

Figure 5.6: Schematic illustration of targeted photoactivatable multi-inhibitory liposomes (TPMIL), **5.5**. (IRI = Irinotecan, BPD-PC = benzoporphyrin derivative 20:0 lyso phosphocholine).

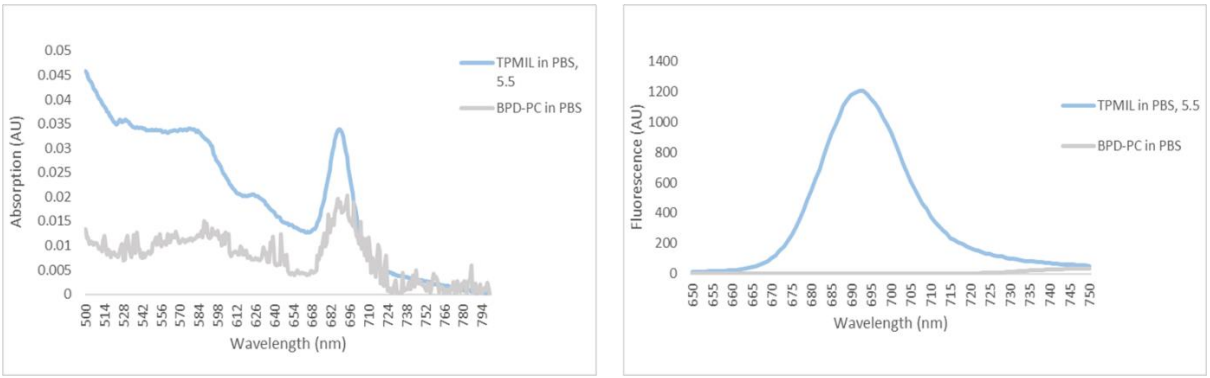

Figure 5.7: Absorption (left) and fluorescence (right) spectra of TPMIL, **5.5** and BPD-PC in PBS at a concentration of 5 µM. Fluorescence spectra were taken at an excitation wavelength of 435 nm.

The absorption and fluorescence profiles of TPMIL, **5.5** and BPD-PC confirm that BPD-PC molecules are more photoactive in the liposomal formulation compared to the free photosensitiser with approximately 40% quenching of BPD-PC absorbance in the free porphyrin compared to the liposomal formulation in aqueous PBS. **Fig. 5.8** shows that free BPC-PC is active in DMSO but not in PBS.The fluorescence

spectra in **Fig. 5.7** show that the fluorescence of BPD-PC at an excitation wavelength of 435 nm is completely quenched in PBS but a 1200 AU increase in fluorescence signal is observed in the TPMIL construct. This is attributed to the lipid bilayer preventing aggregation of the π-systems in aqueous media and is expected to contribute to successful photoactivation of the construct.

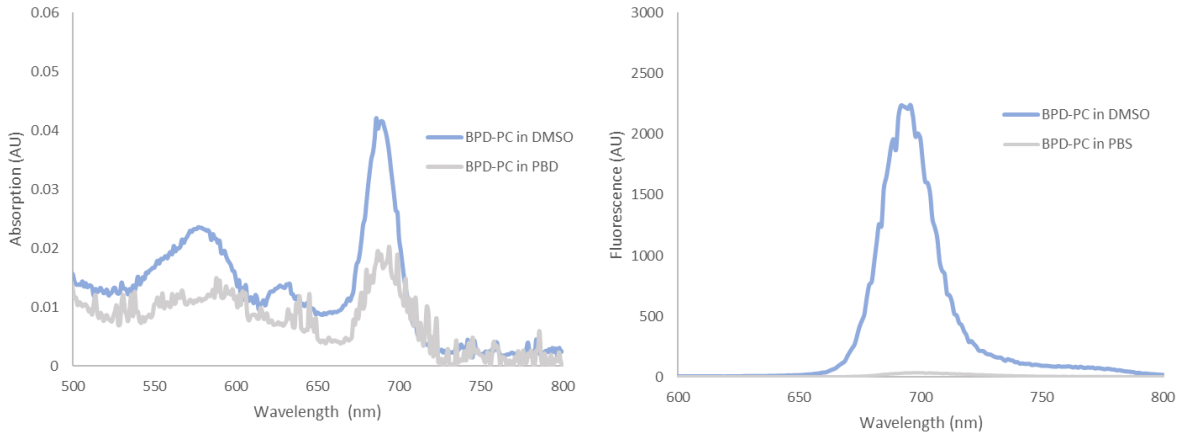

Figure 5.8: Right: Absorption Left: Fluorescence emission (ex. 435 nm) of BPD-PC in DMSO and PBS at a concentration of 5 µM.

An *in vivo* evaluation of the TPMIL construct was then undertaken. On day zero 6-week-old male Swiss nude mice were sedated with 100 mg/kg of ketamine and 10 mg/kg of xylazine. A small left abdominal flank incision was made to exteriorize the pancreas. The pancreas was implanted (orthotropic injection) with a 70 µL solution of 50% matrigel and culture media, 25% MIAPACA-2 (1×10^6), and 25% PCAF (1×10^6) cells. The incision was sutured and 10% povidone/iodine was applied to prevent infection.

On day 9, when the tumour volumes had reached 25 mm^3, the mice were randomised into treatment groups: low-dose TPMIL, high-dose TPMIL, Visudyne and Onivyde (low-dose TPMIL eq.), Visudyne and Onivyde (clinical eq.),[381,382] and high-dose Visudyne. Visudyne and Onivyde are clinical liposomal formulations of BPD and Irinotecan, respectively, and were included for comparison. Additionally, an untreated control group was included in the study.

The experimental mice were injected intravenously (tail vein) with 200 µL of sterile PBS and active agent. For PDT, the tumour was exposed with a small left flank incision. The mice treated with Visudyne were irradiated with the appropriate light dose 1 h after injection and the mice treated with TPMIL were irradiated 24 h after injection, both using NIR light (690 nm diode laser). Ultrasound imaging was used to determine the dimensions of the tumours following implantation (**Fig. 5.9**). The dimensions of the tumour were noted and volume was determined using the ellipsoid formula:

$$\text{volume} = (\pi \times L \times W \times H)/6$$

, where L, W, and H, are the tumour length, width, and height (**Fig. 10** and **Fig. 11**).

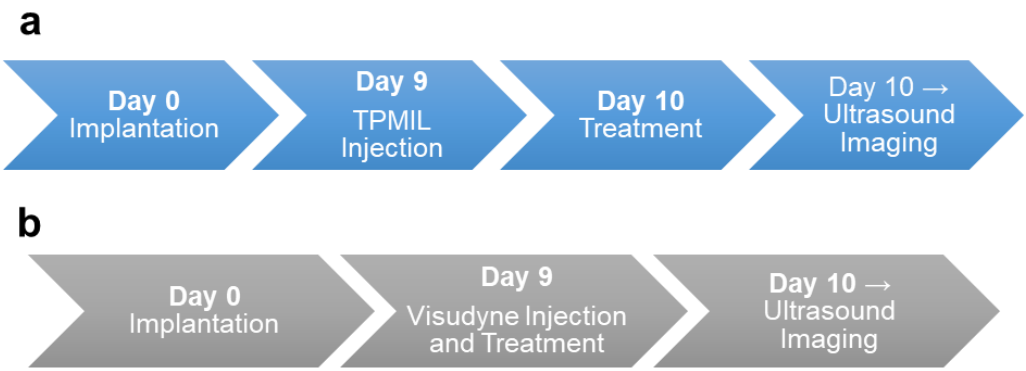

Figure 5.9: Experimental timeline for a) single-dose TPMIL and b) Visudyne experiments.

Fig. 5.10 shows tumour volumes *vs.* days following implantation. The experimental groups treated with low-dose TPMIL, Visudyne and Onivyde (low-dose TPMIL eq.), and Visudyne and Onivyde (clinical eq.) all showed inhibited tumour growth when compared with the untreated control group. Low-dose TPMIL displayed tumour inhibition for 80 days compared with observed regrowth after 30 days for Visudyne and Onivyde (both clinical and TPMIL eq.). A p-value of 0.0354 was calculated between the untreated and low-dose TPMIL groups. The difference in therapeutic response between Visudyne and Onivyde and TPMIL is attributed to both Cet targeting and the synergetic effect between Irinotecan and the photosensitiser.

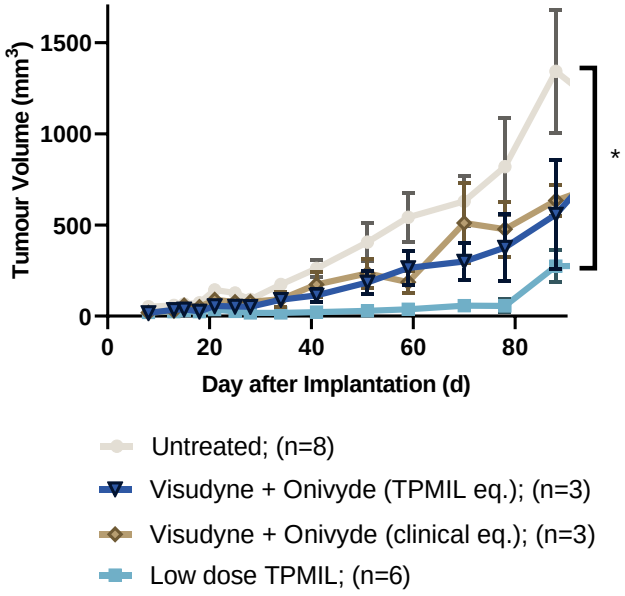

Figure 5.10: Tumour volume *vs.* days after implantation of treatment groups: low-dose TPMIL (0.25 mg/kg BPD + 50 J/cm^2 (4mg/kg Irinotecan)), Visudyne and Onivyde (low-dose TPMIL eq., 0.25 mg/kg + 50 J/cm^2 + 4 mg/kg Onivyde), Visudyne and Onivyde (clinical eq., 0.25 mg/kg + 50 J/cm^2 + 20 mg/kg Onivyde), and untreated. p-value * = 0.0354.

Moreover, low-dose TPMIL has a similar effect to high-dose Visudyne with both showing regrowth after day 80 (**Fig. 5.11**). Significantly, low-dose TPMIL has one third less BPD and a lower light dose than high-dose Visudyne. When the high-dose TPMIL and high-dose Visudyne treatments were compared, 50% more survival was observed 72 h following treatment with TPMIL compared to Visudyne (**Fig. 5.12**). This provides evidence for the benefits of cellular targeting in the TPMIL construct as the treatment is less toxic to healthy tissue, resulting in less organ damage and ultimately higher survival even at high-doses.

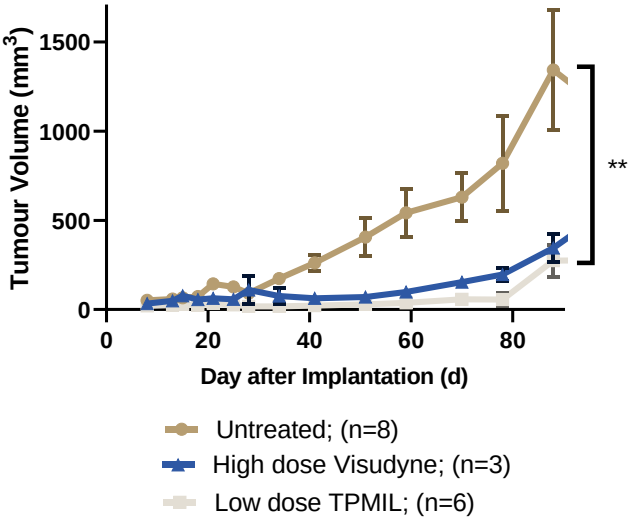

Figure 5.11: Tumour volume *vs.* days after implantation of treatment groups: Untreated, low-dose TPMIL (0.25 mg/kg BPD + 50 J/cm^2 (4 mg/kg Irinotecan), and high-dose Visudyne (0.75 mg/kg + 150 J/cm^2, n=6). p-value ** = 0.0067.

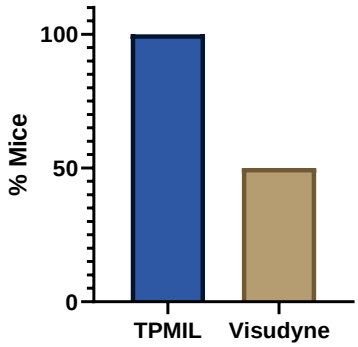

Figure 5.12: Animal survival 72 h after high-dose TPMIL (0.75 mg/kg + 150 J/cm^2 and 12 mg/kg Irinotecan, n=3) or high-dose Visudyne (0.75 mg/kg + 150 J/cm^2, n=6).

The observed lower toxicity in TPMIL *vs.* Visudyne at the same high BPD and light dose was further confirmed by histology studies. Mice treated with high-dose TPMIL and high-dose Visudyne were sacrificed after 72 h to visualise photodamage in the pancreas. The sections were stained with hematoxylin and eosin[‡‡] staining and images were obtained on a Hamamatsu NanoZoomer. **Fig. 5.13** (left) displays an

[‡‡] Hematoxylin and eosin stains were performed by the photopathology core at the Wellman Center for Photomedicine, Massachusetts General Hospital.

image of a pancreas section from an animal treated with high-dose TPMIL and localised tumour cell death is observed, while on the right, an image of a pancreas section from an animal treated with high-dose Visudyne is displayed. In this image, cell death is observed across a larger section, including significant areas of the pancreas. This is consistent with the 72 h survival study (**Fig. 12**) and provides evidence for the advantages of Cet targeting. Clearly, less damage to surrounding tumour tissue is observed for targeted TPMIL construct treatment compared to Visudyne treatment. The lower survival can be attributed to increased organ damage as a result of the high-dose Visudyne regime.

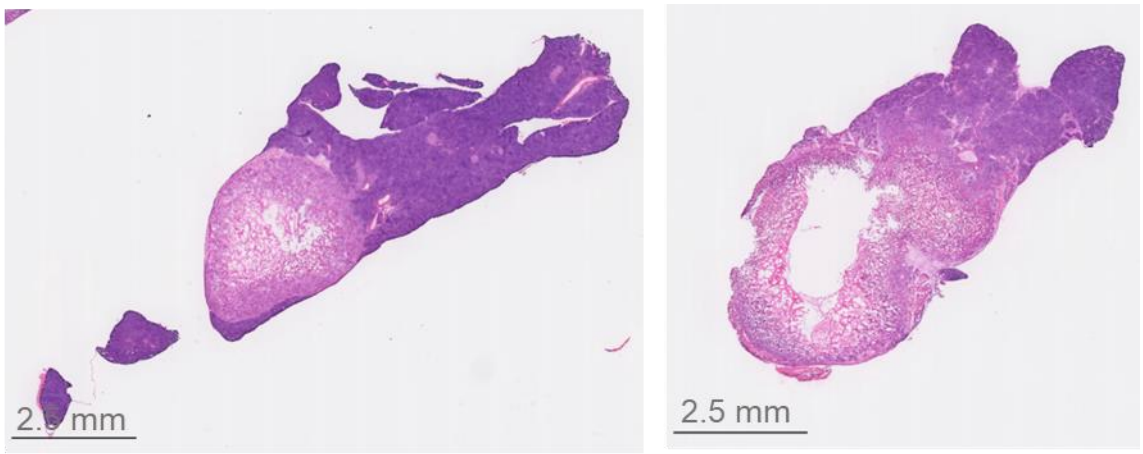

Figure 5.13: Hematoxylin and eosin staining of pancreatic histology sections. Scale bar = 2.5 mm, Left: TPMIL 0.75 mg/kg + 150 J/cm^2 (12 mg/kg Irinotecan), Right: Visudyne 0.75 mg/kg + 150 J/cm^2.

To summarise, the efficiency of the TPMIL construct was evaluated by comparing the tumour volumes of several treatment groups at day 78 after implantation. We can see that there is significant (p-value = 0.0445) tumour growth inhibition when low-dose TPMIL was used compared to the untreated group. Additionally, animals treated with low-dose TPMIL present lower tumour volumes than those treated with high-dose Visudyne, Visudyne and Onivide (TPMIL eq.), or Visudyne and Onivide (clinical eq.), indicating that the targeted delivery system can reduce the required drug doses as well as reducing the overall toxicity (**Fig. 5.14**).

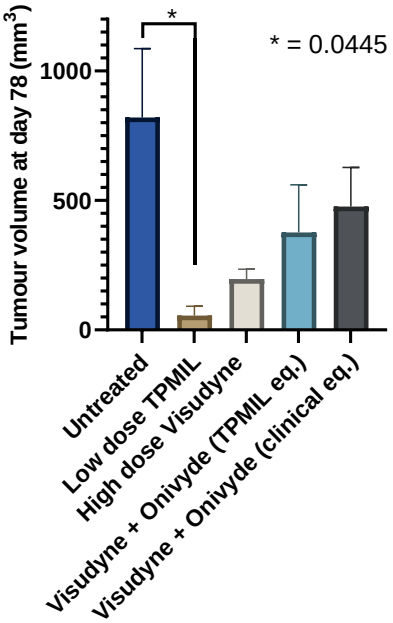

Figure 5.14: Tumour volumes at day 78 after no treatment, low-dose TPMIL: 0.25 mg/kg BPD + 50 J/cm^2 (4 mg/kg Irinotecan), high-dose Visudyne: 0.75 mg/kg + 150 J/cm^2, Visudyne + Onivyde (low-dose TPMIL eq.): 0.25 mg/kg + 50 J/cm^2 (4 mg/kg Onivyde), and Visudyne + Onivyde (clinical eq.): 0.25 mg/kg + 50 J/cm^2 (20 mg/kg Onivyde). p-value * = 0.0445.

Finally, to investigate whether photodynamic priming can influence drug delivery and the therapeutic response of the TPMIL system, we compared the outcome of single-dose treatments to three-cycle treatments. MIAPACA-2 and PCAF cells were cultured, as before, and the mice were implanted, three were administered single cycle low-dose TPMIL and a further six mice we treated with TPMIL three times at either 72 h or 7 d intervals. The tumour volumes were monitored using ultrasound imaging, as before. The experimental timeline is shown in **Fig. 5.15**. All treatment arms show tumour inhibition up to 80 days' post-implantation. The 72 h arm does show a slightly better response when compared to the 7 d arm and this may be due to priming of the tumour environment by the initial PDT treatment; however, there is no significant difference between the single and multiple-dose arms up to 80 days (**Fig. 5.16**). As the multiple treatment arms have only three mice per group, the next step will be to repeat this experiment with more animals to clearly define the advantages, if any, of multiple-dose TPMIL regimes.

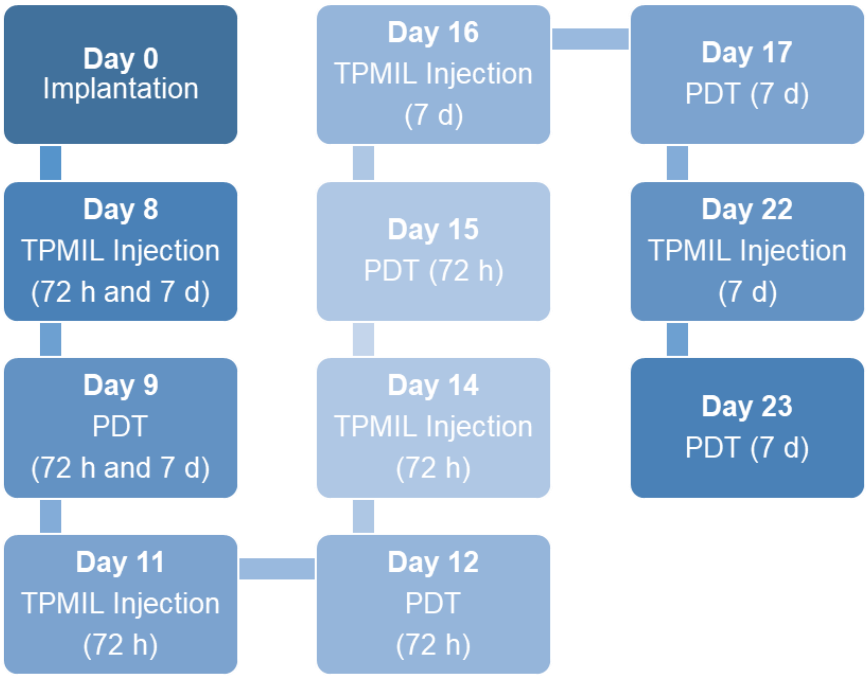

Figure 5.15: Schematic illustration of the experimental timeline for the single-dose TPMIL and multiple-dose TPMIL experiments.

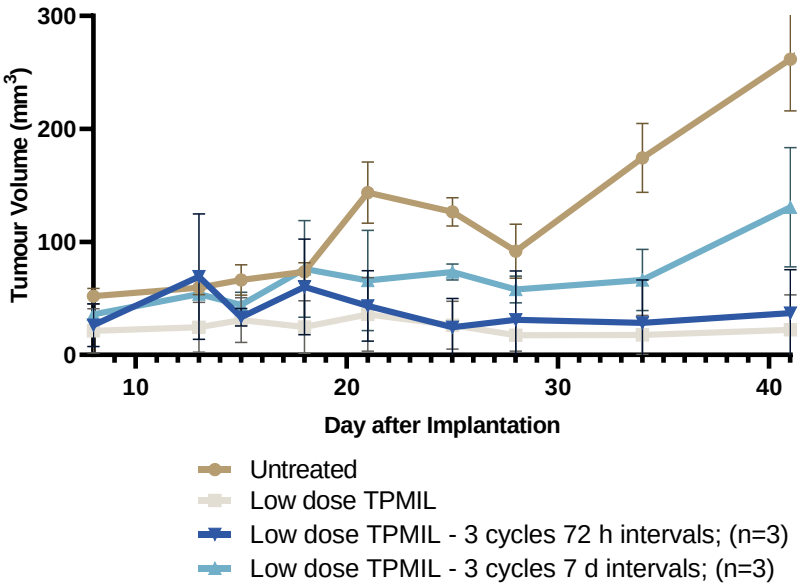

Figure 5.16: Tumour volume *vs.* days after implantation of treatment groups: Untreated, single low-dose TPMIL (0.25 mg/kg BPD + 50 J/cm^2 (4 mg/kg Irinotecan), 3 cycle low-dose TPMIL (0.25 mg/kg BPD + 50 J/cm^2 (4 mg/kg Irinotecan) treatments at 72 h intervals, and 3 cycle low-dose TPMIL (0.25 mg/kg BPD + 50 J/cm^2 (4 mg/kg Irinotecan) treatments at 7 d intervals.

5.3.3 BPD-containing targeted liposomes

In a related project, we also synthesised targeted liposomal formulations that contained BPD-PC. BPD-PC is known to redirect photodamage to the lysosomes and has been shown to be active against ovarian cancer when used in a liposomal formulation.[383] Moreover, we aimed to investigate the activation of BPD-PC by X-ray *in vitro* (Fadu, SCC14, and TR-146 spheroids) and compare the results to light activation. Again, we conjugated Cet to target EGFR and compared targeting effects against the untargeted control.

The liposomes were formulated from DPPC (57.6 mol%) doped with DOPG (7.9 mol%), cholesterol (28.9 mol%), DSPE-mPEG2000 (4.5 mol%), DSPE-mPEG2000-DIBO (0.5 mol%), and BPD-PC (0.5 mol%). The mixture was dried *in vacuo* and then rehydrated with PBS. The solution was then extruded through two 100 nm polycarbonate membranes to yield the untargeted construct. The untargeted liposomes were reacted with a Cet-Alexa488-PEG-N_3 solution at a concentration of 4.2 mg/mL (100 eq.) and stirred at rt overnight on rotation to obtain the targeted analogues. The antibody to liposome ratio was calculated to be between 20-30 using the fluorescence signal of Alexa488 and the polydispersion index. The constructs were purified using size exclusion chromatography. **Fig. 5.17** and **Fig. 5.18** show schematic illustrations of the targeted and untargeted systems. In later experiments, we altered the mol% of BPD-PC (0.6 mol% and 2 mol%) but the formulation approach remained the same. The nanoparticle size varied between 116–143 nm for constructs **5.6**–**5.11** and was measured using dynamic light scattering.

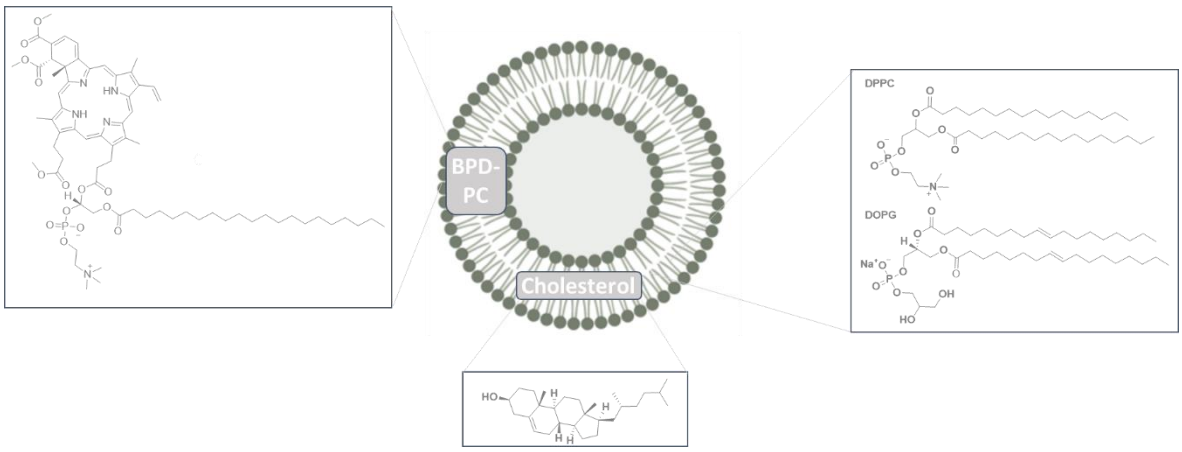

Figure 5.17: Components of untargeted BPD-PC containing liposomes, **5.6** (0.5 mol% BPD-PC), **5.7** (0.6 mol% BPD-PC), and **5.8** (2 mol% BPD-PC). (BPD-PC = benzoporphyrin derivative 20:0 lyso phosphocholine).

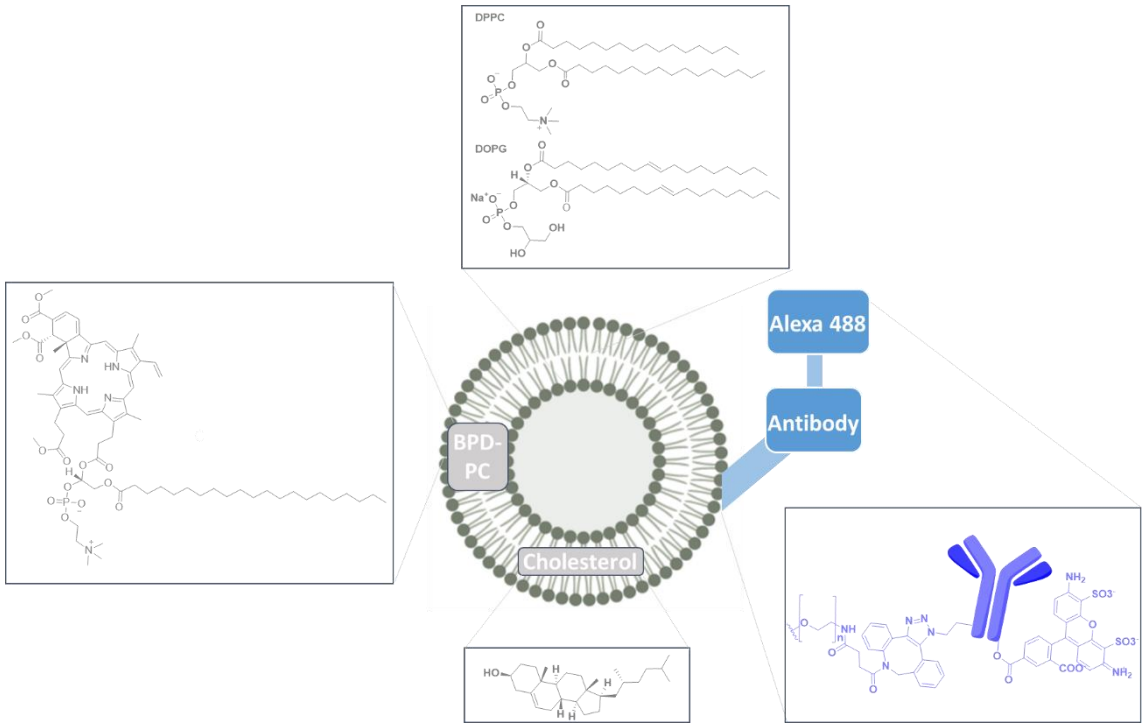

Figure 5.18: Components of targeted BPD-PC containing liposomes, **5.9** (0.5 mol% BPD-PC), **5.10** (0.6 mol% BPD-PC), and **5.11** (2 mol% BPD-PC). (BPD-PC = benzoporphyrin derivative 20:0 lyso phosphocholine).

Similar to the TPMIL formulation, the absorption and fluorescence spectra of constructs **5.6**–**5.11** show that BPD-PC is photophysically active in the liposomal formulations but is quenched in its free form, when in PBS (**Fig. 5.19** – **Fig. 21**).

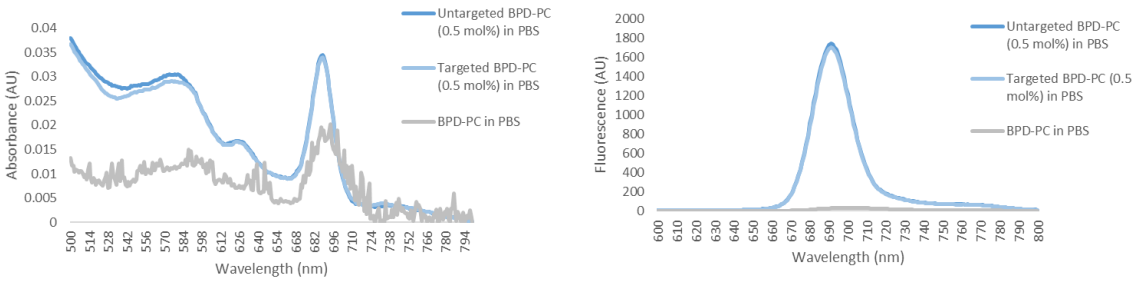

Figure 5.19: Right: Absorption Left: Fluorescence emission (ex. 435 nm) of **5.6** (untargeted 0.5 mol% BPD-PC), **5.9** (targeted 0.5 mol% BPD-PC), and free BPD-PC in PBS at a concentration of 5 µM. (BPD-PC = benzoporphyrin derivative 20:0 lyso phosphocholine, PBS = phosphate buffered saline).

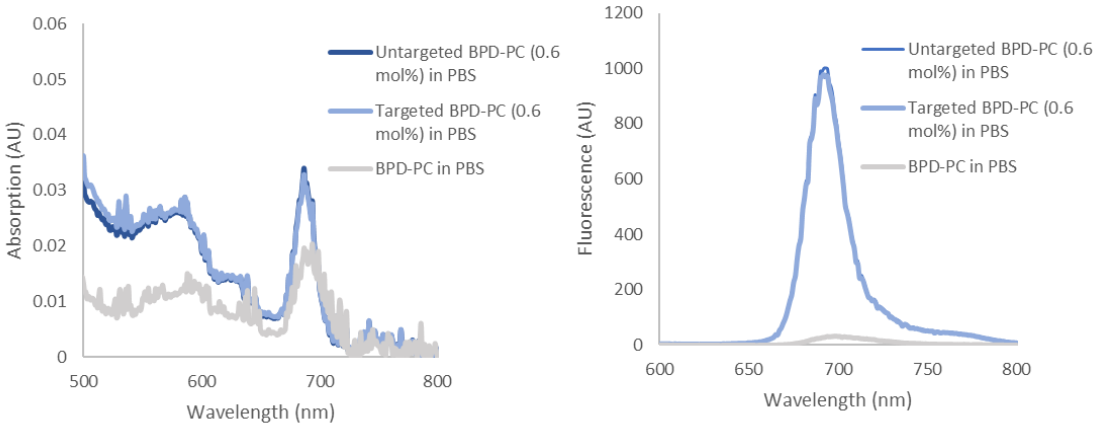

Figure 5.20: Right: Absorption Left: Fluorescence emission (ex. 435 nm) of free BPD-PC and BPD-PC in targeted and untargeted 0.6 mol% constructs, **5.7** and **5.10**. Spectra measured in PBS at a concentration of 5 µM. (BPD-PC = benzoporphyrin derivative 20:0 lyso phosphocholine, PBS = phosphate buffered saline).

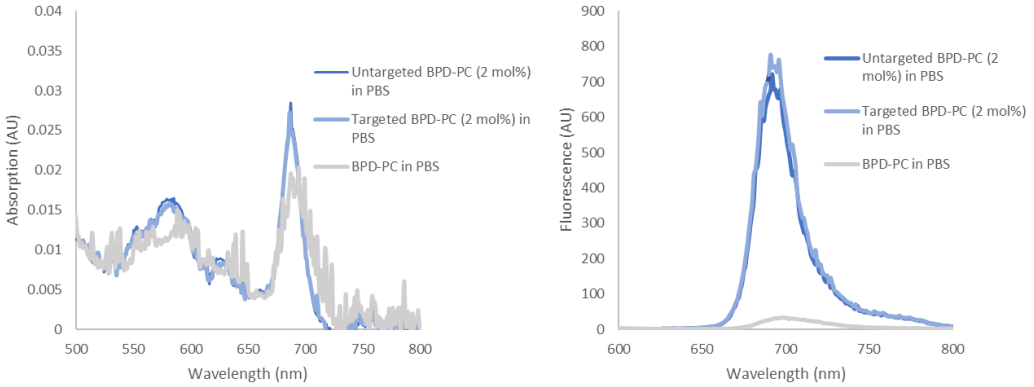

Figure 5.21: Right: Absorption. Left: Fluorescence emission (ex. 435 nm) of **5.8** (untargeted 2 mol% BPD-PC), **5.11** (targeted 2 mol% BPD-PC), and free BPD-PC in PBS at a concentration of 5 µM. (BPD-PC = benzoporphyrin derivative 20:0 lyso phosphocholine, PBS = phosphate buffered saline).

We then introduced our BPD-PC liposome formulations into Fadu spheroids to monitor uptake. On day 0, the cells were cultured into spheroids in 96 wells plates (5000 cells per well). After 48 h, the constructs were added at a BPD-PC concentration of 5 µM. 24 h later BPD-PC fluorescence was imaged using confocal microscopy at an excitation wavelength of 405 nm, **Fig. 5.22**.

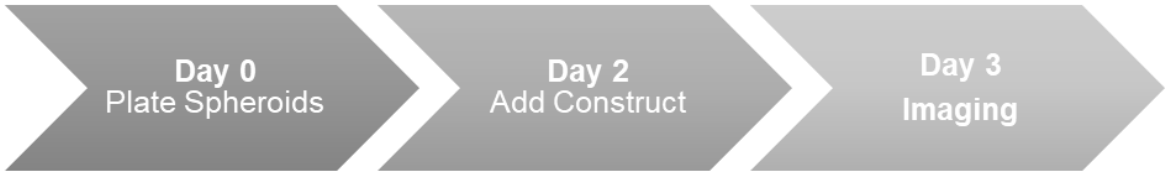

Figure 5.22: Experimental timeline of Fadu spheroid imaging.

Fig. 5.23 shows images of BPD-PC fluorescence taken after 24 h incubation in an untreated spheroid, a spheroid treated with the untargeted construct, and a spheroid treated with the targeted construct (0.5 mol% BPD-PC constructs). After analysis (**Fig. 5.23**), there is no significant difference between the targeted and untargeted constructs. Additionally, Cet (specific) and IgG (non-specific) antibodies were added prior to adding the constructs. Blocking with Cet and IgG resulted in a reduction in fluorescence, indicating that construct binding was preventing but this was not

statistically significant. Overall, we can conclude that the binding observed, in this case, is non-specific.

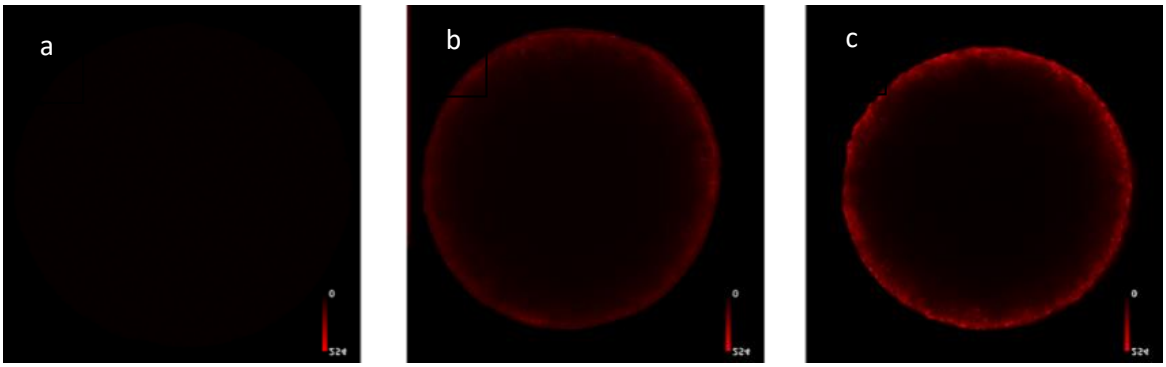

Figure 5.23: Confocal images of BPD-PC fluorescence (405 nm) in Fadu spheroids a) untreated, b) treated with untargeted construct, and c) treated with targeted construct taken 24 h after construct addition (0.5 mol% constructs, BPD-PC concentration of 5 µM).

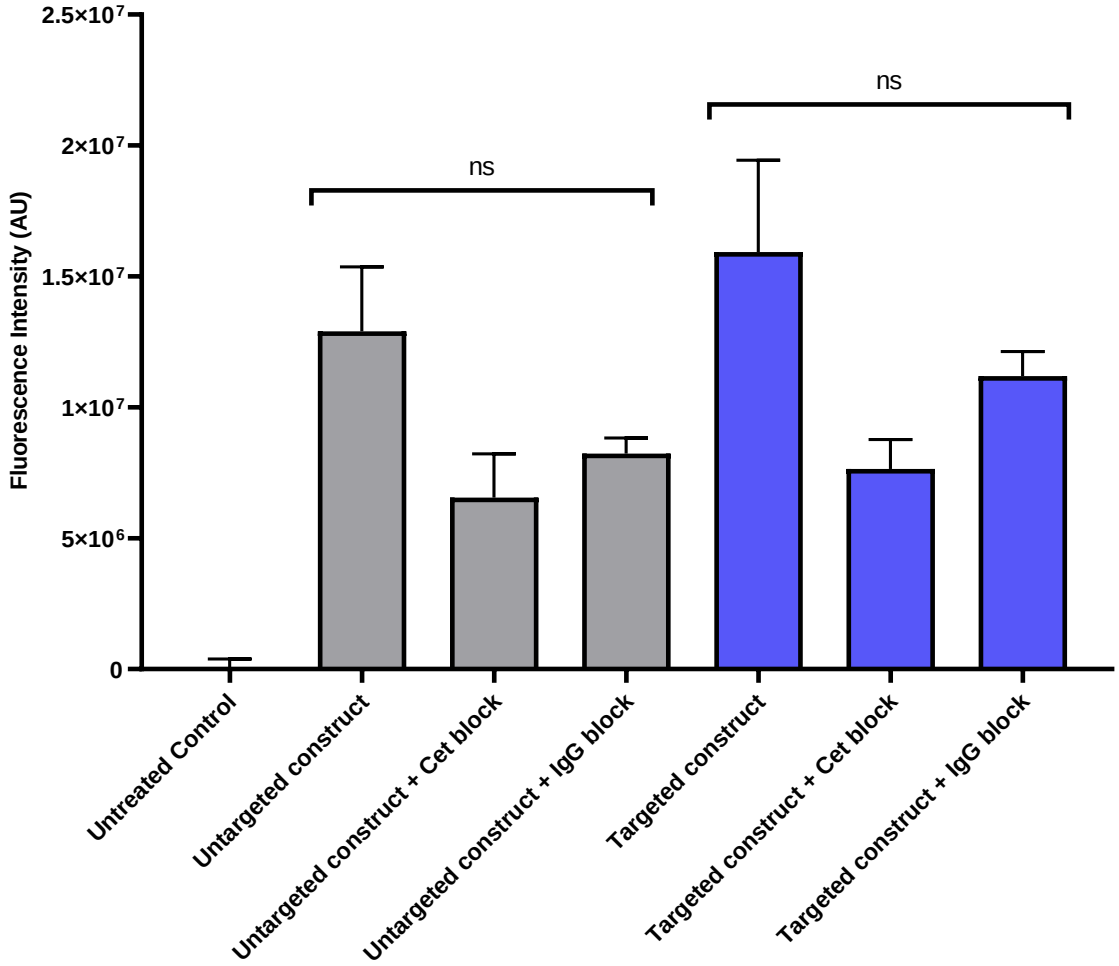

Figure 5.24: Plot of BPD-PC fluorescence intensity of untreated Fadu spheroids, Fadu spheroids treated with untargeted construct, and Fadu spheroids treated with targeted constructs, as well as untargeted and targeted constructs with antibody blocking in Fadu spheroids, 24 h after construct addition (BPD-PC concentration of 5 μM, 0.5 mol% constructs).

We then reformulated the liposomes with 2 mol% BPD-PC, constructs **5.8** and **5.11**, to increase the binding of the targeted construct. The mol% of BPD-PC is a trade-off. If it is too low, as in constructs **5.6** and **5.9**, we only see non-specific binging but if the mol% is too high we can quench the BPC-PC molecules and the liposomes become less stable. The formulated 2 mol% BPD-PC liposomes, constructs **5.8** and **5.11**, did show some BPD-PC when compared to the lower mol% constructs (for example, the fluorescence signal of **5.6** is approximately 1600 AU, while that of construct **5.8** is 800 AU). However, they are still photoactive in PBS and quenching

at these levels is not expected to prevent reactive oxygen species production (**Fig. 5.21**). Thus, we could proceed with the *in vitro* experiments.

When the BPD-PC payload was increased to 2 mol% a significant increase in BPD-PC fluorescence, at 405 nm in the Fadu spheroids 24 h after construct addition, was observed (**Fig. 5.25**). This can be attributed to less non-specific binding in the 2 mol% BPD-PC constructs due to the lower lipid concentration compared to the 0.5 mol% BPD-PC constructs. In **Fig. 5.26**, we see significance between the targeted and untargeted constructs with a p-value of 0.0010.

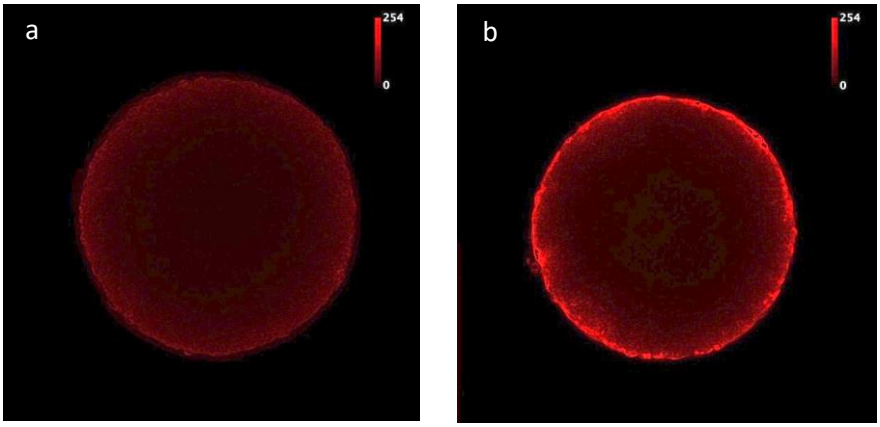

Figure 5.25: Confocal images of BPD-PC fluorescence (405 nm) in Fadu spheroids a) treated with untargeted construct and b) treated with targeted construct, 24 h after construct addition (2 mol% constructs, BPD-PC concentration of 5 µM).

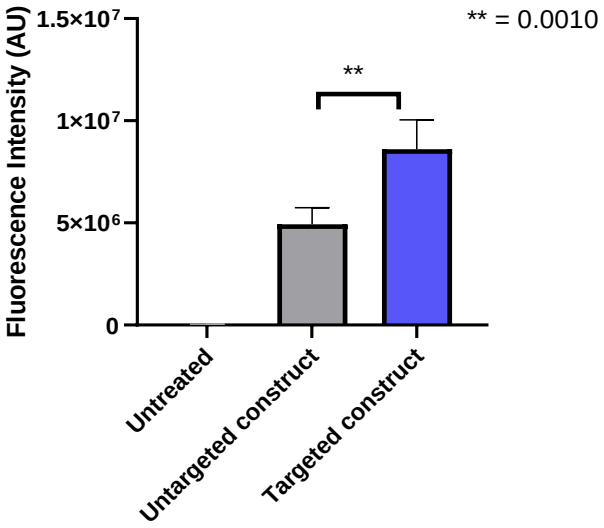

Figure 5.26: Plot of BPD-PC fluorescence intensity of untreated Fadu spheroids, Fadu spheroids treated with untargeted construct and Fadu spheroids treated with targeted constructs 24 h after construct addition (BPD-PC concentration of 5 μM, 2 mol% constructs). ** = 0.0010.

We then investigated whether these liposomes could be activated using X-rays (12 Gy, 320 kV, 12.5 mA). As outlined in the introduction, some photosensitisers can be activated by ionising radiation; thus, we investigated these BPC-PC constructs as radiosensitisers. We conducted probe experiments using HPF (hydroxyphenyl fluorescein, hydroxyl radical and peroxynitrite sensor), SOSG, and MTS (3-(4,5-dimethylthiazol-2-yl)-5-(3-carboxymethoxyphenyl)-2-(4-sulfophenyl)-2H-tetrazolium, detects superoxide and superoxide dismutase). All the experiments were conducted at a BPD-PC concentration of 5 μM for the light irradiation experiments and 7.5 μM for the X-ray radiation experiments.

The first experiment studied singlet oxygen generation (**Fig. 5.27**). Following light irradiation (5 J/cm^2), the 2 mol% BPD-PC constructs (targeted **5.10** and untargeted **5.11**) displayed slightly less singlet oxygen generating ability compared to the 0.6 mol% BPD-PC constructs (targeted **5.8** and untargeted **5.9**), which may be explained by static quenching. As negligible differences in the fluorescence signal of SOSG were observed, it was concluded that X-ray radiation (12 Gy) did not induce significant singlet oxygen generation.

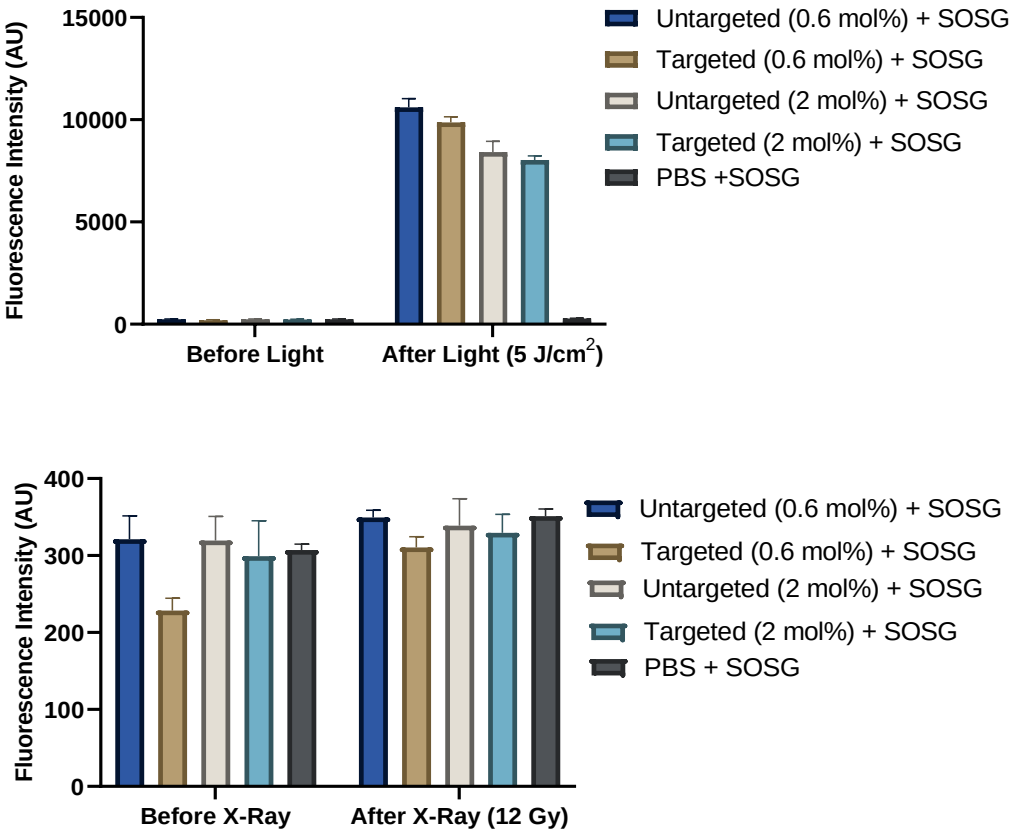

Figure 5.27: SOSG assay on constructs **5.7**, **5.8**, **5.10**, and **5.11** at a BPD-PC concentration of 5 µM for light irradiation (5 J/cm^2, 690 nm) and 7.5 µM for X-ray radiation (12 Gy), n=4. Excitation wavelength = 460 nm, emission wavelength = 525 nm. (SOSG = Singlet oxygen sensor green, PBS = phosphate buffered saline)

For the HPF assay, the 2 mol% BPD-PC (**5.10** and **5.11**) and 0.6 mol% BPD-PC (**5.8** and **5.9**) constructs provided a similar fluorescence response, following both light irradiation (10 J/cm^2) and X-ray radiation (12 Gy). There is also evidence of the radiolysis of water in the PBS control. It can be concluded that both hydroxyl radicals and peroxynitrite molecules are generated following both light and X-ray irradiation (**Fig. 5.28**).

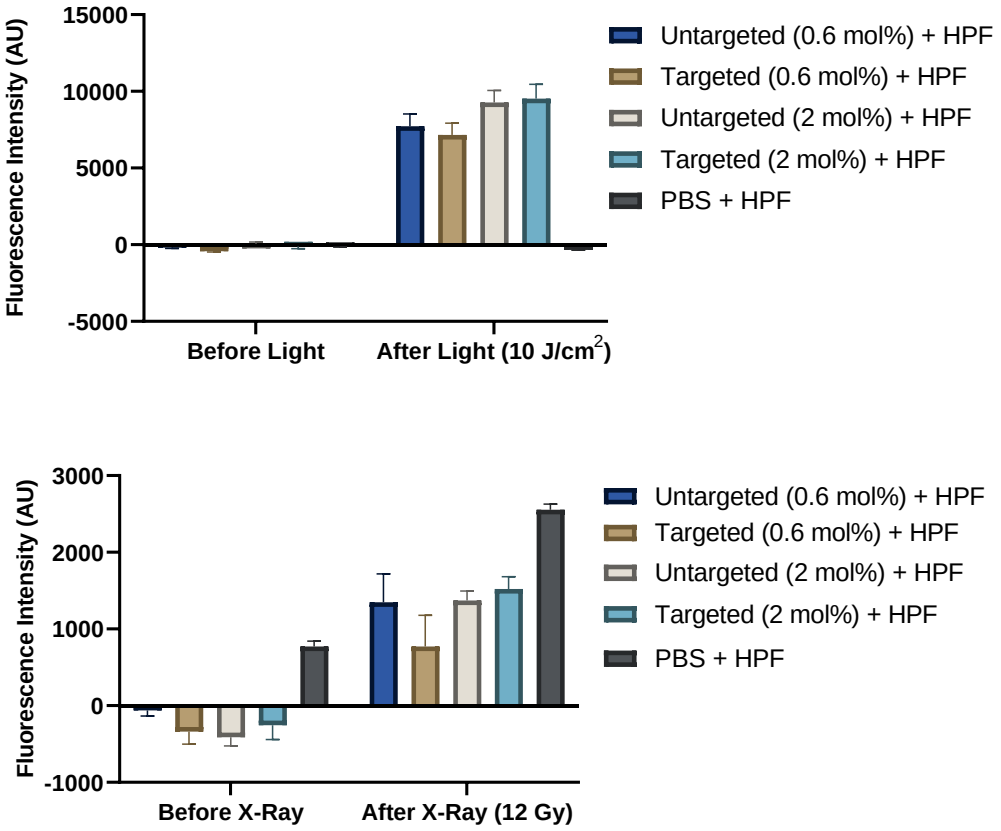

Figure 5.28: HPF assay on constructs **5.7**, **5.8**, **5.10**, and **5.11** at a BPD-PC concentration of 5 µM for light irradiation (10 J/cm^2, 690 nm, 150 mW/cm^2) and 7.5 µM for X-ray radiation (12 Gy), n=4. Excitation wavelength = 490 nm, emission wavelength = 515 nm. (HPF = hydroxyl radical and peroxynitrite sensor, PBS = phosphate buffered saline).

The MTS assay did not show a major increase in any of the constructs, following light irradiation (40 J/cm^2, 690 nm, 150 mW/cm^2) but after X-ray radiation (12 Gy) there was a significant increase in absorbance; thus, superoxide and/or superoxide dismutase are generated during X-ray radiation but not during light irradiation. This confirms that any potential toxicity observed as a result of X-ray radiation may be caused by different mechanisms that are not open to PDT (**Fig. 5.29**).

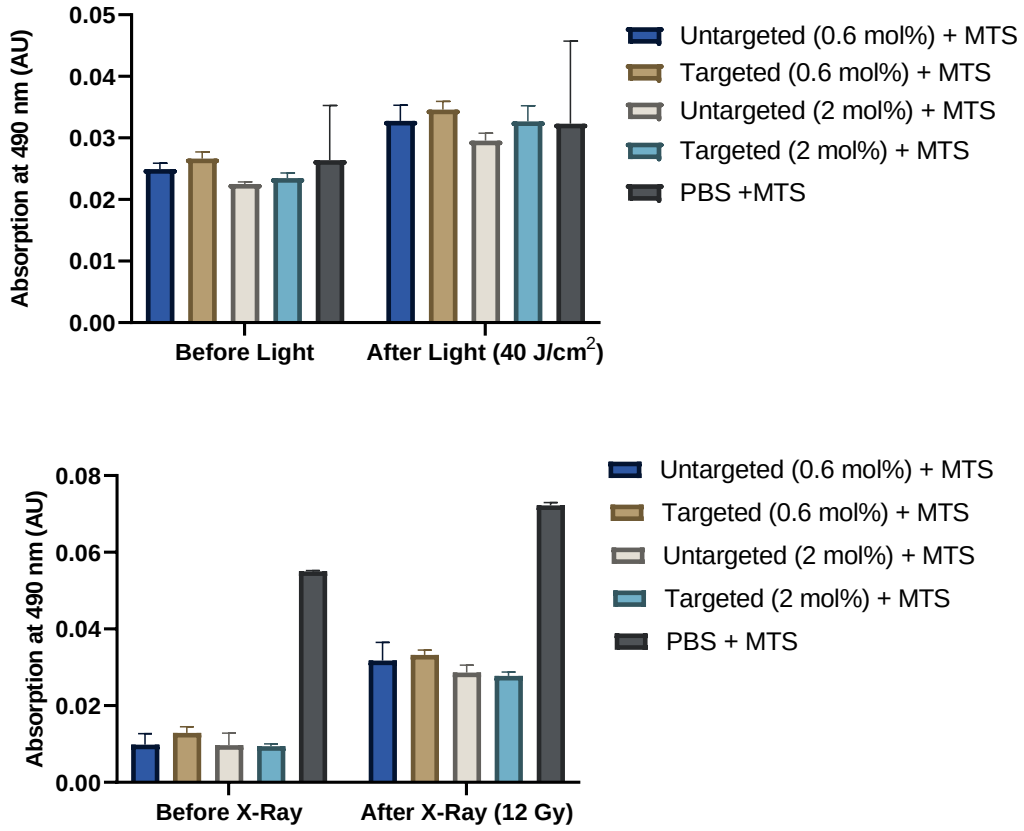

Figure 5.29: MTS assay on constructs **5.7**, **5.8**, **5.10**, and **5.11** at a BPD concentration of 5 µM for light irradiation (5 J/cm^2, 690 nm, 150 mW/cm^2) and 7.5 µM for X-ray radiation (12 Gy), n=4. Absorption at 490 nm. (MTS = (3-(4,5-dimethylthiazol-2-yl)-5-(3-carboxymethoxyphenyl)-2-(4-sulfophenyl)-2H-tetrazolium, PBS = phosphate buffered saline).

We then tested these compounds in head and neck cancer cell lines (Fadu, SCC14, and TR-146). On day 0, the cells were cultured into spheroids in 96 wells plates (5000 cells per well). After 48 h, the 2 mol% constructs were added at a BPD-PC concentration of 7.5 µM. 24 h later, they were treated with radiation therapy at various doses (0 – 15 Gy). The spheroids were imaged using lived/dead assays 72 h later, as represented in the schematic illustration in **Fig. 5.30**. The mean live intensity was analysed using CLYSPO.[384]

Figure 5.30: Schematic illustration of the experimental timeline for *in vitro* live/dead experiments.

Across the three head and neck cancer cell lines, no significant toxicity was observed. In the Fadu and SCC14 cell lines, dark toxicity was observed when using the targeted constructs, this many indicate that Cet is causing toxicity. Also of note is that in the SCC14 and TR-146 cell lines a 5 Gy dose (low-dose) of radiation alone shows higher cell survival and may induce cell survival mechanisms, leading to a radiopositive response, **Fig. 5.31**–**5.33**.

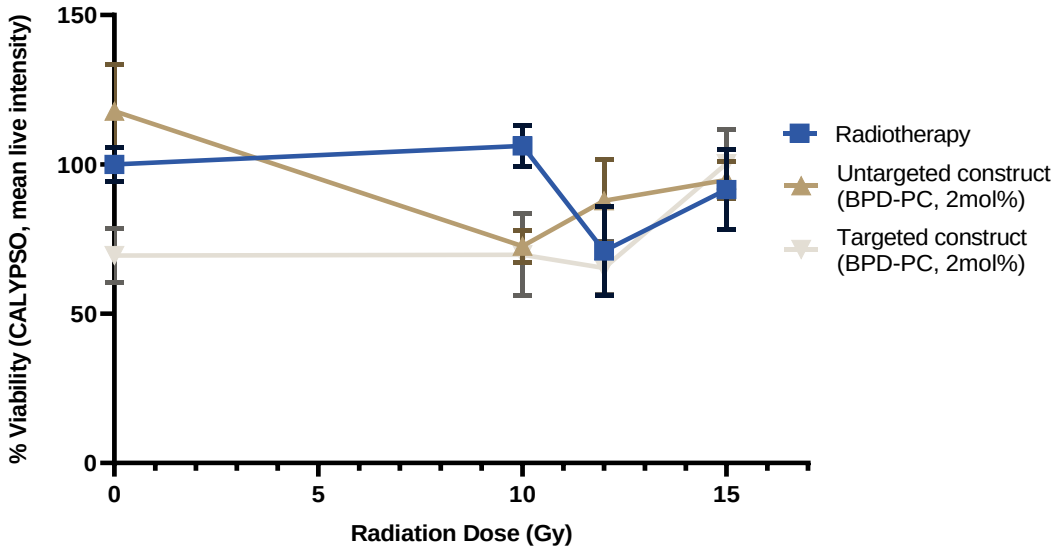

Figure 5.31: Percentage viability of Fadu spheroids with increasing radiation dose. All experiments were at a BPD-PC concentration of 7.5 µM, using targeted and untargeted 2 mol% BPD-PC liposome constructs (n=4).

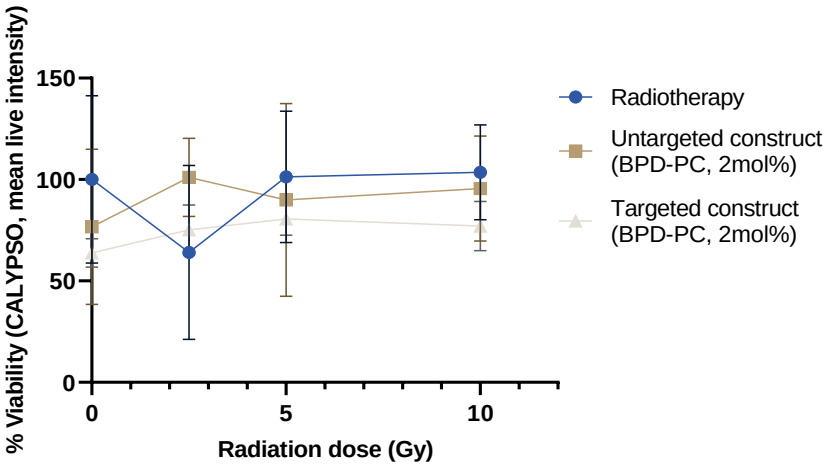

Figure 5.32: Percentage viability of SCC14 spheroids with increasing radiation dose. All experiments were at a BPD-PC concentration of 7.5 µM, using targeted and untargeted 2 mol% BPD-PC liposome constructs (n=4).

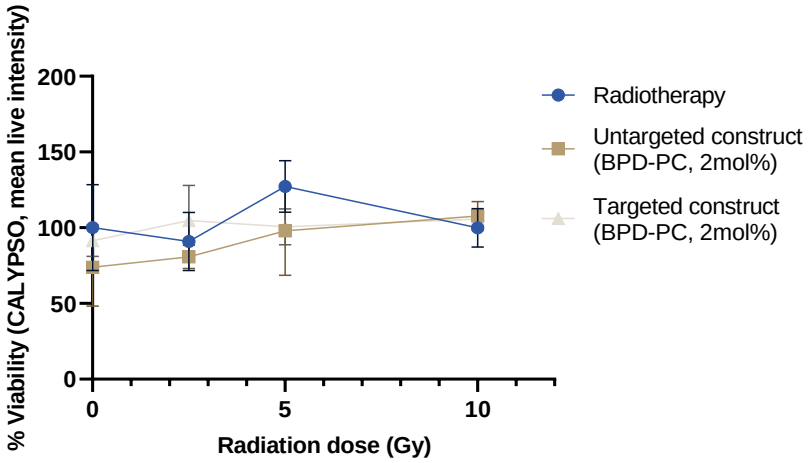

Figure 5.33: Percentage viability of TR-146 spheroids with increasing radiation dose. All experiments were at a BPD-PC concentration of 7.5 µM, using targeted and untargeted 2 mol% BPD-PC liposome constructs (n=4).

Finally, we designed a targeted construct containing both BPD and BPD-PC, construct **5.12** (**Fig. 5.34**). BPD is known to localise in the mitochondria and BPD-PC in the lysosomes; thus, we aim to increase toxicity by targeting both subcellular locations. The construct was synthesised using the same techniques as construct **5.6** and consisted of BPD (1 mol%) and BPD-PC (2 mol%).

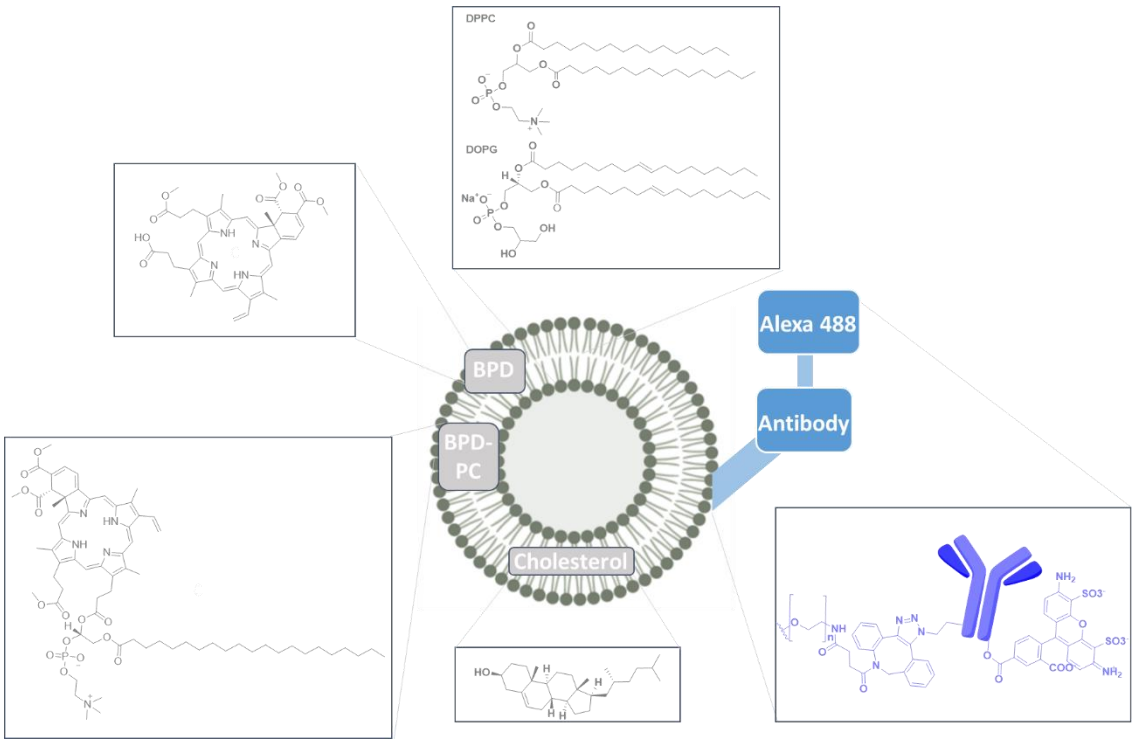

Figure 5.34: Schematic representation of BPD-PC and BPD containing construct, **5.12**.

After purification, a ratio of 4:1 BPD-PC to BPD was calculated by determining the concentration of total BPD and BPD-PC using UV-vis spectroscopy and subtracting that from the BPD concentration calculated from a concentration curve (**Fig. 5.26**) formulated using an internal standard (*N*-(1-naphthyl)ethylenediamine) and liquid chromatography-mass spectrometry (LCMS) to determine the BPD-PC concentration. Construct **5.13**, containing only BPD, was constructed to obtain the concentration curve.

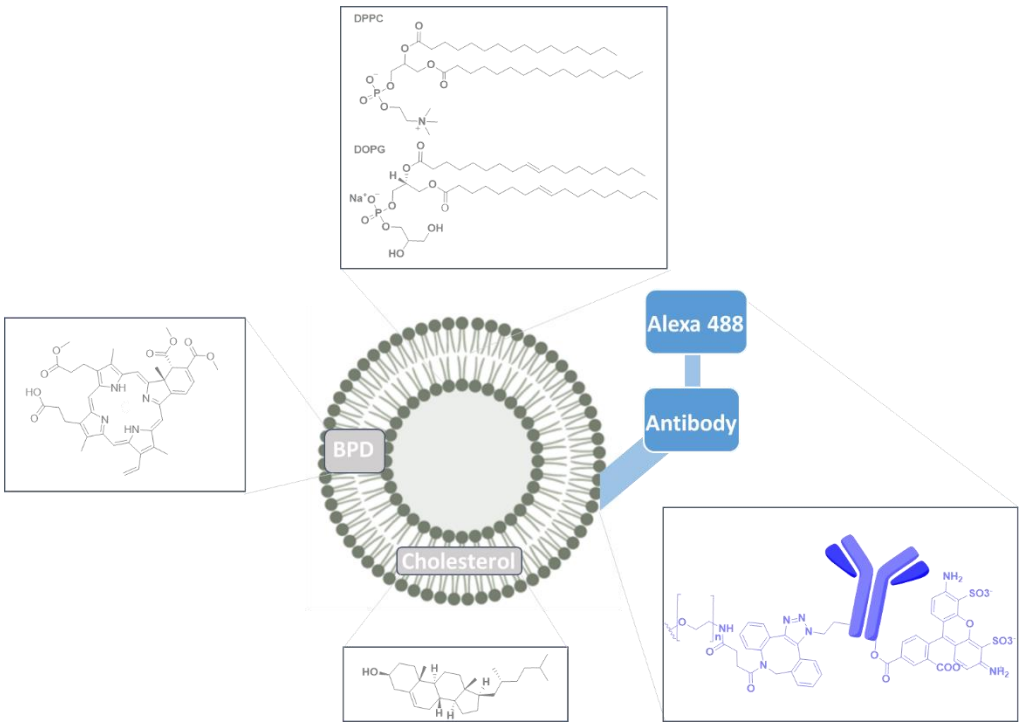

Figure 5.35: Schematic representation of BPD containing construct, **5.13** (1 mol% BPD).

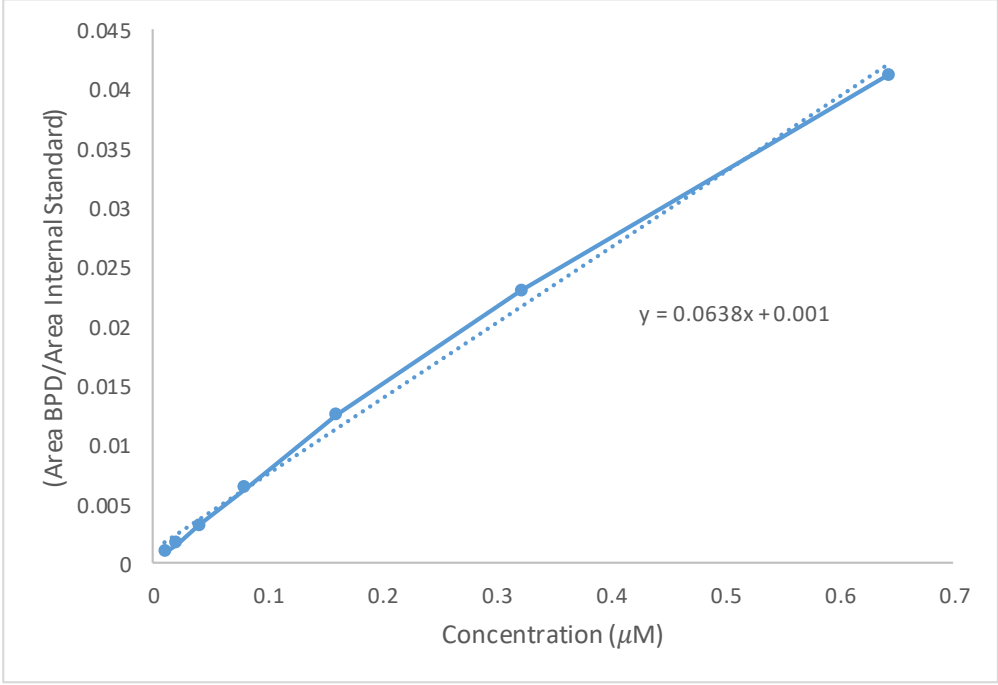

Figure 5.36: Standard concentration curve of untargeted BPD containing construct in PBS using the area under the curve calculated using *N*-(1-naphthyl)ethylenediamine as an internal standard for LCMS.

Both constructs **5.12** and **5.13** Have conjugated Cet to target the EGFR receptor. Fadu spheroids were seeded and treated with construct **5.12**. Then, live/dead assay was performed and the spheroids were imaged and analysed with CLYSPO, as before. Most notably, major dark toxicity was again observed. **Fig. 5.37** shows a steady decrease in cell viability with increasing construct concentration. Additionally, from the absorption and fluorescence spectra in **Fig. 3.38**, we observe significant BPD/BPD-PC quenching as a result of the high payload in construct **5.12**. Therefore, the increased payload is expected to contribute to the dark toxicity.

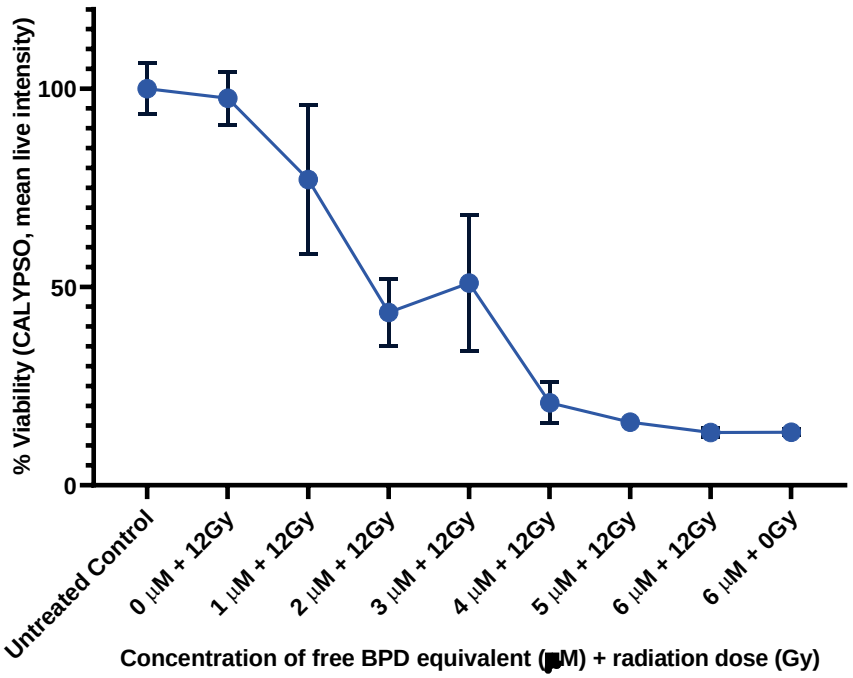

Figure 5.37: Percentage viability of Fadu spheroids with increasing conc. of targeted mixed BPD/BPD-PC construct **5.12** with a 4:1 concentration ratio of BPD-PC to BPD and a 12 Gy radiation dose (n=4).

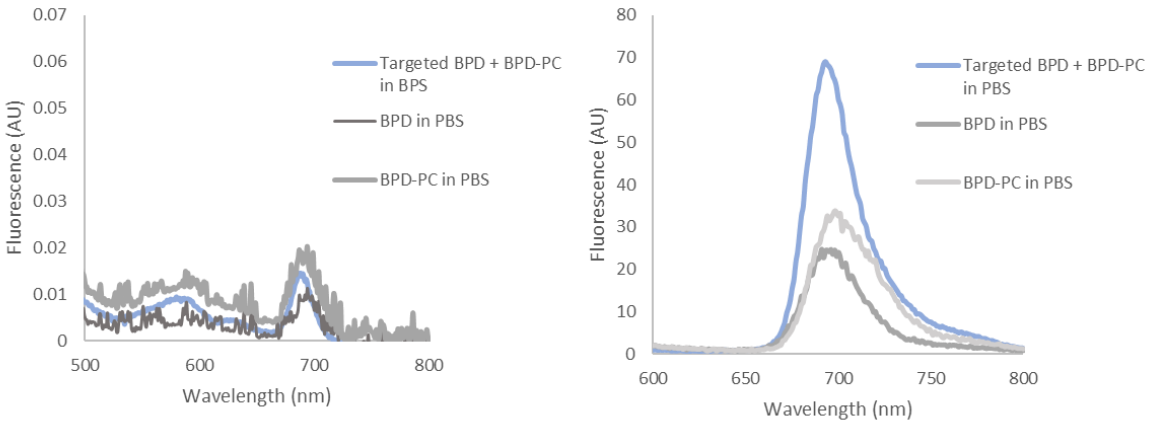

Figure 5.38: Right: Absorption Left: Fluorescence emission (ex. 435 nm) of free BPD-PC, free BPD, and BPD-PC/BPD in targeted constructs, **5.12**. Spectra measured in PBS at a concentration of 5 µM.

5.4 CONCLUSION AND FUTURE WORK

A range of targeted liposomes were synthesised and evaluated for medical applications. We first synthesised IRdye liposomes with conjugated Cet for targeting and an IRDye to quantify targeting *in vivo*. We showed that these liposomes are stable over 40 days. Moreover, under physiological conditions, IgG in this system did not form coronas due to protein opsonization. These findings indicate that the shelf-life of the constructs are suitable for practical application and that the *in vivo* lifetimes of the constructs are unlikely to be shortened by opsonisation.

In the next project, we synthesised the TPMIL construct, which can deliver both BPD-PC and Irinotecan to pancreatic tumour tissue. The combined effect of both the photosensitiser and chemotherapeutic drugs provided an enhanced therapeutic response. This construct contained Cet as a targeting antibody and we tested efficiency *in vivo* against an orthotopic pancreatic cancer model. Moreover, we compared its response to standard liposomal PDT and chemotherapeutic drug formulations (Visudyne and Onivyde). Overall, a low-dose of the TPMIL construct (0.25 mg/kg BPD + 50 J/cm^2 (4 mg/kg Irinotecan)) demonstrated a significantly better response when compared to untreated and standard controls (tumour growth inhibitor up to 80 days). The next stage of this project will be to increase the size of the experimental groups with the aim of translating this construct into clinical application.

We also studied the effect of 3-cycle 24 h or 72 h treatment regimes in an attempt to investigate the effet of photodynamic priming at the tumour site. However, significant therapeutic improvements were not observed in the time period of the experiment. We intend to increase the number of data points in each experimental group to further analyse photodynamic priming.

In the final project, we successfully constructed a library of BPC-PC containing Cet targeted liposomes at 0.5, 0.6, and 2 mol% BPD-PC concentrations. We demonstrated targeting at a higher BPD-PC payload of 2 mol%, however, minor killing in three head and neck cancer cell lines was observed. A future avenue for this work would be to introduce a rare earth metal or heavy atom into the core of the porphyrin to be excited by X-ray radiation, resulting in luminescence to subsequently

active the BPD-PC molecules. This concept was introduced by Chen and Zhang in 2006.[385] There is also the possibility of returning to PDT with these constructs to fully investigate the advantages of targeting for the therapeutic response. Initially, this would require optimisation of the payload and Cet conjugation efficiencies.

Chapter 6: Experimental Details

"In God we trust, others must provide data."

Edwin R. Fisher 1978

6.1 GENERAL CONSIDERATIONS AND INSTRUMENTATION

Unless otherwise specified, all chemicals were commercially sourced and used without further purification. All air and/or water-sensitive materials were handled using standard high vacuum techniques. Dry THF and DCM were obtained by passing through alumina under N_2 in a solvent purification system and then further dried over activated molecular sieves. Dry DMF was purchased from Sigma-Aldrich. Analytical thin-layer chromatography was performed using silica gel 60 (fluorescence indicator F254, pre-coated sheets, 0.2 mm thick, 20 cm × 20 cm; Merck) plates and visualized by UV irradiation (λ = 254 nm). Column chromatography was carried out using Fluka Silica Gel 60 (230–400 mesh; Merck). UV-vis spectra were recorded in solutions using a Specord 250 spectrophotometer from Analytic Jena (1 cm path length quartz cell). Emission, excitation spectra and lifetimes were measured using a Cary Eclipse G9800A fluorescence spectrophotometer and Horiba Jobin Yvon Fluorolog 4. Photo-irradiations were performed in quartz cuvettes (2 × 1 × 1 cm) using a polychromatic light source (Philips, 15V-150 W lamp), equipped with a 400 nm cut-off filter (Schott GG 400). The samples were temperature controlled using a Peltier element (Cary Peltier 1 × 1 Cell Holder). NMR spectra were recorded on a Bruker AV 600, Bruker Advance III 400 MH or a Bruker DPX400 400 MHz or an Agilent 400 spectrometer. Accurate mass measurements (HRMS) were carried out using a Bruker microTOF-Q™ ESI-TOF mass spectrometer. Mass spectrometry was performed with a Q-Tof Premier Waters MALDI quadrupole time-of-flight (Q-TOF) mass spectrometer equipped with Z-spray electrospray ionization (ESI) and matrix assisted laser desorption ionization (MALDI) sources in positive mode with *trans*-2-[3-(4-tert-butylphenyl)-2-methyl-2-propenylidene]malononitrile as the matrix. Melting points were measured using an automated melting point meter, SMP50 (Stuart).

Crystals were grown following the protocol developed by Hope by dissolving the compounds in either CH_2Cl_2 and layering with a second solvent (hexane) for liquid diffusion.[386] Single-crystal X-ray diffraction data for all compounds were collected on a Bruker APEX 2 DUO CCD diffractometer by using graphite-monochromated Cu Kα (λ = 1.54178 Å) radiation. Crystals were mounted on a MiTeGen MicroMount and collected at 100(2) K by using an Oxford Cryosystems Cobra low-temperature device. Data were collected by using omega and phi scans and were corrected for Lorentz and polarization effects by using the APEX software suite.[387–389] Using Olex2, the structure was solved with the XT structure solution program, using the intrinsic phasing solution method and refined against $|F2|$ with XL using least squares minimization.[390,391]

6.2 CHAPTER 2: PYRIDONE-SUBSTITUTED PORPHYRINS FOR SLOW SINGLET OXYGEN RELEASE

6.2.1 Singlet oxygen sensor green assay

SOSG reagent was purchased from Thermo Fischer. Upon receipt, the reagent was stored at -20 °C until required for use. The stock solutions were prepared in MeOH: the content of one 100 µg vial was dissolved in 330 µL of MeOH to make a stock solution of 5×10^{-4} M concentration. The working solutions of the reagent were prepared immediately before use, and any excess diluted reagent was discarded at the end of the work session. A fluorescence cuvette containing 10^{-4} M solution of porphyrin **2.18** or **2.19** in THF was irradiated with broadband visible light for 1 h under stirring and cooling to 0 °C by a Peltier element. Subsequently, 31 µL of a 1 mM NaOH solution in water (final NaOH concentration: 8.9×10^{-6} M) and 70 µL of a 5×10^{-4} M SOSG solution in MeOH (final SOSG concentration: 10^{-5} M) were added. After warming up to rt, the sample was placed into a fluorimeter and the fluorescence of SOSG in this solution was automatically recorded at variable periods of time (every 1-5 min) during 24 h. Fluorescence was excited at 505 nm. In the case of **2.19**, fluorescence measurements were performed at 40 °C using a Peltier element. In the reference experiments, the fluorescence of the SOSG solution was monitored in the absence of the porphyrin under the same conditions. No increase of the sensor fluorescence was observed either at rt or at 40 °C.

6.2.2 Protocol for HT-29 cell cytotoxicity studies

Each compound (**2.13**–**2.16**) was formulated in DMSO (anhydrous >99.9%) and diluted in appropriate medium (Dulbecco's Modified Eagle's Medium with 4.5 g/L Glucose + 2 mM L-glutamine, no FCS) to give a range of concentrations (2×10^{-4}–1×10^{-6} M). The HT-29 cells (human colon adenocarcinoma) were adjusted to a concentration of 1×10^6 cells/mL. 800 µL was added to 200 µL of the porphyrin solution at 5x the desired and incubated in the dark for 1 h at 37 °C in an atmosphere of 5% CO_2, after which they were centrifuged and washed in a 3 × excess of medium to eliminate any unbound compound. Pellets of the cells and compound were resuspended in 1 mL of medium. 4 x 100 µL of the cells (8×10^4) and the porphyrin were transferred to two 96 wells plates. One plate was irradiated with broadband visible light (400–700 nm; 20 J/cm^2 provided by an Oriel quartz tungsten halogen lamp housing model 66188 powered by an Oriel 1100 W radiometric power supply model 69935), while the second plate served as a "dark toxicity" control. After irradiation, 5 µL of Fetal Bovine Serum was added to each well and the plates are returned to the incubator overnight. After 24 h, an MTT cell viability assay was performed and the results were expressed as percentage of cell viability *vs.* compound concentration; an LD 90 (lethal dose where 90% of the cells are killed) was determined from the resulting curves. Each experiment was repeated in triplicate (minimum).

6.2.3 Synthetic details and characterisation

The synthetic procedures used to synthesize methyl-3,5-bis(bromomethyl)benzoate, **2.21**,[245] methyl-3-(bromomethyl)-5-formylbenzoate, **2.28**,[251] (3,5-bis(bromomethyl)phenyl)methanol, **2.22**,[246] 3,5-bis(bromomethyl)benzaldehyde, **2.23**,[247] 5,10,15,20-tetrakis(3,5-bis(bromomethyl)phenyl)porphyrin, **2.25**,[248] 5,10,15,20-tetrakis(4-((2-oxopyridin-1(2H)-yl)methyl)phenyl)porphyrin, **2.18**,[237] 4-(bromomethyl)benzaldehyde, **2.35**,[253] and 5,10,15-tris(4-bromomethylphenyl)-20-(4-methoxycarbonylphenyl)porphyrin, **2.36**,[392] were adapted from literature.

5,10,15,20-Tetrakis(4-((3-methyl-2-oxopyridin-1(2H)-yl)methyl)phenyl) porphyrin, 2.19

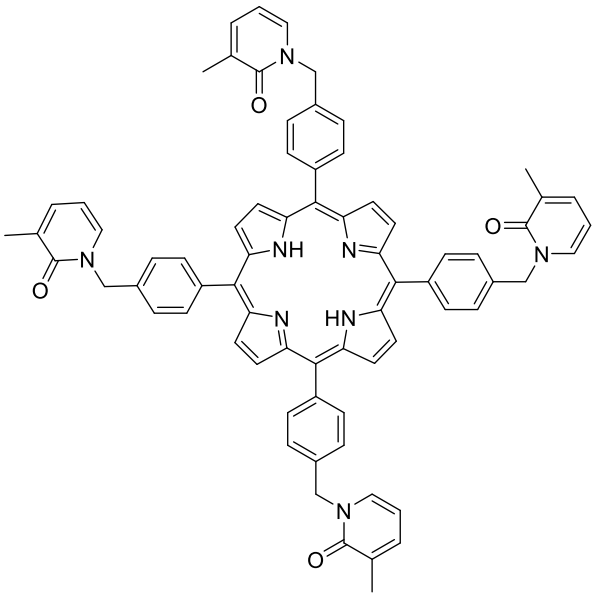

5,10,15,20-Tetrakis(4-(bromomethyl)phenyl)porphyrin, **2.17**, (300 mg, 0.030 mmol) and 2-hydroxy-3-methylpyridine, **2.27**, (337 mg, 3.55 mmol) were dissolved in dry THF (150 mL) under anhydrous conditions. NaH (73 mg, 60% in mineral oil, 3.04 mmol) was washed with hexane, dissolved in dry THF (20 mL) and added to the reaction vessel. The reaction was heated to reflux for 5 h. The reaction was allowed to cool to rt and the percipitate was removed. The product was extracted with DCM (30 mL), dried *in vacuo*, and recrystallised from MeOH and DCM to yield purple crystals (0.80 g, 7.28×10^{-4} mol, 63%). M.p. > 300 °C; ^{1}H NMR (400 MHz, $CDCl_3$) = δ 8.62 (s, 8H, CH_{β}), 8.53 (d, J = 8.0 Hz, 8H, CH_{Ar}), 7.92 (d, J = 8.0 Hz, 8H, CH_{Ar}), 7.66 (d, J = 6.8 Hz, 4H, CH_{Ar}), 7.56 (d, J = 6.9 Hz, 4H, CH_{Ar}), 6.59 (t, J = 6.9 Hz, 4H, CH_{Ar}), 5.67 (s, 8H, CH_2), 2.35 (s, 12H, CH_3), -0.70 ppm (s, 2H, NH); ^{13}C NMR (101 MHz, $CDCl_3$) = δ 163.5, 145.8, 139.4, 139.0, 138.8, 137.7, 135.2, 130.8, 128.4, 127.9, 122.3, 115.3, 112.4, 107.1, 52.8, 17.6 ppm; UV-vis (DMSO): λ_{max} (log ε) = 420 (5.69), 516 (4.29), 550 (4.02), 591 (3.77), 648 nm (3.76); HRMS (ESI): *m/z* calcd. for $C_{72}H_{59}N_8O_4$ $[M+H]^+$: 1098.4581, 1098.4586 found.

5,10,15,20-Tetrakis(3,5-bis((pyridin-2(1H)-one)methyl)phenyl)porphyrin, 2.15

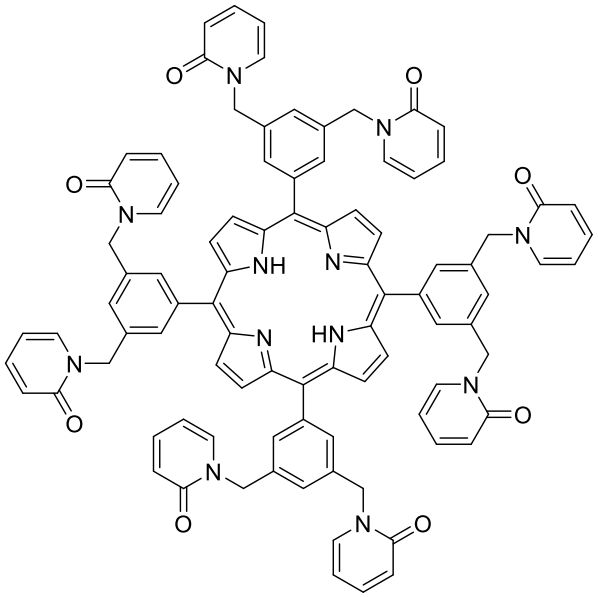

Compound **2.25** (200 mg, 0.15 mmol) and 2-hydroxypyridine, **2.26**, (419 mg, 4.41 mmol) were dissolved in dry THF (100 mL) under anhydrous conditions. NaH (176 mg, 60% in mineral oil, 4.41 mmol) was washed with hexane, dissolved in dry THF (20 mL) and added to the reaction vessel. The reaction was heated to reflux for 5 h. The reaction was allowed to cool to rt and the precipitate was removed. The product was extracted with DCM (30 mL), dried *in vacuo*, and recrystallised from MeOH and DCM to yield purple crystals (126 mg, 8.71×10^{-5} mol, 58%). M.p. > 300 °C; ^{1}H NMR (400 MHz, $CDCl_3$) δ = 8.75 (s, 8H, CH_β), 8.01 (s, 8H, CH_{Ar}), 7.66 (s, 4H, CH_{Ar}), 7.51 (d, J = 4.8 Hz, 8H, CH_{Ar}), 7.38 – 7.32 (m, 8H, CH_{Ar}), 6.64 (d, J = 9.1 Hz, 8H, CH_{Ar}), 6.24 (t, J = 6.0 Hz, 8H, CH_{Ar}), 5.48 (s, 16H, CH_2) -2.96 ppm (s, 2H, NH); UV-vis (DMSO): λ_{max} (log ε) = 422 (5.54), 518 (4.27), 553 (4.08), 592 (3.95), 647 nm (3.93); HRMS (MALDI-TOF) *m/z* calcd. for $C_{92}H_{70}N_{12}O_8$ $[M]^+$: 1470.5440, 1470.5432 found.

5,10,15,20-Tetrakis(3,5-bis((3-methylpyridin-2(1H)-one)methyl)phenyl) porphyrin, 2.16

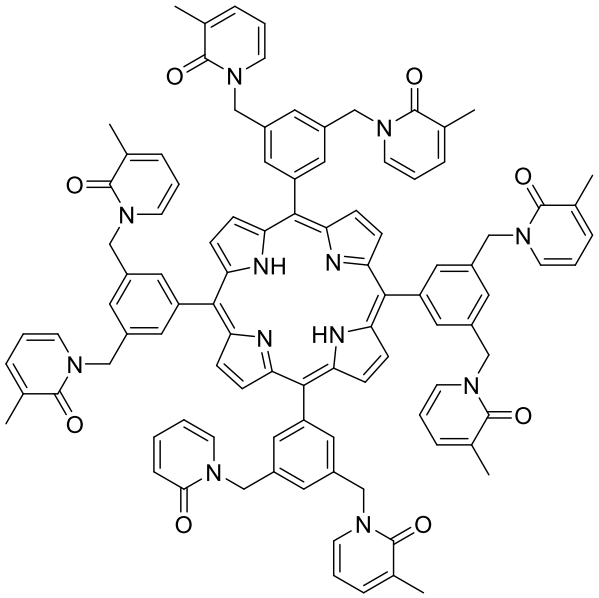

Compound **2.25** (200 mg, 0.15 mmol) and 2-hydroxy-3-methylpyridine, **2.27**, (482 mg, 4.41 mmol) were dissolved in dry THF (100 mL) under anhydrous conditions. NaH (176 mg, 60% in mineral oil, 4.41 mmol) was washed with hexane, dissolved in dry THF (20 mL) and added to the reaction vessel. The reaction was heated to reflux for 5 h. The reaction was allowed to cool to rt and the precipitate was removed. The product was extracted with DCM (30 mL), dried *in vacuo*, and recrystallised from MeOH and DCM to yield purple crystals (152 mg, 9.69×10^{-5} mol, 65%). M.p. > 200 °C; ^{1}H NMR (400 MHz, $CDCl_3$) δ = 8.73 (s, 8H, CH_{β}), 7.97 (s, 8H, CH_{Ar}), 7.62 (s, 4H, CH_{Ar}), 7.36 (d, J = 4.2 Hz, 8H, CH_{Ar}), 7.18 (d, J = 5.9 Hz, 8H, CH_{Ar}), 6.12 (t, J = 6.7 Hz, 8H, CH_{Ar}), 5.42 (s, 16H, CH_2), 2.16 (d, J = 10.6 Hz, 24H, CH_3), -2.96 ppm (s, 2H, NH); ^{13}C NMR (101 MHz, $CDCl_3$) δ = 163.2, 143.1, 138.8, 137.1, 136.2, 135.0, 133.4, 133.3, 130.4, 126.9, 119.3, 106.5, 52.4, 17.6 ppm; UV-vis (DMSO): λ_{max} (log ε) = 423 (5.79), 518 (4.37), 553 (4.12), 592 (3.87), 647 nm (3.83); HRMS (MALDI-TOF): *m/z* calcd. for $C_{100}H_{86}N_{12}O_8$ $[M]^+$: 1582.6692, 1582.6741 found.

5,10,15,20-Tetrakis(3-methoxycarbonyl-5-(bromomethyl)phenyl)porphyrin, 2.29

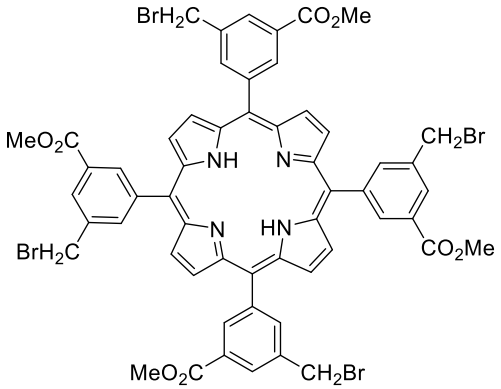

Pyrrole, **2.24**, (50 mg, 0.747 mmol) and methyl 3-(bromomethyl)-5-formylbenzoate, **2.28**, (193 mg, 0.747 mmol) were dissolved in dry DCM (75 mL) under anhydrous conditions. Following the addition of $BF_3 \cdot Et_2O$ (10.5 mg, 7.47×10^{-5} mol), the reaction was stirred at rt for 2 h. DDQ (121 mg, 0.56 mmol) was added and the reaction was stirred at rt for 30 min. TEA (10 µL) was added to convert the product into free-base form. The crude product was purified by filtration through a plug of silica (DCM) to yield a purple solid (96 mg, 7.88×10^{-5} mol, 42%). M.p. >300 °C; R_f = 0.4 (DCM); ^{1}H NMR (400 MHz, $CDCl_3$) δ = 8.81 (s, 12H, C*H*$_{Ar}$), 8.51 (s, 4H, C*H*$_{Ar}$), 8.43 (s, 4H, C*H*$_{Ar}$), 4.80 (s, 8H, C*H*$_2$), 3.99 (s, 12H, C*H*$_3$), -2.83 ppm (s, 2H, N*H*); ^{13}C NMR (101 MHz, $CDCl_3$) δ = 166.7, 142.8, 138.9, 137.1, 134.8, 129.7, 129.6 118.7, 32.4 ppm; UV-vis (DCM): λ_{max} (log ε) = 421 (5.12), 516 (2.71), 550 (2.27), 590 (2.18), 645 nm (1.87); HRMS (MALDI-TOF): *m/z* calcd. for $C_{56}H_{42}Br_4N_4O_8$ $[M]^+$: 1213.9736, 1213.9762 found.

5,10,15,20-Tetrakis(3-methoxycarbonyl-5-(pyridin-2(1H)-one)phenyl)porphyrin, 2.30

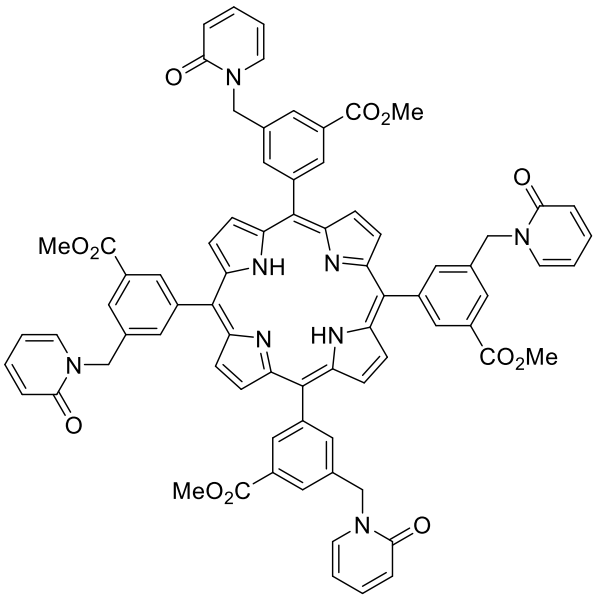

Compound **2.29** (250 mg, 0.21 mmol) and 2-hydroxypyridine, **2.26**, (294 mg, 3.09 mmol) were dissolved in dry THF (100 mL) under anhydrous conditions. NaH (123 mg, 60% in mineral oil, 3.09 mmol) was washed with hexane, dissolved in dry THF (20 mL), and added to the reaction vessel. The reaction was heated to reflux for 5 h. The reaction was allowed to cool to rt and the precipitate was removed. The product was extracted with DCM (30 mL), dried *in vacuo*, and recrystallised from MeOH and DCM to yield purple crystals (200 mg, 1.57×10^{-4} mol, 77%). M.p. >300 °C; ^{1}H NMR (400 MHz, $CDCl_3$) δ = 8.80 (s, 4H, C*H*$_{Ar}$), 8.74 (d, *J* = 3.8 Hz, 8H, C*H*$_{Ar}$), 8.39 (s, 4H, C*H*$_{Ar}$), 8.30 (s, 4H, C*H*$_{Ar}$), 7.51 (d, *J* = 5.7 Hz, 4H, C*H*$_{Ar}$), 7.32 (t, *J* = 7.2 Hz, 4H, C*H*$_{Ar}$), 6.62 (d, *J* = 9.1 Hz, C*H*$_{Ar}$), 6.27 – 6.16 (m, 4H, C*H*$_{Ar}$), 5.47 (s, 8H, C*H*$_2$), 3.97 (s, 12H, C*H*$_3$), -2.91 ppm (s, 2H, N*H*); ^{13}C NMR (101 MHz, $CDCl_3$) δ = 166.9, 162.7, 142.8, 139.9, 137.7, 137.4, 135.7, 134.6, 129.6, 129.2, 128.5, 121.6, 106.7, 52.5, 52.2, 1.0 ppm; UV-vis (DMSO): λ_{max} (log ε) = 421 (5.78), 515 (4.32), 552 (3.92), 591 (3.82), 643 nm (3.54); HRMS (MALDI-TOF): *m/z* calcd. for $C_{76}H_{58}N_8O_{12}$ $[M]^+$: 1274.4174, 1274.4174 found.

5,10,15,20-Tetrakis(3-methoxycarbonyl-5-(methylpyridin-2(1H)-one)phenyl)porphyrin, 2.31

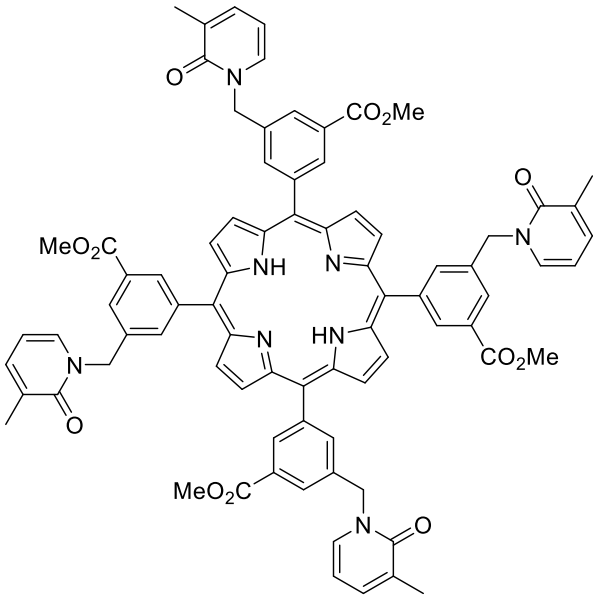

Compound **2.29** (250 mg, 0.206 mmol) and 2-hydroxy-3-methylpyridine, **2.27**, (337 mg, 3.09 mmol) were dissolved in dry THF (100 mL) under anhydrous conditions. NaH (123 mg, 60% in mineral oil, 3.09 mmol) was washed with hexane, dissolved in dry THF (20 mL), and added to the reaction vessel. The reaction was heated to reflux for 5 h. The reaction was allowed to cool to rt and the precipitate was removed. The product was extracted with DCM (30 mL), dried *in vacuo*, and recrystallised from MeOH and DCM to yield purple crystals (149 mg, 5.72 × 10^{-4} mol, 57%). M.p. >300 °C; ^{1}H NMR (400 MHz, $CDCl_3$) δ = 8.79 (s, 4H, C*H*$_{Ar}$), 8.74 (d, *J* = 5.6 Hz, 8H, C*H*$_{\beta}$), 8.38 (s, 4H, C*H*$_{Ar}$), 8.30 (s, 4H, C*H*$_{Ar}$), 7.38 (d, *J* = 5.4 Hz, 4H, C*H*$_{Ar}$), 7.19 (d, *J* = 6.8 Hz, 4H, C*H*$_{Ar}$), 6.21 – 6.06 (m, 4H, C*H*$_{Ar}$), 5.57 – 5.40 (m, 8H, C*H*$_2$), 3.97 (d, *J* = 3.4 Hz, 12H, C*H*$_3$), 2.14 (s, 12H, C*H*$_3$), -2.91 ppm (s, 2H, N*H*); ^{13}C NMR (101 MHz, $CDCl_3$) δ = 170.1, 166.8, 163.1, 143.1, 137.7, 137.0, 135.2, 134.4, 133.8, 130.6, 129.6, 128.5, 106.4, 84.2, 81.7, 52.6, 47.4, 17.4, 14.6 ppm; UV-vis (DMSO): λ_{max} (log ε) = 421 (5.72), 517 (4.34), 551 (3.96), 591 (3.85), 646 nm (3.64); HRMS (MALDI-TOF): *m/z* calcd. for $C_{81}H_{66}N_8O_{12}$ $[M+H]^+$: 1331.4878, 1331.4871 found.

5,10,15,20-Tetrakis(3-carboxy-5-((2-oxopyridin-1(2H)-yl)methyl)phenyl) porphyrin, 2.13

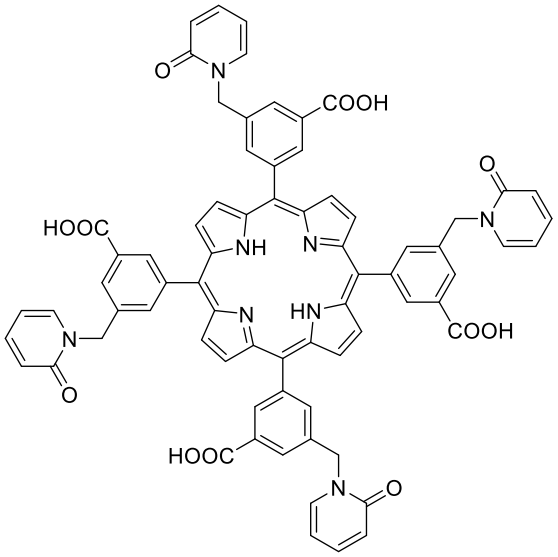

To a solution of compound **2.30** (100 mg, 0.08 mmol) dissolved in THF (110 mL) was added KOH (1 g, 0.02 mol) dissolved in MeOH (20 mL). The reaction was heated to reflux for 24 h. The reaction was allowed to cool to rt, the precipitate was removed, and the solvent was evaporated *in vacuo*. Water (10 mL) was added and the precipitated product was filtered. The product was recrystallised from a mixture of DCM, MeOH, and acetone to yield a green solid (69 mg, 5.66 × 10^{-5} mol, 72%). M.p. >300 °C; ^{1}H NMR (400 MHz, DMSO-d_6) δ = 8.81 (s, 8H, CH_β), 8.57 (s, 4H, CH_{Ar}), 8.19 (s, 8H, CH_{Ar}), 8.01 (d, J = 5.1 Hz, 4H, CH_{Ar}), 7.45 (t, J = 7.8 Hz, 4H, CH_{Ar}), 6.47 (d, J = 8.8 Hz, 4H, CH_{Ar}), 6.30 (s, 4H, CH_{Ar}), 5.43 (s, 8H, CH_2), -2.93 ppm (s, 2H, NH); UV-vis (DMSO): λ_{max} (log ε) = 422 (5.48), 517 (4.65), 551 (3.39), 593 (3.30), 646 nm (3.23); HRMS (MALDI-TOF): *m/z* calcd. for $C_{73}H_{50}N_8O_{12}$ $[M+H]^+$: 1219.3626, 1219.3621 found.

5,10,15,20-Tetrakis(3-carboxy-5-((2-oxomethylpyridin-2(1H)-yl)methyl)phenyl) porphyrin, 2.14

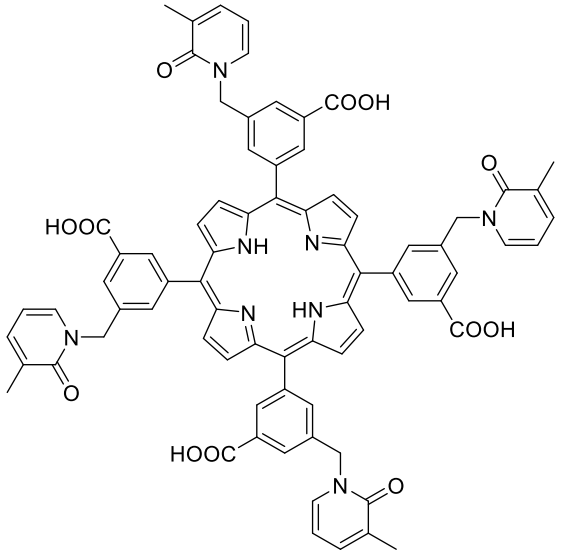

To a solution of compound **2.31** (100 mg, 7.52 × 10^{-5} mol) dissolved in THF (80 mL) was added KOH (1 g, 0.02 mol) dissolved in MeOH (20 mL). The reaction was heated to reflux for 24 h. The reaction was allowed to cool, the precipitate was removed, and the solvent was evaporated *in vacuo*. Water (10 mL) was added and the precipitated product was filtered. The product was recrystallised from a mixture of DCM, MeOH, and acetone to yield a green solid (83 mg, 6.52 × 10^{-5} mol, 87%). ^{1}H NMR (400 MHz, DMSO-d_6) δ = 13.42 (s, br, 4H, CH_{Ar}), 8.84 (s, 8H, CH_{Ar}), 8.69-8.57 (m, 4H, CH_{Ar}), 8.48-8.32 (m, 8H, CH_{Ar}), 7.92 (d, J = 4.7 Hz, 4H, CH_{Ar}), 7.42-7.27 (m, 4H, CH_{Ar}), 6.29-6.15 (m, 4H, CH_{Ar}), 5.51 (s, 8H, CH_2), 2.03 (s, 12H, CH_3), -2.97 ppm (s, 2H, NH) ppm; ^{13}C NMR (101 MHz, DMSO-d_6) δ = 175.5, 167.3, 162.2, 141.4, 137.4, 136.7, 130.0, 128.6, 119.4, 119.1, 105.5, 68.8, 51.5, 48.6, 46.3, 42.2, 29.1, 27.4, 17.1 ppm; UV-vis (DMSO): λ_{max} (log ε) = 422 (5.68), 518 (4.27), 553 (3.94), 592 (3.76), 647 nm (3.65); HRMS (MALDI-TOF): *m/z* calcd. for $C_{76}H_{58}N_8O_{12}$ $[M]^+$: 1274.4174, 1274.4205 found.

5,10,15-Tris(3,5-bis(bromomethyl)phenyl)-20-(4-methoxycarbonylphenyl) porphyrin, 2.33

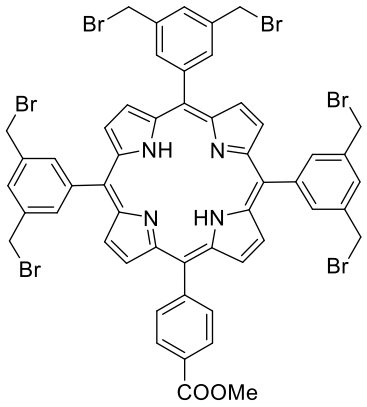

3,5-Bis(bromomethyl)benzaldehyde, **2.23**, (500 mg, 1.71 mmol) and methyl-4-formylbenzoate, **2.32**, (140 mg, 8.56×10^{-4} mol) were dissolved in dry DCM (200 mL) under argon. Pyrrole, **2.24**, (174 mg, 2.59 mmol) and $BF_3 \cdot Et_2O$ (37 mg, 2.25×10^{-4} mol) were added and the reaction was stirred at rt for 2 h. DDQ (588 mg, 2.59 mmol) was added and the reaction was stirred at rt for 2 h. TEA (10 µL) was added. The reaction mixture was filtered through a plug of silica (DCM) and the product was purified by silica gel column chromatography (DCM) to yield a purple solid (99 mg, 8.05×10^{-5} mol, 12%). M.p. = 170 °C; R_f = 0.90 (DCM); ^{1}H NMR (400 MHz, $CDCl_3$) δ = 8.90 – 8.81 (m, 8H, CH_β), 8.44 (d, J = 8.2 Hz, 2H, CH_{Ar}), 8.29 (d, J = 8.0 Hz, 2H, CH_{Ar}), 8.24 – 8.12 (m, 6H, CH_{Ar}), 7.89 – 7.79 (m, 3H, CH_{Ar}), 4.76 (s, 12H, CH_2), 4.11 (s, 3H, CH_3), -2.84 ppm (s, 2H, NH); ^{13}C NMR (101 MHz, $CDCl_3$) δ = 167.2, 146.6, 143.0, 137.1, 136.2, 135.0, 134.5, 131.4, 130.9, 129.8, 128.9, 128.0, 126.3, 118.9, 52.5, 32.8 ppm; UV-vis (DCM): λ_{max} (log ε) = 421 (5.90), 516 (4.30), 551 (3.92), 591 (3.79), 646 nm (3.58); HRMS (MALDI-TOF) m/z calcd. for $C_{52}H_{38}N_4O_2Br_6$ $[M]^+$: 1223.8095, 1223.8115 found.

5,10,15-Tris((4-pyridin-2(1H)-onemethyl)phenyl)-20-(4-methoxycarbonylphenyl)
porphyrin, 2.37

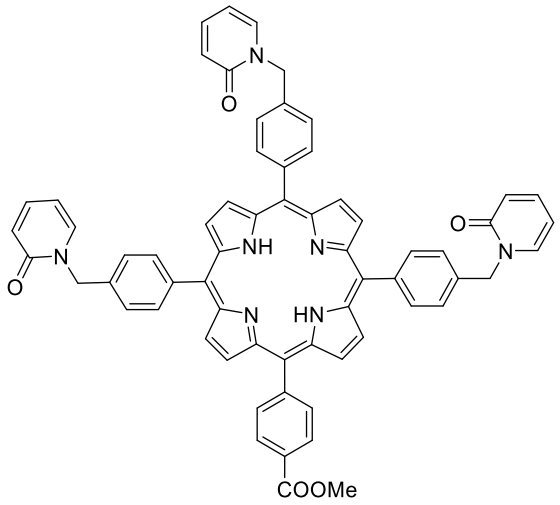

5,10,15-Tris(4-bromomethylphenyl)-20-(4-methoxycarbonylphenyl)porphyrin, **2.36** (300 mg, 3.16×10^{-4} mol) and 2-hydroxypyridine, **2.26**, (361 mg, 3.79 mmol) were dissolved in dry THF (70 mL) under anhydrous conditions. NaH (151 mg, 60% in mineral oil, 3.79 mmol) was washed with hexane, dissolved in dry THF (20 mL), and added to the reaction vessel. The reaction was heated to reflux for 5 h. The reaction was allowed to cool to rt and the precipitate was removed. The product was extracted with DCM (30 mL), dried *in vacuo*, and recrystallised from MeOH and DCM to yield purple crystals (74 mg, 7.44×10^{-5} mol, 23%). M.p. = 277 °C; ^{1}H NMR (400 MHz, $CDCl_3$) δ = 8.86 – 8.69 (m, 8H, CH_β), 8.42 (d, J = 8.2 Hz, 2H, CH_{Ar}), 8.27 (d, J = 8.2 Hz, 2H, CH_{Ar}), 8.17 (dd, J = 16.1, 8.0 Hz, 6H, CH_{Ar}), 7.64 (d, J = 8.0 Hz, 6H, CH_{Ar}), 7.58 (dd, J = 6.8, 1.9 Hz, 3H, CH_{Ar}), 7.44 (ddd, J = 8.8, 6.6, 1.9 Hz, 3H, CH_{Ar}), 6.75 (d, J = 9.2 Hz, 3H, CH_{Ar}), 6.32 (t, J = 6.7 Hz, 3H, CH_{Ar}), 5.49 (s, 6H, CH_2), 4.10 (s, 3H, CH_3), -2.84 ppm (d, J = 7.8 Hz, 2H, NH); ^{13}C NMR (101 MHz, $CDCl_3$) δ = 167.3, 162.9, 146.9, 141.6, 139.7, 137.6, 136.0, 134.9, 134.5, 129.6, 127.9, 126.2, 121.5, 119.7, 119.8, 118.7, 106.5, 52.4, 52.2, 52.1 ppm; UV-vis (DCM): λ_{max} (log ε) = 420 (5.96), 516 (4.12), 551 (3.81), 591 (3.62), 646 nm (3.49); HRMS (ESI) *m/z* calcd. for $C_{64}H_{47}N_7O_5$ $[M]^+$: 993.3639, 993.3638 found.

5,10,15-Tris((4-pyridin-3-methyl-2(1H)-one methyl)phenyl)-20-(4-methoxycarbonylphenyl)porphyrin, 2.38

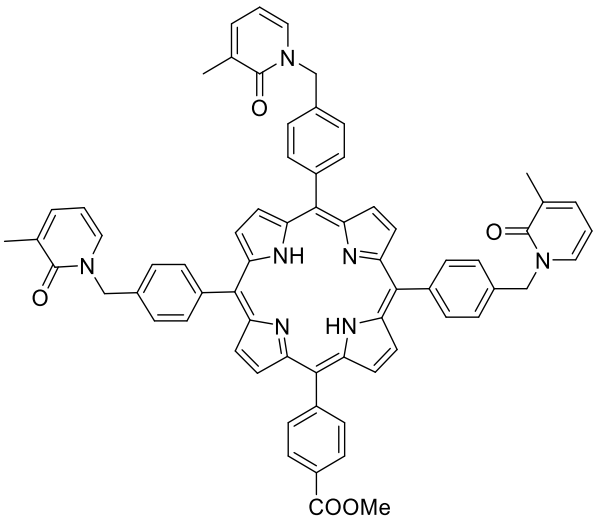

5,10,15-Tris(4-bromomethylphenyl)-20-(4-methoxycarbonylphenyl)porphyrin, **2.36** (200 mg, 2.10 x 10^{-4} mol,) and 2-hydroxy-3-methylpyridine, **2.27**, (345 mg, 3.15 mmol) were dissolved in dry THF (60 mL) under anhydrous conditions. NaH (167 mg, 60%, 4.20 mmol) was washed with hexane, dissolved in dry THF (10 mL), and added to the reaction vessel. The reaction was heated to reflux for 5 h. The reaction was allowed to cool to rt and the precipitate was removed. The product was extracted with DCM (30 mL), dried *in vacuo*, and recrystallised from MeOH and DCM to yield purple crystals (43 mg, 4.16 × 10^{-5} mol, 19% yield). M.p. >300 °C; ^{1}H NMR (400 MHz, $CDCl_3$): δ = 8.89 – 8.72 (m, 8H, CH_β), 8.43 (d, J = 8.3 Hz, 2H, CH_{Ar}), 8.28 (d, J = 8.3 Hz, 2H, CH_{Ar}), 8.18 (d, J = 8.1 Hz, 6H, CH_{Ar}), 7.69 (d, J = 7.6 Hz, 6H, CH_{Ar}), 7.50 (d, J = 7.1 Hz, 3H, CH_{Ar}), 7.30 (d, J = 6.8 Hz, 3H, CH_{Ar}), 6.26 (t, J = 6.8 Hz, 3H, CH_{Ar}), 5.54 (s, 6H, CH_2), 4.11 (s, 3H, COOCH_3), 2.23 (s, 9H, CH_3) - 2.85 ppm (s, 2H, NH); ^{13}C NMR (400 MHz, $CDCl_3$): δ = 163.2, 136.9, 135.0 134.9, 134.90, 134.5, 134.0, 127.9, 126.0, 106.2, 52.4 ppm; UV-vis (DCM): λ_{max} (log ε) = 422 (6.41), 517 (5.05), 552 (4.70), 592 (4.62), 647 nm (4.55).

6.3 CHAPTER 3: HEAVY-ATOM FREE SINGLET OXYGEN GENERATING BODIPY DYADS

6.3.1 Protocol for singlet oxygen quantum yield measurements

The procedure for the singlet oxygen quantum yield measurements was adapted from literature.[256] Solutions of DPBF, with an optical density of 1.0 in air-saturated EtOH were formulated. The corresponding BAD was added to the cuvette and its absorbance was adjusted to approximately 0.01 at the wavelength of irradiation. The solution in the cuvette was irradiated with a 532 nm laser light at a power density of 10 mW/cm^2. The absorption spectra of the solutions were measured every 10 s. The slope of plots of absorbance of DPBF at 414 nm *vs.* irradiation time for each photosensitizer was calculated. Singlet oxygen quantum yields were calculated according to the following equation:

$$\Phi_{\Delta} = \Phi_{\triangle}^{ref} \times \frac{k}{k_{ref}} \times \frac{I_{abs}^{ref}}{I_{abs}}$$

, where $\Phi_{\triangle}$ is the singlet oxygen quantum yield, the superscript *ref* stands for the reference compound, **3.15** (0.67 in EtOH),[265] *k* is the slope of the curves of DPBF absorption (414 nm) change *vs.* irradiation time, *I* represents the absorption correction factor which is given by $I = 1–10^{-OD}$ (OD is the optical density at 532 nm).

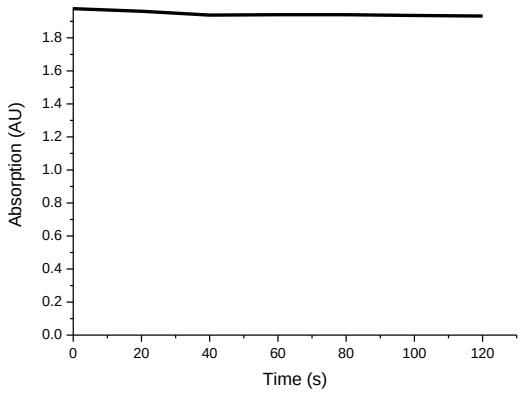

Figure 6.1: Change of DPBF absorption at 414 nm upon irradiation in air-saturated EtOH.

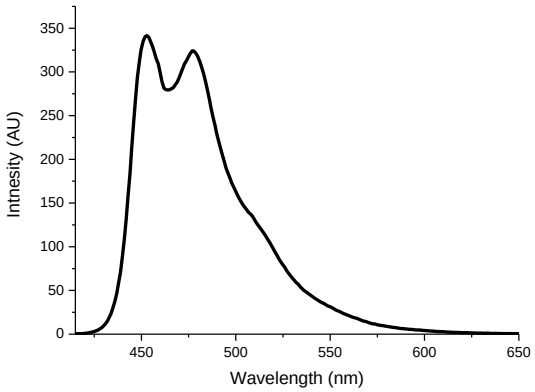

Figure 6.2: Fluorescence emission spectrum of DPBF at an excitation wavelength of 410 nm.

6.3.2 Protocol for fluorescence quantum yield measurements

A solutions of fluorescein in 0.1 M NaOH with an absorption between 0.03-0.07 was formulated. The fluorescence quantum yield of fluorescein is reported as 0.95.[278] The maximum absorbance and area under the curves emission was noted. BAD solutions of concentration 1×10^{-5} M were formulated and the maximum optical density and area under the emission curve was noted. The quantum yields were calculated according to the following equation:

$$\Phi_f = \Phi_{\mathrm{f}}^{ref} \times \frac{OD}{OD_{ref}} \times \frac{I_{abs}^{ref}}{I_{abs}} \times \frac{n^2}{n_{ref}^2}$$

, where Φ_f is the fluorescence quantum yield, the superscript *ref* stands for fluorescein, OD is the optical density, *I* is the integrated intensity, *n* is the refractive index.

6.3.3 Protocol for MDA-MB-468 cell cytotoxicity studies

For the photocytotoxicity studies the BADs were formulated in DMSO and diluted in appropriate medium (Dulbecco's Modified Eagle's Medium with 4.5 gL^{-1} glucose + 2 mM L-glutamine; no FBS) to give a range of concentrations (1–50 µM). The concentration of DMSO never exceeded 5.2%. The cells (MDA-MB-468) were adjusted to a concentration of 1×10^6 cells/mL and 800 µl was added to 200 µl of BAD stock solution to achieve the desired concentrations. The cells were then incubated in the dark for an h at 37 °C and 5% CO_2, after which they were washed with a three times excess of media and centrifuged to eliminate any unbound BAD. The final pellets of cells were re-suspended in 1 mL medium and 100 µL (8×10^4 cells) was transferred into two 96 wells plates in quadruplicate for each concentration. One plate was subsequently irradiated with light (400–700 nm; 20 J/cm^2) from an Oriel quartz tungsten halogen lamp (model 66188 powered by an Oriel 1100W radiometric power supply (model 69935). The second plate was kept in the dark and served as a "no light" control. After irradiation, 5 µL of Fetal Bovine Serum was added to each well and the plates were returned to the incubator overnight. After 18 to 24 h, an MTT cell viability assay[252] was performed and the results were expressed as percentage of cell viability *vs.* compound concentration; an LD_{50} (lethal dose where 50% of the cells are killed) was determined from the resulting curves. Each experiment was repeated in triplicate.[393]

6.3.4 Protocol for AY27 and F98 cell cytotoxicity studies

The cells were cultured and maintained in sterile 75 culture flasks cm^2 at 37 ºC in a humidified atmosphere containing 5% CO_2, in RPMI-1640 growth medium supplemented with 10% fetal bovine serum, 0.33% L-glutamine (200 mM,), and 1% penicillin/ streptomycin (10 U/mL/10 g/mL).

On day one of the PDT experiments, the cells were seeded in Petri dishes (6 cm × 1.5 cm), with 0.5×10^6 cells in 3 mL of media each, and incubated for 24 h at 37 °C. The BAD samples were formulated in DMSO and diluted in appropriate medium to give a concentration of 10 µM. On the second day, the culture medium was replaced with BAD-containing medium (10 µM) in the dishes marked for treatment. The control dishes and dishes only receiving light were refilled with the same amount of growth medium. From this point on, all of the cell dishes were maintained under dark

conditions using aluminum foil when not undergoing illumination. The cells were incubated for 24 h at 37 °C in the dark. On day three, the BAD-containing medium was removed from the dishes and the cells were washed twice with PBS to remove any extracellular traces of the photosensitiser. Then, a small amount of PBS was added to cover the cells during the illumination process. Immediately after the removal of the BAD-containing medium and the addition of PBS, the cells were placed on the LumiSource® lamp (435 nm, 12.9 mW/cm^2) for the specified time. When removed from the lamp, the dishes were quickly covered to avoid any excess illumination. After irradiation, the PBS was removed from the dishes and the cells were resupplied with growth medium. Before the MTT assay,[252] the cells were incubated overnight for 20 h. On the fourth day, the culture medium was removed and the cells were incubated with MTT solution (0.5 mg/mL) for 1 h at 37 °C. The MTT medium was replaced by isopropanol (2 mL) before being placed on a plate shaker for 30 min at 80 RPM. The cell suspensions were centrifuged for 5 min at 1500 RPM. The supernatants were diluted with isopropanol before the absorbance at 595 nm (using a Shimadzu UV-1700 spectrophotometer, China) was measured. The data was processed and compared to that of the untreated cells.[394]

6.3.5 X-ray crystallography details

The X-ray crystallography details of **3.64** are described in **Table 6.1**. Hydrogen atoms were generally placed in geometrically calculated positions and refined using a riding model. All images of **3.64** shown in Chapter 3 were prepared using Olex2.[391] The C and N bound H atoms were placed in their expected calculated positions and refined as riding model: C–H = 0.95–0.98 Å, with 1.2U_{eq} (C) for all H atoms. Further refinement of the sulfonate moiety proved to be unsuccessful and modelling H7B (water molecule) hampered the overall data quality.

Table 6.1: Details of XRD data refinement.

Compound	**3.64**
Empirical formula	$C_{53}H_{67}BN_4O_7S_2$
Formula weight	947.03
Temperature/K	100(2)
Crystal system	triclinic
Space group	$P\bar{1}$
a/Å	8.9627(4)
b/Å	9.3838(4)
c/Å	29.8177(11)
α/°	94.521(3)
β/°	96.534(3)
γ/°	93.269(3)
Volume/Å³	2478.23(18)
Z	2
D_{calc} *g/cm³*	1.269
μ/mm⁻¹	1.421
F(000)	1012.0
Crystal size/mm³	0.07×0.05×0.01
Radiation	CuK_α
Wavelength/Å	λ = 1.54178
2θ/°	5.988–134.05
Reflections collected	67748
Independent reflections	8733
R_{int}	0.1556
R_{sigma}	0.1152
Restraints	0
Parameters	615
GooF	1.037
R_1 *[I> 2σ (I)]*	0.0751,

wR2 [I> 2σ (I)]	0.1960
R1 [all data]	0.1192
wR2 [all data]	0.2304
Largest peak/e Å-3	0.69
Deepest hole/e Å-3	-0.53

6.3.6 General synthetic procedures

General Procedure A: BODIPY synthesis using unsubstituted pyrrole.

The appropriate aldehyde (1 eq.) and pyrrole (2 eq.) were dissolved in dry DCM and the solution was degassed with argon for 10 min. TFA (cat.) was added and the reaction mixture was stirred for 12 h under argon. NaOH (1 M solution) was added and the reaction was stirred for 20 min. The reaction mixture was washed with H_2O (2 × 50 mL), extracted with DCM, dried over Na_2SO_4 and evaporated *in vacuo*. The product was dissolved in dry DCM under argon and DDQ (1 eq.) was added following stirring at rt for 20 min. Following the addition of H_2O (75 mL), the organic layer was extracted with DCM (3 × 100 mL) and dried over Na_2SO_4. The product was dried *in vacuo* and the resulting solid was dissolved in DCM and stirred under an argon atmosphere. DIPEA (10 eq.) was added and the mixture was stirred for another 5 min. $BF_3 \cdot Et_2O$ (10 eq.) was added, the reaction flask was shielded from light and the solution was stirred for 1.5 h. The reaction mixture was washed with H_2O (2 × 50 mL), extracted with DCM (50 mL), dried over Na_2SO_4 and evaporated *in vacuo*. The crude products were purified by silica gel column chromatography (DCM/hexane, 1:1) or (DCM).

General Procedure B: BODIPY synthesis using substituted pyrrole.

The appropriate aldehyde (1 eq.) and pyrrole (2 eq.) were dissolved in dry DCM and the solution was degassed with argon for 10 min. TFA (cat.) was added and the reaction mixture was stirred for 12 h under argon. DDQ (1 eq.) was added and the mixture was stirred for another 20 min. The reaction mixture was washed with H_2O (2 × 50 mL), extracted with DCM, dried over Na_2SO_4 and evaporated *in vacuo*. The resulting solid was dissolved in DCM and stirred under argon atmosphere. DIPEA (10 eq.) was added and the mixture was stirred for another 5 min. $BF_3 \cdot Et_2O$ (10 eq.) was added, the reaction flask was shielded from light and the solution was stirred

for 1.5 h. The reaction mixture was washed with H_2O (2 × 50 mL), extracted with DCM (50 mL), dried over Na_2SO_4 and evaporated *in vacuo*. The crude products were purified by silica gel column chromatography (DCM/hexane, 1:1) or (DCM).

General Procedure C: Fluorine substitution.

To a solution of 3-dimethylamino-1-propyne (4.5 eq.) in dry THF was added *n*-BuLi (4 eq.). The mixture was stirred at rt for 30 min. BODIPY (1 eq.) dissolved in dry THF was added dropwise to the reaction and the reaction was stirred at rt for 2 h. The reaction was quenched with H_2O and concentrated. The residue was dissolved in DCM, washed with H_2O (3 × 100 mL) and extracted with DCM (3 × 100 mL). The product was purified by silica gel column chromatography (DCM/MeOH, 10:1).

General Procedure D: Sulfonation.

Dimethylaminopropyne-substituted dyad (1 eq.) was dissolved in EtOAc and the solution was heated to reflux under argon. A solution of 1,3-propanesultone (6 eq.) in EtOAc (2 mL) was added and the reaction mixture was refluxed for 2 h. After cooling to rt the precipitate formed was filtered and carefully washed with Et_2O. The obtained product was dried at 80 °C.

6.3.7 Synthetic details and characterisation

9-Bromo-10-phenylanthracene, **2.29**,[275] 10-phenylanthracene-9-carbaldehyde, **3.30**,[274] 4-(10-phenylanthracen-9-yl)benzaldehyde, **3.31**,[275] and 2-methylpyrrole, **3.35**,[276] were synthesised using adapted literature procedures and charaterized in accordance with literature. 1,3,5,7-Tetramethyl-8-(10-methylanthracen-9-yl)-4,4-difluoro-4-bora-3a,4a-diaza-*s*-indacene, **3.15**, was synthesised and characterized in accordance with literature.[265] 8-(Pyren-9-yl)-4,4-difluoro-4-bora-3a,4a-diaza-*s*-indacene, **3.33** was characterized in accordance with literature.[395] 1,3,5,7-Tetramethyl-8-(3,4,5-trimethoxyphenyl)-4,4-difluoro-4-bora-3a,4a-diaza-*s*-indacene, **3.72**,[396] and 1,3,5,7-tetramethyl-8-(2,4,5-trimethoxyphenyl)-4,4-difluoro-4-bora-3a,4a-diaza-*s*-indacene, **3.76**[284,397] were synthesised in accordance with general procedure B and characterized in accordance with literature.

8-(Anthracen-9-yl)-4,4-difluoro-4-bora-3a,4a-diaza-*s*-indacene, 3.38

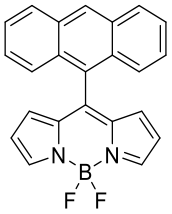

Compound **3.38** was synthesised in accordance with general procedure A using anthracene-9-carbaldehyde (500 mg, 2.43 mmol), 2-methyl-1H-pyrrole (91 mg 4.85 mmol), dry DCM (160 mL), TFA (10 µL), NaOH (1 M solution, 10 mL), DDQ (550 mg, 2.42 mmol), DIPEA (3.13 g, 2.43×10^{-2} mol), and $BF_3 \cdot Et_2O$ (3.44 g, 2.43×10^{-2} mol) to yield a green orange solid (146 mg, 3.96×10^{-4} mol, 17%). M.p. >250 °C; R_f = 0.32 (DCM/hexane, 1:1); ^{1}H NMR (400 MHz, $CDCl_3$) δ = 8.61 (s, 1H, CH_{Ar}), 8.06 (d, J = 8.5 Hz, 2H, CH_{Ar}), 7.99 (s, 2H, CH_{Ar}), 7.79 (dt, J = 4.7, 2.4 Hz, 2H, CH_{Ar}), 7.51 – 7.45 (m, 2H, CH_{Ar}), 7.40 (ddd, J = 8.6, 6.5, 1.3 Hz, 2H, C$H_{pyrrole}$), 6.36 ppm (d, J = 5.3 Hz, 4H, CH_{pyrroe}); ^{13}C NMR (101 MHz, $CDCl_3$) δ = 144.6, 136.9, 131.2, 130.8, 129.1, 128.3, 126.8, 126.0, 125.6, 118.8 ppm; UV-vis (DCM): λ_{max} (log ε) = 351 (4.11), 368 (4.23), 387 (4.16), 507 nm (4.55); HRMS (ESI) *m/z* calcd. for $C_{23}H_{16}BF_2N_2$ $[M+H]^+$: 369.1373, 369.1341 found.

8-(10-Phenylanthracen-9-yl)-4,4-difluoro-4-bora-3a,4a-diaza-*s*-indacene, 3.40

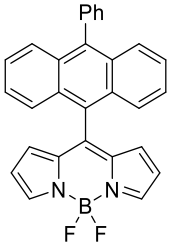

Compound **3.40** was synthesised in accordance with general procedure A using aldehyde **3.30** (300 mg, 1.06 mmol), pyrrole (20 mL), TFA (10 µL), NaOH (1M solution, 10 mL), dry DCM (140 mL), DDQ (240 mg, 1.06 mmol), H_2O (75 mL), DIPEA (1.37 g, 0.01 mol), and $BF_3 \cdot Et_2O$ (1.51 g, 0.01 mol) to yield a green orange solid (165 mg, 3.71×10^{-4} mol, 35%). M.p. >250 °C; R_f = 0.45 (DCM/hexane, 1:1); ^{1}H NMR (400 MHz, $CDCl_3$) δ = 8.03 (s, 2H, CH_{Ar}), 7.88 – 7.85 (m, 2H, CH_{Ar}), 7.73 – 7.70 (m, 2H, CH_{Ar}), 7.66 – 7.56 (m, 3H, CH_{Ar}), 7.53 – 7.47 (m, 2H, CH_{Ar}), 7.43 – 7.33 (m, 4H, C$H_{Ar/pyrrole}$), 6.49 (d, J = 4.1 Hz, 2H, C$H_{pyrrole}$), 6.42 ppm (d, J = 3.1 Hz, 2H, C$H_{pyrrole}$); ^{13}C NMR (100 MHz, $CDCl_3$) δ = 146.0, 144.8, 140.0, 138.4, 137.3,

131.5, 131.2, 130.6, 129.6, 128.7, 128.0, 127.2, 126.6, 126.6, 126.3, 125.6, 119.1 ppm; UV−vis (DCM): λ_{max} (log ε) = 356 (4.21), 374 (4.35), 394 (4.29), 506 nm (4.84); HRMS (ESI): *m/z* calcd. for $C_{29}H_{19}BF_2N_2$ $[M]^+$: 444.1609, 444.1630 found.

8-(9,10-Diphenylanthracen-9-yl)-4,4-difluoro-4-bora-3a,4a-diaza-*s*-indacene, 4.41

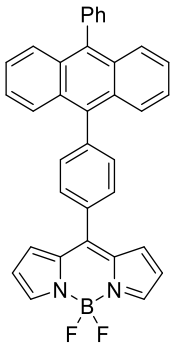

Compound **3.41** was synthesised in accordance with general procedure A using aldehyde **3.31** (200 mg, 5.59 × 10^{-4} mol), pyrrole (75 mg 1.17 mmol), dry DCM (160 mL), TFA (10 µL), NaOH (1 M solution, 10 mL), DDQ (125 mg, 5.59 × 10^{-4} mmol), H_2O (75 mL), DIPEA (720 mg, 5.59 mmol), and $BF_3{\cdot}Et_2O$ (794 mg, 1.53 mmol) to yield a green orange solid (33 mg, 6.35 × 10^{-6} mol, 11%). M.p. >250 °C; R_f = 0.39 (DCM/hexane, 1:1); ^{1}H NMR (400 MHz, $CDCl_3$) δ = 8.01 (s, 2H, C*H*$_{Ar}$), 7.83 (d, *J* = 8.0 Hz, 2H, C*H*$_{Ar}$), 7.75 – 7.57 (m, 9H, C*H*$_{Ar}$), 7.50 – 7.47 (m, 2H, C*H*$_{pyrrole}$), 7.42 – 7.34 (m, 4H, C*H*$_{Ar}$), 7.19 (t, *J* = 4.9 Hz, 2H, C*H*$_{pyrrole}$), 6.63 ppm (dd, *J* = 5.5, 4.2 Hz, 2H, C*H*$_{pyrrole}$); ^{13}C NMR (101 MHz, $CDCl_3$) δ = 144.2, 142.2, 138.8, 137.9, 135.3, 131.6, 131.2, 130.7, 129.9, 129.6, 128.4, 127.9, 127.6, 127.2, 126.3, 125.5, 125.1, 118.6 ppm; UV-vis (DCM): λ_{max} (log ε) = 356 (4.32), 374 (4.35), 393 (4.23), 502 nm (4.72); HRMS (ESI): *m/z* calcd. for $C_{35}H_{23}BF_2N_2$ $[M]^+$: 520.1934, 520.1941 found.

3,5-Dimethyl-8-(anthracen-9-yl)-4,4-difluoro-4-bora-3a,4a-diaza-*s*-indacene, 3.42

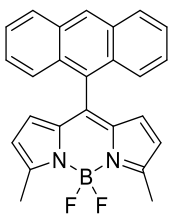

Compound **3.42** was synthesised in accordance with general procedure B using anthracene-9-carbaldehyde (750 mg, 3.64 mmol), 2-methyl-1H-pyrrole (589 mg 7.27 mmol), dry DCM (80 mL), TFA (10 µL), DDQ (826 mg, 3.64 mmol), H_2O (75 mL), DIPEA (4.70 g, 3.64×10^{-2} mol), and $BF_3 \cdot Et_2O$ (5.17 g, 3.64×10^{-2} mol) to yield an orange solid (529 mg, 1.34 mmol, 37%). M.p. >250 °C; R_f = 0.47 (DCM/hexane, 1:1); ^{1}H NMR (400 MHz, $CDCl_3$) δ = 8.57 (s, 1H, CH_{Ar}), 8.03 (d, J = 8.5 Hz, 2H, CH_{Ar}), 7.86 (dd, J = 8.8, 0.8 Hz, 2H, CH_{Ar}), 7.50 – 7.42 (m, 2H, CH_{Ar}), 7.41 – 7.34 (m, 2H, CH_{Ar}), 6.12 (dd, J = 16.3, 4.1 Hz, 4H, C$H_{pyrrole}$), 2.70 ppm (s, 6H, CH_3); ^{13}C NMR (101 MHz, $CDCl_3$) δ = 158.0, 139.9, 136.3, 130.9, 130.8, 130.1, 128.6, 128.2, 127.1, 126.4, 126.3, 125.5, 119.8, 15.0 ppm; UV-vis (DCM): λ_{max} (log ε) = 349 (4.46), 366 (4.57), 386 (4.49), 517 nm (5.31); HRMS (ESI) *m/z* calcd. for $C_{25}H_{20}BF_2N_2$ $[M+H]^+$: 397.1687, 397.1677 found.

3,5-Dimethyl-8-(9-phenylanthracene-9-yl)-4,4-difluoro-4-bora-3a,4a-diaza-*s*-indacene, 3.43

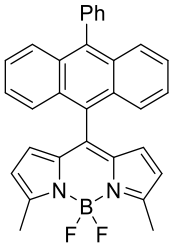

Compound **3.43** was synthesised in accordance with general procedure B using aldehyde **3.30** (200 mg, 7.09×10^{-4} mol), 2-methyl-1H-pyrrole (115 mg 1.42 mmol), dry DCM (40 mL), TFA (10 µL), DDQ (161 mg, 7.09×10^{-4} mol), H_2O (70 mL), DIPEA (915 mg, 7.09 mmol), and $BF_3 \cdot Et_2O$ (1.01 g, 7.09 mmol) to yield an orange solid (117 mg, 2.48×10^{-4} mol, 35%). M.p. = 290 °C; R_f = 0.48 (DCM/hexane, 1:1); ^{1}H NMR (400 MHz, $CDCl_3$) δ = 7.92 (dd, J = 7.9, 1.2 Hz, 2H, CH_{Ar}), 7.69 (dd, J = 7.7, 1.1 Hz, 2H, CH_{Ar}), 7.65 – 7.55 (m, 3H, CH_{Ar}), 7.51 – 7.44 (m, 2H, CH_{Ar}), 7.36 (dddd, J = 10.0, 7.9, 6.5, 1.4 Hz, 4H, CH_{Ar}), 6.26 (d, J = 4.1 Hz, 2H, C$H_{pyrrole}$), 6.15 (d, J = 4.1 Hz, 2H, C$H_{pyrrole}$), 2.72 ppm (s, 6H, CH_3); ^{13}C NMR (101 MHz, $CDCl_3$) δ = 158.0, 140.3, 139.2, 138.4, 136.5, 131.1, 130.6, 130.2, 129.4, 128.5, 127.8, 127.0, 126.4, 126.1, 125.3, 119.8, 15.0 ppm; UV-vis (DCM): λ_{max} (log ε) = 357 (4.09), 374 (4.22), 395 (4.14), 518 nm (4.90); HRMS (ESI) *m/z* calcd. for $C_{31}H_{24}BF_2N_2$ $[M+H]^+$: 473.2001, 473.2017 found.

3,5-Dimethyl-8-(9,10-diphenylanthracen-9-yl)-4,4-difluoro-4-bora-3a,4a-diaza-*s*-indacene, 3.44

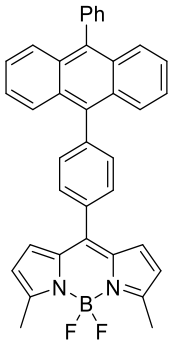

Compound **3.44** was synthesised in accordance with general procedure B using aldehyde **3.31** (200 mg, 5.59 × 10^{-4} mol), 2-methyl-1H-pyrrole (91 mg, 1.12 mmol), dry DCM (140 mL), TFA (10 µL), DDQ (125 mg, 5.59 mmol), DIPEA (712 mg, 1.59 mmol), and $BF_3{\cdot}Et_2O$ (793 mg, 5.59 mmol) to yield an orange solid (52 mg, 9.45 × 10^{-5} mol, 17%). M.p. >250 °C; R_f = 0.45 (DCM/hexane, 1:1); ^{1}H NMR (400 MHz, $CDCl_3$) δ = 7.78 – 7.69 (m, 6H, CH_{Ar}), 7.65 – 7.56 (m, 5H, CH_{Ar}), 7.52 – 7.48 (m, 2H, CH_{Ar}), 7.42 – 7.34 (m, 4H, CH_{Ar}), 6.98 (d, J = 4.1 Hz, 2H, C$H_{pyrrole}$), 6.37 (d, J = 4.1 Hz, 2H, C$H_{pyrrole}$), 2.71 ppm (s, 6H, CH_3); ^{13}C NMR (101 MHz, $CDCl_3$) δ = 157.7, 142.3, 141.2, 138.8, 137.7, 135.7, 134.6, 133.4, 131.2, 130.5, 129.8, 128.4, 127.6, 127.2, 126.5, 125.4, 125.1, 119.5, 15.0 ppm; UV-vis (DCM): λ_{max} (log ε) = 356 (4.30), 376 (4.33), 395 (4.25), 513 nm (4.89); HRMS (ESI) *m/z* calcd. for $C_{37}H_{28}BF_2N_2$ $[M+H]^+$: 549.2315, 549.2282 found.

1,3,5,7-Tetramethyl-8-(10-phenylanthracen-9-yl)-4,4-difluoro-4-bora-3a,4a-diaza-*s*-indacene, 3.46

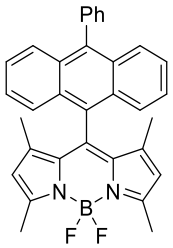

Compound **3.46** was synthesised in accordance with general procedure B using aldehyde **3.30** (200 mg, 7.09 × 10^{-4} mol), 2,4-dimethyl-1H-pyrrole (135 mg 1.42 mmol), DCM (40 mL), TFA (10 µL), DDQ (161 mg, 7.09 × 10^{-4} mol), H_2O (70 mL),

DIPEA (918 mg, 7.09 mmol), and $BF_3{\cdot}Et_2O$ (1 g, 7.09 mmol) to yield an orange solid (270 mg, 5.40 × 10^{-4} mol, 76%). M.p. >250 °C; R_f = 0.32 (DCM/hexane, 1:1); ^{1}H NMR (400 MHz, $CDCl_3$) δ = 7.98 – 7.94 (m, 2H, CH_{Ar}), 7.68 (d, J = 8.5 Hz, 2H, CH_{Ar}), 7.64 – 7.54 (m, 3H, CH_{Ar}), 7.49 – 7.44 (m, 2H, CH_{Ar}), 7.38 (dddd, J = 10.1, 7.8, 6.5, 1.3 Hz, 4H, CH_{Ar}), 5.93 (s, 2H, C$H_{pyrrole}$), 2.64 (s, 6H, CH_3), 0.75 ppm (s, 6H, CH_3); ^{13}C NMR (101 MHz, $CDCl_3$) δ = 155.8, 142.9, 139.4, 139.3, 138.3, 132.5, 131.3, 129.9, 129.3, 128.4, 128.2, 127.7, 127.0, 126.6, 125.6, 125.2, 121.2, 14.7, 13.4 ppm; UV-vis (DCM): λ_{max} (log ε) = 357 (4.15), 375 (4.30), 396 (4.24), 506 nm (4.98); HRMS (ESI) *m/z* calcd. for $C_{33}H_{27}BF_2N_{22}$ $[M+H]^+$: 501.2314, 501.2330 found.

2,6-Diethyl-1,3,5,7-tetramethyl-8-(10-phenylanthracen-9-yl)-4,4-difluoro-4-bora-3a,4a-diaza-*s*-indacene, 3.50

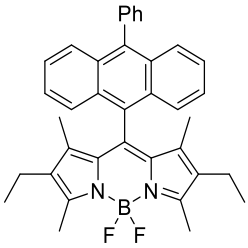

Compound **3.50** was synthesised in accordance with general procedure B using aldehyde **3.30** (300 mg, 1.06 mmol), 3-ethyl-2,4-dimethyl-1H-pyrrole (261 mg, 2.13 mmol), dry DCM (40 mL), TFA (10 µL), DDQ (241 mg, 1.06 mmol), H_2O (30 mL), DIPEA (1.39 g, 1.06 × 10^{-2} mol), $BF_3{\cdot}Et_2O$ (1.3 mL, 1.06 × 10^{-2} mol), and H_2O (70 mL) to yield an orange solid (129 mg, 2.33 × 10^{-4} mol, 22%). M.p. >250 °C; R_f = 0.56 (DCM/hexane, 1:1); ^{1}H NMR (400 MHz, $CDCl_3$) δ = 8.01 – 7.94 (m, 2H, CH_{Ar}), 7.69 – 7.64 (m, 2H, CH_{Ar}), 7.64 – 7.53 (m, 3H, CH_{Ar}), 7.49 – 7.43 (m, 2H, CH_{Ar}), 7.36 (dddd, J = 10.0, 7.8, 6.5, 1.3 Hz, 4H, CH_{Ar}), 2.60 (s, 6H, CH_3), 2.25 – 2.16 (m, 4H, CH_2), 0.92 – 0.78 (m, 6H, CH_3), 0.64 ppm (s, 6H, CH_3); ^{13}C NMR (100 MHz, $CDCl_3$) δ = 154.0, 139.1, 138.4, 138.2, 132.7, 131.8, 131.3, 129.9, 129.5, 128.4, 127.7, 126.9, 126.4, 125.5, 17.0, 14.6, 12.6, 10.6 ppm; UV-vis (DCM): λ_{max} (log ε) = 359 (4.14), 375 (4.31), 396 (4.29), 532 (4.90); HRMS (ESI): *m/z* calcd. for $C_{37}H_{35}BN_2F_2$ $[M]^+$: 556.2861, 556.2861 found.

2,6-Diethyl-1,3,5,7-tetramethyl-8-(9,10-diphenylanthracen-9-yl)-4,4-difluoro-4-bora-3a,4a-diaza-*s*-indacene, 3.51

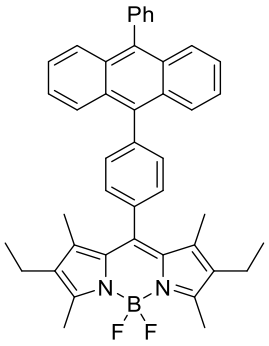

Compound **3.51** was synthesised in accordance with general procedure B using aldehyde **3.31** (200 mg, 5.58 × 10^{-4} mol), 3-ethyl-2,4-dimethyl-1H-pyrrole (138 mg 1.12 mmol), DCM (40 mL), TFA (10 µL), DDQ (125 mg, 5.58 × 10^{-4} mol), H_2O (70 mL), DIPEA (720 mg, 5.58 mmol), and $BF_3{\cdot}Et_2O$ (792 mg, 5.58 mmol) to yield an orange solid (43 mg, 6.8 × 10^{-5} mol, 12%). M.p. >250 °C; R_f = 0.55 (DCM/hexane, 1:1), ^{1}H NMR (400 MHz, $CDCl_3$) δ = 7.76 – 7.46 (m, 13H, CH_{Ar}), 7.40 – 7.31 (m, 4H, CH_{Ar}), 2.58 (s, 6H, CH_3), 2.43 – 2.32 (m, 4H, CH_2), 1.64 (s, 6H, CH_3), 1.05 ppm (t, J = 7.6 Hz, 6H, CH_3); ^{13}C NMR (101 MHz, $CDCl_3$) δ = 153.9, 140.0, 139.6, 138.9, 138.2, 137.6, 136.0, 135.2, 133.0, 132.1, 131.2, 130.9, 129.9, 129.7, 128.5, 127.6, 127.2, 126.3, 125.3, 125.0, 17.2, 14.7, 12.6, 12.0 ppm; UV-vis (DCM): λ_{max} (log ε) = 358 (4.20), 376 (4.37), 396 (4.34), 527 (4.90), HRMS (ESI) *m/z* calcd. for $C_{43}H_{40}BF_2N_2$ $[M+H]^+$: 631.3109, 631.3115 found.

4-(Pyrene-1-yl)benzaldehyde, 3.33

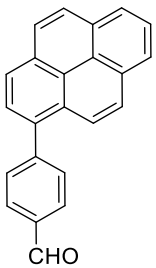

A mixture of bromopyrene, **3.33**, (500 mg, 1.79 mmol), 4-formylphenylboronic acid (320 mg, 2.13 mmol), tetrakis(triphenylphosphine)palladium (104 mg, 8.96 × 10^{-5} mol), K_2CO_3 (589 mg, 2.13 mmol), benzene (20 mL), H_2O (8 mL), and EtOH (4 mL) was heated to reflux for 48 h. The product was extracted with DCM (3 × 100 mL), washed with brine (3 × 100 mL), dried over Na_2SO_4 and the solvent was removed *in*

vacuo. The product was purified by silica gel column chromatography (DCM/hexane 1:1) and recrystallised from DCM and MeOH to yield colorless crystals (438 mg, 1.43 mmol, 80%). M.p. = 147 °C; R_f = 0.62 (DCM/hexane, 1:1); ^{1}H NMR (400 MHz, $CDCl_3$) δ = 10.15 (s, 1H, CH_{Ar}), 8.27 – 7.92 (m, 11H, CH_{Ar}), 7.82 ppm (t, J = 8.3 Hz, 2H, CH_{Ar}); ^{13}C NMR (101 MHz, $CDCl_3$) δ = 192.0, 147.7, 136.0, 135.2, 131.4, 131.3, 131.2, 130.8, 129.8, 128.3, 128.0, 127.9, 127.3, 127.2, 126.2, 125.5, 125.2, 124.9, 124.8, 124.7, 124.6 ppm.

2,6-Diethyl-1,3,5,7-tetramethyl-8-(pyrene-1-yl)-4,4-difluoro-4-bora-3a,4a-diaza-*s*-indacene, 3.55

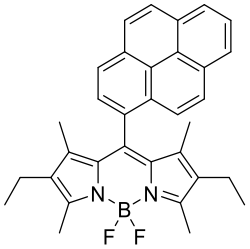

Compound **3.55** was synthesised in accordance with general procedure B using 10-phenylanthracene-9-carbaldehyde (1 g, 4.35 mmol), 3-ethyl-2,4-dimethyl-1H-pyrrole (1.07 g, 8.70 mmol), dry DCM (40 mL) under argon, TFA (10 µL), DDQ (986 mg, 4.35 mmol), H_2O (30 mL), DIPEA (5.6 g, 4.35 × 10^{-2} mol), and $BF_3{\cdot}Et_2O$ (6.12 g, 4.35 × 10^{-2} mol) to yield an orange solid (363 mg, 7.20 × 10^{-4} mol, 16%). M.p. >250 °C; R_f = 0.32 (DCM/hexane, 1:1); ^{1}H NMR (400 MHz, $CDCl_3$) δ = 8.29 – 8.11 (m, 5H, CH_{Ar}), 8.07 – 7.99 (m, 3H, CH_{Ar}), 7.88 (d, J = 7.8 Hz, 1H, CH_{Ar}), 2.59 (s, 6H, CH_3), 2.27 – 2.17 (m, 4H, CH_2), 0.90 (q, J = 7.4 Hz, 6H, CH_3), 0.77 ppm (s, 6H, CH_3); ^{13}C NMR (101 MHz, $CDCl_3$) δ = 153.9, 138.9, 138.4, 132.8, 131.6, 131.3, 131.0, 130.3, 129.5, 128.7, 128.2, 127.3, 126.4, 126.1, 125.6, 125.2, 124.7, 17.0, 14.6, 12.6, 11.1 ppm; UV-vis (DCM): λ_{max} (log ε) = 327 (4.45), 343 (4.59), 5.29 nm (4.79); HRMS (ESI): *m/z* calcd. for $C_{33}H_{32}B_2N_2$ $[M+H]^+$: 505.2626, 505.2628 found.

3,5-Dimethyl-8-(4-phenylpyrene-1-yl)-4,4-difluoro-4-bora-3a,4a-diaza-*s*-indacene, 3.57

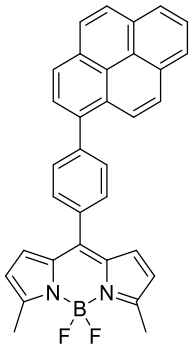

Compound **3.57** was synthesised in accordance with general procedure B using aldehyde **3.33** (130 mg, 4.25×10^{-4} mol), 2-methyl-1H-pyrrole (69 mg, 8.49×10^{-4} mol), DCM (40 mL), TFA (10 µL), DDQ (100 mg, 4.25×10^{-4} mol), H_2O (20 mL), DIPEA (550 mg, 4.25 mmol), and $BF_3 \cdot Et_2O$ (603 mg, 4.25 mmol) to yield an orange solid (28 mg, 5.82×10^{-5} mol, 13%). M.p. >250 °C; R_f = 0.44 (DCM/hexane, 1:1); ^{1}H NMR (400 MHz, $CDCl_3$) δ = 8.28 – 8.16 (m, 4H, CH_{Ar}), 8.13 – 7.99 (m, 5H, CH_{Ar}), 7.72 (dd, J = 23.8, 7.5 Hz, 4H, CH_{Ar}), 6.91 (s, 2H, C$H_{pyrrole}$), 6.33 (s, 2H, C$H_{pyrrole}$), 2.69 ppm (s, 6H, CH_3); ^{13}C NMR (101 MHz, $CDCl_3$) δ = 157.6, 143.1, 142.3, 136.4, 134.5, 133.1, 131.5, 130.9, 130.9, 130.4, 130.5, 130.4, 128.4, 127.9, 127.8, 127.5, 127.4, 126.1, 125.4, 125.0, 125.0, 124.8, 124.8, 124.8, 119.5, 29.7, 14.9, 1.0 ppm; UV-vis (DCM): λ_{max} (log ε) = 375 (4.89), 395 (4.70), 513 nm (4.60); HRMS (ESI) *m/z* calcd. for $C_{33}H_{23}BF_2N_2$ $[M+H]^+$: 497.2001, 497.1997 found.

3,5-Dimethyl-8-(anthracen-9-yl)-4,4-(3-(dimethylamino)prop-1-yn-1-yl)-4-bora-3a,4a-diaza-*s*-indacene, 3.83

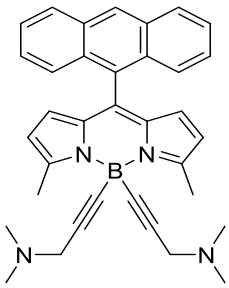

Compound **3.83** was synthesised in accordance with general procedure C using 3-dimethylamino-1-propyne (377 mg, 4.55 mmol), dry THF (20 mL), *n*-BuLi (258 mg, 4.04 mmol), and compound **3.42** (400 mg, 1.01 mmol) dissolved in dry THF (50 mL) to yield an orange solid (388 mg, 7.43×10^{-4} mol, 74%). M.p. >250 °C; R_f = 0.69 (DCM/MeOH, 9:1); ^{1}H NMR (400 MHz, $CDCl_3$) δ = 8.55 (s, 1H, CH_{Ar}), 8.01 (d, J =

8.5 Hz, 2H, CH_{Ar}), 7.84 (dd, J = 8.7, 0.8 Hz, 2H, CH_{Ar}), 7.47 – 7.40 (m, 2H, CH_{Ar}), 7.35 (ddd, J = 8.6, 6.5, 1.3 Hz, 2H, CH_{Ar}), 6.19 – 6.07 (m, 4H, C$H_{pyrrole}$), 3.31 (s, 4H, CH_2), 2.89 (s, 6H CH_3), 2.35 ppm (s, 12H, NCH_3); ^{13}C NMR (101 MHz, $CDCl_3$) δ = 157.3, 139.4, 134.3, 130.9, 130.8, 128.2, 128.1, 128.0, 127.9, 126.4, 126.3, 125.4, 119.8, 49.1, 44.2, 16.4 ppm; UV-vis (DCM): λ_{max} (log ε) = 349 (4.22), 366 (4.34), 386 (4.28), 513 nm (5.11); HRMS (ESI) *m/z* calcd. for $C_{35}H_{36}BN_4$ $[M+H]^+$: 523.2574, 523.2594 found.

1,3,5,7-Tetramethyl-8-(anthracen-9-yl)-4,4-(3-(dimethylamino)prop-1-yn-1-yl)-4-bora-3a,4a-diaza-*s*-indacene, 3.84

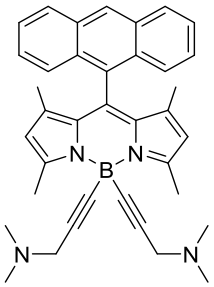

Compound **3.84** was synthesised in accordance with general procedure C using 3-dimethylamino-1-propyne (352 mg, 4.25 mmol), dry THF (20 mL), *n*-BuLi (241 mg, 3.77 mmol), and compound **3.45** (400 mg, 9.43×10^{-4} mol) dissolved in dry THF (50 mL) to yield an orange solid (303 mg, 5.51×10^{-4} mol, 59%). M.p. >250 °C; R_f = 0.50 (DCM/MeOH, 9:1); ^{1}H NMR (400 MHz, $CDCl_3$) δ = 8.55 (s, 1H, CH_{Ar}), 8.01 (d, J = 8.3 Hz, 2H, CH_{Ar}), 7.90 (d, J = 8.7 Hz, 2H, CH_{Ar}), 7.52 – 7.43 (m, 2H, CH_{Ar}), 7.43 – 7.33 (m, 2H, CH_{Ar}), 5.93 (d, J = 14.8 Hz, 2H, C$H_{pyrrole}$), 3.43 – 3.21 (m, 4H, CH_2), 2.82 (s, 6H, C$H_{3pyrrole}$), 2.37 (d, J = 7.3 Hz, 12H, NCH_3), 0.61 ppm (s, 6H, C$H_{3pyrrole}$); ^{13}C NMR (101 MHz, $CDCl_3$) δ = 155.3, 140.6, 138.7, 131.3, 130.4, 129.8, 129.0, 128.2, 128.0, 126.8, 125.7, 125.3, 121.4, 49.0, 44.1, 16.3, 13.5 ppm; UV-vis (DCM): λ_{max} (log ε) = 504 (5.20), 388 (4.33), 368 (4.40), 350 nm (4.25); HRMS (ESI): *m/z* calcd. for $C_{37}H_{40}BN_4$ $[M+H]^+$: 551.3347, 551.3343 found.

3,5-Dimethyl-8-(10-phenylanthracen-9-yl)-4,4-(3-(dimethylamino)prop-1-yn-1-yl)-4-bora-3a,4a-diaza-*s*-indacene, 3.85

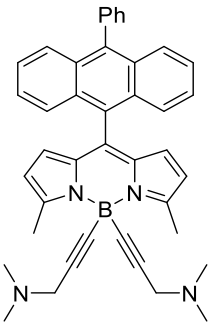

Compound **3.85** was synthesised in accordance with general procedure C using 3-dimethylamino-1-propyne (336 mg, 4.05 mmol), dry THF (20 mL), *n*-BuLi (230 mg, 3.60 mmol), and compound **3.43** (400 mg, 8.99×10^{-4} mol) dissolved in dry THF (50 mL) to yield an orange solid (330 mg, 5.51×10^{-4} mol, 61%). M.p. >250 °C; R_f = 0.54 (DCM/MeOH, 9:1); ^{1}H NMR (400 MHz, $CDCl_3$) δ = 7.92 – 7.86 (m, 2H, CH_{Ar}), 7.69 – 7.64 (m, 2H, CH_{Ar}), 7.63 – 7.53 (m, 3H, CH_{Ar}), 7.49 – 7.45 (m, 2H, CH_{Ar}), 7.36 – 7.28 (m, 4H, CH_{Ar}), 6.23 (d, J = 4.2 Hz, 2H, C$H_{pyrrole}$), 6.17 (d, J = 4.2 Hz, 2H, C$H_{pyrrole}$), 3.35 (d, J = 9.5 Hz, 4H, CH_2), 2.88 (d, J = 10.6 Hz, 6H, C$H_{3pyrrole}$), 2.38 ppm (d, J = 9.9 Hz, 12H, NCH_3); ^{13}C NMR (101 MHz, $CDCl_3$) δ = 157.3, 139.8, 138.9, 138.5, 134.5, 131.1, 130.5, 129.4, 128.4, 128.1, 127.9, 127.7, 126.9, 126.6, 126.0, 125.2, 119.9, 49.0, 44.1, 16.4 ppm; UV-vis (DCM): λ_{max} (log ε) = 355 (4.35), 374 (4.50), 395 (4.43), 512 nm (4.85); HRMS (ESI) *m/z* calcd. for $C_{41}H_{40}BN_4$ $[M+H]^+$: 599.3348, 599.3347 found.

1,3,5,7-Tetramethyl-8-(10-phenylanthracen-9-yl)-4,4-(3-(dimethylamino)prop-1-yn-1-yl)-4-bora-3a,4a-diaza-*s*-indacene, 3.86

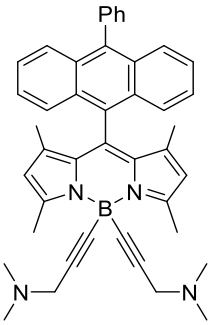

Compound **3.86** was synthesised in accordance with general procedure C using 3-dimethylamino-1-propyne (299 mg, 3.60 mmol), dry THF (20 mL), *n*-BuLi (205 mg, 3.20 mmol), and compound **3.46** (400 mg, 8.00×10^{-4} mol) dissolved in dry THF (50 mL) to yield an orange solid (250 mg, 3.99×10^{-4} mol, 50%). M.p. >250 °C; R_f =

0.42 (DCM/MeOH, 9:1); ^{1}H NMR (400 MHz, $CDCl_3$) δ = 7.92 (t, J = 14.8 Hz, 2H, CH_{Ar}), 7.66 (d, J = 8.4 Hz, 2H, CH_{Ar}), 7.57 (td, J = 14.0, 6.9 Hz, 3H, CH_{Ar}), 7.45 (d, J = 6.8 Hz, 2H, CH_{Ar}), 7.41 – 7.27 (m, 4H, CH_{Ar}), 5.95 (s, 2H, C$H_{pyrrole}$), 3.33 (d, J = 13.9 Hz, 4H, CH_2), 2.91 – 2.72 (m, 6H, C$H_{3pyrrole}$), 2.39 (s, 12H, NCH_3), 0.72 ppm (s, 6H, C$H_{3pyrrole}$); ^{13}C NMR (101 MHz, $CDCl_3$) δ = 155.3, 140.7, 139.2, 139.1, 138.4, 131.3, 130.6, 129.9, 129.4, 128.9, 128.4, 127.7, 126.9, 126.5, 125.5, 125.4, 121.5, 89.2, 49.0, 44.0, 29.7, 16.3, 13.6 ppm; UV-vis (DCM): λ_{max} (log ε) = 356 (4.31), 375 (4.46), 396 (4.40), 504 nm (5.15); HRMS (ESI) *m/z* calcd. for $C_{43}H_{44}BN_4$ $[M+H]^+$: 627.3661, 627.3671 found.

3,5-Dimethyl-8-(pyrene-9-yl)-4,4-(3-(dimethylamino)prop-1-yn-1-yl)-4-bora-3a,4a-diaza-s-indacene, 3.87

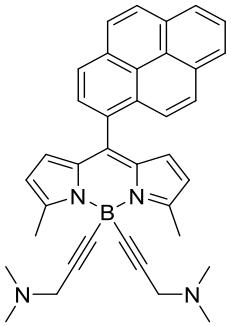

Compound **3.87** was synthesised in accordance with general procedure C using 3-dimethylamino-1-propyne (267 mg, 3.21 mmol), dry THF (20 mL), *n*-BuLi (183 mg, 2.86 mmol), and compound **3.53** (300 mg, 7.14×10^{-4} mol) dissolved in dry THF (50 mL) to yield an orange solid (232 mg, 4.23×10^{-4} mol, 60%). M.p. >250 °C; R_f = 0.58 (DCM/MeOH, 9:1); ^{1}H NMR (400 MHz, $CDCl_3$) δ = 8.29 – 7.91 (m, 9H, CH_{Ar}), 6.35 (d, J = 3.9 Hz, 2H, C$H_{pyrrole}$), 6.21 (d, J = 3.9 Hz, 2H, C$H_{pyrrole}$), 3.32 (d, J = 15.5 Hz, 4H, CH_2), 2.86 (d, J = 25.6 Hz, 6H, C$H_{3pyrrole}$), 2.37 ppm (d, J = 10.8 Hz, 12H, NCH_3); ^{13}C NMR (101 MHz, $CDCl_3$) δ = 157.2, 140.9, 134.1, 131.8, 131.2, 130.8, 130.4, 129.0, 128.5, 128.3, 127.9, 127.2, 126.3, 125.7, 125.6, 125.5, 124.4, 124.3, 123.8, 119.7, 49.0, 44.1, 16.4 ppm; UV-vis (DCM): λ_{max} (log ε) = 311 (4.38), 325 (4.66), 342 (4.77), 511 nm (5.02); HRMS (ESI) *m/z* calcd. for $C_{37}H_{36}BN_4$ $[M+H]^+$: 547.3034, 547.3034 found.

1,3,5,7-Tetramethyl-8-(phenyl-9-yl)-4,4-(3-(dimethylamino)prop-1-yn-1-yl)-4-bora-3a,4a-diaza-*s*-indacene, 3.88

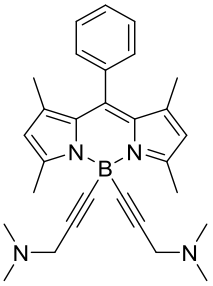

Compound **3.88** was synthesised in accordance with general procedure C using 3-dimethylamino-1-propyne (230 mg, 2.78 mmol), dry THF (20 mL), *n*-BuLi (158 mg, 2.46 mmol), and 1,3,5,7-tetramethyl-8-(phenyl-9-yl)-4,4-difluoro-4-bora-3a,4a-diaza-*s*-indacene (200 mg, 6.17×10^{-4} mol) dissolved in dry THF (50 mL) to yield an orange solid (191 mg, 4.24×10^{-4} mol, 69%). M.p. >250 °C; R_f = 0.42 (DCM/MeOH, 9:1); ^{1}H NMR (400 MHz, $CDCl_3$) δ = 7.48 – 7.40 (m, 3H, C*H*$_{Ar}$), 7.31 – 7.26 (m, 2H, C*H*$_{Ar}$), 5.99 (s, 2H C*H*$_{pyrrole}$), 3.24 (d, *J* = 12.7 Hz, 4H, C*H*$_2$), 2.75 (s, 6H, C*H*$_{3pyrrole}$), 2.32 (s, 12H, NC*H*$_3$), 1.34 ppm (s, 6H, C*H*$_{3pyrrole}$); ^{13}C NMR (101 MHz, $CDCl_3$) δ = 154.8, 141.6, 140.9, 135.5, 129.5, 128.9, 128.6, 128.1, 121.4, 48.9, 44.0, 16.1, 14.5 ppm; UV-vis (DCM): λ_{max} (log ε) = 500 nm (4.68); HRMS (ESI) *m/z* calcd. for $C_{29}H_{36}BN_4$ $[M+H]^+$: 451.3033, 451.3033 found.

3,5-(((Dimethyl-8-(anthracen-9-yl)-4-bora-3a,4a-diaza-*s*-indacene-4,4-diyl)bis(prop-2-yne-3,1-diyl))bis(dimethylammoniumdiyl))bis(propane-1-sulfonate), 3.62

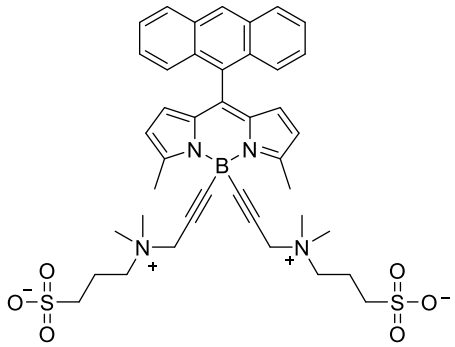

Compound **3.62** was synthesised in accordance with general procedure D using compound **3.83** (250 mg, 4.79×10^{-4} mol), EtOAc (100 mL), and 1,3-propanesultone (350 mg, 2.81 mmol) to yield an orange solid (261 mg, 3.40×10^{-4} mol, 71%). M.p. >250 °C; ^{1}H NMR (400 MHz, DMSO-*d*$_6$) δ = 8.79 (s, 1H, C*H*$_{Ar}$), 8.17 (d, *J* = 8.3 Hz,

2H, C*H*$_{Ar}$), 7.66 (d, *J* = 8.3 Hz, 2H, C*H*$_{Ar}$), 7.48 (ddd, *J* = 19.4, 14.7, 7.2 Hz, 4H, C*H*$_{Ar}$), 6.35 (dd, *J* = 11.7, 4.2 Hz, 2H, C*H*$_{pyrrole}$), 6.21 – 6.13 (m, 2H, C*H*$_{pyrrole}$), 4.44 (d, *J* = 22.9 Hz, 4H, C*H*$_2$), 3.72 – 3.52 (m, 4H, C*H*$_2$), 3.19 (t, *J* = 11.6 Hz, 12H, NC*H*$_3$), 2.85 (s, 6H, C*H*$_3$), 2.59 (dd, *J* = 12.5, 6.4 Hz, 4H, C*H*$_2$), 2.25 – 2.03 ppm (m, 4H C*H*$_2$); ^{13}C NMR (101 MHz, DMSO-*d*$_6$) *δ* = 158.1, 157.8, 134.3, 130.9, 130.7, 128.9, 128.7, 125.9, 125.7, 121.0, 63.3, 50.2, 50.0, 48.3, 43.9, 19.6, 16.7, 16.5 ppm; UV-vis (MeOH): *λ*$_{max}$ (log *ε*) = 347 (4.70), 365 (4.83), 384 (4.76), 511 nm (5.56); HRMS (ESI) *m/z* calcd. for $C_{41}H_{47}BN_4NaO_6S_2$ [M+Na]$^+$: 789.2929, 789.2932 found.

3,3'-(((1,3,5,7-Tetramethyl-8-(anthracen-9-yl)-4-bora-3a,4a-diaza-*s*-indacene-4,4-diyl)bis(prop-2-yne-3,1-diyl))bis(dimethylammoniumdiyl))bis(propane-1-sulfonate), 3.63

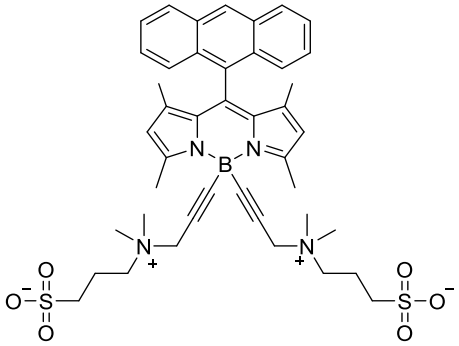

Compound **3.63** was synthesised in accordance with general procedure D using compound **3.84** (200 mg, 3.62 × 10^{-4} mol), EtOAc (100 mL), and 1,3-propanesultone (265 mg, 2.17 mmol) to yield an orange solid (277 mg, 3.49 × 10^{-4} mol, 95%). M.p. >250 °C; ^{1}H NMR (400 MHz, DMSO-*d*$_6$) *δ* = 8.72 (s, 1H, C*H*$_{Ar}$), 8.12 (d, *J* = 8.3 Hz, 2H, C*H*$_{Ar}$), 7.72 (d, *J* = 7.9 Hz, 2H, C*H*$_{Ar}$), 7.48 (ddq, *J* = 15.8, 9.2, 5.3 Hz, 4H, C*H*$_{Ar}$), 6.07 (d, *J* = 8.7 Hz, 2H, C*H*$_{pyrrole}$), 4.37 (d, *J* = 12.6 Hz, 4H, C*H*$_2$), 3.77 – 3.58 (m, 4H, C*H*$_2$), 3.19 (s, 12H, NC*H*$_3$), 2.93 – 2.83 (m, 4H, C*H*$_2$), 2.80 (s, 6H, C*H*$_{3pyrrole}$), 2.24 (ddt, *J* = 30.0, 23.0, 6.8 Hz, 4H, C*H*$_2$), 0.61 ppm (s, 6H, C*H*$_{3pyrrole}$); ^{13}C NMR (101 MHz, DMSO-*d*$_6$) *δ* = 156.0, 141.1, 139.1, 131.3, 130.3, 129.3, 128.1, 126.4, 124.3, 122.6, 63.2, 55.1, 50.2, 48.4, 19.5, 16.5, 13.4 ppm; UV-vis (MeOH): *λ*$_{max}$ (log *ε*) = 502 (4.99), 386 (4.19), 366 (4.25), 349 nm (4.11); HRMS (ESI): *m/z* calcd. for $C_{43}H_{51}BN_4NaO_6S_2$ [M+Na]$^+$: 817.3243, 817.3259 found.

3,5-(((Dimethyl-8-(10-phenylanthracen-9-yl)-4-bora-3a,4a-diaza-*s*-indacene-4,4-diyl)bis(prop-2-yne-3,1-diyl))bis(dimethylammoniumdiyl))bis(propane-1-sulfonate), 3.64

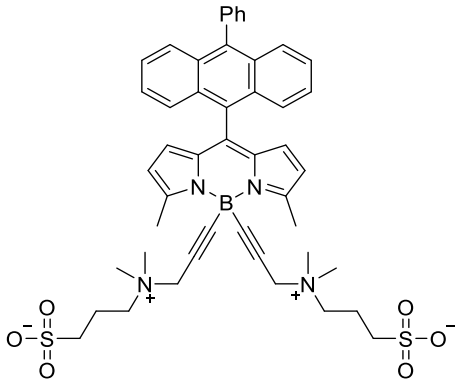

Compound **3.64** was synthesised in accordance with general procedure D using compound **3.85** (250 mg, 4.18×10^{-4} mol), EtOAc (100 mL), and 1,3-propanesultone (306 mg, 2.59 mmol) to yield an orange solid (191 mg, 2.30×10^{-4} mol, 55%). M.p. >250 °C; ^{1}H NMR (400 MHz, DMSO-d_6) δ = 7.69 – 7.63 (m, 4H, CH_{Ar}), 7.62 – 7.56 (m, 3H, CH_{Ar}), 7.48 (dt, J = 5.4, 3.4 Hz, 4H, CH_{Ar}), 7.44 – 7.39 (m, 2H, CH_{Ar}), 6.39 (dd, J = 11.1, 4.3 Hz, 2H, C$H_{pyrrole}$), 6.25 (dd, J = 11.0, 4.2 Hz, 2H, C$H_{pyrrole}$), 4.39 (d, J = 17.8 Hz, 4H, CH_2), 3.59 – 3.49 (m, 4H, CH_2), 3.10 (s, 12H, NCH_3), 2.82 (d, J = 2.7 Hz, 6H, C$H_{3pyrrole}$), 2.52 – 2.48 (m, 4H, CH_2), 2.06 ppm (dd, J = 16.1, 6.6 Hz, 4H, CH_2); ^{13}C NMR (101 MHz, DMSO-d_6) δ = 134.3, 131.2, 130.3, 129.8, 129.1, 128.4, 127.1, 126.1, 127.0, 50.3, 50.1, 48.3, 40.5, 40.2, 40.0, 39.8, 39.4, 39.3, 19.5, 16.5, 16.7 ppm; UV-vis (MeOH): λ_{max} (log ε) = 354 (4.29), 371 (4.44), 392 (4.38), 511 nm (5.08); HRMS (MALDI-TOF) *m/z* calcd. for $C_{47}H_{52}BN_4O_6S_2$ $[M+H]^+$: 843.3421, 843.3444 found.

1,3,5,7-(((Tetramethyl-8-(10-phenylanthracen-9-yl)-4-bora-3a,4a-diaza-*s*-indacene-4,4-diyl)bis(prop-2-yne-3,1-diyl))bis(dimethylammoniumdiyl))bis(propane-1-sulfonate), 3.65

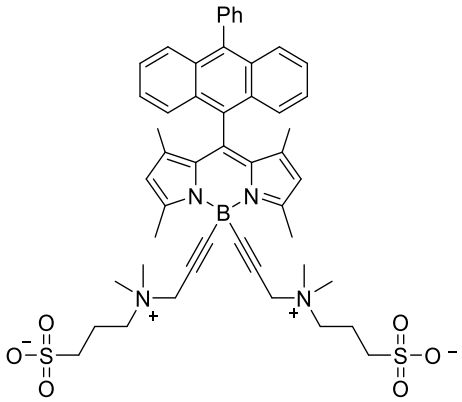

Compound **3.65** was synthesised in accordance with general procedure D using compound **3.86** (200 mg, 3.19×10^{-4} mol), EtOAc (100 mL), and 1,3-propanesultone (234 mg, 1.92 mmol) to yield an orange solid (148 mg, 1.71×10^{-4} mol, 54%). M.p. >250 °C; ^{1}H NMR (400 MHz, DMSO-d_6) δ = 7.70 (dd, J = 8.5, 3.5 Hz, 2H, CH_{Ar}), 7.68 – 7.60 (m, 3H, CH_{Ar}), 7.59 (d, J = 9.2 Hz, 2H, CH_{Ar}), 7.56 – 7.49 (m, 2H, CH_{Ar}), 7.48 – 7.38 (m, 4H, CH_{Ar}), 6.19 (s, 2H, C$H_{pyrrole}$), 4.45 – 4.33 (m, 4H, CH_2), 3.58 – 3.46 (m, 4H, CH_2), 3.12 (d, J = 18.1 Hz, 12H, NCH_3), 2.74 (s, 6H, C$H_{3pyrrole}$), 2.51 – 2.48 (m, 4H, CH_2), 2.11 – 1.98 (m, 4H, CH_2), 0.64 ppm (s, 6H, C$H_{3pyrrole}$); ^{13}C NMR (101 MHz, DMSO-d_6) δ = 156.1, 141.2, 139.6, 139.2, 137.8, 131.4, 130.4, 129.7, 129.2, 129.1, 127.9, 127.8, 127.1, 126.6, 124.6, 122.7, 84.7, 63.2, 55.1, 50.2, 48.9, 48.4, 45.2, 42.2, 29.3, 19.5, 16.5, 13.4 ppm; UV-vis (MeOH): λ_{max} (log ε) = 355 (4.07), 372 (4.22), 393 (4.17), 502 nm (4.85); HRMS (ESI) *m/z* calcd. for $C_{49}H_{55}BN_4NaO_6S_2$ $[M+Na]^+$: 893.3557, 893.3568 found.

3,3'-(((3,5-Dimethyl-8-(pyrene-9-yl)-4-bora-3a,4a-diaza-*s*-indacene-4,4-diyl)bis(prop-2-yne-3,1-diyl))bis(dimethylammoniumdiyl))bis(propane-1-sulfonate), 3.66

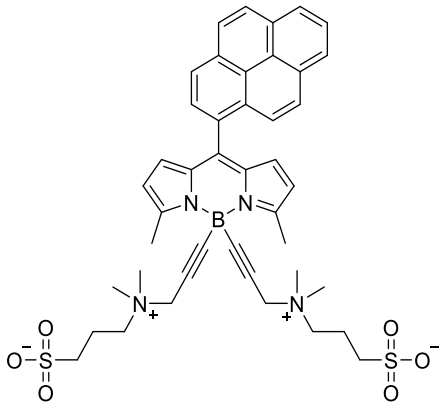

Compound **3.66** was synthesised in accordance with general procedure D using compound **3.87** (175 mg, 3.20×10^{-4} mol), EtOAc (100 mL), and 1,3-propanesultone (235 mg, 1.92 mmol) to yield an orange solid (225 mg, 2.85×10^{-4} mol, 89%). M.p. >250 °C; ^{1}H NMR (400 MHz, DMSO-*d*$_6$) δ = 8.39 (t, *J* = 8.4 Hz, 2H, C*H*$_{Ar}$), 8.33 – 8.25 (m, 3H, C*H*$_{Ar}$), 8.18 – 8.06 (m, 3H, C*H*$_{Ar}$), 7.82 – 7.77 (m, 1H, C*H*$_{Ar}$), 6.51 – 6.37 (m, 4H, C*H*$_{pyrrole}$), 4.45 – 4.30 (m, 4H, C*H*$_2$), 3.62 – 3.45 (m, 4H, C*H*$_2$), 3.11 (t, *J* = 15.5 Hz, 12H, NC*H*$_3$), 2.80 (d, *J* = 2.6 Hz, 6H, C*H*$_{3pyrrole}$), 2.63 (dd, *J* = 26.0, 13.6 Hz, 4H, C*H*$_2$), 2.15 – 1.97 ppm (m, 4H, C*H*$_2$); ^{13}C NMR (101 MHz, DMSO-*d*$_6$) δ = 158.0, 133.8, 132.1, 131.3, 130.6, 130.0, 129.7, 128.2, 127.8, 126.3, 124.0, 121.3, 63.2, 55.0, 50.2, 48.9, 48.4, 45.2, 42.2, 29.3, 19.5, 16.7 ppm; UV-vis (MeOH): λ_{max} (log ε) = 311 (4.25), 323 (4.52), 339 (4.66), 509 nm (4.87); HRMS (ESI) *m/z* calcd. for $C_{43}H_{46}BN_4O_6S_2$ $[M\text{-}H]^-$: 789.2965, 789.2957 found.

1,3,5,7-(((Tetramethyl-8-(phenyl-9-yl)-4-bora-3a,4a-diaza-*s*-indacene-4,4-diyl)bis(prop-2-yne-3,1-diyl))bis(dimethylammoniumdiyl))bis(propane-1-sulfonate), 3.67

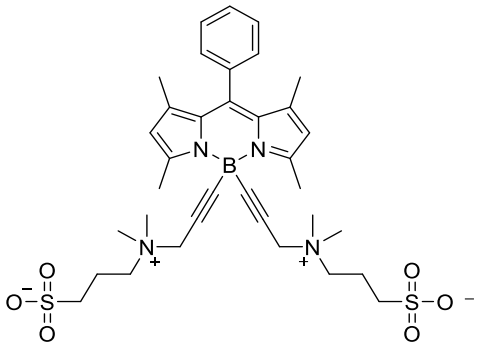

Compound **3.67** was synthesised in accordance with general procedure D using **3.88** (180 mg, 4.00 × 10^{-4} mol), EtOAc (100 mL), and 1,3-propanesultone (296 mg, 2.40 mmol) to yield an orange solid (121 mg, 1.74 × 10^{-4} mol, 45%). M.p. >250 °C; ^{1}H NMR (400 MHz, DMSO-*d*$_6$) δ = 7.57 (d, *J* = 3.6 Hz, 3H, C*H*$_{Ar}$), 7.41 – 7.31 (m, 2H, C*H*$_{Ar}$), 6.26 (d, *J* = 9.9 Hz, 2H, C*H*$_{pyrrole}$), 4.31 (d, *J* = 15.5 Hz, 4H, C*H*$_2$), 3.55 – 3.44 (m, 4H, C*H*$_2$), 3.17 – 2.86 (m, 12H, NC*H*$_3$), 2.73 – 2.66 (m, H, C*H*$_3$), 2.45 – 2.28 (m, 4H, C*H*$_2$), 2.15 – 1.96 (m, 4H, C*H*$_2$), 1.34 ppm (s, 6H, C*H*$_3$); ^{13}C NMR (101 MHz, DMSO-*d*$_6$) δ = 154.9, 154.7, 142.0, 142.0, 141.4, 141.0, 134.2, 134.1, 129.3, 127.8, 121.9, 121.0, 62.6, 62.6, 54.6, 55.5, 49.7, 49.6, 48.4, 47.4, 47.9, 47.8, 47.5, 44.7, 43.0, 28.9, 19.0, 15.9, 15.8, 14.1, 14.1 ppm; UV-vis (DCM): λ_{max} (log ε) = 498 nm (4.49); HRMS (MALDI-TOF) *m/z* calcd. for $C_{35}H_{48}BN_4O_6S_2$ $[M+H]^+$: 695.3108, 695.3135 found.

8-(3,4,5-Trimethoxyphenyl)-4,4-difluoro-4-bora-3a,4a-diaza-*s*-indacene, 3.70

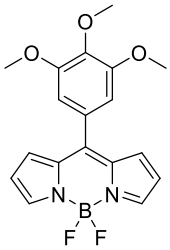

Compound **3.70** was synthesised in accordance with general procedure A using 3,4,5-trimethoxybenzaldehyde (600 mg, 3.06 mmol), pyrrole (20 mL), dry DCM (40 mL) under argon, TFA (10 µL), DDQ (695 mg, 3.06 mmol), H_2O (20 mL), DIPEA (3.95 g, 3.06 × 10^{-2} mol), and $BF_3{\cdot}Et_2O$ (4.35 g, 3.06 × 10^{-2} mol) to yield an orange solid (49 mg, 1.39 × 10^{-5} mol, 5%). M.p. >250 °C; R_f = 0.45 (DCM); ^{1}H NMR (400 MHz, $CDCl_3$) δ = 7.94 (s, 2H, C*H*$_{Ar}$), 7.08 – 6.99 (m, 2H, C*H*$_{Ar}$), 6.82 (s, 2H, C*H*$_{Ar}$),

6.54 (dd, J = 15.7, 3.6 Hz, 2H, CH_{Ar}), 3.97 (d, J = 4.5 Hz, 3H, CH_3), 3.90 ppm (s, 6H, CH); ^{13}C NMR (101 MHz, $CDCl_3$) δ = 153.1, 147.2, 144.0, 140.4, 134.8, 131.4, 129.1, 118.5, 108.2, 61.1, 56.4 ppm; UV-vis (DCM): λ_{max} (log ε) = 376 (3.94), 502 nm (4.77); HRMS (ESI) *m/z* calcd. for $C_{18}H_{17}BF_2N_2NaO_3$ $[M+Na]^+$: 381.1196, 381.1195 found.

8-(2,4,5-Trimethoxyphenyl)-4,4-difluoro-4-bora-3a,4a-diaza-*s*-indacene, 3.74

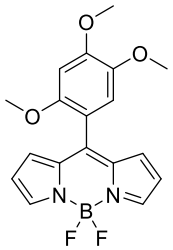

Compound **3.74** was synthesised in accordance with general procedure A using 2,4,5-trimethoxybenzaldehyde (600 mg, 3.06 mmol), pyrrole (752 mg, 6.12 mmol), dry DCM (40 mL) under argon, TFA (10 µL), DDQ (694 mg, 3.06 mmol), H_2O (20 mL), DIPEA (3.95 g, 3.06 × 10^{-2} mol), and $BF_3{\cdot}Et_2O$ (4.35 g, 3.06 × 10^{-2} mol) to yield a green solid (43 mg, 1.22 × 10^{-4} mol, 4%). M.p. >250 °C; R_f = 0.50 (DCM); ^{1}H NMR (400 MHz, $CDCl_3$) δ = 7.88 (s, 2H, CH_{Ar}), 6.86 (d, J = 6.3 Hz, 3H, CH_{Ar}), 6.64 (s, 1H, CH_{Ar}), 6.49 (d, J = 2.9 Hz, 2H, CH_{Ar}), 3.99 (s, 3H, CH_3), 3.84 (s, 3H, CH_3), 3.72 ppm (s, 3H, CH_3); ^{13}C NMR (101 MHz, $CDCl_3$) δ = 151.9, 151.5, 144.4, 143.5, 142.7, 135.8, 131.0, 118.0, 115.3, 113.7, 97.7, 56.6, 56.2 ppm; UV-vis (DCM): λ_{max} (log ε) = 349 (3.89), 504 nm (4.75); HRMS (ESI) *m/z* calcd. for $C_{18}H_{17}BFN_2O_3$ $[M-F]^+$: 339.1314, 339.1307 found.

3,5-Dimethyl-8-(3,4,5-trimethoxyphenyl)-4,4-difluoro-4-bora-3a,4a-diaza-*s*-indacene, 3.71

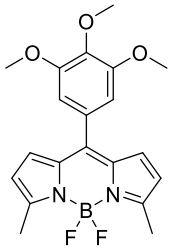

Compound **3.71** was synthesised in accordance with general procedure B using 3,4,5-trimethoxybenzaldehyde (600 mg, 3.06 mmol), 2-methyl-1H-pyrrole (495 mg, 6.12 mmol), dry DCM (60 mL) under argon, TFA (10 µL), DDQ (695 mg, 3.06 mmol),

H_2O (20 mL), DIPEA (3.95 g, 3.06 × 10^{-2} mol), and $BF_3{\cdot}Et_2O$ (4.35 g, 3.06 × 10^{-2} mol) to yield an orange solid (318 mg, 8.26 × 10^{-4} mol, 27%). M.p. >250 °C; R_f = 0.60 (DCM); ^{1}H NMR (400 MHz, $CDCl_3$) δ = 6.81 (d, J = 4.1 Hz, 2H, CH_{Ar}), 6.74 (s, 2H, CH_{Ar}), 6.28 (d, J = 4.1 Hz, 2H, CH_{Ar}), 3.94 (s, 3H, CH_3), 3.87 (s, 6H, CH_3), 2.65 ppm (s, 6H, CH_3); ^{13}C NMR (101 MHz, $CDCl_3$) δ = 157.6, 152.9, 142.4, 139.5, 134.4, 130.2, 129.5, 119.3, 108.1, 61.0, 56.3, 14.9 ppm; UV-vis (DCM): λ_{max} (log ε) = 361 (4.03), 513 nm (4.98); HRMS (ESI) *m/z* calcd. for $C_{20}H_{21}BF2N_2NaO_3$ $[M+Na]^+$: 409.1509, 409.1501 found.

3,5-Dimethyl-8-(2,4,5-trimethoxyphenyl)-4,4-difluoro-4-bora-3a,4a-diaza-*s*-indacene, 3.75

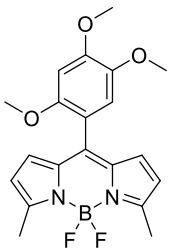

Compound **3.75** was synthesised in accordance with general procedure B using 2,4,5-trimethoxybenzaldehyde (600 mg, 3.06 mmol), 2-methyl-1H-pyrrole (486 mg, 6.12 mmol), dry DCM (40 mL) under argon, TFA (10 µL), DDQ (694 mg, 3.06 mmol), H_2O (20 mL), DIPEA (3.95 g, 3.06 × 10^{-2} mol), and $BF_3{\cdot}Et_2O$ (4.35 g, 3.06 × 10^{-2} mol) to yield an orange solid (75 mg, 1.94 × 10^{-4} mol, 6%). M.p. >250 °C; R_f = 0.56 (DCM); ^{1}H NMR (400 MHz, $CDCl_3$) δ = 6.82 (s, 1H, CH_{Ar}), 6.63 (d, J = 2.2 Hz, 1H, CH_{Ar}), 6.62 (d, J = 2.6 Hz, 2H, C$H_{pyrrole}$), 6.21 (d, J = 4.0 Hz, 2H, C$H_{pyrrole}$), 3.97 (d, J = 1.6 Hz, 3H, CH_3), 3.81 (d, J = 1.2 Hz, 3H, CH_3), 3.73 – 3.63 (m, 3H, CH_3), 2.63 (s, 6H, CH_3) ppm; ^{13}C NMR (101 MHz, $CDCl_3$) δ = 157.0, 151.9, 150.8, 142.6, 139.3, 135.3, 129.8, 119.0, 115.3, 114.2, 97.9, 56.8, 56.5, 56.1, 14.9 ppm; UV-vis (DCM): λ_{max} (log ε) = 380 (3.59), 515 nm (3.95); HRMS (ESI) *m/z* calcd. for $C_{20}H_{33}BF_2N_2NaO_3$ $[M+Na]^+$: 409.1509, 409.1510 found.

2,6-Diethyl-1,3,5,7-tetramethyl-8-(3,4,5-trimethoxyphenyl)-4,4-difluoro-4-bora-3a,4a-diaza-s-indacene, 3.73

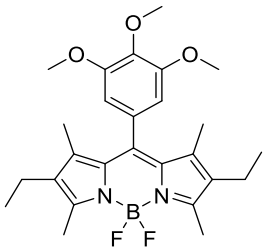

Compound **3.73** was synthesised in accordance with general procedure B using 3,4,5-trimethoxybenzaldehyde (600 mg, 3.06 mmol), 3-ethyl-2,4-dimethyl-1*H*-pyrrole (753 mg, 6.12 mmol), dry DCM (40 mL) under argon, TFA (10 µL), DDQ (694 mg, 3.06 mmol), H_2O (20 mL), DIPEA (3.95 g, 3.06×10^{-2} mol), and $BF_3{\cdot}Et_2O$ (4.35 g, 3.06×10^{-2} mol) to yield an orange solid (360 mg, 7.65×10^{-4} mol, 25%). M.p. >250 °C; R_f = 0.66 (DCM); ^{1}H NMR (400 MHz, $CDCl_3$) δ = 6.53 (s, 2H, CH_{Ar}), 3.92 (s, 3H, CH_3), 3.83 (s, 6H, CH_3), 2.53 (s, 6H, CH_3), 2.32 (q, J = 7.6 Hz, 4H, CH_2), 1.44 (s, 6H, CH_3), 1.00 ppm (t, J = 7.6 Hz, 6H, CH_3); ^{13}C NMR (101 MHz, $CDCl_3$) δ = 154.1, 153.9, 139.8, 138.5, 138.3, 132.8, 130.9, 105.5, 61.3, 56.4, 17.1, 14.6, 12.5, 11.5 ppm; UV-vis (DCM): λ_{max} (log ε) = 378 (3.61), 527 nm (4.56); HRMS (ESI) *m/z* calcd. for $C_{26}H_{33}BF_2N_2NaO_3$ $[M+Na]^+$: 493.2449, 493.2455 found.

2,6-Diethyl-1,3,5,7-tetramethyl-8-(2,4,5-trimethoxyphenyl)-4,4-difluoro-4-bora-3a,4a-diaza-s-indacene, 3.77

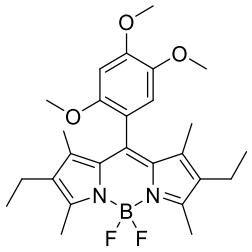

Compound **3.77** was synthesised in accordance with general procedure B using 2,4,5-trimethoxybenzaldehyde (600 mg, 3.06 mmol), 3-ethyl-2,4-dimethyl-1*H*-pyrrole (752 mg, 6.12 mmol), dry DCM (40 mL) under argon, TFA (10 µL), DDQ (694 mg, 3.06 mmol), H_2O (20 mL), DIPEA (3.95 g, 3.06×10^{-2} mol), and $BF_3{\cdot}Et_2O$ (4.35 g, 3.06×10^{-2} mol) to yield an orange solid (497 mg, 1.07 mmol, 35%). M.p. >250 °C; R_f = 0.70 (DCM); ^{1}H NMR (400 MHz, $CDCl_3$) δ = 6.64 (d, J = 25.2 Hz, 2H, CH_{Ar}), 3.97 (s, 3H, CH_3), 3.77 (d, J = 24.7 Hz, 6H, CH_3), 2.53 (s, 6H, CH_3), 2.32 (d, J = 6.9 Hz, 4H, CH_2), 1.43 (s, 6H, CH_3), 1.00 ppm (m, 6H, CH_3); ^{13}C NMR (101 MHz,

$CDCl_3$) δ = 153.2, 150.6, 150.3, 144.1, 137.9, 137.0, 132.3, 131.2, 115.4, 112.9, 97.5, 56.6, 56.4, 56.1, 17.1, 14.6, 12.5, 11.2 ppm; UV-vis (DCM): λ_{max} (log ε) = 381 (3.98), 529 nm (4.97); HRMS (ESI) *m/z* calcd. for $C_{26}H_{33}BF_2N_2NaO_3$ $[M+Na]^+$: 493.2449, 493.2440 found.

6.4 CHAPTER 4: SHORT-CHAINED ANTHRACENE-STRAPPED PORPHYRINS AND THEIR ENDOPEROXIDES

6.4.1 General synthetic procedures

General Procedure A – Porphyrin Condensation DPM (2 eq.) and aldehyde (2 eq.) were dissolved in dry DCM (120 mL). The reaction was shielded from light and TFA (cat.) was added. The reaction was stirred at rt for 3.5 h. TEA (3 µL) and *p*-chloranil (6 eq.) were added and the mixture was heated to 70 °C for 1 h. The product was purified on a silica plug (1:1, DCM:hexane) followed by column chromatography (hexane with 2% ethyl acetate). The porphyrin was then precipitated from DCM and MeOH or recrystallised from DCM and hexane.

General Procedure B – Endoperoxide Formation: Parent anthracene strapped porphyrin (1 eq.) was dissolved in chloroform-*d* (3 mL) and irradiated with broad-spectrum light for 15 min. Endoperoxide formation was monitored using ^{1}H NMR.

General Procedure C – Zinc(II) Insertion: To a solution of parent porphyrin (1 eq.) in DCM (10 mL) was added Zn(II)acetate (10 eq.) in MeOH (6 mL) and the reaction was stirred at 80 °C for 12 h. The product was purified on a silica plug (DCM) followed by column chromatography (3:1, DCM:hexane) and was recrystallised from DCM/MeOH.

6.4.2 Synthetic details and characterisation

5,10-[9',10'-Bis(phenoxymethyl)anthracene]porphyrin, 4.38

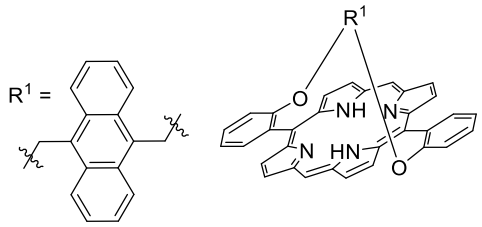

Porphyrin **4.37** was synthesised in accordance with general procedure A using DPM (393 mg, 2.69 mmol), 2,2'-((anthracene-9,10-diylbis(methylene))bis(oxy))dibenzaldehyde (600 mg, 1.35 mmol), DCM (120 mL), and *p*-chloranil (1.98 g, 8.08 mmol) to yield a purple solid (178 mg, 2.57×10^{-4} mol, 19%). M.p. >200 °C; R_f = 0.87 (DCM); ^{1}H NMR (600 MHz, $CDCl_3$) δ = 9.64 (s, 2H, CH_{meso}), 9.04 (d, J = 4.3 Hz, 4H, CH_β), 9.01 (d, J = 7.1 Hz, 2H, CH_{Ar}), 8.84 (d, J =

4.3 Hz, 4H, CH_{β}), 7.74 – 7.70 (m, 2H, CH_{Ar}), 7.67 – 7.64 (m, 2H, CH_{Ar}), 7.00 (d, J = 7.8 Hz, 2H, CH_{Ar}), 6.32 (dd, J = 6.9, 2.7 Hz, 4H, CH_{Ar}), 6.25 (dd, J = 6.6, 3.1 Hz, 4H, CH_{Ar}), 4.59 (s, 4H, CH_2), -3.50 ppm (s, 2H, NH); ^{13}C NMR (151 MHz, $CDCl_3$) δ = 158.6, 131.4, 130.1, 128.7, 127.1, 126.3, 122.9, 121.6, 120.1, 111.9, 111.8, 103.8, 61.6, 53.4 ppm; UV-vis (DCM): λ_{max} (log ε) = 359 (4.41), 378 (4.62), 418 (5.34), 511 (4.06), 543 (3.19), 584 (3.53), 632 nm (2.64); IR (ATR): $\tilde{\nu}$ = 3296, 2545, 2162, 1690, 1596, 1575, 1530, 1474, 1444, 1405, 1283, 1217, 1139, 1105, 1058, 1045, 997, 974, 955, 857, 847, 821, 788, 749, 722, 692, 658, 639, 600, 568 cm^{-1}; HRMS (MALDI-TOF) m/z calcd. for $C_{48}H_{32}N_4O_2$ [M]$^+$: 696.2525, 696.2524 found.

5,10-[9',10'-Dihydro-9',10'-epidioxyanthracene]porphyrin, 4.40

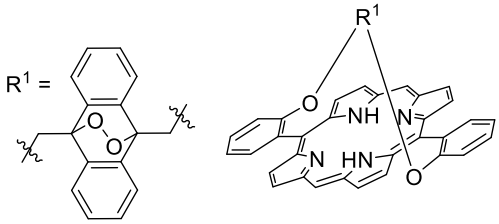

Porphyrin **4.40** was synthesised in accordance with general procedure B using porphyrin **4.38** (19 mg, 2.75 × 10^{-5} mol) to yield a purple solid (20 mg, 2.75 × 10^{-5} mol, quant.). M.p. >200 °C; R_f = 0.54 (3:1, DCM:Hexane); ^{1}H NMR (400 MHz, $CDCl_3$) δ = 9.62 (s, 2H, CH_{meso}), 9.12 (d, J = 4.5 Hz, 4H, CH_{β}), 9.07 – 9.05 (m, 2H, CH_{Ar}), 8.90 (d, J = 4.5 Hz, 4H, CH_{β}), 7.71 – 7.68 (m, 4H, CH_{Ar}), 6.78 – 6.70 (m, 2H, CH_{Ar}), 5.93 – 5.91 (m, 4H, CH_{Ar}), 4.89 – 4.86 (m, 4H, CH_{Ar}), 3.57 (s, 4H, CH_2), -3.24 ppm (br, 1H, NH); ^{13}C NMR (101 MHz, $CDCl_3$) δ = 155.9, 132.7, 132.3, 130.8, 130.3, 130.0, 129.0, 124.1, 120.5, 117.9, 110.6, 110.2, 104.5, 78.4, 61.9 ppm; UV-vis (DCM): λ_{max} (log ε) = 420 (6.22), 515 (4.88), 545 (3.28), 587 (4.44) 634 nm (2.44); IR (ATR): $\tilde{\nu}$ = 1574, 1447, 1408, 1237, 1111, 1042, 976, 957, 908, 882, 787, 746, 892, 829, 848, 571 cm^{-1}; HRMS (MALDI-TOF) m/z calcd. for $C_{48}H_{32}N_4O_4$ [M]$^+$: 728.2424, 728.2458 found.

5,10-[{9',10'-Bis(phenoxymethyl)anthracene}porphyrinato]zinc(II), 4.53

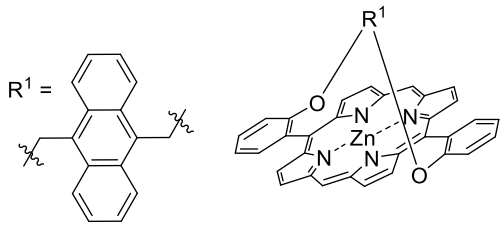

Porphyrin **4.53** was synthesised in accordance with general procedure C using porphyrin **4.38** (50 mg, 7.18 × 10^{-5} mol), DCM (10 mL), Zn(II)acetate (131 mg, 7.18 × 10^{-4} mol), and MeOH (2 mL) to yield a pink solid (47 mg, 6.25 × 10^{-5} mol, 87%). M.p. >200 °C; R_f = 0.88 (3:1, DCM:Hexane); ^{1}H NMR (400 MHz, $CDCl_3$) δ = 9.77 (s, 2H, CH_{Ar}), 9.17 (d, J = 4.3 Hz, 4H, CH_{β}), 9.05 (d, J = 8.6 Hz, 2H, CH_{Ar}), 9.01 (d, J = 4.3 Hz, 4H, CH_{β}), 7.73 (t, J = 6.2 Hz, 4H, CH_{Ar}), 7.03 – 6.95 (m, 2H, CH_{Ar}), 6.32 (d, J = 6.8 Hz, 4H, CH_{Ar}), 6.13 (dd, J = 6.6, 3.2 Hz, 4H, CH_{Ar}), 4.48 ppm (s, 4H, CH_2); ^{13}C NMR (101 MHz, $CDCl_3$) δ = 158.7, 150.7, 148.2, 132.8, 131.9, 131.5, 129.8, 128.0, 126.6, 126.3, 123.0, 121.3, 120.3, 113.5, 112.2, 105.2, 62.0 ppm; UV-vis (DCM): λ_{max} (log ε) = 361 (3.12), 385 (3.23), 433 (4.28), 560 nm (3.01); IR (ATR): $\tilde{\nu}$ = 2922, 1884, 1597, 1558, 1445, 1339, 1231, 1109, 1060, 996, 858, 789, 748, 715, 699, 654 cm^{-1}; HRMS (MALDI-TOF) *m/z* calcd. for $C_{48}H_{30}N_4O_2Zn$ $[M]^+$: 758.1660, 758.1650 found.

5,10-[{9',10'-Bis(phenoxymethyl)anthracene}-5,15-diphenyl]porphyrin, 4.51

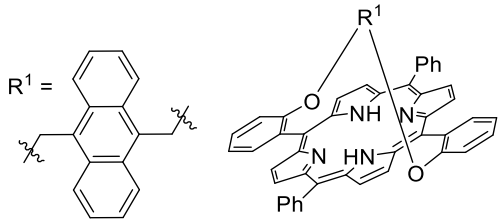

Porphyrin **4.51** was prepared in accordance with general procedure A using 2,2'-(phenylmethylene)bis(1H-pyrrole) (1.07 g, 4.82 mmol), 2,2'-((anthracene-9,10-diylbis(methylene))bis(oxy))dibenzaldehyde (1.07 g, 2.41 mmol), DCM (350 mL), and *p*-chloranil (7.06 g, 28.8 mmol) to yield a purple solid (278 mg, 3.31 × 10^{-4} mol, 14%). M.p. >200 °C; R_f = 0.84 (3:1, DCM:Hexane); ^{1}H NMR (400 MHz, $CDCl_3$) δ = 8.95 (dd, J = 7.3, 1.6 Hz, 2H, CH_{Ar}), 8.77 (d, J = 4.7 Hz, 4H, CH_{β}), 8.59 (d, J = 4.7 Hz, 4H, CH_{β}), 7.87 –7.85 (m, 10H, CH_{Ar}), 7.75 (t, J = 7.8, 3.9 Hz, 2H, CH_{Ar}), 7.67 (t,

J = 7.3 Hz, 2H, C*H*$_{Ar}$), 7.06 (d, *J* = 7.7 Hz, 2H, C*H*$_{Ar}$), 6.37 (dd, *J* = 6.8, 3.2 Hz, 4H, C*H*$_{Ar}$), 6.32 – 6.25 (m, 4H, C*H*$_{Ar}$), 4.71 (s, 4H, C*H*$_2$), -2.81 ppm (s, 2H, N*H*); ^{13}C NMR (101 MHz, $CDCl_3$) δ = 169.6, 140.8, 135.5, 131.0, 130.6, 130.0, 128.9, 127.3, 126.7, 122.7, 122.1, 120.3, 112.4, 62.2 ppm; UV-vis (DCM): λ_{max} (log ε) = 360 (3.79), 384 (3.92), 431 (4.81), 526 (3.50), 564 (3.19), 600 (3.10) 658 nm (2.87); IR (ATR): $\tilde{\nu}$ = 3359, 1878, 1588, 1445, 1407, 1307, 1107, 983, 966, 908, 882, 858, 794, 748, 711, 600, 575 cm^{-1}; HRMS (MALDI-TOF) *m/z* calcd. for $C_{60}H_{40}N_4O_2$ [M]$^+$: 848.3141, 848.3151 found.

5,10-[{9',10'-Bis(phenoxymethyl)-9',10'-dihydro-9',10'-epidioxyanthracene}-5,15-diphenyl]porphyrin, 4.56

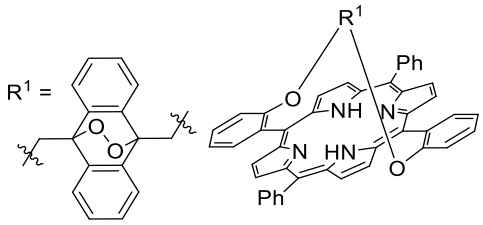

Porphyrin **4.56** was synthesised in accordance with general procedure B using porphyrin **4.51** (20 mg, 2.27 × 10^{-5} mol) to yield a purple solid (20 mg, 2.27 × 10^{-5} mol, quant.). M.p. >200 °C; R_f = 0.74 (3:1, DCM:Hexane); ^{1}H NMR (400 MHz, $CDCl_3$) δ = 8.98 (d, *J* = 7.0 Hz, 2H, C*H*$_{Ar}$), 8.83 (d, *J* = 4.8 Hz, 4H, C*H*$_\beta$), 8.70 (d, *J* = 4.7 Hz, 4H, C*H*$_\beta$), 7.92 (s, 10H, C*H*$_{Ar}$), 7.70 (t, *J* = 7.7 Hz, 4H, C*H*$_{Ar}$), 6.81 (d, *J* = 7.8 Hz, 2H. C*H*$_{Ar}$), 6.04 (d, *J* = 3.3 Hz, 4H, C*H*$_{Ar}$), 5.09 (s, 4H, C*H*$_{Ar}$), 3.72 (s, 4H, C*H*$_2$), -2.57 ppm (s, 12H, N*H*); ^{13}C NMR (101 MHz, $CDCl_3$) δ = 155.9, 140.1, 133.6, 131.3, 130.4, 130.2, 130.0, 129.1, 123.6, 122.7, 122.3, 122.2, 120.6, 118.6, 117.2, 112.4, 110.3, 78.6, 62.0 ppm; UV-vis (DCM): λ_{max} (log ε) = 433 (5.03), 528 (3.77), 567 (3.67), 601 (3.65), 657 nm (3.48); IR (ATR): $\tilde{\nu}$ = 3273, 3066, 2932, 3883, 1787, 1688, 1598, 1560, 1466, 1447, 1241, 1110, 983, 967, 905, 792, 750, 730 cm^{-1}; HRMS (ESI) m/z calcd. for $C_{60}H_{41}N_4O_4$ [M+H]$^+$: 881.3050, 881.3125 found.

5,10-[{9',10'-Bis(phenoxymethyl)anthracene}-5,15 diphenylporphyrinato]zinc(II), 4.54

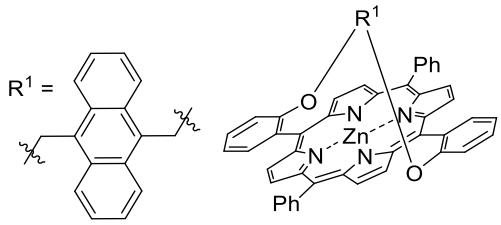

Porphyrin **4.54** was synthesised in accordance with general procedure C using porphyrin **4.51** (100 mg, 1.18×10^{-4} mol), DCM (6 mL), Zn(II)acetate (424 mg, 2.34 × 10 mmol), and MeOH (1 mL) to yield a purple/pink solid (50 mg, 5.49×10^{-5} mol, 47%). M.p. >200 °C; R_f = 0.88 (3:1, DCM:Hexane); ^{1}H NMR (400 MHz, $CDCl_3$) δ = 8.91 (dd, J = 7.0, 1.8 Hz, 2H, CH_{Ar}), 8.83 (d, J = 4.6 Hz, 4H, CH_{β}), 8.65 (d, J = 4.6 Hz, 4H, CH_{β}), 7.67 (ddd, J = 21.8, 10.2, 6.1 Hz, 14H, CH_{Ar}), 6.96 (d, J = 7.4 Hz, 2H, CH_{Ar}), 6.34 – 6.29 (m, 4H, CH_{Ar}), 6.15 (dd, J = 6.7, 2.9 Hz, 4H, CH_{Ar}), 4.45 ppm (s, 4H, CH_2); ^{13}C NMR (101 MHz, $CDCl_3$) δ = 158.7, 150.2, 148.4, 142.7, 133.1, 131.9, 130.9, 129.8, 128.0, 127.1, 126.8, 126.2, 122.8, 121.6, 120.5, 119.8, 114.5, 112.8, 62.6 ppm; UV-vis (DCM): λ_{max}(log ε) = 357 (4.08), 380 (4.28), 420 (5.16), 548 nm (3.87); IR (ATR): $\tilde{\nu}$ = 1638, 1878, 15889 1449, 1230, 1107, 1053, 993, 848, 745, 891, 845, 579 cm^{-1}; HRMS (MALDI-TOF) *m/z* calcd. for $C_{60}H_{38}N_4O_2Zn$ $[M]^+$: 910.2286, 910.2273 found.

5,10-[{9',10'-Bis(phenoxymethyl)anthracene}-5,15-bis(4-bromophenyl)]porphyrin, 4.52

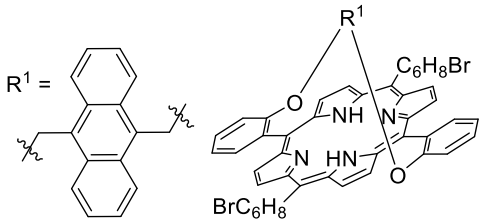

Porphyrin **4.52** was synthesised in accordance with general procedure A using 2,2'-((4-bromophenyl)methylene)bis(1H-pyrrole) (1.29 g, 4.31 mmol), 2,2'-((anthracene-9,10-diylbis(methylene))bis(oxy))dibenzaldehyde (959 mg, 2.15 mmol), DCM (300 mL), and *p*-chloranil (7.06 g, 28.8 mmol) to yield a purple solid (328 mg, 3.31×10^{-4} mol, 15%). M.p. >200 °C; R_f = 0.84 (3:1, DCM:Hexane); ^{1}H NMR (400 MHz, $CDCl_3$)

δ = 8.95 (dd, J = 7.3, 1.7 Hz, 2H, CH_{Ar}), 8.77 (d, J = 4.7 Hz, 4H, CH_{β}), 8.62 (d, J = 4.7 Hz, 4H, CH_{β}), 7.77 – 7.70 (m, 8H, CH_{Ar}), 7.66 (t, J = 7.4 Hz, 2H, CH_{Ar}), 7.06 (d, J = 7.5 Hz, 2H, CH_{Ar}), 6.45 – 6.35 (m, 8H, CH_{Ar}), 4.74 (s, 4H, CH_2), -2.85 ppm (s, 2H, NH); ^{13}C NMR (101 MHz, $CDCl_3$) δ = 169.6, 158.9, 140.8, 134.2, 130.8, 128.9, 127.3, 126.8, 122.8, 122.1, 120.2, 112.3, 77.3, 77.1, 76.7, 62.2 ppm; UV-vis (DCM): λ_{max} (log ε) = 361 (3.08), 382 (3.16), 432 (4.01), 527 (2.71), 565 (2.41), 601 (2.30), 658 nm (2.07); IR (ATR): $\tilde{\nu}$ = 3358, 1888, 1877, 1588, 1258, 1234, 1106, 984, 908, 792, 754, 710 cm^{-1}; HRMS (MALDI-TOF) m/z calcd. for $C_{60}H_{40}N_4O_2$ $[M]^+$: 1004.1361, 1004.1334 found.

5,10-[{9',10'-Bis(phenoxymethyl)-9',10'-dihydro-9',10'-epidioxyanthracene}-5,15-bis(4-bromophenyl)}]porphyrin, 4.57

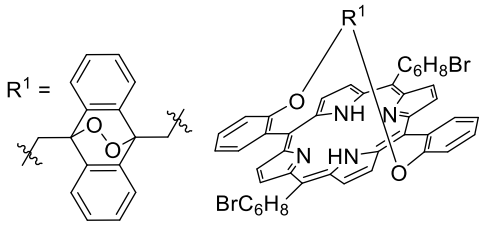

Porphyrin **4.57** was synthesised in accordance with general procedure B using porphyrin **4.52** (20 mg, 1.99 × 10^{-5} mol) to yield a purple solid (21 mg, 1.99 × 10^{-5} mol, quant.). M.p. >200 °C; R_f = 0.66 (3:1, DCM:Hexane); ^{1}H NMR (400 MHz, $CDCl_3$) δ = 8.98 (dd, J = 6.9, 2.0 Hz, 2H, CH_{Ar}), 8.81 (d, J = 4.8 Hz, 4H, CH_{β}), 8.73 (d, J = 4.7 Hz, 4H, CH_{β}), 7.83 – 7.72 (m, 8H, CH_{Ar}), 7.71 – 7.65 (m, 4H, CH_{Ar}), 6.84 – 6.78 (m, 2H, CH_{Ar}), 6.08 (dd, J = 5.7, 3.2 Hz, 4H, CH_{Ar}), 5.10 (dd, J = 5.5, 3.3 Hz, 4H, CH_{Ar}), 3.73 (s, 4H. CH_2), -2.53 ppm (s, 2H, NH); ^{13}C NMR (101 MHz, $CDCl_3$) δ =156.0, 144.7, 141.2, 133.5, 130.9, 130.2, 129.2, 127.5, 127.2, 123.7, 120.5, 120.6, 118.6, 112.0, 110.3, 78.7, 62.0 ppm; UV-vis (DCM): λ_{max} (log ε) = 434 (5.46), 529 (4.10), 566 (3.81), 604 (3.81), 660 nm (3.50); IR (ATR): $\tilde{\nu}$ = 3359, 3081, 2544, 1790, 1689, 1679, 1570, 1464, 1408, 1011, 983, 966, 884, 792, 751, 712 cm^{-1}; HRMS (APCI) m/z calcd. for $C_{60}H_{39}Br_2N_4O_4$ $[M+H]^+$: 1037.1334, 1037.1334 found.

5,10-[{9',10'-Bis(phenoxymethyl)anthracene}-5,15-bis(4-bromophenyl)porphyrinato]zinc(II), 4.55

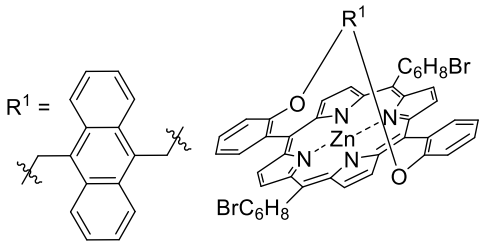

Porphyrin **4.55** was synthesised in accordance with general procedure C using porphyrin **4.52** (50 mg, 4. 98 × 10^{-5} mol) dissolved in DCM (6 mL), Zn(II)acetate (140 mg, 4.98 × 10^{-4} mol), and MeOH (1 mL) to yield a purple solid (52 mg, 4.90 × 10^{-5} mol, 98%); M.p. >200 °C; R_f = 0.87 (3:1, DCM:Hexane); ^{1}H NMR (400 MHz, $CDCl_3$) δ = 8.92 (dd, J = 7.1, 2.0 Hz, 2H, CH_{Ar}), 8.87 (d, J = 4.6 Hz, 4H, CH_{β}), 8.63 (d, J = 4.6 Hz, 4H, CH_{β}), 7.84 (s, 6H, CH_{Ar}), 7.68 (tdd, J = 14.9, 10.6, 4.2 Hz, 6H, CH_{Ar}), 6.99 (d, J = 7.9 Hz, 2H, CH_{Ar}), 6.34 (dd, J = 6.9, 3.1 Hz, 4H, CH_{Ar}), 6.20 (dd, J = 6.8, 3.2 Hz, 4H, CH_{Ar}), 4.50 ppm (s, 4H, CH_2); ^{13}C NMR (101 MHz, $CDCl_3$) δ = 158.7, 150.5, 148.2, 141.6, 140.7, 135.4, 133.0, 131.7, 131.3, 130.0, 129.6, 128.2, 128.0, 126.8, 126.6, 126.2, 125.3, 122.7, 121.9, 121.8, 120.6, 118.3, 115.1, 113.1, 62.7, 29.7 ppm; UV-vis (DCM): λ_{max} (log ε) = 362 (3.96), 384 (4.05), 432 (5.11), 560 nm (3.84); IR (ATR): $\tilde{\nu}$ = 2922, 1680, 1558, 1482, 1445, 1230, 1109, 1068, 999, 790, 717, 749, 645 cm^{-1}; HRMS (MALDI-TOF) *m/z* calcd. for $C_{60}H_{36}N_4O_2Br_2Zn$ $[M]^+$: 1066.0496, 1066.0493 found.

6.5 CHAPTER 5: SYNTHESIS AND EVALUATION OF TARGETED NANOCONSTRUCTS FOR MEDICAL APPLICATIONS

6.5.1 Near-infrared light-active targeted liposomes

Near-infrared light-active targeted liposomes

Anti-body conjugated liposomes **5.1** *and* **5.2**: DPPC in chloroform (58.2 mol%, 19.80 µmol, 14.54 mg), DOPG in chloroform (7.9 mol%, 2.68 µmol, 2.14 mg), cholesterol in chloroform (28.9 mol%, 9.85 µmol, 3.81 mg), DSPE-mPEG2000 in chloroform (4.3 mol%, 1.46 µmol, 4.10 mg), DSPE-mPEG2000-DIBO in chloroform (0.5 mol%, 0.17 µmol, 0.524 mg) and DSPE-mPEG2000-NH_2 in chloroform (0.2 mol%, 0.068 µmol, 0.19 mg) were added to a glass tube.

Anti-body free liposomes **5.3** *and* **5.4**: DPPC (58.2 mol%, 19.80 µmol, 14.54 mg) DOPG (7.9 mol%, 2.68 µmol, 2.14 mg), cholesterol (28.9 mol%, 9.85 µmol, 3.81 mg), DSPE-mPEG2000 (4.8 mol%, 1.63 µmol, 4.58 mg), DSPE-mPEG2000-NH_2 (0.2 mol%, 0.07 µmol, 0.19 mg) were added to a glass tube.

The solvent was removed under a flow of nitrogen. The reaction was dried under vacuum for 1 h. The films were hydrated using PBS (1 mL) and heated to 45 ºC for 10 min. The mixture was then extruded 11 times through two 100 nm polycarbonate membranes (Whatman) using a mini-extruder system (Avanti Polar Lipids). NHS esters of the dyes (10 mg/mL anhydrous DMSO solution, IRdye680RD-NHS, 10 eq., 34.23 µL, 3.41×10^{-7} mol, IRdye800RD-NHS, 10 eq., 39.78 µL, 3.41×10^{-7} mol) were added in 2 µL aliquots to the liposome with stirring at 2500 RPM. The reaction was stirred overnight at rt. The liposomes were dialysed against PBS (1 L) for 48 h (Float-A-Lyzer dialysis membrane, 100 kDa). The IRdye concentration (calculated using UV-vis spectroscopy, Thermo Scientific Evolution 300 UV-Visible absorption spectrophotometer) and the mean polydispersion index (Malvern Zetasizer NanoZS Dynamic Light Scattering Instrument) of the liposomes were used to determine a 50 eq. excess of Cet-Alexa488-PEG-N_3 or IgG-Alexa488-PEG-N_3 (4.2 mg/mL solution in HEPES saline (5 mmol/1000 mL HEPES, 145 mmol/1000 mL NaCl, pH 6.5)) per liposome required for 200 mL aliquots of the liposome solution. This volume was added to 200 mL aliquots of the liposome solution and the reaction was rotated overnight at rt. The liposomes were purified using size exclusion chromatography

(sepharose CL-4B using HEPES saline, 5 mmol/1000 mL HEPES, 145 mmol/1000 mL NaCl, pH 6.5, solution as eluent). The fluorescence and absorption spectra were measured on a Spex Fluorolog 2 spectrofluorometer and Thermo Scientific Evolution 300 UV-Visible absorption spectrophotometer, respectively. The Z-averages and PDIs of the constructs, measured using a Malvern Zetasizer NanoZS Dynamic Light Scattering Instrument, are as follows:

5.1 *Targeted IRdye 680-Cet:* Z-average = 126.8 nm, PDI = 0.051. 23.8 Cet molecules per liposome.
5.2 *Control Targeted IRdye 800-IGg:* Z-average = 132.7 nm, PDI = 0.032. 23.6 IgG molecules per liposomes.
5.3 *Untargeted IRdye 680:* Z-average = 129.9 nm, PDI = 0.083.
5.4 *Untargeted IRdye 800:* Z-average = 132.5 nm, PDI = 0.033.

NHS-PEG-N_3 conjugation to Cet and IgG

A solution Cet or IgG (2 mg/mL) in PBS was prepared using a 30 kDa Amicon tube centrifuged for 30 min at 3000 g, following washing with PBS. The concentration was confirmed using absorption spectroscopy (Thermo Scientific Evolution 300 UV-Visible absorption spectrophotometer). A solution of NHS-PEG-N_3 in anhydrous DMSO (10 mg/mL) was prepared and added (for Cet = 2.66 µL, 0.027 mg, 6.86×10^{-8} mol, for IgG = 2.59 µL, 0.026 mg, 6.67×10^{-8} mol, 2.5 eq.) to the reaction vessel. To this was added Alexa488-NHS solution (1 mg/mL stock, 2.5 eq., for Cet (44.13 µL, 6.86×10^{-8} mol, 0.044 mg) for IgG (42.89 µL, 6.67×10^{8} mol, 0.043 mg) and rotated for 24 h at 4 ºC using an orbital mixer. The reaction mixture was purified using a PD-10 column equilibrated with PBS. The collected fraction was concentrated using centrifugation in an Amicon 30 kDa tube for 20 min at 3000 g and washed with PBS (5 mL) following another centrifugation cycle. A solution of concentration of 4.2 mg/mL in PBS was prepared and confirmed using absorption spectroscopy (Thermo Scientific Evolution 300 UV-Visible absorption spectrophotometer).

6.5.2 Targeted photoactivatable multi inhibitory liposomes

TPMIL Synthesis: DSPC (28.62 mg, 33.22 µmol, 0.53 eq.), cholesterol in chloroform (12.08 mg, 31.25 µmol, 0.46 eq.), DSPE-mPEG (0.57 mg, 0.20 µmol,

0.003 eq.), and BPD-PC (0.51 mg, 0.41 µmol, 0.006 eq.) were added to a glass tube and dried over a nitrogen flow, followed by drying *in vacuo* for 1 h.

An Irinotecan stock solution (20 mg/mL) in HEPES dextrose (3 mmol/1000 mL HEPES, 125 mmol/1000 mL dextrose, pH 6.5) was prepared. The solution was heated to 60 ºC for 2 min and vortexed for 30 s. This was repeated four times. The solution was centrifuged for 30 s at 10,000 g at 4 ºC and the supernatant was collected. The supernatant was cooled to -4 ºC and filtered using a sterile syringe and a 0.22 µm Millex-GS filter. The exact concentration was determined using UV-vis spectroscopy (Thermo Scientific Evolution 300 UV-Visible absorption spectrophotometer). The lipid films were rehydrated in EtOH (86.88 µL), heated to 65 ºC for 10 min, and vortexed for 30 s. Pre-heated ammonium sulfate (250 mM, 868.88 µL) was added at 65 ºC and the solution was vortexed for 1 min to homogenise.

The solution was immersed in liquid nitrogen for 3 min and thawed at 65 ℃ for 5 min. 5 freeze thaw cycles were performed. The liposomes were extruded 15 times through two 100 nm polycarbonate membranes (Whatman).

The liposomes were purified using a sepharose CL-4B column equilibrated with HEPES dextrose (3 mmol/1000 mL HEPES, 125 mmol/1000 mL dextrose, pH 6.5) solution and the BPD-PC concentration of the liposomes was calculated using UV-vis spectroscopy (Thermo Scientific Evolution 300 UV-Visible absorption spectrophotometer). Using the measured BPD-PC concentration, the correct volume of the Irinotecan stock was added to the liposomes in aliquots of 250 µL to give 284 g of Irinotecan per mol of phospholipid (1.09 mg, 62 µL) and left to react for 30 min at 65 °C Then, the solution was quenched on ice for 15 min.

DSPE-mPEG (1.15 mg, 0.41 µmol) that provides 4.2% PEG surface coverage and DOPG (0.55 mg, 0.69 µmol) were added to the reaction vessel and dried with nitrogen and under vacuum for 10 min. An equal volume of HEPES dextrose (3 mmol/1000 mL HEPES, 125 mmol/1000 mL dextrose, pH 6.5) solution was then added. The liposomes were vortexed for 3 min and sonicated for 10 min. They were centrifuged at 1000 g for 20 s. The Irinotecan-loaded liposomes were added to the

DSPE-mPEG and DOPG micelles and mixed gently. They were incubated at 65 °C for 60 min. The liposomes were dialyzed against 1 L of HEPES saline (5 mmol/1000 mL HEPES, 145 mmol/1000 mL NaCl, pH 6.5, 100 kDa Floa-A-Lyzer) for 24 h.

DSPE-PEG2000-DBCO (1.15 mg, 0.37 µmol, 0.91 eq.) was dried with nitrogen, evaporated under vacuum for 30 min, and then an equal volume of HEPES saline (5 mmol/1000 mL HEPES, 145 mmol/1000 mL NaCl, pH 6.5) was added. The reaction was vortexed for 3 min and sonicated for 20 min. The solution was centrifuged at 1000 g for 20 s. AF488-CET-PEG-N_3 (5.460 mg, 0.0372 µmol, 0.091 eq.) was added to DSPE-PEG2000-DBCO micelles and mixed. They were rotated on an optical rotator at rt for 24 h.

Following dialysis, DSPE-PEG2000-DBCO-Cet micelles (100 eq. of Cet-Alexa488-PEG-N_3 per liposome) were post inserted and incubated at 37 °C overnight. The liposomes were quenched on ice for 15 min and the purified with size exclusion chromatography (sepharose CL-4B column equilibrated with HEPES saline, 5 mmol/1000 mL HEPES, 145 mmol/1000 mL NaCl, pH 6.5). The concentration of BPD-PC, Irinotecan and the post insertion efficiency was calculated. The Z-averages and PDI of the construct were measured using a Malvern Zetasizer NanoZS Dynamic Light Scattering Instrument. The fluorescence and absorption spectra were measured on a Spex Fluorolog 2 spectrofluorometer and Thermo Scientific Evolution 300 UV-Visible absorption spectrophotometer, respectively.

Construct **5.5** *TPMIL:* Z-average = 122.8, PDI = 0.02, IRI entrapment = 70%, 30.5 Cet per liposomes.

Note: All animal experiments were conducted with approval and according to guidelines established by the Massachusetts General Hospital Institutional Animal Care and Use Committee.

Implantation

MIAPACA-2 and PCAF cells were cultured in Dulbecco's modified eagle media (DMEM) complete with 10% FBS and 2% penicillin/streptomycin. When confluent, the media was removed and the cells were washed with PBS (10 mL). The cells were treated with trypsin and collected in media (5 mL). The cells were diluted in

media to make a 70 µL solution of 50% Matrigel (BD Biosciences) and culture media, 25% MIAPACA-2 ($1x10^6$ cells) and 25% PCAF ($1x10^6$ cells). The 6-week-old male Swiss nude mice (Cox Breeding Laboratories) weighing 20–25 grams were sedated with 100 mg/kg ketamine and 10 mg/kg xylazine and the pancreas was exposed through a small left abdominal flank incision. The cell Matrigel mixture was injected into the pancreases and after 60 s the mouse incision was sutured. 10% povidone/iodine was applied topically to the sutured tissue. Butamorphine (0.1 mg/kg) was administered before and after the incision and twice a day for the next two days.

In vivo photodynamic therapy

After 9 d the orthotropic tumors had reached a volume of 25 mm^3 and the mice were sedated with 100 mg/kg ketamine and 10 mg/kg xylazine mixture. The mice were randomised and injected intravenously (tail vein) with 200 µL of sterile PBS and active agent. The tumour was exposed with a small left flank incision. Mice treated with Visudyne were irradiated with the appropriate light dose 1 h after injection and the mice treated with TPMIL were irradiated 24 h after injection, both using NIR light (690 nm diode laser, High Power Devices, Inc). Following PDT, the mice were sutured and topically treated with 10% povidone/iodine solution. Butamorphine (0.1 mg/kg) was administered before and after PDT and twice a day for the next two days.

Ultrasound Imaging

The mice were sedated under a flow of isoflurane and oxygen. The mouse was laid on its side, ultrasound gel was applied and the mouse was imaged (IVIS Lumina Series III whole animal pre-clinical imaging). The dimensions of the tumour were noted, and volume was determined using the ellipsoid formula:

$$\text{volume} = (\pi \times L \times W \times H)/6$$

, where L, W and H, are the tumour length, width and height.

6.5.3 BPD-containing targeted liposomes

Untargeted Construct General Method: The contents of the lipid film were added to a glass tube. The solvent was removed under a flow of nitrogen. The reaction was dried under vacuum for 1 h. The films were hydrated using PBS (1 mL) and heated

to 45 ºC for 10 min. The mixture was then extruded 11 times in two 100 nm polycarbonate membranes (Whatman). The constructs were purified using size exclusion chromatography (sepharose CL-4B column, PBS).

Targeted Construct General Method: Untargeted construct was aliquoted into 100 µL units. The Z-average was used to calculate the moles of liposomes in 100 µM. This was reacted with Cet-Alexa488-PEG-N_3 (100 eq.) and stirred at rt overnight on an orbital rotator. The constructs were purified using size exclusion chromatography (sepharose CL-4B column, PBS). The Z-averages and PDIs of the constructs were measured using a Malvern Zetasizer NanoZS Dynamic Light Scattering Instrument. The fluorescence and absorption spectra were measured on a Spex Fluorolog 2 spectrofluorometer and Thermo Scientific Evolution 300 UV-Visible absorption spectrophotometer, respectively.

5.6 Untargeted Construct BPD-PC (0.5 mol%)

DPPC in chloroform (57.6 mol%, 19.60 µmol, 14.39 mg, 575.60 µL), DOPG in chloroform (7.9 mol%, 2.68 µmol, 2.14 mg, 85.6 µL), cholesterol in chloroform (28.9 mol%, 9.85 µmol, 3.81 mg, 381.0 µL), DSPE-mPEG2000 in chloroform (4.5 mol%, 1.53 µmol, 4.30 mg, 171.8 µL), DSPE-mPEG2000-DIBO in chloroform (0.5 mol%, 0.17 µmol, 0.52 mg, 21.0 µL), and BPD-PC (0.5 mol%, 0.175 µmol, 0.22 mg, 249.9 µL) were used. Z-average = 119.2 nm, PDI = 0.10.

5.9 Targeted Construct BPD-PC (0.5 mol%)

The moles of untargeted liposomes in 100 µL (2.76×10^{-11} mol) was calculated. This was reacted with a Cet-Alexa488-PEG-N_3 solution at a concentration of 4.2 mg/mL (100 eq., 2.76×10^{-9} mol, 96.6 µL). Z-average = 121.5 nm, PDI = 0.10. Cet to liposome ratio = 23.22.

5.7 Untargeted Construct BPD-PC (0.6 mol%)

DPPC in chloroform (57.6 mol%, 19.60 µmol, 14.39 mg, 575.6 µL), DOPG in chloroform (7.9 mol%, 2.68 µmol, 2.14 mg, 85.6 µL), cholesterol in chloroform (28.9 mol%, 9.85 µmol, 3.81 mg, 381.0 µL), DSPE-mPEG2000 in chloroform (4.5 mol%, 1.53 µmol, 4.295 mg, 171.8 µL), DSPE-mPEG2000-DIBO in chloroform (0.5 mol%, 0.17 µmol, 0.52 mg, 21.0 µL), and BPD-PC (0.6 mol%, 0.200 µmol, 0.250 mg, 479 µL) were used. Z-average = 130.5 nm, PDI = 0.056.

5.10 Targeted Construct BPD-PC (0.6 mol%)

The moles of untargeted liposomes in 100 µL (2.44×10^{-11} mol) was calculated. This was reacted with a Cet-Alexa488-PEG-N_3 solution at a concentration of 4.2 mg/mL (100 eq., 2.44×10^{-9} mol, 96.6 µL). Z-average = 142.8 nm, PDI =0.064. Cet to liposome ratio = 19.38.

5.8 Untargeted Construct BPD-PC (2 mol%)

DPPC in chloroform (57.6 mol%, 19.60 µmol, 14.39 mg, 575.6 µL), DOPG in chloroform (7.9 mol%, 2.68 µmol, 2.14 mg, 85.6 µL), cholesterol in chloroform (28.9 mol%, 9.85 µmol, 3.81 mg, 381.0 µL), DSPE-mPEG2000 in chloroform (4.5 mol%, 1.53 µmol, 4.295 mg, 171.8 µL), DSPE-mPEG2000-DIBO in chloroform (0.5 mol%, 0.17 µmol, 0.52 mg, 21.0 µL), and BPD-PC (2 mol%, 0.680 µmol, 0.812 mg, 1650 µL) were used. Z-average = 110.7 nm, PDI = 0.073.

5.11 Targeted Construct BPD-PC (2 mol%)

The moles of untargeted liposomes in 100 µL (3.44×10^{-11} mol) was calculated. This was reacted with Cet-Alexa488-PEG-N_3 (100 eq., 3.44×10^{-9} mol, 128.96 µM). Z-average = 116.3 nm, PDI =0.059. Cet to liposome ratio = 26.03.

5.12 Targeted Construct BPD and BPD-PC (2 mol%)

DPPC in chloroform (56.2 mol%, 19.12 µmol, 14.04 mg, 561.44 µL), DOPG in chloroform (7.9 mol%, 2.68 µmol, 2.14 mg, 85.6 µL), cholesterol in chloroform (28.9 mol%, 9.85 µmol, 3.81 mg, 381.0 µL), DSPE-mPEG2000 in chloroform (4.5 mol%, 1.53 µmol, 4.295 mg, 171.8 µL), DSPE-mPEG2000-DIBO in chloroform (0.5 mol%, 0.17 µmol, 0.52 mg, 21.0 µL), BPD-PC (2 mol%, 0.68 µmol, 0.85 mg, 1760 µL), and BPD (1 mol%, 0.34 µmol, 0.25 mg, 376 µL) were added to a glass tube. The solvent was removed under a flow of nitrogen. The reaction was dried under vacuum for 1 h. The films were hydrated using PBS (1 mL) and heated to 45 ºC for 10 min. The mixture was then extruded 11 times through two 100 nm polycarbonate membranes.

The untargeted construct was aliquoted into 100 µL units. The Z-average was used to calculate the moles of liposomes in 100 µL (6.60×10^{-11} mol). This was reacted with a Cet-Alexa488-PEG-N_3 solution at 4.2 mg/mL (100 eq., 6.60×10^{-9} mol, 235.8

µL) and stirred at rt overnight on rotation. The construct was purified using size exclusion chromatography (sepharose CL-4B column, PBS). Z-average = 122.8 nm, PDI = 0.21, Cet to liposome ratio = 26.03.

5.13 Targeted Construct BPD (1 mol%)

DPPC in chloroform (57.2 mol%, 19.46 µmol, 14.29 mg, 571.44 µL), DOPG in chloroform (7.9 mol%, 2.68 µmol, 2.14 mg, 85.6 µL), cholesterol in chloroform (28.9 mol%, 9.85 µmol, 3.81 mg, 381.0 µL), DSPE-mPEG2000 in chloroform (4.5 mol%, 1.53 µmol, 4.295 mg, 171.8 µL), DSPE-mPEG2000-DIBO in chloroform (0.5 mol%, 0.17 µmol, 0.52 mg, 21.0 µL), and BPD (1 mol%, 0.34 µmol, 0.25 mg, 376.3 µL) were added to the reaction vessel. The solvent was removed under a flow of nitrogen. The reaction was dried under vacuum for 1 h. The films were hydrated using PBS (1 mL) and heated to 45 ºC for 10 min. The mixture was then extruded 11 times through two 100 nm polycarbonate membranes (Whatman).

The untargeted construct was aliquoted into 100 µL units. The Z-average was used to calculate the moles of liposomes in 100 µL (2.28×10^{-11} mol). This was reacted with a Cet-Alexa488-PEG-N_3 solution at 4.2 mg/mL (100 eq., 2.28×10^{-9} mol, 81.38 µL) and stirred at rt overnight on rotation. The construct was purified using size exclusion chromatography (sepharose CL-4B column, PBS). Z-average = 133.8 nm, PDI = 0.082, Cet to liposome ratio = 40.40.

Nodule preparation

DMEM or eagle's minimum essential medium media (complete with 10% FBS and 2% penicillin/streptomycin) was aspirated and the cells were washed with PBS (10 mL). Trypsin (3 mL) was added and removed after 20 s. Media (10 mL) was added and the cells were removed. The cells were counted and diluted in media to 50,000 cells/mL. The cell solution (100 µL) was added to each well to give 5000 cells/mL. The nodules were incubated for 48 h at 37 ºC.

Treatment

The experimental groups were treated as specified with either a 690 nm diode laser (Model 7404, Intense Inc.) at an irradiance of 150 mW/cm^2 or an X-rad 320 irradiator (320 kV, 12.5 mA). The X-ray radiation was given to the spheroid cultures through

a 2 mm aluminium filter. The samples were maintained under dark conditions unless undergoing treatment.

Probe experiments

A solution of SOSG in MeOH (10 µL, 100 µM) was added to the experiental groups and PBS control in a glass bottom 96-well plate that contained the spheroids. The fluorescence spectra were measured before and after treatment using a SpectraMax M Series Multi-Mode Microplate Reader at an excitation wavelength of 460 nm, cut off of 515 nm, emission wavelength of 525 nm. The background fluoresence was also measured and subtracted from the measured fluorescence

A solution of HPF in DMF (20 µL, 200 µM) was added to the experiental groups and PBS control in a glass bottom 96-well plate that contained the spheroids. The fluorescence spectra were measured before and after treatment using a SpectraMax M Series Multi-Mode Microplate Reader at an excitation wavelength of 490 nm, emission wavelength of 515 nm. The background fluoresence was also measured and subtracted from the measured fluorescence

A solution of MTS in DMSO (40 µL, 100 µM) was added to the experiental groups and PBS control in a glass bottom 96-well plate that contained the spheroids. The absorption spectra were measured before and after treatment using a SpectraMax M Series Multi-Mode Microplate Reader at an absorbance wavelength of 490 nm.

Live dead assay

The following protocol was performed under dark conditions 24 h after treatment. Media (100 µL) was removed from the total killing wells. The total killing wells were fixed with 10% formalin solution in PBS (100 µL) for 2–5 min at rt. 1% Triton X-100 in PBS (100 µL) was added to the total killing group and the cells were incubated for 1 h at 37 °C. Following incubation, the total killing wells were washed with 0.1 M glycine (3 x 100 µL). The live/dead imaging mixture was prepared by adding DMSO (25 mL) to two calcein AM (50 µg) vials and transferred to PBS (25 mL, per two 96 well plates). Propidium iodide solution (1.0 mg/mL in water, 100 µL) was added. Media (100 µL) was removed from each well and add the live/dead solution (100 µL) reagent was added to each well. The cells were incubated for 1 h and imaged with a confocal microscope (Olympus FluoView 1000 automated confocal microscope). λ_{ex} = 488–494 nm/λ_{em} = 515–520 nm (calcein) and λ_{ex} = 528–559

nm/λ_{em} = 617–630 nm (propidium iodide). The bright-field images were acquired under 559 nm light.

References

1. R. David, M. R. Zimmerman, *Nat. Rev. Cancer* **2010**, *10*, 728–733.
2. The Edwin Smith Surgical Papyrus, Volume 1: Hieroglyphic Transliteration, Translation, and Commentary, The University of Chicago Press, Chicago, **1930**.
3. The Papyrus Ebers: the greatest Egyptian medical document, Levin & Munksgaard, Copenhagen, London, **1937**.
4. A. Ghossain, M. A. Ghossain, *J. Med. Liban.* **2009**, *57*, 65–71.
5. E. H. Grubbé, *Radiology* **1933**, *21*, 156–162.
6. P. Curie, H. Becquerel, *Compt. Rend. Acad. Sci*. **1901**, 1289–1291.
7. M. L. M. Boone, J. H. Lawrence, W. G. Connor, R. Morgado, J. A. Hicks, R. C. Brown, *Int. J. Radiat. Oncol. Biol. Phys.* **1977**, *3*, 65–69.
8. D. W. Fry, R. B. R.-S.-Harvie, L. B. Mullett, W. Walkinshaw, *Nature* **1948**, *162*, 859–861.
9. R. Mohan, *Semin. Radiat. Oncol*. **1995**, *5*, 86–99.
10. A. Gilman, *Am. J. Surg.* **1963**, *105*, 574–578.
11. A. Gilman, F. S. Philips, *Science* **1946**, *103*, 409–436.
12. A. Haddow, G. A. R. Kon, W. C. J. Ross, *Nature* **1948**, *162*, 824–825.
13. R. J. Goldacre, A. Loveless, W. C. J. Ross, *Nature* **1949**, *163*, 667–669.
14. K. R. Shankland, J. O. Armitage, B. W. Hancock, *Lancet* **2012**, *380*, 848–857.
15. S. Farber, L. K. Diamond, *N. Engl. J. Med*. **1948**, *238*, 787–793.
16. L. D. Longo, M. C. Li, *Am. J. Obstet. Gynecol.* **1979**, *135*, 266–272.
17. R. Hertz, M. C. Li, D. B. Spencer, *Proc. Soc. Exp. Biol. Med*. **1956**, *93*, 361–366.
18. M. C. Wani, H. L. Taylor, M. E. Wall, P. Coggon, A. T. McPhail, *J. Am. Chem. Soc.* **1971**, *93*, 2325–2327.
19. I. S. Johnson, J. G. Armstrong, M. Gorman, J. P. Burnett, *Cancer Res*. **1963**, *23*, 1390–1427.
20. E. Wiltshaw, *Platinum Metals Rev*. **1979**, *23*, 90–98.
21. B. Rosenberg, L. Vancamp, T. Krigas, *Nature* **1965**, *205*, 698–699.
22. V. C. Jordan, *Br. J. Pharmacol*. **2006**, *147*, S269–S276.
23. C. Heidelberger, N. K. Chaudhuri, P. Danneberg, D. Mooren, L. Griesbach, R. Duschinsky, R. J. Schnitzer, E. Pleven, J. Scheiner, *Nature* **1957**, *179*, 663–666.

24. F. M. Schabel, *Cancer* **1975**, *35*, 15–24.
25. H. E. Skipper, F. M. Schabel, W. S. Wilcox, *Cancer Chemother. Rep.* **1967**, *51*, 125–165.
26. V. T. Devita, *Br. J. Haematol.* **2003**, 122, *5*, 718–727.
27. V. T. Devita, A. A. Serpick, P. P. Carbone, *Ann. Intern. Med.* **1970**, *73*, 881–895.
28. A. F. Shaughnessy, *BMJ* **2012**, *345*: e8346.
29. G. Bonadonna, *Tumori J.* **1972**, *58*, 179–179.
30. J. S. James, G. Dubs, *AIDS Treat. News* **1997**, *284*, 2–3.
31. R. O. Dillman, *Cancer Biother. Radiopharm*. **1999**, *14*, 5–10.
32. M. A. Cheever, C. S. Higano, *Clin. Cancer Res*. **2011**, *17*, 3520–3526.
33. Herodotus, The Histories, Penguin, UK, **2003**.
34. A. M. W. Downing, T. P. Blunt, *Proc. R. Soc*. **1878**, *26*, 488–500.
35. T. A. Palm, *Practitioner* **1890**, *45*, 270–279.
36. The Nobel Prize in Physiology or Medicine **1903**. https://www.nobelprize.org/prizes/medicine/1903/summary/ (accessed March 2020).
37. K. I. Møller, B. Kongshoj, P. A. Philipsen, V. O. Thomsen, H. C. Wulf, *Photodermatol. Photoimmunol. Photomed*. **2005**, *21*, 118–124.
38. N. Finsen, *Phototherapy*, Edward Arnold, UK, **1901**.
39. E. C. Titus, *Sci. Am*. **1915**, *79*, 255.
40. M. Zanolli, *Clin. Dermatol.* **2003**, *21*, 398–406.
41. J. A. Parrish, T. B. Fitzpatrick, L. Tanenbaum, M. A. Pathak, *N. Engl. J. Med*. **1974**, *291*, 1207–1211.
42. O. Raab, *Z. Biol.* **1900**, *39*, 524–546.
43. H. von Tappeiner, *Munch. Med. Wochenschr*. **1903**, *1*, 2042–2044.
44. A. Jesionek, H. von Tappeiner, *Dtsch. Arch. Klin. Med.* **1905**, *85*, 223–239.
45. H. von Tappeiner, *Dtsch. Arch. Klin. Med.* **1904**, *80*, 427–487.
46. H. von Tappeiner, A. Jodlbauer, *Die sensibilisierende Wirkung fluorescierender Substanzen: Gesammelte Untersuchungen über die photodynamische Erscheinung: aus dem pharmakologischen Institute der K. Universität München*, Verlag von FCW Vogel, Leipzig, **1907**.
47. J. Scherer, *Ann. Chem. Pharm*. **1841**, *40*, 1–64.
48. F. Meyer-Betz, *Dtsch. Arch. Klin. Med.* **1913**, *112*, 476–503.
49. W. Hausmann, *Wien. Klin. Wochenschr*. **1908**, *21*, 1527–1528.

50. W. Hausmann, *Biochem. Z*. **1914**, *67*, 309.
51. H. Pfeiffer, *Der nachweis photodynamischer wirkungen fluoreszierender stoffe am lebenden warmblüter*, Urban & Schwarzenberg, Germany, **1935**.
52. A. Policard, *C. R. Biol.* **1924**, *91*, 1423–1424.
53. H. Auler, G. Banzer, *J. Cancer Res. Clin. Oncol*. **1942**, *53*, 65–68.
54. F. H. J. Figge, G. S. Weiland, L. O. J. Manganiello, *SEBM*, **1948**, *68*, 640–641.
55. S. Schwartz, K. Absolon, H. Vermund, *Univ. Minn. Med. Bull.* **1955**, *27*, 7–8.
56. R. L. Lipson, J. H. Pratt, E. J. Baldes, M. B. Dockerty, *Obstet. Gynecol*. **1964**, *24*, 78–84.
57. R. L. Lipson, E. J. Baldes, A. M. Olsen, *J. Natl. Cancer Inst*. **1961**, *26*, 1–11.
58. R. L. Lipson, E. J. Baldes, M. J. Gray, *Cancer* **1967**, *20*, 2255–2257.
59. T. J. Dougherty, G. B. Grindey, R. Fiel, K. R. Weishaupt, D. G. Boyle, *J. Natl. Cancer Inst.* **1975**, *55*, 115–121.
60. S. H. Tomson, E. A. Emmett, S. H. Fox, *Cancer Res*. **1974**, *34*, 3124–3127.
61. I. Diamond, A. F. Mcdonagh, C. B. Wilson, S. G. Granelli, S. Nielsen, R. Jaenicke, *Lancet* **1972**, *300*, 1175–1177.
62. T. J. Dougherty, J. E. Kaufman, A. Goldfarb, K. R. Weishaupt, D. Boyle, A. Mittleman, *Cancer Res*. **1978**, *38*, 2628–2635.
63. J. R. Benson, G. M. Farrow, J. H. Kinsey, D. A. Cortese, H. Zincke, D. C. Utz, *Mayo Clin. Proc.* **1982***, 57*, 548–555.
64. B. G. Ward, I. J. Forbes, P. A. Cowled, M. M. McEvoy, L. W. Cox, *Am. J. Obstet. Gynecol*. **1982**, *142*, 356–357.
65. E. R. Laws, D. A. Cortese, J. H. Kinsey, R. T. Lagan, R. L. Anderson, *Neurosurgery* **1981**, *9*, 672–678.
66. Z. Huang, *Technol. Cancer Res. Treat.* **2005**, *4*, 283–293.
67. B. W. Henderson, T. J. Dougherty, *Photochem. Photobiol*. **1992**, *55*, 145–157.
68. J. C. Kennedy, R. H. Pottier, D. C. Pross, *J. Photochem. Photobiol. B, Biol.* **1990**, *6*, 143–148.
69. R. J. Cremer, P. W. Perryman, D. H. Richards, *Lancet* **1958**, *271*, 1094–1097.
70. J. Lucey, M. Ferreiro, J. Hewitt, *Pediatrics* **1968**, *41*, 1047–1054.
71. D. Van Straten, V. Mashayekhi, H. S. De Bruijn, S. Oliveira, D. J. Robinson, *Cancers* **2017**, *9*, 19.
72. S. B. Brown, E. A. Brown, I. Walker, *Lancet Oncol.* **2004**, *5*, 497–508.
73. S. Choudhary, K. Nouri, M. L. Elsaie, *Lasers Med. Sci*. **2009**, *24*, 971–980.

74. T. Kormeili, P. S. Yamauchi, N. J. Lowe, *Br. J. Dermatol*. **2004**, *150*, 1061–1069.
75. U. Schmidt-Erfurth, T. Hasan, *Surv. Ophthalmol.* **2000**, *45*, 195–214.
76. M. R. Hamblin, T. Hasan, *Photochem. Photobiol. Sci*. **2004**, *3*, 436–450.
77. A. P. Castano, T. N. Demidova, M. R. Hamblin, *Photodiagnosis Photodyn. Ther.* **2004**, *1*, 279–293.
78. J. Moan, K. Berg, *Photochem Photobiol.* **1991**, *53*, 549–553.
79. E. Skovsen, J. W. Snyder, J. D. Lambert, P. R. Ogilby, *J. Phys. Chem. B.* **2005**, *109*, 8570–8573.
80. C. Flors, M. J. Fryer, J. Waring, B. Reeder, U. Bechtold, P. M. Mullineaux, S. Nonell, M. T. Wilson, N. R. Baker, *J. Exp. Bot.* **2006**, *57*, 1725–1734.
81. M. L. Kremer, *Phys. Chem. Chem. Phys*., **1999**, *1*, 3595–3605.
82. J. Ma, L. Jiang, *Free Radic Res*. **2001**, *35*, 767–77.
83. a) T. Grune, L. O. Klotz, J. Gieche, M. Rudeck, H. Sies, *Free Radic. Biol. Med*. **2001**, *30*, 1243–1253. b) T. A. Dix, J. Aikens, *Chem. Res. Toxicol.* **1993**, *6*, 2–18.
84. L. F. Agnez-Lima, J. T. A. Melo, A. E. Silva, A. H. S. Oliveira, A. R. S. Timoteo, K. M. Lima-Bessa, G. R. Martinez, M. H. G. Medeiros, P. Di Mascio, R. S. Galhardo, C. F. M. Menck, *Mutat. Res. Rev. Mutat. Res.* **2012**, *751*, 15–28.
85. W. Küster, Hoppe Seylers, *Z. Physiol. Chem.* **1912**, *82*, 463–483.
86. A. Kamkaew, S. H. Lim, H. B. Lee, L. V. Kiew, L. Y. Chung, K. Burgess, *Chem. Soc. Rev*. **2012**, *42*, 77–88.
87. A. Treibs, F.-H. Kreuzer, *Justus Liebigs Ann. Chem*. **1968**, *718*, 208–223.
88. M. O. Senge, *Chem. Commun*. **2011**, *47*, 1943–1960.
89. P. Rothemund, *J. Am. Chem. Soc*. **1935**, *57*, 2010–2011.
90. P. Rothemund, AR Menotti, *J. Am. Chem. Soc.* **1941**, 63, 267–270.
91. A. D. Adler, F. R. Longo, J. D. Finarelli, J. Goldmacher, J. Assour, L. Korsakoff, *J. Org. Chem*. **1967**, *32*, 476–476.
92. J. S. Lindsey, Synthesis of meso-Substituted Porphyrins, in: *The Porphyrin Handbook*, (ed. 1 K. M. Kadish, K. M. Smith, R. Guilard) Vol 1, Academic Press, London/San Diego, **2000**.
93. S. Plunkett, M. O. Senge, *ECS Trans*. **2011**, *35*, 147–157.
94. G. P. Arsenault, E. Bullock, S. F. MacDonald, *J. Am. Chem. Soc*. **1960**, *82*, 4384–4389.
95. T. D. Lash, *J. Porphyrins Phthalocyanines* **2016**, *20*, 855–888.

96. J. S. Lindsey, *Acc. Chem. Res*. **2010**, *43*, 300–311.
97. D. K. Dogutan, J. S. Lindsey, *J. Org. Chem*. **2008**, *73*, 6728–6742.
98. A. Loudet, K. Burgess, *Chem. Rev*. **2007**, *107*, 4891–4932.
99. M. Kielmann, K. J. Flanagan, K. Norvaiša, D. Intrieri, M. O. Senge, *J. Org. Chem*. **2017**, *82*, 5122–5134.
100. S. Hiroto, Y. Miyake, H. Shinokubo, *Chem. Rev*. **2017**, *117*, 2910–3043.
101. H. L. Kee, C. Kirmaier, L. Yu, P. Thamyongkit, W. J. Youngblood, M. E. Calder, L. Ramos, B. C. Noll, D. F. Bocian, W. R. Scheidt, R. R. Birge, J. S. Lindsey, D. Holten, *J. Phys. Chem. B* **2005**, *109*, 20433–20443.
102. C. Goze, G. Ulrich, L. J. Mallon, B. D. Allen, A. Harriman, R. Ziessel, *J. Am. Chem. Soc*. **2006**, *128*, 10231–10239.
103. G. Ulrich, C. Goze, M. Guardigli, A. Roda, R. Ziessel, *Angew Chem. Int. Ed. Engl*. **2005**, *44*, 3694–3698.
104. Y. Gabe, T. Ueno, Y. Urano, H. Kojima, T. Nagano, *Anal. Bioanal. Chem*. **2006**, *386*, 621–626.
105. C. Tahtaoui, C. Thomas, F. Rohmer, P. Klotz, G. Duportail, Y. Mély, D. Bonnet, M. Hibert, *J. Org. Chem*. **2007**, *72*, 269–272.
106. X.-D. Jiang, J. Zhang, T. Furuyama, W. Zhao, *Org. Lett*. **2012**, *14*, 248–251.
107. H. Brockmann, K.-M. Bliesener, H. H. Inhoffen, *Liebigs Ann. Chem.* **1968**, *718*, 148–161.
108. R. Bonnett, G. F. Stephenson, *J. Org. Chem.* **1965**, *30*, 2791–2798.
109. E. Watanabe, S. Nishimura, H. Ogoshi, Z. Yoshida, *Tetrahedron* **1975**, *31*, 1385–1390.
110. J. E. Baldwin, J. F. DeBernardis, *J. Org. Chem.* **1977**, *42*, 3986–3987.
111. W. W. Kalisch, M. O. Senge, *Angew Chem. Int. Ed.* **1998**, *37*, 1107–1109.
112. M. O. Senge, *Acc. Chem. Res*. **2005**, *38*, 733–743.
113. H. J. Wories, J. H. Koek, G. Lodder, J. Lugtenburg, R. Fokkens, O. Driessen, G. R. Mohn, *Recl. Trav. Chim. Pays-Bas* **1985**, *104*, 288–291.
114. M. Shah, K. Thangaraj, M.-L. Soong, L. T. Wolford, J. H. Boyer, I. R. Politzer, T. G. Pavlopoulos, *Heteroat. Chem*. **1990**, *1*, 389–399.
115. L. Jiao, W. Pang, J. Zhou, Y. Wei, X. Mu, G. Bai, E. Hao, *J. Org. Chem*. **2011**, *76*, 9988–9996.
116. C. Thivierge, R. Bandichhor, K. Burgess, *Org. Lett*. **2007**, *9*, 2135–2138.
117. N. Miyaura, A. Suzuki, *Chem. Rev.* **1995**, *95*, 2457–2483.

118. A. G. Hyslop, M. A. Kellett, P. M. Iovine, M. J. Therien, *J. Am. Chem. Soc*. **1998**, *120*, 12676–12677.
119. V. S. Lin, S. G. DiMagno, M. J. Therien, *Science* **1994**, *264*, 1105–1111.
120. R. Gauler, N. Risch, *Eur. J. Org. Chem*.**1998**, *1998*, 1193–1200.
121. T. Rohand, W. Qin, N. Boens, W. Dehaen, *Eur. J. Org. Chem*. **2006**,, 4658–4663.
122. S. G. DiMagno, V. S. Y. Lin, M. J. Therien, *J. Am. Chem. Soc*. **1993**, *115*, 2513–2515.
123. Y. Chen, X. P. Zhang, *J. Org. Chem*. **2003**, *68*, 4432–4438.
124. T. Rohand, M. Baruah, W. Qin, N. Boens, W. Dehaen, *Chem. Commun.* **2006**, 266–268.
125. M. M. Kim, A. A. Ghogare, A. Greer, T. C. Zhu, *Phys. Med. Biol*. **2017**, 62, R1.
126. M. O. Senge, J. C. Brandt, *Photochem. Photobiol.* **2011**, *87*, 1240–1296.
127. P. Grosjean, J.-F. Savary, G. Wagnières, J. Mizeret, A. Woodtli, J.-F. Theumann, C. Fontolliet, H. Van Den Bergh, P. Monnier, *Laser Med. Sci.* **1996**, *11*, 227–235.
128. B. M. Aveline, T. Hasan, R. W. Redmond, *J. Photochem. Photobiol. B Biol.* **1995**, *30*, 161–169.
129. J. G. Levy, E. Waterfield, A. M. Richter, C. Smits, H. Lui, L. Hruza, R. R. Anderson, V. Salvatori, *Proc. SPIE*, **1994**, *2078*, 91–101.
130. A. F. Cruess, G. Zlateva, A. M. Pleil, B. Wirostko, *Acta Ophthalmol*. **2009**, *87*, 118–132.
131. L. P. Roguin, N. Chiarante, M. C. García Vior, J. Marino, *Int. J. Biochem. Cell B* **2019**, *114*, 105575.
132. Q. Peng, K. Berg, J. Moan, M. Kongshaug, J. M. Nesland, *Photochem. Photobiol.* **1997**, *65*, 235–251.
133. G. Yi, S. Ho Hong, J. Son, J. Yoo, C. Park, Y. Choi, H. Koo, *Quant. Imaging Med. Surg.* **2018**, *8*, 433–443.
134. S. Callaghan, M. O. Senge, *Photochem. Photobiol. Sci.* **2018**, *17*, 1490–1514.
135. J. Winkelman, *Cancer Res*. **1962**, *22*, 589–596.
136. J. Winkelman, J. G. McAfee, H. N. J. Wagner, R. G. Long, *J. Nuclear Med.* **1962**, *3,* 249–253.
137. J. Moan, S. Sommer, *Cancer Lett*. **1983**, *21*, 167–174.

138. G. Oenbrink, P. Jurgenlimke, D. Gabel, *Photochem. Photobiol.* **1988**, *48*, 451–456.
139. D. A. Bellnier, T. J. Dougherty, *Photochem. Photobiol*. **1982**, *36*, 43–47.
140. D. A. Bellnier, C. W. Lin, *Photobiochem. Photobiophys.* **1983**, *6*, 357–366.
141. W. T. Morgan*, Ann. N. Y. Acad. Sci.* **1975**, *244*, 624-650.
142. J. P. Reyftmann, P. Morliere, S. Goldstein, R. Santus, L. Dubertret, D. Lagrange, *Photochem. Photobiol.* **1984**, *40*, 721–730.
143. D. A. Musser, J. M. Wagner, M. Datta-Gupta, *Res. Commun. Chem. Pathol. Pharmacol.* **1982**, *36*, 251–259.
144. J. Kloek, W. Akkermans, G. M. Beijersbergen van Henegouwen, *Photochem. Photobiol.* **1998**, *67*, 150–154.
145. C. A. Morton, *J. Dermatolog. Treat*. **2003**, *3*, 23–26.
146. J. Folkman, *Cancer Res.* **1986**, *46*, 467–473.
147. H. Maeda, J. Wu, T. Sawa, Y. Matsumura, K. Hori, *J. Control. Release* **2000**, *65*, 271–284.
148. J. C. Underwood, I. Carr, *J. Pathol.* **1972**, *107*, 157–166.
149. G. B. Feldman, R. C. Knapp, S. E. Order, S. Hellman, *Cancer Res.* **1972**, *32*, 1663–1666.
150. P. M. Gullino, F. H. Grantham, S. H. Smith, A. C. Haggerty, *J. Natl. Cancer Inst.* **1965**, *34*, 857–869.
151. J. P. Thomas, A. W. Girotti, *Photochem. Photobiol.* **1989**, *49*, 241–247.
152. J. W. Dennis, M. Granovsky, C. E. Warren, *Biochim. Biophys. Acta* **1999**, *1473*, 21–34.
153. M. J. Birnbaum, H. C. Haspel, O. M. Rosen, *Science* **1987**, *235,* 1495–1498.
154. C. Moylan, E. M. Scanlan, M. O. Senge, *Curr. Med. Chem.* **2015**, *22*, 2238–348.
155. S. Singh, A. Aggarwal, N. V. S. D. K. Bhupathiraju, G. Arianna, K. Tiwari, C. Michael Drain, *Chem. Rev.* **2015**, *115*, 10261–10306.
156. M. Zhang, Z. Zhang, D. Blessington, H. Li, T. M. Busch, V. Madrak, J. Miles, B. Chance, J. D. Glickson, G. Zheng *Bioconj. Chem.* **2003**, *14*, 709–14.
157. J. Králová, J. Koivukorpi, Z. Kejík, P. Poučková, E. Sievänen, E. Kolehmainen, V. Král *Org. Biomol. Chem.* **2008**, *6*, 1548–1552.
158. L. Rogers, F. Majer, N. N. Sergeeva. E. Paszko. J. F. Gilmer, M. O. Senge, *Bioorg. Med. Chem. Lett*. **2013**, *23*, 2495–2499.

159. W.-J. Syu, H.-P. Yu, C.-Y. Hsu, Y. C. Rajan, Y.-H. Hsu, Y.-C. Chang, W.-Y. Hsieh, C.-H. Wang, P.-S. Lai, *Small* **2012**, *8*, 2060–2069.
160. M. Sibrian-Vazquez, T. J. Jensen, M. G. Vicente, *Bioconj. Chem.* **2007**, *18*, 1185–1193.
161. N. Gueddari, G. Favre, H. Hachem, E. Marek, F. Le Gaillard, G. Soula, *Biochimie* **1993**, *75*, 811–819.
162. U. Schmidt-Erfurth, H. Diddens, R. Birngruber, T. Hasan, *Br. J. Cancer.* **1997**, *75*, 54–61.
163. M. D. Savellano, T. Hasan, *Clin. Cancer Res.* **2005**, 11, 1658–1668.
164. M. Mitsunaga, M. Ogawa, N. Kosaka, L. T. Rosenblum, P. L. Choyke, H. Kobayashi, *Nat. Med.* **2011**, *17*, 1685–1691.
165. R. Hudson, M. Carcenac, K. Smith, L. Madden, O. J. Clarke, A. Pelegrin, J. Greenman, R. W. Boyle, *Br. J. Cancer* **2005**, *92*, 1442–1449.
166. N. Malatesti, K. Smith, H. Savoie, J. Greenman, R. W. Boyle, *Int. J. Oncol.* **2006**, *28*, 1561–1569.
167. C. Staneloudi, K. A. Smith, R. Hudson, N. Malatesti, H. Savoie, R. W. Boyle, J. Greenman, *Immunology* **2007**, *120*, 512–517.
168. B. C. Wilson, M. Olivo, G. Singh, *Photochem Photobiol*. **1997,** *65*,166–76.
169. X. Sun, W. N. Leung, *Photochem Photobiol.* **2002**, *75*, 644–651.
170. B. M. Aveline, R. W. Redmond, *Photochem Photobiol.* **1999**, *69*, 306–316.
171. Y. J. Hsieh, C. C. Wu, C. J. Chang, J. S. Yu, *J. Cell. Physiol.* **2003**, *194*, 363–375.
172. M.-H. Teiten, L. Bezdetnaya, P. Morlière, R. Santus, F. Guillemin, *Br. J. Cancer* **2003**, *88*, 146–152.
173. A. R. Oseroff, D. Ohuoha, G. Ara, D. McAuliffe, J. Foley, L. Cincotta, *Proc. Natl. Acad. Sci. U.S.A.* **1986**, *83*, 9729–9733.
174. H. Dummin, T. Cernay, H. W. Zimmermann, *J. Photochem. Photobiol. B Biol.* **1997**, *37*, 219–229.
175. J. M. Runnels, N. Chen, B. Ortel, D. Kato, T. Hasan, *Br. J. Cancer* **1999**, *80*, 946–953.
176. I. J. MacDonald, J. Morgan, D. A. Bellnier, G. M. Paszkiewicz, J. E. Whitaker, D. J. Litchfield, T. J. Dougherty, *Photochem. Photobiol.* **1999**, *70*, 789–797.
177. K. W. Woodburn, N. J. Vardaxis, J. S. Hill, A. H. Kaye, D. R. Phillips, *Photochem. Photobiol.* **1991**, *54*, 725–732.

178. M. L. Agarwal, M. E. Clay, E. J. Harvey, H. H. Evans, A. R. Antunez, N. L. Oleinick, *Cancer Res*. **1991**, *51*, 5993–5996.
179. S. M. Chiu, H. H. Evans, M. Lam, A. L. Nieminen, N. L. Oleinick, *Cancer Lett.* **2001**, *165*, 51–58.
180. H.-R. C. Kim, Y. Luo, G. Li, D. Kessel, *Cancer Res.* **1999**, *59*, 3429–3432.
181. J. J. Reiners, J. A. Caruso, P. Mathieu, B. Chelladurai, X. M. Yin, D. Kessel *Cell Death Differ.* **2002**, *9*, 934–944.
182. L. Y. Xue, S. M. Chiu, K. Azizuddin, S. Joseph, N. L. Oleinick, *Autophagy* **2008**, *4*, 125–127.
183. D. Kessel, J. J. Reiners, *Photochem. Photobiol*. **2007**, *83*, 1024–1028.
184. M. E. Rodriguez, P. Zhang, K. Azizuddin, G. B. Delos Santos, S. Chiu, L. Xue, J. C. Berlin, X. Peng, H. Wu, M. Lam, A.-L. Nieminen, M. E. Kenney, N. L. Oleinick, *Photochem. Photobiol*. **2009**, *85*, 1189–1200.
185. D. Kessel, J. J. Reiners, *Photochem Photobiol.* **2017**, 93, 1502–1508.
186. Y. Luo, D. Kessel, *Photochem. Photobiol.* **1997**, *66*, 479–483.
187. D. Kessel, N. L. Oleinick, *Photochem. Photobiol.* **2018**, *94*, 213–218.
188. J. Folkman, *N. Engl. J. Med.* **1971**, *285*, 1182–1186.
189. B. W. Henderson, V. H. Fingar, *Photochem. Photobiol.* **1989**, *49*, 299–304.
190. C. J. Gomer, A. Ferrario, M. Luna, N. Rucker, S. Wong, *Lasers Surg. Med.* **2006**, *38*, 516–521.
191. M. Khurana, E. H. Moriyama, A. Mariampillai, B. C. Wilson, *J. Biomed. Opt.* **2008**, *13*, 040502.
192. B. Chen, T. Roskams, P. A. M. de Witte, *Photochem. Photobiol*. **2002**, *76*, 509–513.
193. A. P. Castano, P. Mroz, M. R. Hamblin, *Nat. Rev. Cancer* **2006**, *6*, 535–545.
194. W. J. A. de Vree, M. C. Essers, J. F. Koster, W. Sluiter, *Cancer Res.* **1997**, *57*, 2555–2558.
195. M. Korbelik, *Lasers Surg. Med*. **2006**, *38*, 500–508.
196. G. Krosl, M. Korbelik, J. Krosl, G. J. Dougherty, *Cancer Res.* **1996**, *56*, 3281–3286.
197. G. Canti, A. D. Simone, M. Korbelik, *Photochem. Photobiol. Sci.* **2002**, *1*, 79–80.
198. A. D. Garg, D. Nowis, J. Golab, P. Vandenabeele, D. V. Krysko, P. Agostinis, *BBA-Rev. Cancer* **2010**, *1805*, 53–71.

199. M. Korbelik, G. Krosl, J. Krosl, G. J. Dougherty, *Cancer Res*. **1996**, 56, 5647–5652.
200. P. S. Thong, K. W. Ong, N. S. Goh, K. W. Kho, V. Manivasager, R. Bhuvaneswari, M. Olivo, K. C. Soo. *Lancet Oncol.* **2007**, *10*, 950–952.
201. C. A. Elmets, K. D. Bowen, *Cancer Res.* **1986**, *46*, 1608-1611.
202. B. Q. Spring, I. Rizvi, N. Xu, T. Hasan, *Photochem. Photobiol. Sci.* **2015**, *14*, 1476–1491.
203. M.-F. Zuluaga, N. Lange, *Curr. Med. Chem*. **2008**, *15*, 1655–1673.
204. H. S. de Bruijn, S. Brooks, A. van der Ploeg-van den Heuvel, T. L. M. ten Hagen, E. R. M. de Haas, D. J. Robinson, *PLoS One* **2016**, *11*, e0148850.
205. K. Plaetzer, B. Krammer, J. Berlanda, F. Berr, T. Kiesslich, *Lasers Med. Sci.* **2009**, *24*, 259–268.
206. J. Rotomskien, R. Kapočiūt, R. Rotomskis, G. Jonušauskas, T. Szitó, A. Nizhnik, *J. Photochem. Photobiol. B Biol.* **1988**, *2*, 373–379.
207. T. Yogo, Y. Urano, Y. Ishitsuka, F. Maniwa, T. Nagano*, J. Am. Chem. Soc.* **2005**, 127, 12162–12163.
208. S. I. Moriwaki, J. Misawa, Y. Yoshinari, I. Yamada, M. Takigawa, Y. Tokura, *Photodermatol. Photoimmunol. Photomed.* **2001**, *17*, 241–243.
209. C. Moureu, C. Dufraisse, P. M. Dean, *C. R. Acad. Sci.* **1926**, *182*, 1584–1587.
210. M. A. Filatov, M. O. Senge, *Mol. Syst. Des. Eng*. **2016**, *1*, 258–272.
211. O. Diels, K. Alder, *Justus Liebigs Ann. Chem.* **1928**, *460*, 98–122.
212. C. S. Foote, S. Wexler, *J. Am. Chem. Soc.* **1964**, *86*, 3879–3880.
213. H. H. Wasserman, J. R. Scheffer, *J. Am. Chem. Soc.* **1967**, *89*, 3073–3075.
214. A. J. Bloodworth, H. J. Eggelte, Endoperoxides in Singlet O_2 (A. A. Frimer, ed.), CRC Press: Boca Raton, FL, **1985,** 193–203.
215. M. Schäfer-Ridder, U. Brocker, E. Vogel, *Angew Chem. Int. Ed. Engl.* **1976**, *15*, 228–229.
216. T. Noh, H. Gan, S. Halfon, B. J. Hrnjez, N. C. Yang, *J. Am. Chem. Soc*. **1997**, *119*, 7470–7482.
217. M. Seip, H. D. Brauer, *J. Am. Chem. Soc*. **1992**, *114*, 4486–4490.
218. B. Stevens, S. R. Perez, J. A. Ors, *J. Am. Chem. Soc*. **1974**, *96*, 6846–6850.
219. C. J. M. van den Heuvel, A. Hofland, H. Steinberg, T. J. de Boer, *Recl. Trav. Chim. Pays-Bas* **1980**, *99*, 275–278.

220. I. Erden, P. Gölitz, R. Näder, A. de Meijere, *Angew Chem. Int. Ed. Engl.* **1981**, *20*, 583–585.
221. N. J. Turro, M. F. Chow, *J. Am. Chem. Soc.* **1981**, *103*, 7218–7224.
222. H. H. Wasserman, K. B. Wiberg, D. L. Larsen, J. Parr, *J. Org. Chem.* **2005**, *70*, 105–109.
223. M. Klaper, T. Linker, *Chem. Eur. J* **2015**, *21*, 8569–8577.
224. B. D. Rihter, M. E. Kenney, W. E. Ford, M. A. J. Rodgers, *J. Am. Chem. Soc.* **1993**, *115*, 8146–8152.
225. I. Saito, R. Nagata, T. Matsuura, *J. Am. Chem. Soc*. **1985**, *107*, 6329–6334.
226. S. Kim, M. Fujitsuka, T. Majima, *J. Phys. Chem. B* **2013**, *117*, 13985–13992.
227. D. Arian, L. Kovbasyuk, A. Mokhir, *J. Am. Chem. Soc*. **2011**, *133*, 3972–3980.
228. W. Fudickar, A. Fery, T. Linker, *J. Am. Chem. Soc.* **2005**, *127*, 26, 9386–9387.
229. S. Hettiaratchy, J. Clarke, J. Taubel, C. Besa, *BMJ* **2000**, *320*, 1245.
230. A. M. Asadirad, Z. Erno, N. R. Branda, *Chem. Commun*. **2013**, *49*, 5639–5641.
231. S. Martins, J. P. S. Farinha, C. Baleizão, M. N. Berberan-Santos, *Chem. Commun*. **2014**, *50*, 3317–3320.
232. S. Kolemen, T. Ozdemir, D. Lee, G. M. Kim, T. Karatas, J. Yoon, E. U. Akkaya, *Angew. Chem. Int. Ed. Engl.* **2016**, *55*, 3606–3610.
233. W. Lv, H. Xia, K. Y. Zhang, Z. Chen, S. Liu, W. Huang, Q. Zhao, *Mater. Horiz*. **2017**, *4*, 1185–1189.
234. E. Ucar, D. Xi, O. Seven, C. Kaya, X. Peng, W. Sun, E. U. Akkaya, *Chem. Commun*. **2019**, *55*, 13808–13811.
235. C. K. Sen, *Wound Repair Regen*. **2009**, *17*, 1–18.
236. S. Benz, S. Nötzli, J. S. Siegel, D. Eberli, H. J. Jessen, *J. Med. Chem*. **2013**, *56*, 10171–10182.
237. C. Changtong, D. W. Carney, L. Luo, C. A. Zoto, J. L. Lombardi, R. E. Connors, *J. Photochem. Photobiol. A Chem*. **2013**, *260*, 9–13.
238. I. S. Turan, D. Yildiz, A. Turksoy, G. Gunaydin, E. U. Akkaya, *Angew. Chem. Int. Ed.* **2016**, *55*, 2875–2878.
239. S. Callaghan, M. A. Filatov, E. Sitte, H. Savoie, R. W. Boyle, K. J. Flanagan, M. O. Senge, *Photochem. Photobiol. Sci*. **2017**, *16*, 1371–1374.
240. W. Xiao, P. Wang, C. Ou, X. Huang, Y. Tang, M. Wu, W. Si, J. Shao, W. Huang, X. Dong, *Biomaterials* **2018**, *183*, 1–9.

241. L. Jiao, X. Zhang, J. Cui, X. Peng, F. Song, *ACS Appl. Mater. Interfaces* **2019**, *11*, 25750–25757.
242. Y. Jing, Q. Xu, M. Chen, X. Shao, *Bioorg. Med. Chem*. **2019**, *27*, 2201–2208.
243. H. C. Kolb, M. G. Finn, K. B. Sharpless, *Angew. Chem. Int. Ed*., **2001**, *40*, 2004–2021.
244. J. Chen, D. Li, B. Huo, F. Zhang, X. Zhao, G. Yuan, D. Chen, M. Song, J. Xue, *Mol. Pharmaceutics* **2019**, *16*, 3703–3710.
245. A. Markovac, M. P. LaMontagne, *J. Med. Chem.* **1980**, *23*, 1198–1201.
246. A. Nayak, S. Roy, B. D. Sherman, L. Alibabaei, A. M. Lapides, M. K. Brennaman, K.-R. Wee, T. J. Meyer, *ACS Appl. Mater. Interfaces* **2016**, *8*, 3853–3860.
247. A. Garofalo, A. Parat, C. Bordeianu, C. Ghobril, M. Kueny-Stotz, A. Walter, J. Jouhannaud, S. Begin-Colin, D. Felder-Flesch, *New J. Chem.* **2014**, *38*, 5226–5239.
248. B. M. J. M. Suijkerbuijk, M. Lutz, A. L. Spek, G. van Koten, R. J. M. Klein Gebbink, *Org. Lett*. **2004**, *6*, 3023–3026.
249. K. Kulangiappar, M. Anbu Kulandainath, T. Raju, *Ind. Eng. Chem. Res*. **2010**, *49*, 146670–146673.
250. Y. Du, D. Zhang, W. Chen, M. Zhang, Y. Zhou, X. Zhou, *Bioorg. Med. Chem.* **2010**, *18*, 1111–1116.
251. J. F. W. Keana, S. Pou, *Org. Prep. Proced. Int*. **1989**, *21*, 303–308.
252. T. Mosmann, *J. Immunol. Methods* **1983**, *65*, 55–63.
253. Y. Yang, Y. Yu, X. Li, J. Li, Y. Wu, J. Yu, J. Ge, Z. Huang, L. Jiang, Y. Rao, M. Yang, *J. Med. Chem*. **2017**, *60*, 1994–2005.
254. J. Zhao, K. Xu, W. Yang, Z. Wang, F. Zhong, *Chem. Soc. Rev*. **2015**, *44*, 8904–8939.
255. D. S. McClure, *J. Chem. Phys*. **1949**, *17*, 905 –913.
256. S. P. McGlynn, T. Azuml, M. Klnoshlta, Molecular spectroscopy of the triplet state, Prentice-Hall, Inc., Englewood Cliffs, New Jersey **1969**.
257. P. Batat, M. Cantuel, G. Jonusauskas, L. Scarpantonio, A. Palma, D. F. O'Shea, N. D. McClenaghan, *J. Phys. Chem. A*, **2011**, *115*, 14034–14039.
258. A. T. Byrne, A. E. O'Connor, M. Hall, J. Murtagh, K. O'Neill, K. M. Curran, K. Mongrain, J. A. Rousseau, R. Lecomte, S. McGee, J. J. Callanan, D. F. O'Shea, W. M. Gallagher, *Br. J. Cancer* **2009**, *101*, 1565–1573.

259. S. O. McDonnell, M. J. Hall, L. T. Allen, A. Byrne, W. M. Gallagher, D. F. O'Shea *J. Am. Chem. Soc*., **2005**, *127*, 16360–16361.
260. Y. Cakmak, S. Kolemen, S. Duman, Y. Dede, Y. Dolen, B. Kilic, Z. Kostereli, L. T. Yildirim, A. L. Dogan, D. Guc, E. U. Akkaya, *Angew. Chem. Int. Ed.* **2011**, *50*, 11937–11941.
261. L. Huang, X. Yu, W. Wu, J. Zhao, *Org. Lett*., **2012**, *14*, 2594–2597.
262. W. Wu, J. Zhao, J. Sun, S. Guo, *J. Org. Chem*., **2012**, *77*, 5305–5312.
263. V.-N. Nguyen, Y. Yim, S. Kim, B. Ryu, K. M. K. Swamy, G. Kim, N. Kwon, C.-Y. Kim, S. Park, J. Yoon*, Angew. Chem. Int. Ed.* **2020**, *9*, 8957–8962.
264. S. Qi, N. Kwon, Y. Yim, V. N. Nguyen, J. Yoon, *Chem. Sci.* **2020**, *11*, 6479–6484.
265. M. A. Filatov, S. Karuthedath, P. M. Polestshuk, H. Savoie*,* K. J. Flanagan, C. Sy, E. Sitte, M. Telitchko, F. Laquai, R. W. Boyle, M. O. Senge, *J. Am. Chem. Soc.* **2017**, *139*, 6282-6285.
266. Z. Wang, A. A. Sukhanov, A. Toffoletti, F. Sadiq, J. Zhao, A. Barbon, V. K. Voronkova, B. Dick, *J. Phys. Chem. C* **2019**, *123*, 265–274.
267. A. Harriman, L. J. Mallon, G. Ulrich, R. Ziessel, *ChemPhysChem* **2007**, *8*, 1207–1214.
268. K. Chen, W. Yang, Z. Wang, A. Lagatti, L. Bussotti, P. Foggi, W. Ji*,* J. Zhao, M. Di Donato, *J. Phys. Chem. A* **2017**, *121*, 7550–7564.
269. Y. Dong, A. A. Sukhanov, J. Zhao, A. Elmali, X. Li, B. Dick, A. Karatay, V. K. Voronkova, *J. Phys. Chem. C* **2019**, *123*, 22793–22811.
270. I. S. Turan, G. Gunaydin, S. Ayan, E. U. Akkaya, *Nat. Commun.* **2018**, *9*, 805.
271. S. Mukherjee, P. Thilagar, *RSC Adv*. **2014**, *5*, 2706–2714.
272. M. A. Filatov, S. Karuthedath, P. M. Polestshuk, S. Callaghan, K. J. Flanagan, T. Wiesner, F. Laquai, M. O. Senge, *ChemPhotoChem* **2018**, *2*, 606–615.
273. M. A. Filatov, S. Karuthedath, P. M. Polestshuk, S. Callaghan, K. J. Flanagan, M. Telitchko, T. Wiesner, F. Laquai, M. O. Senge, *Phys. Chem. Chem. Phy*s. **2018**, *20*, 8016–8031.
274. M. A. Filatov, R. Guilard, P. D. Harvey, *Org. Lett*. **2010**, *12*, 196–199.
275. M. A. Filatov, E. Heinrich, D. Busko, I. Z. Ilieva, K. Landfester, S. Baluschev, *Phys. Chem. Chem. Phys.* **2015**, *17*, 6501–6510.
276. B. Michelet, C. Deldaele, S. Kajouj, C. Moucheron, G. Evano, *Org. Lett.* **2017**, *19*, 3576–3579.

277. X.-F. Zhang, X. Li, *J. Lumin.* **2011**, *131*, 2263–2266.
278. J. R. Lakowicz, *Principles of Fluorescence Spectroscopy*, Kluwer Academic/Plenum Publishers, New York, London, Moscow, Dordrecht, **1999**.
279. D. M. E. Freeman, A. J. Musser, J. M. Frost, H. L. Stern, A. K. Forster, K. J. Fallon, A. G. Rapidis, F. Cacialli, I. McCulloch, T. M. Clarke, R. H. Friend, H. Bronstein, *J. Am. Chem. Soc*. **2017**, *139*, 11073–11080.
280. F. B. Dias, J. Santos, D. R. Graves, P. Data, R. S. Nobuyasu, M. A. Fox, A. S. Batsanov, T. Palmeira, M. N. Berberan-Santos, M. R. Bryce, A. P. Monkman, *Adv. Sci.* **2016**, *3*, 1600080.
281. G. J. Kavarnos, N. J. Turro, *Chem. Rev.* **1986**, *86*, 2, 401–449.
282. S. L. Niu, C. Massif, G. Ulrich, R. Ziessel, P.-Y. Renard, A. Romieu, *Org. Biomol. Chem*. **2011**, *9*, 66–69.
283. J.-M. Aubry, C. Pierlot, J. Rigaudy, R. Schmidt, *Acc. Chem. Res*. **2003**, *36*, 668–675.
284. H. Sunahara, Y. Urano, H. Kojima, T. Nagano, *J. Am. Chem. Soc*. **2007**, *129*, 5597–5604.
285. C. –H. Lee, C. –K. Lee, *Bull. Korean Chem. Soc.* **1992**, *13*, 352–354.
286. A. C. Gehrold, T. Bruhn, H. Schneider, U. Radius, G. Bringmann, *Org. Lett.* **2015**, *17*, 210–213.
287. U. Simonis, F. A. Walker, P. L. Lee, B. J. Hanquet, D. J. Meyerhoff, W. R. Scheidt, *J. Am. Chem. Soc.* **1987**, *109*, 2659–2668.
288. M. Urbani, T. Torres, *Chem. Eur. J*. **2014**, *20*, 16337–16349.
289. J. Almog, J. E. Baldwin, M. J. Crossley, J. F. Debernardis, R. L. Dyer, J. R. Huff, M. K. Peters, *Tetrahedron*, **1981**, *37*, 3589–3601.
290. A. Osuka, T. Nagata, K. Maruyama, *Chem. Lett.* **1991**, *20*, 1687–1690.
291. Y. Uemori, E. Kyuno, *Inorg. Chim. Acta*, **1989**, *165*, 115–122.
292. J. P. Collman, R. Boulatov, C. J. Sunderland, L. Fu, *Chem. Rev*. **2004**, *104*, 561–588.
293. E. Rose, B. Andrioletti, S. Zrig, M. Quelquejeu-Ethève, *Chem. Soc. Rev.* **2005**, *34*, 573–583.
294. S. Fantauzzi, E. Gallo, E. Rose, N. Raoul, A. Caselli, S. Issa, F. Ragaini, S. Cenini, *Organometallics* **2008**, *27*, 6143–6151.
295. M. Takeuchi, T. Shioya, T. M. Swager, *Angew Chem. Int. Ed.* **2001**, *40*, 3372–3376.

296. X. Bao, H. Zhang, Z. Zhang, L. Wu, Z. Li, *Inorg. Chem. Commun.* **2007**, *10*, 728–730.
297. J. A. Wytko, E. Graf, J. Weiss, *J. Org. Chem.* **1992**, *57*, 1050–1018.
298. C.-H. Lee, E. Galoppini, *J. Org. Chem*. **2010**, *75*, 3692–3704.
299. T. P. Wijesekera, J. B. Paine III, D. Dolphin, *J. Am. Chem. Soc.* **1983**, 105, 6747–6749.
300. T. G. Traylor, H. Diekmann, C. K. Chang, *J. Am. Chem. Soc*. **1971**, *93*, 4068–4070.
301. A. R. Battersby, W. Howson, A. D. Hamilton, *J. Chem. Soc*., *Chem. Commun*. **1982**, 1266–1268.
302. M. Momenteau, B. Loock, *J. Mol. Catal.* **1980**, *7*, 315–320.
303. R. W. Wagner, T. E. Johnson, J. S. Lindsey, *Tetrahedron* **1997**, *53*, 6755–6790.
304. M. Momenteau, J. Mispelter, B. Loock, E. Bisagni, *J. Chem. Soc*., *Perkin Trans. 1* **1983**, 189–196.
305. E. Rose, Q.-Z. Ren, B. Andrioletti, *Chem. Eur. J.* **2004**, *10*, 224–230.
306. J. P. Collman, X. Zhang, V. J. Lee, J. I. Brauman, *J. Chem. Soc*., *Chem. Commun.* **1992**, 1647–1649.
307. J. Almog, J. E. Baldwin, R. L. Dyer, M. Peters, *J. Am. Chem. Soc.* **1975**, *97*, 226–227.
308. M. R. Johnson, W. K. Seok, W. Ma, C. Slebodnick, K. M. Wilcoxen, J. A. Ibers, *J. Org. Chem*. **1996**, *61*, 3298–3303.
309. C.-H. Lee, K. Chitre, E. Galoppini, *J. Chin. Chem. Soc.* **2010**, *57*, 1103–1110.
310. J. Webb, F. Maharaj, I. Blake, M. Crossley, *Synlett* **2008**, *2008*, 2147–2149.
311. J. P. Collman, P. C. Herrmann, L. Fu, T. A. Eberspacher, M. Eubanks, B. Boitrel, P. Hayoz, X. Zhang, J. I. Brauman, V. W. Day, *J. Am. Chem. Soc*. **1997**, *119*, 3481–3489.
312. J. P. Coliman, X. Zhang, P. C. Herrmann, E. S. Uffelman, B. Boitrel, A. Straumanis, J. I. Brauman, *J. Am. Chem. Soc.* **1994**, *116*, 2681–2682.
313. C. J. Medforth, M. O. Senge, K. M. Smith, L. D. Sparks, J. A. Shelnutt, *J. Am. Chem. Soc.* **1992**, *114*, 9859–9869.
314. Z. Zhou, M. Shen, C. Cao, Q. Liu, Z. Yan, *Chem. Eur. J.* **2012**, *18*, 7675–7679.
315. M. Newcomb, R. Zhang, R. E. P. Chandrasena, J. A. Halgrimson, J. H. Horner, T. M. Makris, S. G. Sligar, *J. Am. Chem. Soc*. **2006**, *128*, 4580–4581.

316. M. Roucan, M. Kielmann, S. J. Connon, S. S. R. Bernhard, M. O. Senge, *Chem. Commun*. **2017**, *54*, 26–29.
317. D. Reddy, T. K. Chandrashekar, *J. Chem. Soc., Dalton Trans*. **1992**, 619–625.
318. M. Ravikanth, D. Reddy, T. K. Chandrashekar, *J. Photochem. Photobiol. A: Chem.* **1993**, *72*, 61–67.
319. D. Reddy, T. K. Chandrashekar, H. van Willigen, *Chem. Phys. Lett.* **1993**, *202*, 120–126.
320. D. Reddy, M. Ravikanth, T. K. Chandrashekar, *J. Chem. Soc., Dalton Trans.* **1993**, 3575–3580.
321. Z. Zhou, X. Zhou, Q. Liu, X. Zhang, H. Liu, *Org. Lett.* **2015,** *17*, 4078–4081.
322. C. Roche, Q. Luo, G. Gil-Ramírez, H. W. Jiang, D. R. Kohn, Y. Xiong, A. L. Thompson, H. L. Anderson, *J. Org. Chem.* **2017**, *82*, 7446–7462.
323. T. G. Traylor, M. J. Mitchell, S. Tsuchiya, D. H. Campbell, D. V. Stynes, N. Koga, *J. Am. Chem. Soc*. **1981**, *103*, 5234–5236.
324. T. G. Traylor, S. Tsuchiya, D. Campbell, M. Mitchell, D. Stynes, N. Koga, *J. Am. Chem. Soc.* **1985**, *107*, 60–614.
325. J. M. Baldwin, *Prog. Biophys. Mol. Biol.* **1976**, *29*, 225–320.
326. T. G. Traylor, D. Campbell, S. Tsuchiya, *J. Am. Chem. Soc.* **1979**, *101*, 4748–4749.
327. W. B. Cruse, O. Kennard, G. M. Sheldrick, A. D. Hamilton, S. G. Hartley, A. R. Battersby, *J. Chem. Soc., Chem. Commun*. **1980**, 700–701.
328. A. Osuka, F. Kobayashi, K. Maruyama, *B. Chem. Soc. Jpn.*, **1991**, *64*, 1213–1225.
329. Q. M. Wang, D. W. Bruce, *Synlett*. **1995**, *1995*, 1267–1268.
330. B. J. Littler, M. A. Miller, C.-H. Hung, R. W. Wagner, D. F. O'Shea, P. D. Boyle, J. S. Lindsey, *J. Org. Chem*. **1999**, *64*, 1391–1396.
331. S. R. Halper, S. M. Cohen, *Chem. Eur. J.* **2003**, *9*, 4661–4669.
332. A. B. J. Parusel, T. Wondimagegn, A. Ghosh, *J. Am. Chem. Soc.* **2000**, *122*, 6371–6374.
333. J. A. Shelnutt, X.-Z. Song, J.-G. Ma, S.-L. Jia, W. Jentzen, C. J. Medforth, C. J. Medforth, *Chem. Soc. Rev.* **1998**, *27*, 31–42.
334. A. D. Bond, N. Feeder, J. E. Redman, S. J. Teat, J. K. M. Sanders, *Cryst. Growth Des.* **2002**, *2*, 27–39.
335. W. Jentzen, J. G. Ma, J. A. Shelnutt, *Biophys. J* **1998**, *74*, 753–763.

336. W. Jentzen, X. Z. Song, J. A. Shelnutt, *J. Phys. Chem. B* **1997**, *101*, 1684–1699.
337. A. D. Bangham, M. W. Hill, N. G. A. Miller, Methods in Membrane Biology: (Vol. 1, ed. E. D. Korn), Springer US, Boston, MA, **1974**.
338. A. S. L. Derycke, P. A. M. de Witte, *Adv. Drug Deliv. Rev.* **2004**, *56*, 17–30.
339. R. L. Juliano, D. Stamp, *Biochem. Biophys. Res. Commun*. **1975**, *63*, 651–658.
340. A. Molinari, C. Bombelli, S. Mannino, A. Stringaro, L. Toccacieli, A. Calcabrini, M. Colone, A. Mangiola, G. Maira, P. Luciani, G. Mancini, G. Arancia, *Int. J. Cancer*, **2007**, *121*, 1149–1155.
341. F. Jiang, L. Lilge, J. Grenier, Y. Li, M. D. Wilson, M. Chopp, *Laser Surg. Med.* **1998**, *22*, 74–80.
342. G. D. Venosa, L. Hermida, H. Fukuda, M. V. Defain, L. Rodriguez, L. Mamone, A. MacRobert, A. Casas, A. Batlle, *J. Photochem. Photobiol. B Biol*. **2009**, *96*, 152–158.
343. L. Gryziewicz, *Adv. Drug Deliv. Rev*. **2005**, *57*, 2092–2098.
344. W. M. Chan, T.-H. Lim, A. Pece, R. Silva, N. Yoshimura, *Graefes Arch. Clin. Exp. Ophthalmol.* **2010**, *248*, 613–626.
345. V. Torchilin, *Adv. Drug Deliv. Rev.* **2011**, *63*, 131–135.
346. ClinicalTrials.gov, https://clinicaltrials.gov/ct2/show/NCT02340156, (accessed 20 May 2020).
347. ClinicalTrials.gov, https://clinicaltrials.gov/ct2/show/NCT03076372, (accessed 20 May 2020).
348. C. M. Barton, S. L. Staddon, C. M. Hughes, P. A. Hall, C. O'sullivan, G. Klöppel, B. Theis, R. C. G. Russell, J. Neoptolemos, R. C. N. Williamson, Br. J. *Cancer* **1991**, *64*, 1076–1082.
349. ClinicalTrials.gov, https://clinicaltrials.gov/ct2/show/NCT02833766, (accessed 17 May 2020).
350. ClinicalTrials.gov, https://clinicaltrials.gov/ct2/show/NCT03384238, (accessed 20 May 2020).
351. S. Wilhelm, A. J. Tavares, Q. Dai, S. Ohta, J. Audet, H. F. Dvorak, W. C. Chan, *Nat. Rev. Mater.* **2016**, *1*, 1–12.
352. M. M. Schmidt, K. D. Wittrup, *Mol. Cancer Ther*. **2009**, *8*, 2861–2871.
353. H. Han, M. E. Davis, *Mol. Pharmaceutics* **2013**, *10*, 2558–2567.
354. D. B. Kirpotin, D. C. Drummond, Y. Shao, M. R. Shalaby, K. Hong, U. B. Nielsen, J. D. Marks, C. C. Benz, J. W. Park, *Cancer Res*. **2006**, *66*, 6732–6740.

355. C. Mamot, D. C. Drummond, C. O. Noble, V. Kallab, Z. Guo, K. Hong, D. B. Kirpotin, J. W. Park, *Cancer Res*. **2005**, *65*, 11631–11638.
356. D. W. Bartlett, H. Su, I. J. Hildebrandt, W. A. Weber, M. E. Davis, *PNAS* **2007**, *104*, 15549–15554.
357. J. A. O'Hara, E. B. Douple, M. J. Abrams, D. J. Picker, C. M. Giandomenico, J. F. Vollano, *Int. J. Radiat. Oncol. Biol. Phys.* **1989**, *16*, 1049–1052.
358. H. P. Mack, W. K. Diehl, G. C. Peck, F. H. Figge, *Cancer* **1957**, *10*, 529–539.
359. L. Cohen, S. Schwartz, *Cancer Res*. **1966**, *26*, 1769–1773.
360. M. Schaffer, P. M. Schaffer, L. Corti, G. Sotti, A. Hofstetter, G. Jori, E. Dühmke, ORT **2001**, *24*, 482–485.
361. M. Schaffer, P. M. Schaffer, M. Vogesser, B. Ertl-Wagner, J. Rauch, R. Oberneder, G. Jori, A. Hofstetter, E. Dühmke, *Photochem. Photobiol. Sci.* **2002**, *1*, 686–689.
362. U. Kulka, M. Schaffer, A. Siefert, P. M. Schaffer, A. Olsner, K. Kasseb, A. Hofstetter, E. Dühmke, G. Jori, *Biochem. Biophys. Res. Commun*. **2003**, *311*, 98–103.
363. J. Moan, E. O. Pettersen, *Int. J. Radiat. Biol*. **1981**, *40*, 107–109.
364. J. Yamamoto, S.-I. Ogura, T. Tanaka, T. Kitagawa, Y. Nakano, T. Saito, M. Takahashi, D. Akiba, S. Nishizawa, *Oncol. Rep.* **2012**, *27*, 1748–1752.
365. J. Takahashi, M. Misawa, H. Iwahashi, *Genom. Data* **2015**, *5*, 192–194.
366. J. Takahashi, M. Misawa, H. Iwahashi, *Microarrays (Basel)* **2015**, *4*, 25–40.
367. J. Takahashi, M. Misawa, H. Iwahashi, *Int. J. Radiat. Biol.* **2016**, *92*, 774–789.
368. J. Takahashi, M. Misawa, M. Murakami, T. Mori, K. Nomura, H. Iwahashi, *Springerplus*, **2013**, *2*, 602.
369. J. Takahashi, M. Misawa, *Radiat Phys Chem.* **2009**, *78*, 889–898.
370. F. Bistolfi, *Panminerva Med.* **2000**, *42*, 69–75.
371. M. Schaffer, B. Ertl-Wagner, P. M. Schaffer, U. Kulka, G. Jori, E. Duhmke, A. Hofstetter, *Curr. Med. Chem*. **2005**, *12*, 1209–1215.
372. G. Obaid, K. Samkoe, K. Tichauer, S. Bano, Y. Park, Z. Silber, S. Hodge, S. Callaghan, S. Mallidi, B. Pogue, T. Hasan, submitted article.
373. K. Maruyama, T. Takizawa, T. Yuda, S. J. Kennel, L. Huang, M. Iwatsuru, *BBA-Biomembranes* **1995**, *1234*, 74–80.
374. J. A. Harding, C. M. Engbers, M. S. Newman, N. I. Goldstein, S. Zalipsky, *BBA-Biomembranes*, **1997**, *1327*, 181–192.

375. S. E. Miller, W. S. Tummers, N. Teraphongphom, N. S. van den Berg, A. Hasan, R. D. Ertsey, S. Nagpal, L. D. Recht, E. D. Plowey, H. Vogel, G. R. Harsh, *J. Neuro-Oncol*. **2018**, *139*, 135–143.
376. S. C. Semple, A. Chonn, P. R. Cullis, *Adv. Drug Deliv. Rev.* **1998**, *32*, 3–17.
377. A. Gonzalez-Quintela, R. Alende, F. Gude, J. Campos, J. Rey, L. M. Meijide, C. Fernandez-Merino, C. Vidal, *Clin. Exp. Immunol.* **2008**, *151*, 42–50.
378. B. A. Faller, B. Burtness, *Biologics* **2009**, *3*, 419–428.
379. G. Obaid, S. Bano, S. Mallidi, M. Broekgaarden, J. Kuriakose, Z. Silber, A. L. Bulin, Y. Wang, Z. Mai, W. Jin, D. Simeone, *Nano Lett.* **2019**, *19*, 7573–7587.
380. H. C. Huang, I. Rizvi, J. Liu, S. Anbil, A. Kalra, H. Lee, Y. Baglo, N. Paz, D. Hayden, S. Pereira, B. W. Pogue, *Cancer Res*. **2018**, *78*, 558–571.
381. L. J. Scott, K. L. Goa, *Drugs Aging*, **2000**, *16*, 139–146.
382. M. T. Huggett, M. Jermyn, A. Gillams, R. Illing, S. Mosse, M. Novelli, E. Kent, S. G. Bown, T. Hasan, B. W. Pogue, S. P. Pereira, *Br. J. Cancer* **2014**, *110*, 1698–1704.
383. I. Rizvi, S. Nath, G. Obaid, M. K. Ruhi, K. Moore, S. Bano, D. Kessel, T. Hasan, *Photochem. Photobiol*. **2019**, *95*, 419–429.
384. A.-L. Bulin, M. Broekgaarden, T. Hasan, *Sci. Rep*. **2017**, *7*, 16645.
385. W. Chen, J. Zhang, *J. Nanosci. Nanotechnol*. **2006**, *6*, 1159–1166.
386. H. Hope, *Prog. Inorg. Chem.* **1994**, 1–19.
387. Saint, Version 8.37a; Bruker AXS, Inc.: Madison, WI, 2013.
388. APEX3, Version **2016**.9–0; Bruker AXS, Inc.: Madison, WI, 2016.
389. SADABS, version **2016**/2; Bruker AXS, Inc.: Madison, WI, 2014.
390. G. Sheldrick, *Acta Crystallogr., Sect. A* **2015**, *71*, 3–8.
391. O. V. Dolomanov, L. J. Bourhis, R. J. Gildea, J. A. K. Howard, H. Puschmann, *J. Appl. Crystallogr*. **2009**, 42, 339–341.
392. M. S. Kang, J. B. Oh, S. G. Roh, M. R. Kim, J. K. Lee, S. H. Jin, H. K. Kim, B. *Bull. Korean Chem. Soc*. **2007**, *28*, 33–40.
393. S. Callaghan, M. A. Filatov, H. Savoie, R. W. Boyle, M. O. Senge, *Photochem. Photobiol. Sci.* **2019**, *18*, 495–504.
394. V. Bogoeva, M. Siksjø, K. G Sæterbø, T. B. Melø, A. Bjørkøy, M. Lindgren, O. A. Gederaas, *Photodiagnosis. Photodyn. Ther.* **2016**, *14*, 9–17.

395. E. Peña-Cabrera, A. Aguilar-Aguilar, M. González-Domínguez, E. Lager, R. Zamudio-Vázquez, J. Godoy-Vargas, F. Villanueva-García, *Org. Lett.* **2007**, *9*, 3985–3988.
396. G. Meng, S. Velayudham, A. Smith, R. Luck, H., Liu, Macromolecules **2009**, *42*, 1995–2001.
397. S. Hattori, K. Ohkubo, Y. Urano, H. Sunahara, T. Nagano, Y. Wada, N. V. Tkachenko, H. Lemmetyinen, S. Fukuzumi, *J. Phys. Chem. B.* **2005**, *109*, 15368–15375.